Aerial Cooperative Manipulation : full pose manipulation in air and in interaction with the environment

Dario Sanalitro

THÈSE

En vue de l'obtention du

DOCTORAT DE L'UNIVERSITÉ FÉDÉRALE TOULOUSE MIDI-PYRÉNÉES

Délivré par :

l'Institut National des Sciences Appliquées de Toulouse (INSA de Toulouse)

Présentée et soutenue le *08/04/2022* **par :**

DARIO SANALITRO

Aerial Cooperative Manipulation: full pose manipulation in air and in interaction with the environment

---

JURY

JACQUES GANGLOFF	Professeur Université de Strasbourg	Rapporteur
STÉPHANE CARO	Directeur de Recherche au CNRS, LS2N, Nantes	Rapporteur
IVANA PALUNKO	Associate Professor Université de Dubrovnik	Examinatrice
JUAN CORTÉS	Directeur de Recherche au CNRS, LAAS, Toulouse	Examinateur
ANTONIO FRANCHI	Chercheur CNRS et Professeur Université de Twente, Pays-Bas	Directeur de thèse

---

École doctorale et spécialité :
EDSYS : Robotique 4200046

Unité de Recherche :
Laboratoire d'analyse et d'architecture des systèmes

Directeur de Thèse :
Antonio FRANCHI

Rapporteurs :
Jacques GANGLOFF et *Stéphane CARO*

Abstract

One of the major abilities of robotic systems is to provide a contribution to the perception of the surrounding environment through the set of sensors they are equipped with. Such a capacity has been largely exploited since their first appearance in the real world. The Unmanned Aerial Vehicles (UAVs) advent has even accelerated such process. In fact, aerial vehicles are able to reach larger workspaces with respect to other classes of robots. Moreover, in recent years, technological advancements have led to the employment of robotic systems in more complex operations where the robots interact with the external environment. This challenge is particularly relevant in many robotics applications such as grasping, transporting, positioning, assembling, decommissioning.

Single aerial vehicles are capable of performing such assignments. As a matter of fact, the variety of proposed solutions endows the aerial platforms with specific interaction tools. Among them, one can find multi degrees-of-freedom arms, gripping systems, robotic hands, cables, etc. Nevertheless, in certain cases, the manipulation workspace and the overall payload of a single UAV result limited. Therefore, multi-robot systems could be employed.

In such a context, these considerations have motivated the study on the *cooperative manipulation problem* whose principle goal is to regulate all the degrees-of-freedom of a manipulated payload with a team of multiple robots. Such a problem finds its place in a wide range of applications such as contact-based inspections, structure assembling, decommissioning or maintenance, precision manipulation in agriculture, in environmental protection, in space explorations etc.

The core contribution of this thesis is a set of models and control algorithms defined to solve the aforementioned cooperative multi-robot manipulation problem. We aimed at addressing the main challenges related to such a topic in two principal contexts: *in air* and *in interaction* with the environment.

In contact-free scenarios, we first propose a generic dynamical formulation of the problem whose generality resides in the type, in the number of robots that can be employed and in the type of payload-robots connections that can be used. A decentralized control action has subsequently been developed. It is based on a leader-follower paradigm which allows steering the payload to the specific desired position and orientation. The equilibria and the stability of the system together with the robustness against external disturbances and noisy measurements have been deeply analyzed and discussed with the aid of an extensive numerical campaign of simulations.

We then formulated and solved the cooperation problem examining a more spe-

cific solution that constitutes the minimum setup to obtain full pose regulation of a payload employing cables. Three robots and six cables are sufficient to obtain a statically-rigid system suitable for such a goal. A kinematic centralized approach, robust against model uncertainties and dynamical disturbances, allows the system's control in fulfilling the 6 degrees of freedom regulation of the manipulated payload. Moreover, with the aim of performing pick-and-place operations in an efficient way, we considered the multi-robot system as a Cable-Suspended Aerial Multi-Robot Manipulator (CS-AMRM) and we extended the entire control architecture with a methodology based on a dynamical formulation to estimate mass and center of mass of the manipulator's end-effector in order to estimate possible additional payloads. The usefulness of the proposed algorithms has been demonstrated through simulations and experimental results.

Finally, we considered the problem of cooperative manipulations in interactions with the environment. First, we propose a shared control strategy that allows the collaboration between the CS-AMRM and a human operator in construction assembly and decommissioning tasks. Specifically, the requested task consists of performing pick-and-place operations. Secondly, building on top of the motion controller presented for contact-free assignments, we provide a solution that takes care of the interaction tasks acting with a self-regulatory behavior. Therefore, an admittance control framework allows to generate compliant system trajectories and a model-based wrench observer retrieves the external wrenches acting on the end-effector of the CS-AMRM. In both cases, the performed experimental results show the effectiveness of the proposed approaches.

In our belief, the proposed set of model designs and control algorithms represents a contribution towards the development of multi-robot systems able to perform coordinated manipulation tasks in an effective manner. Although much work remains to be done, our analytical and experimental results demonstrate theoretically-interesting and practically-relevant properties that may encourage the use of the proposed approaches in practice.

Keywords

Aerial physical interaction, Multi-Robot Systems, Cooperative manipulation, Robust/Adaptive Control of Robotic Systems.

Resumé

L'une des capacités majeures des systèmes robotiques est d'apporter une contribution à la perception de l'environnement qui les entoure grâce à l'ensemble des capteurs dont ils sont équipés. Une telle capacité a été largement exploitée depuis leur première apparition dans le monde réel. L'avènement des véhicules aériens sans pilote (UAV) a même accéléré ce processus. En fait, les véhicules aériens sont capables d'atteindre des espaces de travail plus grands par rapport aux autres classes de robots. De plus, ces dernières années, les progrès technologiques ont conduit à l'utilisation de systèmes robotiques dans des opérations plus complexes où les robots interagissent avec l'environnement extérieur. Ce défi est particulièrement pertinent dans de nombreuses applications robotiques telles que la préhension, le transport, le positionnement, l'assemblage, le démantèlement.

Les véhicules aériens simples sont capables d'effectuer de telles missions. En effet, la variété des solutions proposées dote les plateformes aériennes d'outils d'interaction spécifiques. Parmi eux, on trouve des bras multidegrés de liberté, des systèmes de préhension, des mains robotisées, des câbles, etc. Néanmoins, dans certains cas, l'espace de travail de manipulation et la charge utile globale d'un seul UAV sont limités. Par conséquent, des systèmes multirobots pourraient être utilisés.

Dans un tel contexte, ces considérations ont motivé l'étude du problème de *manipulation coopérative* dont le but principal est de réguler tous les degrés de liberté d'une charge manipulée avec une équipe de plusieurs robots. Un tel problème trouve sa place dans un large éventail d'applications telles que les inspections par contact, l'assemblage de structures, le démantèlement ou la maintenance, la manipulation de précision dans l'agriculture, la protection de l'environnement, les explorations spatiales, etc.

La contribution principale de cette thèse est un ensemble de modèles et d'algorithmes de contrôle définis pour résoudre le problème de manipulation multirobot coopératif mentionné ci-dessus. Nous avons cherché à aborder les principaux enjeux liés à un tel sujet dans deux contextes principaux : *dans l'air* et *en interaction avec l'environnement.*

Dans des scénarios sans contact, nous proposons d'abord une formulation dynamique générique du problème dont la généralité réside dans le type, dans le nombre de robots pouvant être employés et dans le type de connexions charge utile robots pouvant être utilisées. Une action de contrôle décentralisée a ensuite été développée. Il est basé sur un paradigme leader suiveur (leader follower) qui permet de diriger la charge vers la position et l'orientation spécifiques souhaitées. Les équilibres et la stabilité du système ainsi que la robustesse contre les perturbations externes et les mesures bruyantes ont été profondément analysés et discutés à l'aide

d'une vaste campagne numérique de simulations.

Nous avons ensuite formulé et résolu le problème de coopération en examinant une solution plus spécifique qui constitue la configuration minimale pour obtenir une régulation complète de la pose d'une charge utilisant des câbles. Trois robots et six câbles suffisent pour obtenir un système rigide statiquement adapté à un tel objectif. Une approche cinématique centralisée, robuste aux incertitudes du modèle et aux perturbations dynamiques, permet le contrôle du système en respectant les 6 degrés de liberté de régulation de la charge manipulée. Dans le but d'effectuer des opérations de prélèvement et de placement de manière efficace, nous avons considéré le système multirobot comme un manipulateur aérien multirobot suspendu par câble (CS-AMRM) et nous avons étendu l'ensemble de l'architecture de contrôle avec une méthodologie basée sur une formulation dynamique pour estimer la masse et le centre de masse de l'effecteur terminal du manipulateur afin d'estimer d'éventuelles charges supplémentaires. L'utilité des algorithmes proposés a été démontrée par des simulations et des résultats expérimentaux.

Enfin, nous avons considéré le problème des manipulations coopératives dans les interactions avec l'environnement. Premièrement, nous proposons une stratégie de contrôle partagé qui permet la collaboration entre le CS-AMRM et un opérateur humain dans les tâches d'assemblage et de démantèlement de la construction. Plus précisément, la tâche demandée consiste à effectuer des opérations de prélèvement et placement d'objets. Deuxièmement, en s'appuyant sur le contrôleur de mouvement présenté pour les affectations sans contact, nous proposons une solution qui prend en charge les tâches d'interaction agissant avec un comportement d'autorégulation. Par conséquent, un cadre de contrôle "d'admittance" permet de générer des trajectoires de système conformes et un observateur de clé basé sur un modèle récupère les clés externes agissant sur l'effecteur terminal du CS-AMRM. Dans les deux cas, les résultats expérimentaux réalisés montrent l'efficacité des approches proposées.

À notre avis, l'ensemble proposé de conceptions de modèles et d'algorithmes de contrôle représente une contribution au développement de systèmes multirobots capables d'effectuer des tâches de manipulation coordonnées de manière efficace. Bien que beaucoup de travail reste à faire, nos résultats analytiques et expérimentaux démontrent des propriétés théoriquement intéressantes et pratiquement pertinentes qui peuvent encourager l'utilisation des approches proposées dans la pratique.

Keywords

Interaction Physique Robots Aériens avec l'environnement, Systèmes multirobot, Manipulation coopérative, Contrôle robuste/adaptatif des systèmes robotiques.

Contents

List of Figures

List of Tables

List of Symbols

AM Aerial Manipulator

APhI Aerial Physical Interaction

CS-AMRM Cable-suspended Aerial Multi-Robot Manipulator

ESC Electronic Stability Control

DoF Degrees of Freedom

GNSS Global Navigation Satellite System

GPS Global Positioning System

MoCap Motion Capture System

IMU Inertia Measurement Unit

PID Proportional Integral Derivative

RPV Remotely Piloted Vehicle

UAV Unmanned Aerial Vehicle

UAR Unmanned Aerial Robot

UKF Unscented Kalman Filter

VTOL Vertical Takeoff and Landing

List of Multimedia

[**video-1**] Full-pose Manipulation Control of a Cable-suspended Load with Multiple UAVs under Uncertainties. https://www.youtube.com/watch?v=2NDgsvjvg38. 2020 (Cited in page 100.)

[**video-2**] Inertial Estimation and Energy-Efficient Control of a Cable-suspended Load with a Team of UAVs. 2020 (Cited in page 108.)

[**video-3**] Precise Cable-suspended Pick-and-Place with an Aerial Multi-robot System. 2021 (Cited in page 119.)

[**video-4**] Indirect Force Control of a Cable-suspended Aerial Multi-Robot Manipulator. 2022 (Cited in page 126.)

Part I

Preliminaries

Chapter 1

Introduction

This first chapter intends to be the introduction of the entire manuscript. First, the objective is to outline the research topic that the whole manuscript aims at investigating. The second purpose is to offer the literature context where this work finds its place. Lastly, the target is to reason about the main contributions this work has brought to the state-of-the-art.

1.1 Motivation

Over the course of centuries, human beings have constantly attempted to conceive solutions able either to mimic the behaviour of the creatures in nature in the various interactions with the environment or to modify the environment in which they operate. Nowadays, humans are highly familiar with these creations that they refer to as "robots". The term made its first appearance in 1920 when the playwright Karel Čapek in the play Rossum's Universal Robots coined the term deriving it from the term *robota* that means executive labour in Slav languages.

Besides being familiar with robots, human beings also comprehend the considerable impact these systems have in many aspects of modern life, from health-care to industrial manufacturing, safety, transportation and many other fields. Several of today's most exciting robots have their roots in systems that scientists and engineers invented as long ago as 60 years. They have been pioneering robots because of their revolutionary impact. Among them, *Unimate*, the first robotic arm and the precursor of the well-known fixed-based industrial manipulators thoroughly studied in many works in robotics as [Paul 1983, Siciliano 2009] which was able to lift pieces of hot metal from die casting machines operating from a fixed based on the ground (see Fig. 1.1a). An increased workspace of the robots has been obtained by controlling the base position. In 1972, the Artificial Intelligence Center of Stanford Research Institute showed the first general-purpose mobile robot, *Shakey*, which could break down simple commands into a specific sequence of actions needed to achieve an objective (see Fig. 1.1b). In this case, the locomotion was achieved through wheels, however bipeds, quadrupeds and humanoids started to appear as well. In 1995, *General Atomics' Predator* cleared the way for *aerial robots* (see Fig. 1.1c). First designed for reconnaissance purposes, the remotely piloted aircraft was able to fly in the 3D space unquestionably reaching more extensive workspaces. This main achievement was facilitated by the development of accurate sensors, the advent of Global Navigation Satellite Systems (GNSSs) and the growth of lightweight and

(a) (b) (c)

Figure 1.1: (a) Unimate, the first robotic arm (1961); (b) Shakey the first general-purpose mobile robot (1972); (c) General Atomics' Predator, the first remoted piloted aircraft (1995)

compact processors that characterized the early 80s and provided better sensing and navigation capabilities.

The central purpose of aerial roboticists is to study, design and conceive aerial systems capable of performing, autonomously or partially autonomously, given tasks. Not considering military applications in which aerial robots are defined as Remotely Piloted Vehicle (RPV), the literature refers to civil aerial robots as Unmanned Aerial Vehicles (UAVs) or Unmanned Aerial Robots (UARs), and in the following, these two last denominations will be used. However, given their world-wide achieved success, it is worth mentioning that they are nowadays commonly known as drones. In actual fact, since the beginning, the interest in UAVs has seen significant growth. Their low cost compared to other robotic solutions, their versatility and the theoretically limitless workspace they can reach, have made them suitable for a wide range of applications. A list of such applications encloses search and rescue operations, pollution monitoring, hurricane inspecting, wildfire surveillance, agriculture monitoring, remote patrolling, aerial surveying, mapping, filming, etc. For a more complete overview of the current state-of-the-art on remote sensing applications, the reader is referred to [Pajares 2015]. Moreover, such list clarify that the research community and the industry represent the main interested actors in the aerial robotics domain. As a matter of fact, over the years, they have also been contributors to the development of several types of UAVs to answer the request of a wide variety of applications.

The technique employed by UAVs to counterbalance the gravitational force represents one of the classification methodologies that can be considered. The outcome is a taxonomy that comprehends four leading types of UAVs: *Fixed-wing* UAVs, *Flapping wings* UAVs, *Convertible* UAVs and *Rotary wings* UAVs.

Fixed-wing designs benefit from generating a difference in the air pressure on precise points of the floating platform. Conversely, inspired by birds' flights, *flapping wings* can generate lift forces used to counteract the gravitational force. The two

approaches are not free of shortcomings. High cruise velocities are required for the first ones precluding, in this way, the possibility to use such platforms in cluttered environments or in situations where stable positions in time have to be maintained. By contrast, on the one hand, *flapping wings* models require arduous mechanical designs. On the other hand, they are ill-suited to accomplish precise manoeuvres. To face these challenges, researchers and engineers have found rotating propellers solutions to be valid alternatives. In the beginning, particular attention was given to *convertible* UAVs which combine cruising flight and vertical takeoff and landing (VTOL) capabilities [Morin 2015]. However, small-scale helicopters, or rotor-craft designs such as ducted fan [Hofer 2016] or multi-rotors platforms, belonging to the category of *rotary wings* UAVs, have resulted more effective for applications where small sizes and static thrusts are the principal requirements. Their main characteristic is that their control is obtained by regulating the speed of the rotors. In doing so, the wrench applied to the Center of Mass (CoM) of the platforms can be changed. Apart from helicopters, which have been extensively studied in the literature [Ren 2012], one of the most famous and representative model of such category is the quadrotor. However, as a drawback, it has to be mentioned that all these designs require an increased power consumption and therefore, they can fly for a limited time. In conclusion, in such a wide range of platforms that can be employed, most of the time, the main characteristics in accomplishing a particular task suggest the decision on the most suitable vehicles.

Another way of classifying this broad set of aircraft is by considering their dimensions. The interested reader is referred to [Cai 2014] for a detailed review of such vehicles with particular attention to their size. For the purposes that will be described in this thesis, the focus of our attention will be on small-scale UAVs, with an emphasis on the employment of such vehicles for civil applications. In particular, quadrotors will be the employed vehicles in light of the previous and coming considerations.

1.2 Aerial Physical Interactions

Coming in almost all possible forms and sizes, the UAVs platform presented until now find their employment in a wide range of applications. In particular, as already discussed, they have represented the means to fly a multitude of remote sensing instruments in several scenarios which have allowed to accomplish *contact-less* assignments. However, over the recent years, such platforms have demonstrated that it is possible to extend the spectrum of their potential applications. Thus, *in-contact* operations, where physical contacts with the environment are requested, can be performed. These demonstrations have led to extremely promising studies in the Aerial Physical Interaction (APhI) and aerial manipulation fields, which in turn have guided the community to conceive prototypes, functionalities and capabilities with the final aim of performing manipulation tasks while flying. Such activities are characterized by active exchanges of forces and torques between the aerial vehicles

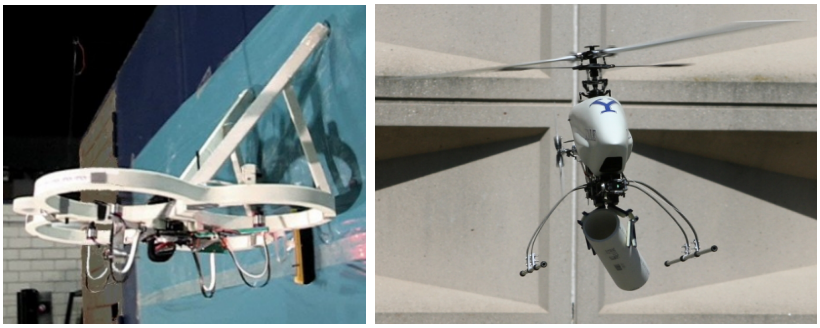

(a) (b)

Figure 1.2: First generation of aerial manipulators: (a) Flying robot interacting with a wall during a stable flight [Albers 2010]; (b) Aerial manipulation testbed carrying a tube [Pounds 2012]

and the environment. Therefore, the list of real-life employments of aerial robots can be extended appending tasks as, contact-based inspection and maintenance, assembly/construction and decommissioning of structures, transportation. The use of aerial robots in such unsafe or hazardous scenarios, provides, as a first result, the reduction of the risks for human operators and, from another point of view, the lowering of the costs related to such activities. An extensive and detailed survey on the topic that illustrates the assortment of the obtained achievements over the last 40 years can be found in [Ollero 2021]. Three predominant generations of aerial manipulators have ensued:

- Fist Generation: *Conventional quadrotors with small enhanced capabilities*;
- Second generation: *Aerial platforms adapted to interactions*;
- Third Generation: *Advanced aerial platforms.*

Examples of the *first generation* (see Fig. 1.2) are aerial platforms enriched with the ability to shove into walls [Albers 2010], grasping objects [Mellinger 2011], transporting objects with passive links [Palunko 2012, Palunko 2013], constructing structures [Lindsey 2012]. With the promising advancements, the transition from conventional designs to less conventional ones has been moderately straightforward. Helicopters have contributed to such rapid growth - especially in outdoor environments - with introductory works in load transportation [Bernard 2010, Bernard 2011, Pounds 2012], interaction with the environment [Pounds 2010b] and object manipulation [Kondak 2014]. In such scenarios, their abilities of a major operational time and payload capacity have been significantly evident. Nevertheless, the same attention has been given both to helicopters and multi-rotor solutions. In particular, the advancements of the *second generation* provide relevant evidence of this statement (some examples are presented in Fig. 1.3). Rigid and compliant arms have started to be designed and placed on aerial platforms. Outdoor navigation sensors or the improvements of indoor navigation

(a) (b)

Figure 1.3: Second generation of aerial manipulators: (a) Flying Mobile Manipulator Unmanned Aerial Vehicle [Morton 2016]; (b) Aerial manipulator in an indoor environment [Muscio 2018]

devices have offered more reliable state estimation and thus more suitable flights for such platforms [Jimenez-Cano 2013, Danko 2015, Lippiello 2015, Kamel 2016, Morton 2016, Kanellakis 2017, Muscio 2018]. Although the obtained achievements, the whole picture of aerial manipulators cannot be deprived of the *third generation* that represents, up to now, the category that contains the most advanced exemplars (see Fig. 1.4 for some examples). This last family includes platforms reliable in both indoor/outdoor environments [Ollero 2018], fully actuated platforms [Brescianini 2018, Ryll 2019], multiple arms [Suarez 2020], cable-suspended aerial manipulators [Sarkisov 2019, Yiğit 2021], vehicles that leverage on on-board SLAM [Pumarola 2019].

Moreover, it has to be mentioned that all the achieved results are a direct consequence of the international synergies that have converged on several collaborative projects whose a partial list that includes some projects already concluded and some still ongoing is presented in the following. In particular, the proposed list gives a small overview and the main scopes of each project which are:

- ARCAS: the design of ARs for assembly and construction of structures;
- AEROARMS: the design and the production of ARs with high manipulation capabilities which can rely on tele-manipulation for industrial inspection and maintenance;
- AEROWORKS: the conceiving of heterogeneous and collaborative aerial robotic workers which can be involved in inspection and maintenance of infrastructure environments;
- AIROBOTS: the development of robotics systems able to perform interactive tasks and remote inspection by contact;
- AEROBI: the elaboration of ARs with specialized multi-joint arms conceived for in-depth structural inspection of concrete bridges and with short term

(a) (b)

Figure 1.4: Second generation of aerial manipulators: (a) An aerial dual-arm manipulator with compliant joints [Ollero 2018]; (b) A fully actuated platform interacting with the environment [Ryll 2019]

marketing scope;

- ARCOW: the production of aerial co-workers collaborating with humans;
- HYFLIERS: the development of a robot with hybrid capabilities in terms of mobility (air and ground mobility) with a long-reach hyper-redundant manipulator capable of accomplishing tasks in hardly-accessible sites;
- SPECTORS: the design of prototypes in the direction of the sensing technologies, big data cloud computing, applications in precision agriculture, environmental protection;
- PRO-ACT: the design and the demonstration of cooperative manipulations capabilities between different robots in the context of space explorations;
- AERIAL-CORE: the development of advanced robotic systems with high capabilities on the operational range and on safety in interacting with people from one side, and the design of aerial co-workers for applications in the context of inspection and maintenance;
- MUROPHEN: the design of control strategies for a team of robots to reach the cooperation toward the common goal of monitoring dynamic phenomenon;
- FLYING CO-WORKERS: the design of robots capable of cooperative handling and assisting workers by directly delivering objects and tools safely and efficiently.

Nevertheless, the development of autonomous or semi-autonomous manipulation systems still requires to solve open challenges. Payload capacity or wide-ranging workspace coverage are the most evident. Possible solutions have been found in combining the effort of several UAVs to cooperatively transport and/or manipulate objects.

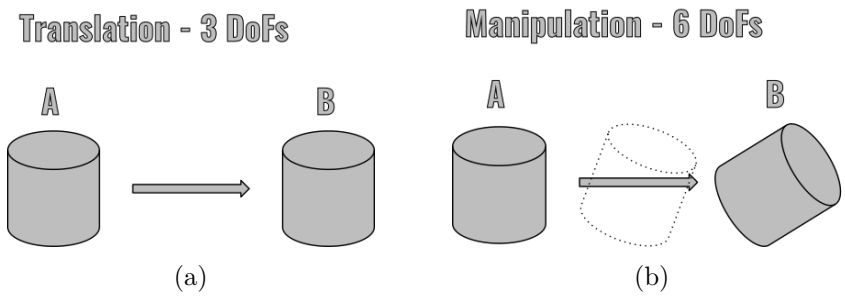

Figure 1.5: Difference between translation and manipulation

1.3 Cooperative Transportation and Manipulation

Cooperative transportation and/or manipulation are primary abilities in groups of living beings. They represent powerful ways through which humans or animals interact with the environment and the external world in general. In the context of this thesis, the terms *transportation* and *manipulation* will be largely used. Although it may sound like they refer to the same action, we will highlight their difference with the aid of a simple example. With the term transportation, one or more entities are assumed to be able to move an object from one location to another, specifically from a point A to a point B (see Fig. 1.5a). Hence, only three Degrees of Freedom (DoFs) of the object are managed. Conversely, with the term *manipulation*, one or more entities are assumed to be capable of transporting and changing the orientation of the object at the same time and at any moment of the route (see Fig. 1.5b). Therefore, the full-pose control can be obtained.

The distinction has been made to emphasize the major effectiveness of the manipulation. As a matter of fact, in most of the physical interaction tasks, the full pose control can represent either a strong requirement or an advanced feature. One may think of transporting objects that cannot enter in limited spaces unless tilting them, or peg-in-hole operations where the control of the position of the load is not enough.

Cooperative manipulation skills involve a series of control decisions that mainly concern the definition of objects to interact with, the comprehension of the relative positioning, the determination of the sequence of actions to perform, the awareness of the uncertainties. Living beings perform such tasks requiring a dynamic perception, control and adjustment of their manipulation "tools", on the one hand, and sharp transitions between the body and the environment dynamics on the other hand [Sugasawa 2021].

With the aim of mimicking nature but also with the recent development of an increasingly technological world, significant efforts have been made by scientists and engineers to investigate whether a swarm of robots could be envisioned with such skills. The relevant results that have been obtained will be discussed in the following.

One first line of works embraces cooperative manipulations performed through

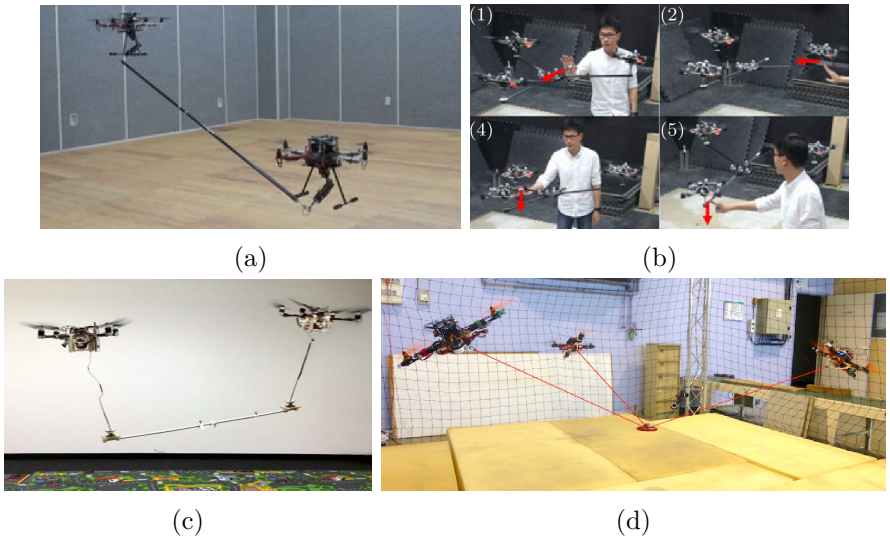

(a) (b)

(c) (d)

Figure 1.6: Cooperative manipulations: (a) performed with two AMs [Kim 2018b]; (b) performed using rigid links attached through spherical joints to a payload [Nguyen 2015]; (c) performed using cables and a vision-based approach based on a leader-follower scheme [Gassner 2017];(d) performed using cables [Erskine 2019].

two or more AMs (Aerial Manipulators) that consist of aerial vehicles equipped with multi-DoFs arms [Lee 2015, Yang 2015, Kim 2018a, Kim 2018b]. In such scenarios, high precision of payloads' pose control can be obtained. Nevertheless, simultaneously managing the high-dimensional dynamics of the entire systems and the interactions with the environment and the objects still represent a considerable challenge.

Aerial vehicles can also be used as distributed actuators. Solutions where multiple quadrotors have been rigidly attached to the objects, are presented in [Mellinger 2013, Loianno 2018]. However, in such cases, the manipulation has been much demanding to obtain than the transportation. Such shortcoming is caused by the under-actuation property of the multi-rotors, especially when all the rotors are parallel. To overcome such limitations, the combination of rigid links attached through spherical joints to the payload has resulted reliably effective as demonstrated in [Nguyen 2015, Mohammadi 2016, Nguyen 2018, Tagliabue 2019, Six 2021] guaranteeing the full actuation of the platform handled by the robots.

Moreover, if the rigid links are replaced with cables, flexible floating transportation structures can be designed. One of the interesting features is that such cables allow to partially decouple the rotational dynamics of the vehicle w.r.t. the one of the carried payload. In addition, the robots' payload capacity significantly increases due to their lightweight and the robot formation shapes become more flexible, provided that spherical joints are employed.

Although the community has been focusing on the topic for a while now, it is still in the process of studying the problem of the cable-suspended transporta-

tion/manipulation investigating models, developing suitable planning tool and control strategies.

Among the earliest demonstrations, it is possible to register [Bernard 2010] where helicopters have been used to transport an object. A dynamical formulation of the aforementioned system has been illustrated in [Bernard 2011]. In the latter, a two-DoFs cable angle sensor and a cable-tension sensor were employed to measure and compensate for the cable tension affecting the helicopter dynamics. The transportation of a point-mass has been performed in [Erskine 2019] by means of an aerial cable towed system. An advanced solution in which the cable lengths can be changed while flying has been presented in [Li 2020]. In [De Marina 2019], the transportation task has been performed by means of two UAVs. The authors presented a distributed controller based on an incremental nonlinear dynamic inversion that relies only on relative measurements and does not require global positioning. In [Gassner 2017], two UAVs perform the transportation task with a vision-based approach based on a leader-follower scheme with the use of an admittance control framework and a wrench observer. A formation control to transport the payload with the focus on robustness is described in [Rossomando 2020]. Perturbations and modeling uncertainties are taken into account.

However, in all the mentioned works the orientation of the payload was not fully controlled. For this reason, in the following, special attention will be devoted to solutions where the full manipulation of objects performed by flying cable-suspended systems is addressed.

1.4 Cable-suspended cooperative manipulation

Full pose aerial cooperative manipulations of cable-suspended loads has provided several advantages in recent developments. Configurations involving solely two robots have been presented. In [Tognon 2018] the authors propose a communication-less approach, which relies on the sensing of contact forces and a leader-follower paradigm; in [Villa 2021] the virtual structure approach has been used to define the multi-robot system. The dynamic effects of the cables and the quadrotors are then treated by means of an adaptive compensator. However, despite full pose manipulations can be achieved, the payload control can be quite limited if the number of robots is inadequate. The oscillations generated by the cable-suspended load and perturbations in the robot positions, restrict the system to transport the load using smooth and, to some extent, slow motions.

Conversely, a full pose control of the load is possible when the robotic system can attain a six-dimensional wrench on the load by controlling the orientation of the cables and the force applied by them. The minimum setup with this ability is a system composed of three vehicles connected, through three cables, to three non-collinear points on the load [Prattichizzo 2008] (see Fig. 1.7 (a) for a schematic example). In [Michael 2009, Michael 2011, Fink 2011, Jiang 2013], the authors considered the problem of transporting a triangular plate-like payload with three quadrotors and

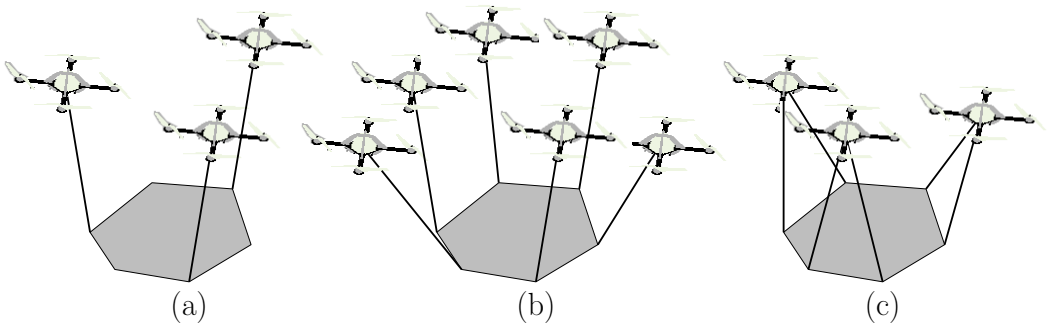

Figure 1.7: Cable-suspended load configurations: (a) Three robots and three cables [Sreenath 2013]; (b) Six robots and six cables [Masone 2016]; (c) Three robots and six cables (the Fly-Crane).

three cables. Specifically, in [Michael 2009, Michael 2011, Fink 2011] the problem was treated as a quasi-static motion planning challenge where the authors compute the position of the robots as a consequence of the desired payload pose in $SE(3)$. In the meantime, the generated solutions take into account some feasibility conditions, such as cable tension and collision avoidance, optimization and non-trivial payload motion plans. In [Sreenath 2013], the dynamical formulation of the triangular plate-like transportation has been presented to realize high-speed payload motions. The UAVs follow in open-loop the nominal references computed from the desired load trajectory using differential flatness. In [Lee 2017], a configuration with three robots and three cables attached to the load has been controlled employing a geometric control technique capable of dealing with model errors and external disturbances.

However, the main drawback of these setups is that the compensation of a time-varying external disturbing wrench - such as it might be the wind - must be obtained by moving the three aerial vehicles to reorient the three cables. This makes the overall systems sluggish and imprecise in real-world conditions. To overcome such drawback one has to employ a *statically rigid* [Connelly 2015] (or *force-closure* [Prattichizzo 2008]) design. Such design allows to compensate time-varying external wrenches, almost instantaneously, by solely varying the stresses while keeping all the cables in the same orientation. Six is the minimum number of cables in order to gain such a property. A possible setup is the one using six cable-robot pairs [Masone 2016], as in Fig. 1.7 (b). However, the use of six aerial vehicles considerably increases the overall system complexity and costs. A simpler and more efficient choice consists in using only three aerial vehicles connected to a pair of cables each [Manubens 2013] (see Fig. 1.7 (c)). From now on, we will refer to such multi-robot aerial systems, that make use of cables to manipulate objects, as Cable-suspended Aerial Multi-Robot Manipulators (CS-AMRMs).

Up to here, the focus has been on finding the best designs that are the most suitable for controlling the full pose of the cable-suspended payloads. However, another distinction could be made by looking at the characteristics of the imple-

mented coordination mechanisms. In particular, in the literature panorama, the resolution of the multi-robot problem can be faced in two principal ways. The first one relies on centralized approaches and consists of control architectures where the robotic agents can communicate and share information with a centralized station or each other. In this way, the global information about the state of the whole system is maintained. However, despite being straightforward to design, such architectures are not robust against common failures or unpredictable situations. The second strategy is represented by decentralized approaches where the agents rely on local information. Therefore, communication-less or neighbour-to-neighbour solutions are the most employed ones. Such strategies have the advantage of reducing the potential communication delay between the robots, showing greater robustness, flexibility and scalability.

Along with the already presented, several other works develop control architectures where the regulation among the UAVs is achieved using a communication-based formation control [Dhiman 2018, Tan 2018, Geng 2019, De Marina 2019]. Distributed methodologies have also been proposed [Farivarnejad 2018, Gabellieri 2018].

1.5 Cooperative manipulation: *in-contact* scenarios

Another interesting direction for the compelling problem of the cooperative manipulation is represented by the management of the interactions with the surrounding environment in an *active* fashion. Ground robots are able to use the ground reactions provided by their constrained bases to counteract external forces and torques. Single AMs have to generate appropriate control inputs to produce the precise forces and torques to counteract the external disturbances. For CS-AMRMs, the payload's accurate control of such forces and moments requires that each robot has to always guarantee that a six-dimensional wrench is exerted on the platform even if contacts with the environment can affect the cables' tightness.

In such context, it is possible to recognize three main classes of interactions, in which such systems can be implicated:

1. *Unexpected-collision interactions*: where the transportation or the manipulation of objects in adverse circumstances may arise in unexpected collisions which have to be carefully managed

2. *Expected-collision interactions*: where it is known in advance that contacts will take place. As a consequence, such interactions have to be carefully regulated. Examples are pick-and-place operations, inspections, or peg-in-hole tasks.

3. *Active interactions*: where the transportation or the manipulation can be reinforced through direct collaboration with an active external source such as another robot or a human.

An interesting and exhaustive framework for collisions, in which robotic manipulators are the main agents, was introduced in [Haddadin 2017] where the authors

described a detailed collision event pipeline, composed of detection, isolation, identification and reaction phases.

One of the critical issues for aerial robot interactions is mainly represented by the measurement of the interaction wrench (identification phase) which allows to determine the directional information and the intensity of the interaction/collision force. One of the most reliable solutions for single UAV manipulators [Nava 2020, Cataldi 2016, Peric 2021], is to make use of force/torque sensors to measure the interaction forces. However, the costs and weight of such devices cannot be considered negligible for aerial platforms. Last but not least, force/torque sensors can only punctually measure the interaction , i.e., where the sensor is placed, while collision can happen at any point of the platform. Therefore, alternative solutions based on wrench estimation have been investigated. In [Meng 2018], the authors showed a contact force control for an aerial manipulator where the UAV acts as the sensor of the exerted force on the environment. In [Ryll 2019], an IMU-enhanced momentum-based observer was presented.

In the context of multi-robot systems, wrench estimators have mainly been employed in evaluating the role of the internal forces in co-manipulation tasks as in [Kim 2018c, Tognon 2018] while they have never been employed in the identification of possible external forces/torques acting on the payload of CS-AMRMs.

After the identification phase, the aerial multi-robot system has to properly react according to the interaction forces resulting from an interaction event. Only a few works have considered this aspect. In [Nguyen 2018], the authors firstly investigated the problem of cooperatively controlling the six DoFs of the flexible platform rigidly attached to three quadrotors by means of three movable bars. In addition, they proved its efficacy in rejecting external disturbances showing, as well, an example of object tele-manipulation. Nevertheless, the authors' main focus was the analysis of the effectiveness of the compliant properties of the system. Therefore, intensity and directional information of the external disturbances, as well as a deeper characterization of the compliant behavior were not entirely described.

Besides, another aspect of CS-AMRMs that has been marginally addressed in the literature is the problem of enabling single human operators to control the manipulated objects in an intuitive way. In actual fact, the major concern for a single person in dealing with such systems is represented by the difficulty to command each independent vehicle involved in the multi-robot system. Shared control strategies represent an effective way to cope with the complexity of such systems. These approaches have received particular attention in aerial robotics cause they are considerably promising means to intensify the use of UAVs in real-world scenarios. In the context of applications where the aerial vehicles are used to perceive the environment, as optimal coverage, mapping, etc., apart from single robot applications [Jiang 2015, Masone 2018], a collaborative force-feedback architecture has been presented in [Lee 2013] where the teleoperation of a formation of MAVs is performed. A single remote human can steer all (or some) robots controlling their velocities while haptically perceiving the UAVs' state. A multi-master/multi-slave

bilateral shared control system has been presented in [Franchi 2012] to control the remaining DoF of a multi-robot system. The control scheme provides feedback signals to the operator of the quality of the execution of the human's intended motion plan while fulfilling the relative-bearing constraints.

In the context of shared control strategies for APhI involving multi-robot systems interacting with the environment, the problem of reliably including human operators is at its preliminary stages and a little investigation has been performed so far. However, in [Orsag 2016], the authors show a consensus-based formation control strategy for a team of three UAVs, among which one is equipped with a multi-DoF manipulator, Therein, human operators can enter the control loop, in case of failures for example, by passing motion commands to the UAVs and to the AM; in [Prajapati 2020], leveraging on a classical methodology, a human is able to control the leader of a formation in a leader-follower paradigm, without haptic feedback nor other types of support; in [Masone 2021] the authors present a bilateral shared control framework in which the operator can command the payload as well as the shape of the formation. In the meantime, an obstacle avoidance algorithm runs to avoid collisions with the static environment. The feedback allows the human to realize possible obstacles and singularities of the formation.

This overview of works related to the problem of transportation and full pose manipulation of cable-suspended load in air and in-contact scenarios illustrates that the community has been visibly active in investigating new solutions in the field of cooperative aerial robotics. Nevertheless, at the time this thesis started, there was significant room for improvements, especially in connection to the implementation and the production of multi-robot solutions for physical interaction tasks that could be employed in real-world scenarios. With this in mind, this thesis presents the results obtained in the design and the implementation of a multi-robot system for the manipulation of objects, with special attention on cable-suspended solutions, given the good trade-off of using cables in the increased payload capacity and the decoupling of the dynamics of the robots w.r.t. the carried objects.

1.6 Contribution of the Thesis

In this section, the aim is to provide a global overview of the scientific contributions described by this thesis. In addition, the reader can find a supplement in Tab. 1.1 where a schematic presentation of the main publications and achievements that constitute the skeleton of this manuscript is shown.

As already corroborated in the previous sections, statements about the relevant extent of the aerial robotics field and in particular of the aerial physical interaction field can be treated as facts. However, despite the profuse amount of effort and works in this domain, the open challenges that result to be not yet solved deserve additional investigation. In this context, the design and the development of multi-robot systems capable of exchanging forces and torques with the surrounding environment have been tackled. Moreover, a multi-robot system, composed of three aerial vehicles that carry a suspended load through cables, has been designed, built and implemented. Such a system, called Fly-Crane, is able to achieve decoupled tracking of 6D trajectories in position and orientation. This characteristic makes it suitable to perform APhI tasks. Specifically, transportation and manipulation, since the suspended load can be endowed with specific tools, such as fingers, magnetic grippers, etc., that can grasp objects.

Precisely controlling the motion of such systems and enlarging the set of their capabilities without ignoring their physical limitations has been the major concern after the designing phase. As a result, the made efforts drew to different control algorithms. The first control strategy aims at solving the problem of the cooperative manipulation through a communication-less approach based on a leader-follower scheme. The method relies on the sensed contact forces exchanged between the robots and between the robots and the carried payload. Conversely, the second control architecture is based on a centralized approach that relies on an inverse kinematic proportional controller augmented with a feed-forward term. The method has been refined to guarantee the stability of the closed-loop and to minimize the effects of external disturbances and model errors. Moreover, the accurate knowledge of some dynamical parameters, such as mass and CoM of the carried payload can result crucial when physical interaction tasks have to be accomplished. Therefore, with this in mind, a supplementary inertial parameter estimation algorithm improves the already designed control architecture in order to obtain better performances.

Moreover, to perform APhI tasks, the motion control strategies have been extended in order to manage the interactions with the environment. The considered scenarios are, on the one hand, collaborative tasks with humans and, on the other hand, direct exchanges with the surrounding environment. To allow the cooperation between a human and the multi-robot system in performing manipulations, starting from the already developed inverse kinematic controller, a shared control layer has been included in the control architecture. The goal is to make the human capable of having full control of the manipulation task, without the need of independently controlling each UAV. Conversely, to handle the exchanges with the

Part II - Aerial Cooperative Manipulations in Air

Publication	Contribution
[Gabellieri 2020] Journal Swarm Intelligence	A study on force-based collaboration in swarms • Generic model for robotic agents for full pose cooperative manipulation of objects; • Control law based on a leader-follower paradigm relying only on implicit communication; • Analyses on the equilibrium configurations, their stability, the robustness of the system, corroborated with numerical simulations.
[Sanalitro 2020] Journal RAL/ICRA 2020	Full-pose Manipulation Control of a Cable-suspended Load with Multiple UAVs under Uncertainties • Model, design and realization of the statically rigid CS-AMRM Fly-Crane; • Uncertainty-aware controller which guarantees the robustness of a proportional IKC controller augmented with a feed-forward term; • Experimental validation assessing stability and robustness.
[Petitti 2020] Conference ICUAS 2020	Inertial Estimation and Energy-Efficient Control of a Cable-suspended Load with a Team of UAVs • Method to estimate mass and CoM position of a loaded platform (i.e. the Fly-Crane platform including a transported load); • Method to minimize the total effort exerted during a full-pose manipulation task; • Validation of the proposed algorithms in non-ideal conditions through simulations performed on the Gazebo simulator.

Part III - Aerial Cooperative Manipulations in Interaction with the Environment

Publication	Contribution
[Jimenez Cano 2021] Journal *Submitted to* JINT	Precise Cable-suspended Pick-and-Place with an Aerial Multi-robot System • Shared control strategy involving a human operator in the task accomplishment; • Pick-and-place and manipulation tasks in construction/decommissioning scenarios.
[Sanalitro 2022] Journal *Submitted to* RAL	Indirect Force Control of a Cable-suspended Aerial Multi-Robot Manipulator • Control strategy which allows to handle the interactions of the Fly-Crane with the environment; • Admittance framework to generate new reference trajectories; • Contact estimation through a generalized momentum based observer; • Validation in real-world scenarios;

Table 1.1: Summary of the publications in Part II-III and corresponding contribution list

surrounding environment, the architecture has been extended with a model-based wrench observer to estimate the contact wrenches. An admittance filter shapes the compliant behavior of the multi-robot system at will. All these methods have found their validation in extensive experimental and numerical campaigns. Furthermore, the results of such advancements brought to arrange, to some extent, challenging demonstrations. Among them, the flight of three aerial vehicles carrying a load, pick-and-place operations in construction and decommissioning scenarios, manipulations where unexpected interactions with the environment take place or manipulations that can be reinforced through direct collaboration with an external source. All these demonstrations have allowed us to demonstrate the efficacy and the practicability of cooperative cable-suspended manipulations. As a matter of fact, despite not being at its very early stage, this line of research still represents an attractive domain for the research community and there is still plenty of room for improvement. In conclusion, the interested reader is referred to the multimedia material to visually appreciate the proposed systems in action in the different experimental campaigns.

1.7 Thesis Organization

This section is meant to be a sort of guide for the reader. The goal is to show the organization of the thesis in which the summary of each chapter is presented.

The thesis has been essentially divided into three main parts:

Part I has a twofold objective. First, it is characterized by some preliminary concepts presented with the intent of smoothing the way, whether necessary, for the problems tackled in this manuscript. The second purpose is to provide the general context in the aerial robotics domain from which this work has taken inspiration and where it aims at contributing.

Part II introduces the section of the modeling and the motion control strategies for the multi-robot aerial systems in the context of performing APhI tasks. Particular relevance has been given to the accomplishment of the much more arduous assignment of full pose manipulation with and without relying on explicit communication. Additionally, the conditions for preserving the system stability throughout the assigned tasks have been assessed and analyzed. The part ends with offering a section with the details about the results of the validation of the control strategies in *free-contact* scenarios, i.e. applications where any contact occurs between the multi-robot aerial system and the surrounding environment.

Part III has been conceived to contain the extensions of the motion control laws developed in Part II to deal with interactions with humans, on one hand and the surrounding environment on the other hand. In these particular *in-contact* scenarios, the interactions between the multi-robot aerial system and the environment besides to be expected are as well purposefully managed. Even in such cases, the theoretical outcomes coming from the extension of the control architecture are supported with real experimental results.

With the previously described subdivision in mind, an additional partition in chapters of the manuscript will allow to develop in a concise way the content of each of them.

Concerning Part I:

Chap. 2 serves as a preliminary step, whether necessary, to recollect the mathematical methodologies which represent the bases on which the theoretical analysis on aerial vehicles and on multi-robot aerial systems have been developed. Specifically, the Lagrangian and the Newton-Euler formalisms will be revised to then derive the dynamical model of a rigid body. Then, using the same formalisms and given the similarity of flying parallel robots (FPRs) with the CS-AMRMs, we will provide an overview on the kinematics and the dynamics of FPRs. To conlcude, the inverse kinematic control algorithm will be presented.

Chap. 3 is meant to describe, in the details, first, the models of the possible links used to connect robots and payloads. Then, we focus on the models of the subsystems composing the aerial vehicles under examination, i.e actuators and sensors. In addition, the generic mathematical model of the employed unidirectional-thrust aerial vehicle in free-flight and a possible strategy for its dynamic control will be given, together with the model for the aerial vehicle's propellers and onboard sensors.

Regarding Part II:

Chap. 4 proposes two models of multi-robot systems involved in cooperative manipulations. While the first is a general formulation based on leader-follower scheme not relying on explicit communication, the second one aims at modeling an optimized solution to perform full pose manipulations in a centralized way.

Chap. 5 details two control algorithms for the tracking of 6D pose trajectories, i.e. position and orientation. While the former consists of a force-based controller obtained through an admittance-filter paradigm, the latter relies on an inverse kinematic proportional controller augmented with a feed-forward term which is capable of dealing with model uncertainties and external disturbances. The inertial parameter estimation and an optimization strategy to solve the redundancy of the manipulator finalize the control architecture.

Chap. 6 offers the results of the extensive numerical simulations and the experimental campaign of the control strategies devised in Chap. 5

Regarding Part III:

Chap. 7 shows the accomplishments of the challenging task of performing pick-and-place operations in construction of structure and decommissioning scenarios. The control architecture has been extended to include human operators in the control loop.

Chap. 8 contains the theoretical principles to move from motion control to interaction control. Building on top of the inverse kinematic controller presented in Chap. 5, the multi-robot has been provided with the abilities of interacting with the surrounding environment. Experimental results show such capabilities in a diverse set of conditions.

Chap. 9 brings to an end this manuscript by concisely summarizing the presented scientific content and the extensions for possible future works.

In conclusion, it has to be mentioned that all the accomplishments presented in this thesis have been conducted within the context of two projects. On the one hand, the European project AERIAL-CORE, whose purposes are related to produce progress in the state-of-the-art of aerial manipulation systems by increasingly

augmenting their capabilities. The final and arduous objective is employing such platforms for applications connected to inspection and maintenance of wide-ranging infrastructures. Among the several examples that can be offered, transportation and manipulation of objects, pick-and-place operations in decommissioning contingencies, active interactions with other active external sources such as other robots or humans. All these tasks require advanced designs and highly-developed control strategies to guarantee stable flights of the platforms while the exchanges with the external environment are suitably managed.

On the other hand, the MuRoPhen project whose goals are mainly the design of control strategies for teams of robots to reach the cooperation toward the common goal of monitoring dynamic phenomenon. With the aim of fulfilling the challenges that such projects delineate, the effort of these last three years of work has shown in-line outcomes. As a matter of fact, the presented multi-robot aerial manipulator, the Fly-Crane, encompasses a series of abilities that correspond to the demand for skillful aerial platforms. In addition, the discussed motion and interaction control strategies strengthen the potential of such a system due to their interchangeability in driving it in *contact-less* and *in-contact* flights. Furthermore, the performed pick-and-place operations described in Chap. 7 represent the first proof-of-concept of an aerial manipulator achieving assembly and decommissioning tasks in an effective way.

1.8 Publication Note

This thesis is based on four journal papers (two of which are still under review process) and one conference paper. With the aid of Tab. 1.1, the list of the publications is reported in a more schematic way. A further conference paper [Umili 2020] has been co-authored, but it is not reported in this thesis. It describes different methodologies for the coordination problem of aerial robots for assembly applications and not the cooperative problem which has been the aim of the manuscript. For such reason, we evaluated to not consider it inside the general discussion of this work.

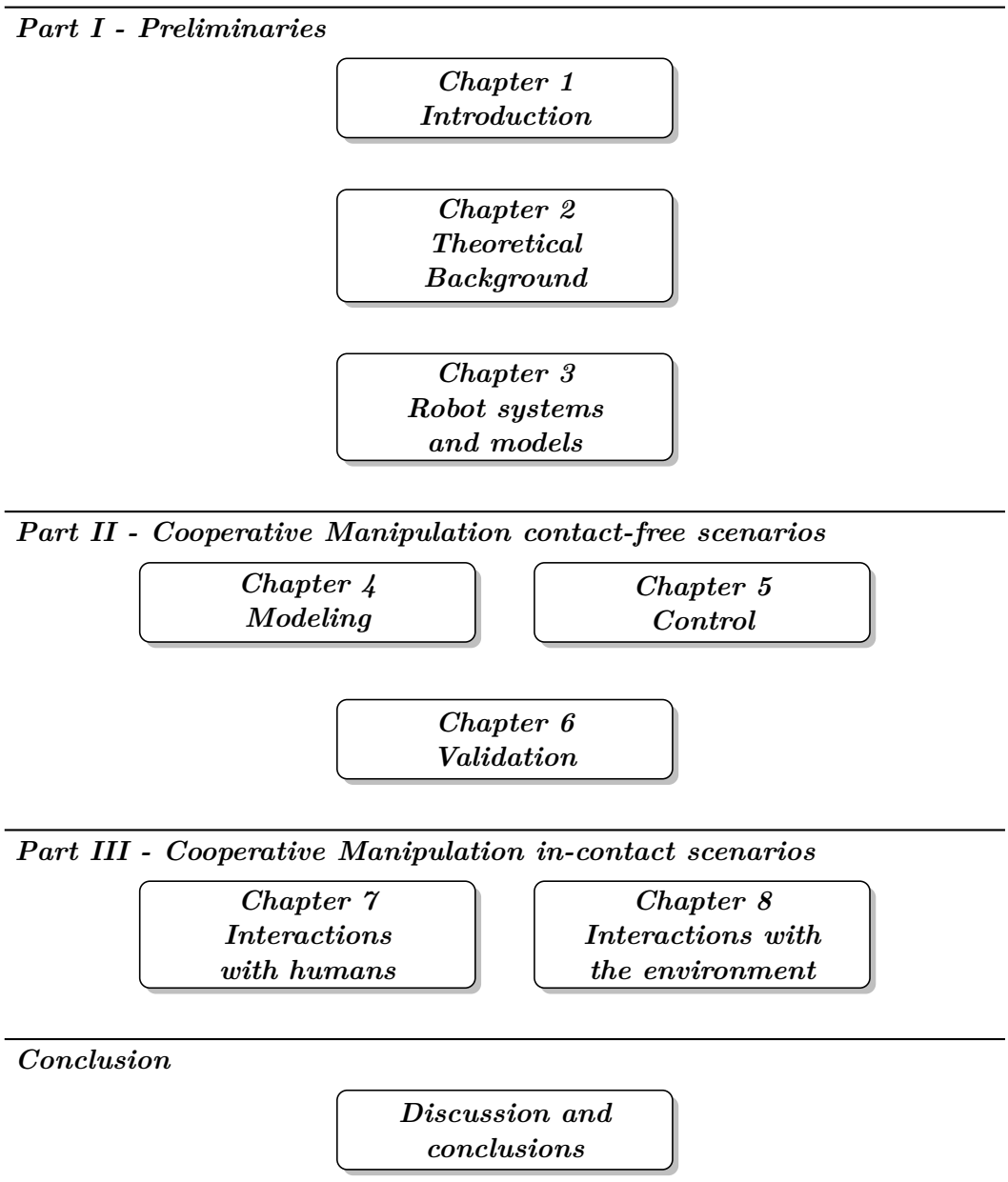

Figure 1.8: Structure of the thesis

Chapter 2

Theoretical Background

This chapter is dedicated to an overview of the theoretical methodologies that have been fundamental mathematical tools in the development of the concepts presented in the following chapters. In particular, this review contains functional general methods to *model* generic mechanical systems with a specific focus on rigid bodies and to analyze their *dynamic properties*. These concepts will be the basis to describe a particular class of aerial robots, i.e. the unidirectional thrust vehicles, commonly known as quadrotors.

Moreover, since this thesis will also deal with multi-robot aerial manipulators, which are very close to parallel robots, we propose a brief outline on the modeling and the control of such complex systems. In particular, in order to manipulate an object in space, the end-effector position and orientation have to be necessarily described. Therefore, the kinematics, and, afterwards, the differential kinematics of a multi-robot system will be provided. In this way, we elucidate both the relationship between the joint variables and the end-effector pose and the relationship between the joint velocities and the corresponding end-effector linear and angular velocities. A general inverse kinematic algorithm together with the derivation of the dynamical model for such systems will conclude this further introductory chapter.

Before diving into the details of the aforementioned notions, let us introduce a minute summary of the adopted notation to ease the reader understanding.

Notation In this thesis, we denote (column) vectors and matrices in bold font, with lower and upper case, respectively. The transpose operator is denoted with the superscript $\bullet^\top$. Letter superscripts of vectors represent the reference frame w.r.t. which these vectors are expressed[1]. The notation $\mathbb{R}^{n\times m}$ points to the set of real matrices with m rows and n columns. $\mathbf{1}_{m\times n}$ and $\mathbf{0}_{m\times n}$ indicates the matrices with with m rows and n columns with all the elements equal to 1 and 0 respectively. The notations $SO(3)$ and $SE(3)$ are related to the special orthogonal group of 3D rotations and the special Euclidean group of 3D rotations and translations, respectively. The operator $[\bullet]_\times \in so(3)$ represents the skew-symmetric matrix associated to any vector $\bullet \in \mathbb{R}^3$, while its inverse operator $\bullet^\vee \in \mathbb{R}^3$ denotes the vector associated with any skew-symmetric matrix $\bullet$.

2.1 Modeling

The derivation of a dynamical model represents a crucial phase in the analysis of rigid bodies, their motion and the conception of control strategies. Particularly

[1] If there is no specification, the inertial world frame has to be considered as the reference frame.

relevant is the study of the relation between motion and forces.

In the literature, two are the principal methodologies applied to derive the equations of motion of a mechanical system. However, despite producing the same outcome, the procedures are considerably different.

The first method is based on the *Lagrange formulation* that retains the properties of being simple, systematic and suitable to derive the dynamic equations that describe the model, independently from the reference frame. Condensing the procedure, by selecting the proper set of generalized coordinates, one can compute the kinematics and potential energy functions that, afterwards, the formalism employs to derive the dynamic equations. Constraints and reaction forces are also taken into account. Despite this, the method results quite impractical in the context of complex systems with many degrees of freedom.

The second method relies on the *Newton-Euler formulation*. It is an efficient and recursive method that finds its best applications in manipulators with open kinematic chains and complex systems. Its main feature is that it allows, first, to separately describe each joint of a robot and then to compute all the couplings through the so-called *forward-backwards* algorithm.

Throughout this thesis, these will be the two approaches taken into consideration for the derivation of the dynamical equations of the rigid bodies under examination. Therefore, in the following, the implementation bases of the two methodologies will be outlined. However, we refer the reader to more complete and exhaustive theoretical explanations [Spong 2006, Siciliano 2009, Lynch 2017].

2.1.1 Lagrange Formalism

As a first step, the Lagrangian formulation requires the choice of a set of independent coordinates $\boldsymbol{q} = [q_1 \ ... \ q_{\bar{n}}]^\top \in \mathbb{R}^{\bar{n}}$, called *generalized coordinates*. These quantities describe the configuration of the system and its $\bar{n} \in \mathbb{N}_{>0}$ DoF. The choice of the generalized coordinates is crucial to properly define the constraints of the system. The following step is to compute the *generalized forces* according to the chosen generalized coordinates. Considering a set of forces $\boldsymbol{f} = [\boldsymbol{f}_1^\top \ ... \ \boldsymbol{f}_{\bar{m}}^\top]^\top \in \mathbb{R}^{3\bar{m}}$, where the generic force $\boldsymbol{f}_i \in \mathbb{R}^3$ is applied on the system at point $\boldsymbol{r}_i \in \mathbb{R}^3$, with $i = 1, ..., \bar{m}$ and $\bar{m} \in \mathbb{N}_{\geq 0}$. We can then compute the generalized force $\xi_j(\boldsymbol{f}, \boldsymbol{q}) \in \mathbb{R}$ w.r.t. the j-th generalized coordinate q_j as

$$\xi_j(\boldsymbol{f}, \boldsymbol{q}) = \sum_{i=1}^{m} \boldsymbol{f}_i^\top \frac{\partial \boldsymbol{r}_i}{\partial q_j}, \quad j = 1, ..., \bar{n} \tag{2.1}$$

At this stage, the *Lagrangian* function $\mathcal{L}(\boldsymbol{q}, \dot{\boldsymbol{q}})$ can be defined as the difference between the total kinetic energy $\mathcal{K}(\boldsymbol{q}, \dot{\boldsymbol{q}})$ and the potential energy $\mathcal{U}(\boldsymbol{q}, \dot{\boldsymbol{q}})$, i.e. $\mathcal{L}(\boldsymbol{q}, \dot{\boldsymbol{q}}) = \mathcal{K}(\boldsymbol{q}, \dot{\boldsymbol{q}}) - \mathcal{U}(\boldsymbol{q}, \dot{\boldsymbol{q}})$. Applying the following Lagrange equations, it's possible to derive the equations of motion as

$$\frac{d}{dt} \frac{\partial \mathcal{L}(\boldsymbol{q}, \dot{\boldsymbol{q}})}{\partial \dot{q}_j} - \frac{\partial \mathcal{L}(\boldsymbol{q}, \dot{\boldsymbol{q}})}{\partial q_j} = \xi_j(\boldsymbol{f}, \boldsymbol{q}), \quad j = 1, ..., \bar{n} \tag{2.2}$$

The computation of the potential and the kinetic energy for the systems objects of this manuscript can be reduced to the sole gravitational potential energy, for the first case, and the quadratic form $\mathcal{K}(\boldsymbol{q}, \dot{\boldsymbol{q}}) = \frac{1}{2}\dot{\boldsymbol{q}}^\top \boldsymbol{M}(\boldsymbol{q})\dot{\boldsymbol{q}}$ for the kinetic energy, where $\boldsymbol{M}(\boldsymbol{q}) \in \mathbb{R}^{\bar{n}\times\bar{n}}$ is the inertia matrix of the system. The equations of motion (2.2), can be rewritten in the typical form:

$$\boldsymbol{M}(\boldsymbol{q})\ddot{\boldsymbol{q}} + \boldsymbol{C}(\boldsymbol{q}, \dot{\boldsymbol{q}})\dot{\boldsymbol{q}} + \boldsymbol{g}(\boldsymbol{q}) = \boldsymbol{\xi}(\boldsymbol{f}, \boldsymbol{q}) \tag{2.3}$$

where $\boldsymbol{C}(\boldsymbol{q}, \dot{\boldsymbol{q}})\dot{\boldsymbol{q}} \in \mathbb{R}^{\bar{n}}$ contains the centrifugal and Coriolis terms, while $\boldsymbol{g}(\boldsymbol{q}) \in \mathbb{R}^{\bar{n}}$ is the gravitational term, and $\boldsymbol{\xi}(\boldsymbol{f}, \boldsymbol{q}) = [\xi_1(\boldsymbol{f}, \boldsymbol{q}) \ ... \ \xi_{\bar{n}}(\boldsymbol{f}, \boldsymbol{q})]^\top \in \mathbb{R}^{\bar{n}}$. Within this type of formulation, the contributions to the generalized forces in $\boldsymbol{\xi}(\boldsymbol{f}, \boldsymbol{q})$ are represented by the non-conservative forces, i.e. the joint actuators, friction wrenches and external wrenches, in the case of a robotic manipulator.

In such a context, two types of problems can be defined in the study of the dynamics: the *direct dynamics* problem and the *inverse dynamic* problem. The objective is to find a solution to the two aforementioned problems. In particular, the direct dynamics problem consists of deriving the accelerations $\ddot{\boldsymbol{q}}$, the velocities $\dot{\boldsymbol{q}}$ and the position $\boldsymbol{q}$ that result from the vector of the generalized forces $\boldsymbol{\xi}(\boldsymbol{f}, \boldsymbol{q})$.

Conversely, the inverse dynamic problem allows to determine the generalized forces $\boldsymbol{\xi}(\boldsymbol{f}, \boldsymbol{q})$ suitable to produce the quantities $\ddot{\boldsymbol{q}}$, $\dot{\boldsymbol{q}}$ and $\boldsymbol{q}$.

While the Lagrangian formalism is often employed in solving the inverse dynamic problem and, hence, the control problem, the recursive algorithm provided by the Newton-Euler formalism allows to efficiently find the solutions of both the direct dynamics problem and the inverse dynamics problem.

2.1.2 Newton-Euler formalism

The Newtonian mechanics plays a fundamental role in the definition of the Newtown-Euler formalism. The conservation of the linear and the angular momentum applied to a rigid body is indeed the basis on which the formulation can be derived. Then, if the system experiences a wrench, the derivatives of the linear and angular momentum, considered w.r.t. an inertial reference frame, result to be equal to the total contribution of the forces and torques applied to the CoM. This outcome can be described through the following mathematical derivation

$$\begin{aligned} \frac{d(m\boldsymbol{v})}{dt}\Big|_I &= \boldsymbol{f} \\ \frac{d(\boldsymbol{J}^I\boldsymbol{\omega})}{dt}\Big|_I &= \boldsymbol{\tau} \end{aligned} \tag{2.4}$$

with $m \in \mathbb{R}_{>0}$ and $\boldsymbol{J}^I \in \mathbb{R}^{3\times3}_{>0}$ being mass and inertia matrix of the rigid body about the inertial frame I whose origin is the body CoM, with $\boldsymbol{v}$ and $\boldsymbol{\omega} \in \mathbb{R}^3$ that are the linear and angular velocity of the rigid body under exam. Ultimately, $\boldsymbol{f}$ and $\boldsymbol{\tau} \in \mathbb{R}^3$ represent the total contribution of the forces and torques applied to the

CoM.

In the case of a multi-link body system, which is the example that will be given in the following, each link is handled by first describing the equations of its linear and angular motions and then by considering the coupling effect that the adjacent links exert on it. Thus, the algorithm which is based on two recursive steps, i.e *forward recursion* and *backward recursion*, can be applied. By doing so, all the coupling terms can be properly managed and, a description of the entire multi-body system can be obtained. More into the details, with the forward recursion the links' velocities and accelerations are propagated from the first link to the final one. The translational and rotational velocities and accelerations of the i-th link are derived by means of the ones of the previous one ($(i-1)$-th link) and of the i-joint, according to their type (either prismatic or revolute). With the aim of deriving the end-effector velocities and accelerations, the method is repeated for all the links of the chain, starting from the base link and terminating with the last one. With the second step, the backward recursion, forces and torques are then propagated from the last link to the first one. Thus, the knowledge of the total force and moment applied to the $(i+1)$-th link, $\boldsymbol{f}_{i+1}$, $\boldsymbol{\tau}_{i+1} \in \mathbb{R}^3$ allows to compute the ones applied to the i-th link, $\boldsymbol{f}_i$, $\boldsymbol{\tau}_i \in \mathbb{R}^3$ resolving the Newton-Euler equations. Once again, the method is applied to all the links composing the multi-body system, from the end-effector back to the base link.

The resulting equations applying the Newton-Euler formalism, not being in *closed-form* given the coupling of each link with the neighboring ones, emerge to be considerably suited to efficiently solve the direct and the inverse dynamics problem.

2.1.3 Rigid body dynamics

In the literature and consequently, in this manuscript, the aerial vehicles are often modeled as rigid bodies. Hence, an overview of the dynamical modeling of this essential elements will be provided. With reference to Fig. 2.1, we denote with $\mathcal{F}_W = O_W, \{\boldsymbol{x}_W, \boldsymbol{y}_W, \boldsymbol{z}_W\}$ and $\mathcal{F}_B = O_B, \{\boldsymbol{x}_B, \boldsymbol{y}_B, \boldsymbol{z}_B\}$, respectively, the inertial world frame and the body frame attached to the rigid body. The origin of $\mathcal{F}_B$ is chosen coincident with the CoM of the rigid body and its position is described by the vector ${}^W_B\boldsymbol{p} \in \mathbb{R}^3$. The orientation of $\mathcal{F}_B$ w.r.t. $\mathcal{F}_W$ can be described with several different formalism. Among them, the prevalent ones used by the robotic community are: *i)* the *exponential coordinates*, *ii)* the *Euler-angles*, *iii)* the *Rotation matrix* and, *iv)* the *unit quaternions*. In the following, we present a summary of them underlining the pros and cons of each of them:

i) The *exponential coordinates* or *axis-angle* representation allows to represent relative orientations between frames by means of a single rotation about a specific axis $\boldsymbol{v} \in \mathbb{R}^3$ of an angle $\theta \in \mathbb{R}$. Hence, four parameters are needed: three for the rotation axis and the remaining one is for the angle of rotation. However, since one of the three parameters of the unit vector can be derived from the other two, the formalism represents a minimal three-parameter description. Nevertheless, the

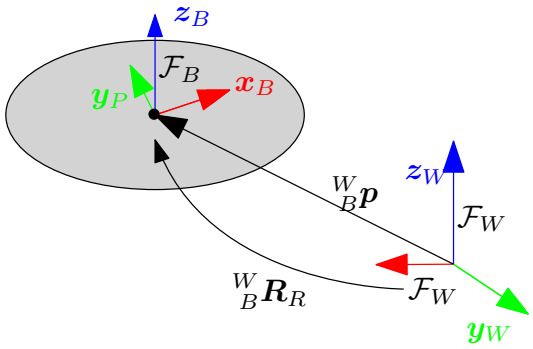

Figure 2.1: Schematic representation of a rigid bod with its reference frames

drawback of the approach is that the representation is not unique, i.e. a rotation of $-\theta$ around $-\boldsymbol{v}$ results in the same orientation of a rotation θ around $\boldsymbol{v}$. Moreover, the rotation combinations are complicated to express and when the rotation angle is zero, the axis of rotation result undetermined;

ii) The *Euler-angles*, which is a minimum representation based on three angles, describes the rotation of a rigid body with solely three parameters. These latter are the angles of the ordered sequence of rotations around three selected axes. According to the chosen axes sequence and the order of the rotations, several names can be given to refer to the specific representation. One of the well-known conventions, particularly relevant in the aeronautic field, is the *intrinsic yaw-pitch-roll* sequence[2] which consists of successive rotations about the moving axes $\boldsymbol{z}_B$, $\boldsymbol{y}_B$, $\boldsymbol{x}_B$ with the angles ψ, θ, ϕ. Nevertheless, the shortcoming of such representation is that it has a singularity when the rotational axis of the middle term in the sequence becomes parallel to the first or the third axis of rotation;

iii) The *Rotation matrix* delineated as ${}^W_B\boldsymbol{R}_R \in SO(3)$ is a transformation matrix that describes the rotation of $\mathcal{F}_B$ w.r.t. $\mathcal{F}_W$. One of its main properties is ${}^W_B\boldsymbol{R}_R\,{}^W_B\boldsymbol{R}_R{}^\top = {}^W_B\boldsymbol{R}_R{}^\top\,{}^W_B\boldsymbol{R}_R = \boldsymbol{I}_3$. Not presenting any singularity and despite being a redundant description, this notation is one of the most preferred for control design purposes, especially in the aerial robotics domain;

iv) The *unit quaternions* is a four-parameter notation that solves the singularity problems of the other representations, especially the non-uniqueness of the angle-axis representation. Compactness and efficiency are the additional properties.

Within this manuscript, we will make use of the rotation matrix notation due to its property of being simple. Furthermore, this choice has led to the use of the Newton-Euler methodology for the modeling of the rigid body. As already mentioned, such formalism allows to derive the dynamics of the rigid body in order to relate the motion of its CoM, i.e. linear and angular accelerations (${}^W_B\ddot{\boldsymbol{p}}$ and

[2]The convention is equivalent to the *extrinsic roll-pitch-yaw* sequence whose rotations are about the axes $\boldsymbol{x}_W$, $\boldsymbol{y}_W$ and $\boldsymbol{z}_W$ with angles ϕ, θ and ψ

${}^{B}_{B}\boldsymbol{\omega}$, respectively), to forces $\boldsymbol{f} \in \mathbb{R}^3$ and torques $\boldsymbol{\tau} \in \mathbb{R}^3$ acting on the body. As in most of the texts presented in the literature, the translational dynamics will be derived in world frame while the rotational one will be defined in body frame with the advantage that the inertia, expressed in body frame, will be independent of the particular orientation of the body.

Therefore, one can write the dynamics as

$$\begin{bmatrix} m\boldsymbol{I}_3 & \boldsymbol{0}_3 \\ \boldsymbol{0}_3 & \boldsymbol{J} \end{bmatrix} \begin{bmatrix} {}^{W}_{B}\ddot{\boldsymbol{p}} \\ {}^{B}_{B}\dot{\boldsymbol{\omega}} \end{bmatrix} = \begin{bmatrix} -mg\boldsymbol{e}_3 \\ -{}^{B}_{B}\boldsymbol{\omega} \times \boldsymbol{J}\,{}^{B}_{B}\boldsymbol{\omega} \end{bmatrix} + \left(\begin{bmatrix} \boldsymbol{f} \\ \boldsymbol{\tau} \end{bmatrix} + \begin{bmatrix} \boldsymbol{f}_{ext} \\ \boldsymbol{\tau}_{ext} \end{bmatrix} \right) \tag{2.5}$$

where g is the gravitational acceleration, $\boldsymbol{e}_3 = [0\ 0\ 1]^\top$, $\boldsymbol{I}_3 \in \mathbb{R}^{3\times3}$ represents the identity matrix, ${}^{B}_{B}\dot{\boldsymbol{\omega}}$, ${}^{B}_{B}\boldsymbol{\omega}$ are the angular acceleration and the angular velocity w.r.t. $\mathcal{F}_W$ expressed in $\mathcal{F}_B$ and ultimately, $\boldsymbol{f}_{ext}$ and $\boldsymbol{\tau}_{ext} \in \mathbb{R}^3$ are the external forces and torques.

In conclusion, the presented model turns out to be considerably general and therefore, it can be used to describe the dynamics of a generic aerial vehicle. This will be done in the following chapter, in which a detailed model of a Unidirectional Thrust vehicle will be given. Moreover, in the presence of the external wrenches $\boldsymbol{f}_{ext}$ and $\boldsymbol{\tau}_{ext}$, the interactions with possible external sources can also be taken into consideration. Therefore, while in the case of *contact-less* operations, the term can be approximated to zero, *in-contact* operations will require this term to be considered, as it will more detailed in Chap. 8.

2.2 Parallel Robots and Aerial Multi-Robot Manipulators

In the previous sections, we described the derivation of the dynamical model of a rigid body. In the following one, we will define some of the mechanical systems that, among the tasks that are capable to do, they are able to move rigid bodies. The considered mechanical systems are the Flying Parallel Robots (FPRs). The rigid body under exam is, instead, their end-effector.

FPRs are a particular subclass of the more general set of parallel robots. Their main difference w.r.t. classical parallel robots lies in the employed actuators that, in the case of flying parallel robots, are aerial vehicles and whose detailed dynamical model will be discussed in Chap. 3. Therefore, part of the already acquired knowledge in the domain of parallel robots is applicable to describe this recent particular class of systems. In particular, the previous studies allow to introduce the derivation of their kinematic and dynamical models, as well as their possible singularities. Once again, in the following, an outline of the fundamentals will be presented. However, the interested reader could find more complete and exhaustive theoretical explanations in [Merlet 2005, Briot 2015].

A formal description suggests that a generalized parallel manipulator is a closed-loop kinematic chain mechanism whose end-effector is linked to the base by several

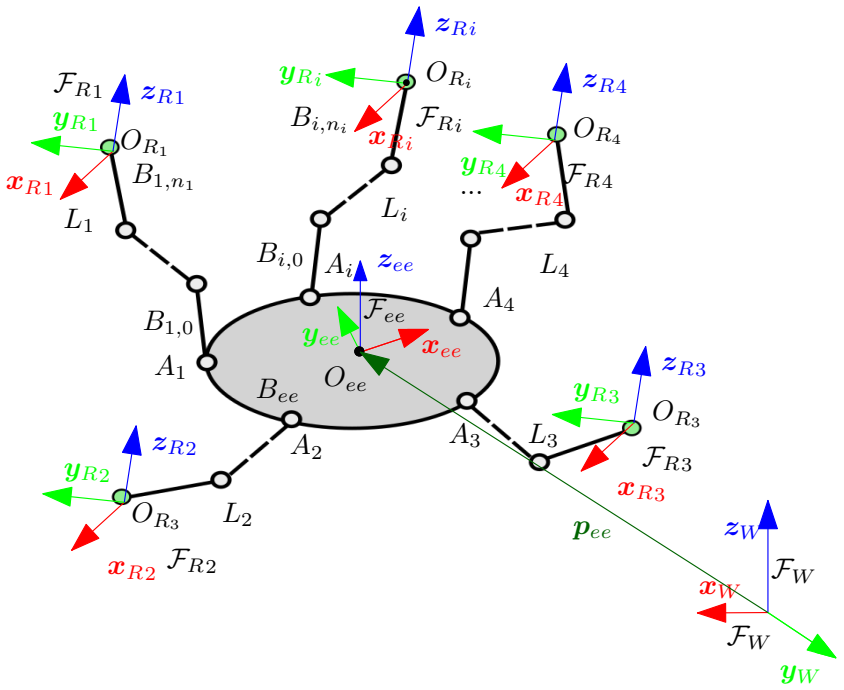

Figure 2.2: General scheme of a flying parallel robot (FPR) and its main variables.

independent kinematic chains [Merlet 2005]. A more practical definition allows to depict a parallel robot as a system composed of: *i)* an end-effector with n DoF, *ii)* a fixed-base, *iii)* at least two independent kinematic chains. Parallel robots for which the number of chains is strictly equal to the number of DoF of the end-effector are called *fully parallel manipulators*.

2.2.1 Kinematics of Flying Parallel Robots

To derive the FPRs dynamics, there are two fundamental aspects to consider beforehand: their kinematic representations and the study of the singularities. For such a goal, the resolution of the inverse geometric problem and/or the resolution of the direct geometric problem are required. With the former, the velocities of the end-effector are used to compute the velocities of the aerial vehicles. Conversely, the latter requires the knowledge of the velocities of the aerial vehicles to compute the end-effector velocities.

A general FPR (shown in Fig. 2.2) is a multi-body mechanism composed of an end-effector B_{ee}, n legs L_i with $i = 1, ..., n$ and n aerial vehicles. The i-th leg is composed of n_i rigid bodies $B_{i,j}$ with $j = 1, .., n_i$ connected by means of passive joints such that they compose a kinematic chain.

As for the rigid body, we denote with $\mathcal{F}_W$ the inertial world frame, with $\mathcal{F}_{ee}$ the body frame attached to the center O_{ee} of the FPR's end-effector, with $\mathcal{F}_{R_i}$ the frame attached to the CoM of the robot R_i. Each leg L_i relates each aerial vehicle with the platform. In particular, the body $B_{i,0}$ of the kinematic chain is attached to

the platform at A_i through a passive joint which can be of any type. The body B_{i,n_i} joins the kinematic chain and each robot by means of a spherical joint at O_{R_i}. The choice of a spherical joint allows to obtain a decoupling between the UAV rotational dynamics and the passive architecture dynamics, i.e. the platform and the legs.

The position and the orientation of the end-effector w.r.t. $\mathcal{F}_W$ will be then described by the vector $\boldsymbol{p}_{ee} \in \mathbb{R}^3$ and the Euler angles $\boldsymbol{\eta}_{ee} = [\phi\ \theta\ \psi]^\top$. Hence, the passive architecture can be defined by the vector $\boldsymbol{q} = [\boldsymbol{p}_{ee}^\top\ \boldsymbol{\eta}_{ee}^\top\ \boldsymbol{q}_1^\top\ ...\ \boldsymbol{q}_n^\top]^\top$ where the joint coordinates of each leg are grouped in the vector $\boldsymbol{q}_i$. If n_q is the number of DoF of the passive architecture, then $\boldsymbol{q} \in \mathbb{R}^{n_q}$. The velocity vector $\dot{\boldsymbol{q}} = [\dot{\boldsymbol{p}}_{ee}^\top\ \boldsymbol{\omega}_{ee}^\top\ \dot{\boldsymbol{q}}_1^\top\ ...\ \dot{\boldsymbol{q}}_n^\top]^\top \in \mathbb{R}^{n_q}$ where $\boldsymbol{\omega}_{ee} \in \mathbb{R}^3$ represents the angular velocity of the end-effector. Ultimately, the position of each aerial vehicle is defined as $\boldsymbol{p}_{Ri} \in \mathbb{R}^3$.

To reach the final goal of deriving the kinematic formulation of the multi-body system, the position and the velocities of the aerial vehicles have to be related to the configuration coordinates velocities of the passive architecture. This fact is related to the solution of two main problems, the *inverse geometric problem* and the *direct geometric problem*. The former, i.e. the inverse geometric problem, consists of computing the position of the robots, $\boldsymbol{p}_R = [\boldsymbol{p}_{R1}^\top\ ...\ \boldsymbol{p}_{Rn}^\top]^\top \in \mathbb{R}^{3n}$ as a function of the passive architecture coordinates $\boldsymbol{q}$

$$\boldsymbol{p}_R = \boldsymbol{h}(\boldsymbol{q}) \tag{2.6}$$

Conversely, the direct geometric problem allows to define the configurations of the passive architecture as a function of the aerial vehicles' positions as

$$\boldsymbol{q} = \boldsymbol{h}(\boldsymbol{p}_{R1}, ..., \boldsymbol{p}_{Rn}) \tag{2.7}$$

While for the inverse geometric problem, the analytical expression is simple to be obtained with conventional methodologies, the solution of the direct geometric problem is often harder to be retrieved. In particular, a specific study of the specific FPR has to be performed. Nevertheless, some numerical algorithms are available in the literature and could be employed if necessary.

In this manuscript, the pose of the end-effector will be always assumed available. Therefore, we will use the solution of the inverse geometric problem to describe the specific FPRs that we will present in the following chapters.

The kinematic model of an FPR relates the velocities of the aerial vehicles $\boldsymbol{v}_R$ with the velocities of the end-effector and it can be obtained differentiating (2.6) as follows

$$\boldsymbol{v}_R \coloneqq \dot{\boldsymbol{p}}_R = \frac{\partial \boldsymbol{h}(\boldsymbol{q})}{\partial \boldsymbol{q}} \dot{\boldsymbol{q}} = \boldsymbol{J}(\boldsymbol{q}) \dot{\boldsymbol{q}}, \tag{2.8}$$

where $\boldsymbol{J}(\boldsymbol{q}) \in \mathbb{R}^{3n \times n_q}$ is defined as the Jacobian Matrix. On the basis of the characteristics of the linear mapping, $\boldsymbol{J}(\boldsymbol{q})$, between the vector $\dot{\boldsymbol{q}}$ and $\boldsymbol{v}_R$, some

considerations can be made on the configurations the system can achieve. Mathematically, such considerations strictly depend on the rank of the Jacobian matrix. In particular, in those configurations at which the matrix $\boldsymbol{J}(\boldsymbol{q})$ is rank-deficient, i.e. $rank(\boldsymbol{J}(\boldsymbol{q})) \leq n_q$, a unique solution of the inverse kinematic problem cannot be found. As a consequence, the mobility of the structure is reduced and arbitrary motions of the end-effector cannot be assessed. The condition for which such occurrences arise are either the matrix $\boldsymbol{J}(\boldsymbol{q})$ is singular or the robots' DoFs ($3n$) are less than the end-effector DoFs (i.e. $3n \leq n_q$). Conversely, in those configurations at which the Jacobian is full-rank, i.e. $rank(\boldsymbol{J}(\boldsymbol{q})) = n_q$, any solution of the inverse kinematic problem is unique. As a result, the system is in control of all the DoFs and, therefore, every imposed arbitrary motion to the end-effector is attainable. Moreover, if $3n \geq n_q$, the multi-body system is kinematically redundant and, there exist $(3n - n_q)$ redundant DoFs.

Throughout this thesis, the case in which the matrix $\boldsymbol{J}(\boldsymbol{q})$ is full-rank will be covered. In particular, the specifically designed FPR that will be described starting from Chap. 3 is a redundant CS-AMRM.

2.2.2 Inverse Differential Algorithms

In the previous section, the methodologies to solve the kinematic problem were outlined. In particular, it turned out that the inverse kinematic problem can be smoothly solved in the case of FPRs with a full-rank Jacobian. As a result, arbitrary movements of the end-effector can be imposed. A possible control scheme which reasons at the operational space error ($\boldsymbol{e_q} = \boldsymbol{q}^d - \boldsymbol{q}$) between the desired and the actual end-effector coordinates, is the Inverse Kinematic Control (IKC). The approach consists of considering the time derivative of $\boldsymbol{e_q}$ ($\dot{\boldsymbol{e}}_{\boldsymbol{q}} = \dot{\boldsymbol{q}}^d - \dot{\boldsymbol{q}}$) which according to (2.8) becomes

$$\dot{\boldsymbol{e}}_{\boldsymbol{q}} = \dot{\boldsymbol{q}}^d - \boldsymbol{J}^{-1}(\boldsymbol{q})\boldsymbol{v}_R \tag{2.9}$$

If the Jacobian $\boldsymbol{J}(\boldsymbol{q})$ is a square and non singular matrix, the inverse kinematic algorithm that can be adopted for a kinematic control of the FPR, can be written as

$$\boldsymbol{v}_R = \boldsymbol{J}(\boldsymbol{q})\Big(\dot{\boldsymbol{q}}^d + \boldsymbol{K}\boldsymbol{e_q}\Big) \tag{2.10}$$

where $\boldsymbol{K} = diagK \in \mathbb{R}^{n_q \times n_q}$ and $K \in \mathbb{R}$ is a matrix of gains. The block scheme of such control strategy can be seen in Fig. 2.3.

Conversely, a second term can be added to the generalized solution in the case of a redundant manipulator as

$$\boldsymbol{v}_R = \boldsymbol{J}(\boldsymbol{q})(\dot{\boldsymbol{q}}^d + \boldsymbol{K}\boldsymbol{e_q}) + \Big(\boldsymbol{I}_{n_q} - \boldsymbol{J}(\boldsymbol{q})\boldsymbol{J}^{\dagger}(\boldsymbol{q})\Big)\dot{\boldsymbol{q}}_0 \tag{2.11}$$

with $\boldsymbol{J}^{\dagger}(\boldsymbol{q})$ being the Jacobian pseudo-inverse and $\boldsymbol{q}_0 \in \mathbb{R}^{n_q}$ an arbitrary configuration.

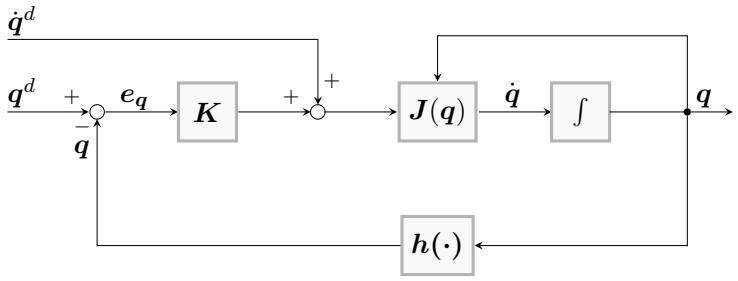

Figure 2.3: Inverse Kinematic Control Scheme

2.2.3 Dynamical Model of a FPR

In the general context of redundant and non-redundant parallel robots, the derivation of dynamical models for such complex schemes results crucial to reproduce systems' motion, entirely analyze the structures and conceive suitable control algorithms. To determinate both inverse and direct dynamics models, all the closed loops composing the system are virtually disassembled, thus assuming the form of an open tree structure. The description of the dynamical model is subsequently obtained by means of the already discussed Newton-Euler or Lagrange formalisms. The loop-closure equations and the virtual power principle allow to conclude the entire procedure [Briot 2015].

Contrarily to what happens in the context of parallel robots, the loop-closure equations are not required for FPRs since the systems under exam are already open three structures. Thus, solely the virtual power principle, known as well as the Lagrange-D'Alembert's principle, suffices. The principle states that, at the equilibrium, the power developed by the inertial effects of a body (or a system of bodies) moving with a virtual velocity is equal to the power developed by the external forces applied on the body (or on the system of bodies) with the addition of the power produced by the internal forces inside the body (or system of bodies).

In light of these considerations, in the following, we will consider FPRs as open tree structures composed by the robots (the actuators) and the passive architectures (links and end-effector). In particular, we will separate the dynamical modeling of the entire structure into two parts with the aim of joining them at the end of the procedure. While the first part will concern the dynamics of the passive architecture, the second part, which will be further detailed in Chap. 3, tackles the dynamical model of the employed UAVs.

More into the details, first, we recall the made assumption on the connection between the i-th robot and the passive architecture characterized by a spherical passive joint. This particular choice provides decoupling between the dynamics of the two elements with the consequence that there is no transfer of torques between the two. Secondly, as extensively adopted in the literature, the hypothesis of quasi-stationary flights has been considered, such that friction and aerodynamics effects can be considered negligible [Mahony 2012].

2.2.3.1 Dynamic Model of the passive architecture

As previously mentioned, the actuation units of a FPR are represented by aerial vehicles. Therefore, the motion of the passive architecture (composed of links and end-effector) strictly depends on the interaction forces that each UAV produces on the last body of each leg. Let us define such force as $\boldsymbol{f}_{d_i} \in \mathbb{R}^3$ for $i = 1, ..., n$.

One of the possible approaches to derive a dynamical model of the passive architecture requires to follow three main steps. The outcome of the first provides the dynamical model of a virtual structure, similar to the passive architecture, with the difference that all the joints of the links will be considered actuated. The second step will relate the dynamics of such virtual structure with the real dynamics of the robots by means of the principle of virtual powers. To complete, the full dynamics will be derived correlating the interaction forces $\boldsymbol{f}_{d_i}$ with the thrusts generated by each aerial vehicle $\boldsymbol{f}_{R_i} \in \mathbb{R}^3$. A better explanation of the latter, especially for unidirectional aerial vehicles will be provided in Chap. 3.

Going into the mathematical details, we consider a virtual architecture, similar to the passive one, with the difference w.r.t. the latter that it is fully actuated by its active joints. Its dynamical model is defined as

$$\boldsymbol{\tau}_e = \boldsymbol{M}_e \dot{\boldsymbol{q}} + \boldsymbol{C}_e(\boldsymbol{q}, \dot{\boldsymbol{q}}) \tag{2.12}$$

where $\boldsymbol{\tau}_e \in \mathbb{R}^{n_q}$ is the vector grouping all the efforts acting on the virtual architecture; $\boldsymbol{M}_e(\boldsymbol{q}) \in \mathbb{R}^{n_q \times n_q}$ is the generalized inertia matrix and $\boldsymbol{C}_e \in \mathbb{R}^{n_q}$ is the Coriolis vector. Under the made assumptions of quasi-static motions and near-hovering configurations, friction and aerodynamics effects can be considered negligible.

Each aerial vehicle exerts a force on the passive joint in which it is attached. Therefore, whenever the robots move with a virtual velocity $\boldsymbol{v}^*_{Ri}$, it generates a virtual velocity $\dot{\boldsymbol{q}}^*$ of the virtual architecture. In mathematical formulation, the concept can be encapsulated in the principle of the virtual power. Therefore, for the virtual architecture we can write

$$P_p + P_{\tau_e} = 0 \tag{2.13}$$

and for the real robot system

$$P_p + P_R = 0 \tag{2.14}$$

where P_p is the power developed by the inertial effect and the gravitational forces on the passive architecture, P_{τ_e} is the power which arises from the *virtual* joint actuation in the virtual architecture and P_R is the power developed by the interaction forces between the drones and the *real* passive architecture. Merging Eq. (2.13) and Eq. (2.14) and making explicit the power, the following relation can be written

$$\boldsymbol{v}_R^{*\top} \boldsymbol{f}_d = \dot{\boldsymbol{q}}^{*\top} \boldsymbol{\tau}_e \tag{2.15}$$

with $\boldsymbol{v}^*_R = [\boldsymbol{v}^{*\top}_{R1} \ ... \ \boldsymbol{v}^{*\top}_{Rn}]^\top$ and $\boldsymbol{f}_d = [\boldsymbol{f}^\top_{d_1} \ ... \ \boldsymbol{f}^\top_{d_n}]^\top$. Using the kinematic rela-

tion (2.8), Eq. (2.15) becomes

$$\boldsymbol{J}(\boldsymbol{q})^{\top}\boldsymbol{f}_d = \boldsymbol{\tau_e} \tag{2.16}$$

which relates the interaction forces generated by the drones and the wrenches providing actuation on each joint of each leg.

Moreover, for each leg, the interaction force applied in the center of each drone O_R can be obtained by computing the resultant force applied on each drone as

$$\boldsymbol{f}_{R_i} - \boldsymbol{f}_{d_i} + m_R\boldsymbol{g} = m_R\dot{\boldsymbol{v}}_{Ri} \tag{2.17}$$

where $m_R \in \mathbb{R}_{>0}$ is the mass of the robot and $\boldsymbol{g} = [0\ 0\ g]^{\top}$ is the gravity vector. Grouping for all the aerial vehicles involved in the multi-robot system and computing the total interaction force, it is then possible to obtain the total interaction force of all the robots composing the FPR

$$\boldsymbol{f}_d = \boldsymbol{f}_R + \boldsymbol{M}_R\boldsymbol{g}_R - \boldsymbol{M}_R\dot{\boldsymbol{v}}_R \tag{2.18}$$

where $\boldsymbol{M}_R \in \mathbb{R}^{3n\times 3n}$ is the diagonal matrix which takes the following form

$$\boldsymbol{M}_R = \begin{bmatrix} m_{R1}\boldsymbol{I}_3 & ... & \boldsymbol{0}_{3\times 3} \\ ... & ... & ... \\ \boldsymbol{0}_{3\times 3} & ... & m_{Rn}\boldsymbol{I}_3 \end{bmatrix} \tag{2.19}$$

while $\boldsymbol{f}_R = [\boldsymbol{f}_{R_1}^{\top}\ ...\ \boldsymbol{f}_{R_n}^{\top}]^{\top}$ and $\boldsymbol{g}_R = [\boldsymbol{g}^{\top}\ ...\ \boldsymbol{g}^{\top}]^{\top}$.

Finally, combining Eq. (2.18) with Eq. (2.16) the full dynamical model can be derived and written as

$$\boldsymbol{J}(\boldsymbol{q})^{\top}\tilde{\boldsymbol{f}}_R = \boldsymbol{M}(\boldsymbol{q})\dot{\boldsymbol{q}} + \boldsymbol{C}(\boldsymbol{q},\dot{\boldsymbol{q}}) \tag{2.20}$$

where $\boldsymbol{M} = (\boldsymbol{M}_e + \boldsymbol{J}^{\top}\boldsymbol{M}_R\boldsymbol{J})$ and $\boldsymbol{C} = \boldsymbol{C}_e + \boldsymbol{J}^{\top}\boldsymbol{M}_R(\dot{\boldsymbol{J}}\dot{\boldsymbol{q}} - \boldsymbol{g}_R)$. Eq. (2.20) represents the dynamical model of a FPR.

Chapter 3

Robot Systems and Models

In Chap. 2, we provided an overview of the fundamental methodologies which have mainly been employed in the literature and in this thesis. Nevertheless, in this chapter, we continue proposing additional analyses on the basic subsystems which make possible the realization of control and estimation algorithms on real robotic platforms. Such fundamental components are actuators and sensors whose models have been extensively investigated in recent years.

Additionally, in the context of aerial cooperative manipulations, the aerial vehicles are often provisioned with physical tools to create connections with the carried payloads. Once again, the research community has contributed by providing detailed models of such devices.

In light of these considerations, in the following, first, we describe a characterization of the set of conceived links and their models. Then, we focus on the generic dynamical model, extensively employed on the validation phases described throughout this thesis, of the unidirectional-thrust aerial vehicle (UDT AV) in free-flight circumstances. Afterwards, looking at the actuators units of the UDT AV, we examined the thrust systems composed by the brushless motors and the propellers and we devised one of the possible control strategy available in the literature. Ultimately, since any control action can be performed without a monitoring process of the performance of the system, we propose an overview of the set of the sensors necessary to fly an aerial vehicle.

Once again, the goal of this chapter is to highlight the fundamentals of the specific UDT AV employed in this thesis, its sensors and actuators, without pretending to deeply cover all the aspects that an interested reader may find in more advanced manuals.

3.1 Thetering Link

Part II of this manuscript will deal with the design, estimation and control of multi-robot systems. In particular, in the proposed approaches for the cooperative manipulations, we consider that the robots are connected to the payloads through different types of connections. Therefore, we provide an overview of the possible categories of links through which the cooperative manipulations can be performed. For the most part, they can be divided into three main categories:

- *only stretchable* links which can solely support tensions. Examples of such links are cable-like links such as chains, ropes.

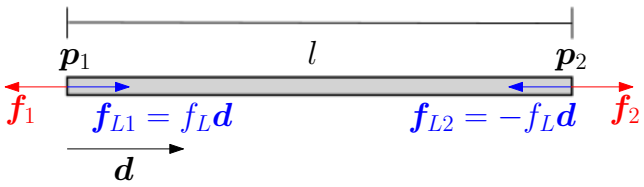

Figure 3.1: Schematic representation of a generic link and its main variables

- *only compressible* links which can solely support compression. Strut-like links, such as pneumatic suspensions belong to this category.
- *stretchable and compressible* links which can support both the stresses. Bar-like links fall into this category whose examples are beams or poles.

From a modeling point of view, five are the main variables that describe a generic link: *i)* the positions $\boldsymbol{p}_1$ and $\boldsymbol{p}_2 \in \mathbb{R}^3$ defined as the edges of the link; *ii)* the unstressed length $l_0 \in \mathbb{R}_{>0}$; *iii)* the intensity of the link's internal force $f_L \in \mathbb{R}$; *iv)* the link's length which corresponds to the difference between the edges, i.e. $l = ||\boldsymbol{p}_1 - \boldsymbol{p}_2|| \in \mathbb{R}^3$; *v)* the link's normalized direction which is given by $\boldsymbol{d} = (\boldsymbol{p}_1 - \boldsymbol{p}_2)/l \in \mathbb{R}^3$. A picture of the aforementioned variables is depicted in Fig. 3.1

According to the external action performed on the link, the internal force produced along the direction of the cable can be of two different types. When the link resists a pulling action, the internal force generated is a *tension* with the characteristic that $f_L > 0$. Conversely, when the link sustains a pressing motion, the internal force is called *compression* and $f_L < 0$. In case any force is applied ($f_L = 0$), the link is defined as slack. Throughout the thesis, the assumption to have far-from slack links will be made, especially for only stretchable links as cables. In addition, preserving the tightness of the cables will be one of our control purposes.

Moreover, the effects of the elasticity and the deformation in the case of non-slack links will be considered negligible. This hypothesis has been widely adopted in the literature [Lupashin 2013, Nicotra 2017]. Nevertheless, it has to be considered that the condition holds as soon as the maximum internal force is smaller than the link's stiffness coefficient. In mathematical terms, this means that first the length of the link will always remain constant, i.e $l = l_0$, regardless of the performed action ($f_L \neq 0$). Secondly, the forces at the two ends of the link, $\boldsymbol{f}_{L1}$ and $\boldsymbol{f}_{L2}$ are opposite and lie on the same axis, i.e. $\boldsymbol{f}_{L2} = -\boldsymbol{f}_{L1} = -f_L\boldsymbol{d}$.

Regarding the contribution of the mass and the inertia of the links, in light of their marginally influence w.r.t. the robot ones, they can also be considered negligible. Links as cables or links made in carbon fiber properly match these assumptions.

However, in order to consider all the previously mentioned effects or to add other possible details, more complex models have been investigated. A *spring-damper* system can describe the deformations of a link subjected to external forces.

A *Standard Linear Solid model* [Sandino 2015, Zienkiewicz 2005] allows to describe cable links as series and/or parallel of spring-damper systems. Furthermore, with the *finite element approximation* [Zienkiewicz 2005], it is possible to model the link as a chain of elements so that the flexibility and the bending properties can also be taken into account [Goodarzi 2016].

Although the previously mentioned methods result more accurate and precise in describing some of the behaviors of the links under exams, in our belief, the aspects that they consider specify details that are out of the scope of this thesis. Hence, the simple and often more general model which has been presented in the first part of this section will be preferred over the other ones, without losing of generality due to its vast use in the literature.

3.2 Unidirectional thrust vehicles

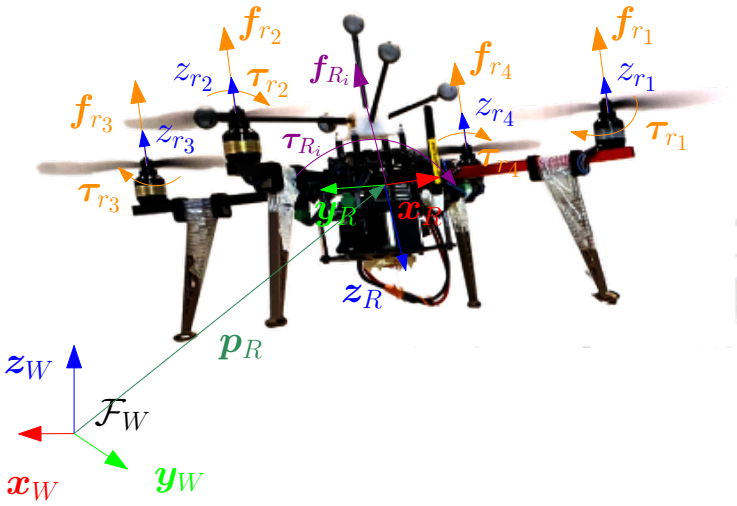

Figure 3.2: Schematic representation of the vehicle model.

Following the analysis of a rigid body presented in Sec. 2.1.3, in this section we present the dynamical model of the unidirectional thrust aerial vehicle. To this end, we define an inertial world frame $\mathcal{F}_W = O_W, \{\boldsymbol{x}_W, \boldsymbol{y}_W, \boldsymbol{z}_W\}$ where O_W is its origin, arbitrarily placed, and $\{\boldsymbol{x}_W, \boldsymbol{y}_W, \boldsymbol{z}_W\}$ are the orthogonal unit vectors. $\boldsymbol{z}_W$ is considered parallel and opposite to the gravity vector. Moreover, rigidly attached to the vehicle we define the body frame $\mathcal{F}_R = O_R, \{\boldsymbol{x}_R, \boldsymbol{y}_R, \boldsymbol{z}_R\}$ with its origin in O_R. $\boldsymbol{z}_R$ is considered parallel and opposite to the thrust vector. The position of O_R and orientation of $\mathcal{F}_R$ w.r.t $\mathcal{F}_W$ are described by the vector $\boldsymbol{p}_R \in \mathbb{R}^3$ and the rotation matrix $\boldsymbol{R}_R \in SO(3)$, respectively. The vector $\boldsymbol{\omega}_R \in \mathbb{R}^3$ denotes the angular velocity of $\mathcal{F}_R$ w.r.t. $\mathcal{F}_W$, expressed in $\mathcal{F}_R$. The reader can find the aforementioned variables depicted in Fig. 3.2 The mass of the robot is defined as $m_R \in \mathbb{R}_{>0}$ and the inertia is described by the matrix $\boldsymbol{J}_R \in \mathbb{R}^{3\times3}_{>0}$.

Four control inputs manage the motion of the vehicle. The first one is $f_R \in \mathbb{R}_{\geq0}$

which represents the intensity of the total thrust applied in O_R. Thus, the thrust that produces the aerial vehicle motion can be derived as $\boldsymbol{f}_{R_i} = -f_R \boldsymbol{z}_R$. The other three are represented by the total moment $\boldsymbol{\tau}_{R_i} = [\tau_{R_x} \ \tau_{R_y} \ \tau_{R_z}]^\top \in \mathbb{R}^3$ applied to $\mathcal{F}_R$ and expressed in $\mathcal{F}_W$. The three components are responsible for the generation of the platform rotational motion.

Applying the Newton-Euler equations, in view of the proposed reference system, the dynamics of the system becomes

$$\begin{aligned} m_R \ddot{\boldsymbol{p}}_R &= -m_R g \boldsymbol{e}_3 - f_R \, \boldsymbol{R}_R \boldsymbol{e}_3 \\ \boldsymbol{J}_R \dot{\boldsymbol{\omega}}_R &= -\boldsymbol{\omega}_R \times \boldsymbol{J}_R \boldsymbol{\omega}_R + \boldsymbol{\tau}_{R_i} \end{aligned} \tag{3.1}$$

The model, here presented, shows the property of being general and well-suited to represent a vast set of UDT AVs dealing with their non-linearities, strongly coupling and underactuation. Among them ducted fan UAVs or multi-rotors vehicles with $n \geq 4$ rotors. Thanks to this property, the formalization has been chosen to depict the dynamics of the UAV largely adopted in the context of this thesis. Moreover, the next two sections will provide an overview of the technique applied to generally control the aerial vehicles. In particular, we focus on the thrust/torque generation and the state estimation of the platforms.

3.3 Actuators

The model developed in 3.1, derived from the dynamics of a floating rigid body, properly depicts the dynamics of an UAV. Thanks to its generality, this mathematical description will be used as a basis for the modeling of the employed UAVs presented in this manuscript. In this specific representation, the motion of the aerial platform is characterized by the forces and moments imposed on the vehicle's CoM. Those responsible for the generation of such wrenches are the actuators. Assuming an UDT AV provided with $n \in \mathbb{N}_{\geq 4}$ spinning rotors coupled with propellers, rigidly attached to the main frame in $\boldsymbol{b}_k \in \mathbb{R}^3$ with $k = 1, ..., n$ w.r.t. $\mathcal{F}_R$ and oriented as $-\boldsymbol{z}_R$, the total thrust applied is

$$\boldsymbol{f}_{R_i} = \sum_{k=1}^{n} c_f \omega_k^2 \tag{3.2}$$

where $w_k \in \mathbb{R}_{\geq 0}$ is the speed of the k-th propeller and $c_f \in \mathbb{R}_{>0}$ is the lift factor. The latter depends on the aerodynamic properties of the propeller blade. Conversely, the body torque is the result of two different effects: the moments generated by the actuator forces and the drag torques generated by the resistance of the air to the rotation of the propellers' blades. In mathematical terms, this becomes

$$\boldsymbol{\tau}_{R_i} = \sum_{k=1}^{4} (c_f \boldsymbol{b}_k \times \boldsymbol{e}_3 + c_k c_\tau \boldsymbol{e}_3) \omega_k^2 \tag{3.3}$$

where $c_\tau \in \mathbb{R}_{>0}$ represents the intensity ratio (in absolute value) between the thrust produced by the propellers rotation and the generated drag torque; $c_k \in \{-1, 1\}$ is a variable used to describe clock-wise or counter-clockwise rotation w.r.t. the axis z_{r_k} fo each rotor. Hence, it assumes the value 1 (-1) for a clock-wise (counter-clockwise) rotation.

The presented model is a well-established model [Mahony 2012, Hamel 2002, Pounds 2010a, Pucci 2013] that for a quadrotor-like vehicle ($n = 4$) can be written in a compact form as

$$\begin{bmatrix} \boldsymbol{f}_{R_i} \\ \boldsymbol{\tau}_{R_i} \end{bmatrix} = \boldsymbol{G}\boldsymbol{\gamma} \tag{3.4}$$

where

$$\boldsymbol{G} = \begin{bmatrix} c_f & c_f & c_f & c_f \\ 0 & -c_f b & 0 & c_f b \\ c_f b & 0 & -c_f b & 0 \\ -c_\tau & c_\tau & -c_\tau & c_\tau \end{bmatrix} \tag{3.5}$$

is the allocation matrix,

$$\boldsymbol{\gamma} = \begin{bmatrix} \omega_1^2 \\ \omega_2^2 \\ \omega_3^2 \\ \omega_4^2 \end{bmatrix} \tag{3.6}$$

$\boldsymbol{b}_k = b[\cos(\alpha_k)\ \sin(\alpha_k)\ 0]$ with $b \in \mathbb{R}_{>0}$ and $\alpha = (k-1)\pi/2$ and $c_k = (-1)^k$ with $k = 1, ..., 4$. In such configuration, the allocation matrix has the property of being always full-rank and invertible. Hence, from a control point of view, Eq. (3.4) results crucial to identify the control inputs (the speed of the propellers) to obtain the desired thrusts and torques. The procedure merely requires the inversion of Eq. (3.4).

Although the generality of the proposed model, certain degrees of simplification characterize such formalization. First, the blade flapping and the rotor induced drag are not taken into account. Additional aerodynamics effects, as the ground and the ceiling effects, should be added for a finer characterization. Finally, the presented actuation model is based on the hypothesis that the motors can instantaneously apply a spinning velocity.

For what concerns blade flapping and rotor induced drag effect, they are generated by the interaction with the air and are associated with the flexibility and rigidity properties of the UAVs. As a result, the rotors experience an exogenous lateral force in the x-y plane. However, as for the ground and ceiling effects, their contribution will be considered negligible in the context of this thesis. Regarding the assumption of the instantaneous application of a spinning velocity in the rotors actuation, such a process would require an infinite torque which would be unfeasible in a real-world scenario. To overcome such a limitation, the dynamics of the rotor could be extended to encompass on one side mechanical and electrical effects and on the other side the dynamics of the Electronic Speed Controllers (ESCs). However, for our control purposes, we can first consider confined actuation force variations

and then, we can make use of the brush-less controller developed in [Franchi 2017] which guarantees a minimal response time. Under these conditions, the model represents a good estimation of the real behavior of the aerial vehicle under exam. Throughout the different proposed choices, the strategy has always been to find a trade-off between accuracy and simplicity. Moreover, the goal has been, as well, to have in mind that a good model should detain the crucial features of a system avoiding, if not by necessity, over-complexity.

3.4 Dynamic Control of an UDT AV

After having presented the general model of an UDT AV in Sec. 3.2 and the model of a quadrotor in Sec. 3.3, in the following, we present one of the possible control strategies that allow to regulate its dynamics. The approach is the so-called *Feedback Linearization* or *Inverse Dynamics Control* and it has been largely studied and investigated in the literature of non-linear control theory [Hamandi 2021]. The main features of the control strategy will be here illustrated on the specific model under exam, i.e. the UDT AV, and a static feedback linearization of the model dynamics will be applied. We propose such methodology since it represents one of the bases upon which most of the conceived controllers, presented in Part. II and Part. III, are formulated. More into the details, let us consider the model in (3.1) in a matrix form. Moreover, by virtue of (3.4) it becomes

$$\begin{bmatrix} m_R \boldsymbol{I}_3 & \boldsymbol{0}_3 \\ \boldsymbol{0}_3 & \boldsymbol{J}_R \end{bmatrix} \begin{bmatrix} \ddot{\boldsymbol{p}}_R \\ \dot{\boldsymbol{\omega}}_R \end{bmatrix} = \begin{bmatrix} -m_R g \boldsymbol{e}_3 \\ -\boldsymbol{\omega}_R \times \boldsymbol{J}_R \boldsymbol{\omega}_R \end{bmatrix} + \boldsymbol{G}\boldsymbol{\gamma}. \tag{3.7}$$

Being the allocation matrix $\boldsymbol{G}$ full rank and invertible for a quadrotor model, the simple static feedback linearization can be applied and therefore the system takes the form

$$\boldsymbol{\gamma} = \boldsymbol{G}^{\dagger} \left(\begin{bmatrix} m_R \boldsymbol{I}_3 & \boldsymbol{0}_3 \\ \boldsymbol{0}_3 & \boldsymbol{J}_R \end{bmatrix} \begin{bmatrix} \ddot{\boldsymbol{p}}_R^{\star} \\ \dot{\boldsymbol{\omega}}_R^{\star} \end{bmatrix} + \begin{bmatrix} m_R g \boldsymbol{e}_3 \\ \boldsymbol{\omega}_R \times \boldsymbol{J}_R \boldsymbol{\omega}_R \end{bmatrix} \right) \tag{3.8}$$

where $\ddot{\boldsymbol{p}}_R^{\star} \in \mathbb{R}^3$ and $\dot{\boldsymbol{\omega}}_R^{\star} \in \mathbb{R}^3$ are the new virtual control inputs. As a consequence, (3.8) allows to directly control linear and angular accelerations. A well-known way to produce such terms is represented by the linear Proportional Derivative Integral (PID) controller that possesses the characteristic of continuously computing the state errors and applying a correction based on the PID terms.

To summarize, the *Feedback Linearization* approach consists of two main phases: first, the algebraical transformation of a non-linear system dynamic into a linear one such that the linear control technique can be employed. Secondly, the linear methodology is applied.

3.5 Sensors

The adoption of sensors is fundamental to obtain high-performance robotic systems. In particular, proprioceptive sensors are widely employed to measure the internal state of aerial vehicles for control purposes. Nevertheless, when these robotic systems are placed in the environment, exteroceptive sensors provide knowledge of the surroundings. The Inertial Measurement Unit (IMU) belongs to the first category, while force/torque sensors, magnetometers, GPS, Motion Capture (MoCap) Systems, proximity sensors, cameras have their place in the second category. The IMU and the MoCap have been the adopted systems to validate the proposed approaches. Hence, they will be discussed more in detail.

For what concerns the IMU, it is an electronic device composed of a three-axis accelerometer and a three-axis gyroscope. The former allows to measure the acceleration of the vehicle w.r.t. its body frame while the latter measures the angular rate. Referring to the quantities described in Fig. 3.2, and supposing to calibrate the IMU with its center in O_R and its axes aligned with $\mathcal{F}_R$, in mathematical terms the measured acceleration of the vehicle $\bar{\boldsymbol{y}}_{acc} \in \mathbb{R}^3$ can be written as

$$\bar{\boldsymbol{y}}_{acc} = \boldsymbol{R}_R{}^{\top}({}^{W}_{B}\ddot{\boldsymbol{p}} + g\boldsymbol{e}_3) \tag{3.9}$$

.

On the other hand, the measured angular rate $\bar{\boldsymbol{y}}_{gyr} \in \mathbb{R}^3$ of $\mathcal{F}_R$ w.r.t. $\mathcal{F}_W$ expressed in $\mathcal{F}_R$ is

$$\bar{\boldsymbol{y}}_{gyr} = \boldsymbol{\omega}_R \tag{3.10}$$

However, the measure of the rotation around $\boldsymbol{z}_R$ has to be added to have a complete estimation of the full time-varying attitude. In actual fact, the two employed sensors result insufficient for such a goal. Therefore, a common strategy is to equip the IMU with a magnetometer. This sensor is commonly used as a heading reference due to its ability of measuring the ambient magnetic field w.r.t. $\mathcal{F}_R$. In mathematical terms, not considering the disturbances and defining the Earth's magnetic field as $\boldsymbol{h}^W \in \mathbb{R}^3$, the measurements coming from the magnetometer can be written as follows

$$\bar{\boldsymbol{y}}_{mag} = \boldsymbol{R}_R{}^{\top}\boldsymbol{h}^W \tag{3.11}$$

in such a way to measure the attitude and the angular velocity of the aerial vehicle.

Once the rotational variables are defined, the remaining elements identifying the entire state of the vehicle, i.e. position and translational velocity, have also to be quantified. For such purpose, the standard method is to use exteroceptive sensors. Designing new localization methods using such sensors is out of the focus of this thesis. Therefore, their models will be defined as a direct measurement of the configuration of the robot. Defining the output measurements as $\bar{\boldsymbol{y}}_{ext}$, we write

$$\bar{\boldsymbol{y}}_{ext} = (\boldsymbol{p}_R, \boldsymbol{R}_R) \tag{3.12}$$

To conclude, the precise estimation of the whole state of the robot requires accurate

procedures to combine all the aforementioned measurements. One of the most popular and effective has been presented in [Mahony 2012].

Part II

Aerial Cooperative Manipulations in air

Chapter 4

Modeling approaches for Full-Pose Cooperative Manipulations

As mentioned in Chap. 3, to some extent, among all the possible types of contact tools that can be used for cooperative manipulation, cables have been proved fairly suited. On the one hand, for their light weight and mechanical simplicity and on the other hand, for the decoupling they induce between the rotational dynamics of the vehicles and the object to be manipulated. Moreover, to reach the goal of full pose manipulation, *statically rigid* or *force-closure* designs have to be employed. Such designs allow to compensate time-varying external wrenches almost instantaneously.

Therefore, the aim of this chapter is to start with a preliminary modeling of such cooperative manipulation with a general formulation that encompasses different kinds of links between the robots and the payload. In particular, the made assumption is that N agents are connected to the load through virtual mass-spring damper systems and distributed along a circle. Such methodology, which does not rely on explicit communication, can be equally applied to ground, aerial, underwater and team of heterogeneous vehicles.

In the second part, the general modeling leaves room to the modeling of a more specific prototype *in-house* conceived and developed, i.e. the already mentioned CS-AMRM, the Fly-Crane. Such design differs from the previous one since it is composed of the minimum number of robots and cables necessary to obtain full pose manipulation capabilities. Moreover, the developed methodology leverages on a centralized way of reasoning which allows to describe the system as a whole and to relate the velocity of the robots with the velocity of the manipulated object. Such kinematic relationship will be described in Sec. 4.2. To conclude, the dynamical formulation of the CS-AMRM which has been used for estimation purposes (see Sec. 4.3) and a comparison of the two methodologies (see Sec. 4.4) will conclude the chapter.

4.1 Generic Model

The goal of this section is to derive the generic model which has been applied for the multi-agent manipulation of objects. The reader is referred to Fig. 4.1a for an introducing picture. For this purpose, it is possible to define an inertial frame

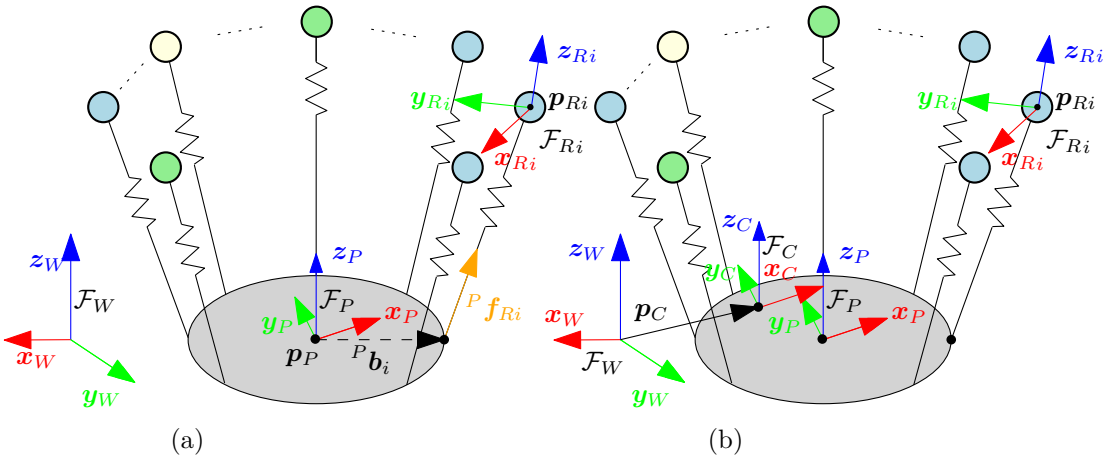

Figure 4.1: *Left* Representative illustration of the considered system and main variables. The load is represented by the gray disk. Each colored circle represents the end-effector of a robot. Different colors represent possible different classes of robots.The behavior of each robot and the physical interconnection model are represented by springs. *Right*: Illustration of the system main variables when the geometric center of the platform and the payload's CoM differ.

$\mathcal{F}_W = \{O_W, \boldsymbol{x}_W, \boldsymbol{y}_W, \boldsymbol{z}_W\}$, where O_W is its origin and $\{\boldsymbol{x}_W, \boldsymbol{y}_W, \boldsymbol{z}_W\}$ are its unit axes.

Then, let us introduce $\mathcal{F}_R = \{O_R, \boldsymbol{x}_R, \boldsymbol{y}_R, \boldsymbol{z}_R\}$ that is rigidly attached to the center of each robot. O_R is its origin and $\{\boldsymbol{x}_R, \boldsymbol{y}_R, \boldsymbol{z}_R\}$ are its unit axes. ${}^W\boldsymbol{R}_R \in SO(3)$ depicts the orientation of $\mathcal{F}_R$ with respect to $\mathcal{F}_W$. The frame $\mathcal{F}_P = \{O_P, \boldsymbol{x}_P, \boldsymbol{y}_P, \boldsymbol{z}_P\}$ is rigidly attached to the object to manipulate. In particular, O_P is the origin of $\mathcal{F}_P$ and $\{\boldsymbol{x}_P, \boldsymbol{y}_P, \boldsymbol{z}_P\}$ are its unit axes. $\mathcal{F}_P$ is placed such that O_P is in the geometric center of the object. The vector ${}^W\boldsymbol{p}_P \in \mathbb{R}^3$ describes the position of O_P with respect to $\mathcal{F}_W$ and ${}^W\boldsymbol{R}_P \in SO(3)$ describes the orientation of $\mathcal{F}_P$ with respect to $\mathcal{F}_W$[1]. As it will be clarified in Sec. 5.1.3, if the payload's mass is uniformly distributed, the geometric center O_P will coincide with the CoM of the platform. However, this is not the case when the payload is used as a a *platform* that contains tools useful for manipulating objects. Therefore, in the following, when the geometric center and the CoM will not coincide, C will be the CoM of the platform and $\boldsymbol{p}_C$ defines the position of C with respect to $\mathcal{F}_W$ or, equivalently, ${}^P\boldsymbol{p}_C$ is the position of C with respect to $\mathcal{F}_P$ (see Fig. 4.1b). Moreover, in such cases, a reference frame can be defined as $\mathcal{F}_C = \{O_C, \boldsymbol{x}_C, \boldsymbol{y}_C, \boldsymbol{z}_C\}$, where its origin O_C is in C and $\{\boldsymbol{x}_C, \boldsymbol{y}_C, \boldsymbol{z}_C\}$ are its unit axes. $\mathcal{F}_C$ is oriented as $\mathcal{F}_P$. Thus, the vector $\boldsymbol{p}_C$ also describes the position of O_C with respect to $\mathcal{F}_W$ and $\boldsymbol{R}_C \in SO(3)$ describes the orientation of $\mathcal{F}_C$ with respect to $\mathcal{F}_W$, resulting that $\boldsymbol{R}_C = \boldsymbol{R}_P$.

In the following, the CoM and the geometric center of the manipulated object

[1]The left superscript indicates the reference frame. From now on, $\mathcal{F}_W$ is considered as reference frame when the superscript is omitted.

will coincide. However, in Sec. 5.1.3.1 as it will be clearly specified, the distinction between the two quantities will be highlighted.

Starting with the Newton-Euler formalism the dynamics of the load can be written as:

$$\begin{aligned} m_P \ddot{\boldsymbol{p}}_P &= -m_P g \boldsymbol{z}_W - \boldsymbol{D}_P \dot{\boldsymbol{p}}_P + \boldsymbol{f}_P + \boldsymbol{f}_e \\ \dot{\boldsymbol{R}}_P &= \boldsymbol{S}({}^P\boldsymbol{\omega}_P)\boldsymbol{R}_P \\ \boldsymbol{J}_P \, {}^P\dot{\boldsymbol{\omega}}_P &= -\boldsymbol{S}({}^P\boldsymbol{\omega}_P)\boldsymbol{J}_P \, {}^P\boldsymbol{\omega}_P - \boldsymbol{B}_P \, {}^P\boldsymbol{\omega}_P + {}^P\boldsymbol{\tau}_P + {}^P\boldsymbol{\tau}_e \end{aligned} \tag{4.1}$$

where $m_P \in \mathbb{R}_{>0}$ is the mass of the load, $g \in \mathbb{R}_{>0}$ is the free fall acceleration, $\boldsymbol{f}_P$ and ${}^P\boldsymbol{\tau}_P \in \mathbb{R}^3$ are the forces and moments connected to the direct interactions of the load with the robots, $\boldsymbol{f}_e$ and ${}^P\boldsymbol{\tau}_e \in \mathbb{R}^3$ are the external forces and moments acting on the platform, i.e. $\boldsymbol{w}_e \in \mathbb{R}^6$, $\boldsymbol{S}(\star)$ is the skew operator[2], ${}^P\boldsymbol{\omega}_P \in \mathbb{R}^3$ is the platform angular velocity, $\boldsymbol{J}_P \in \mathbb{R}^{3\times3}$ the inertia of the platform, $\boldsymbol{D}_P > 0 \in \mathbb{R}^{3\times3}$ and $\boldsymbol{B}_P > 0 \in \mathbb{R}^{3\times3}$ respectively the model drag and the friction effects. It is worthy noting that objects laying on the ground can be modeled, as well, considering the following constraints:

$$\boldsymbol{e}_3^\top \dot{\boldsymbol{p}}_P = 0, \quad \boldsymbol{e}_1^\top \, {}^P\boldsymbol{\omega}_P = 0, \quad \boldsymbol{e}_2^\top \, {}^P\boldsymbol{\omega}_P = 0, \tag{4.2}$$

where $\boldsymbol{e}_i \in \mathbb{R}^3$ is the vector with a 1 in position i, and zero elsewhere.

The payload results manipulated by a team of $N \in \mathbb{N}_{>2}$ robots (the case $N = 2$ *aerial* robots have been already studied in [Tognon 2018]) equipped with a rigid or actuated end-effector whose position can be controlled by the robot.

Let us define the frame $\mathcal{F}_{R_i} = \{O_{R_i}, \boldsymbol{x}_{R_i}, \boldsymbol{y}_{R_i}, \boldsymbol{z}_{R_i}\}$ rigidly attached to the i-th end-effector. Its configuration is then given by the position of O_{R_i}. The end-effector orientation has been assumed to be suitable to grasp the payload according to the selected grasping method. In the following, the assumption that there is no difference between the i-th end-effector and the i-th robot will be made. Thus, the dynamic of the i-th robot has been modeled as a double integrator:

$$\ddot{\boldsymbol{p}}_{R_i} = \boldsymbol{u}_i, \tag{4.3}$$

Additionally, we considered the case in which the robots are attached to the load in an evenly distributed way along a circle centered on O_P with radius $b \in \mathbb{R}_{>0}$. In particular, at this stage assuming that the i-th robot is in contact with the load at the point B_i, described by the vector ${}^P\boldsymbol{b}_i \in \mathbb{R}^3$, without loss of generality

$${}^P\boldsymbol{b}_i = b[\cos\theta_i \;\; \sin\theta_i \;\; 0]^\top =: [x_i \;\; y_i \;\; 0]^\top, \tag{4.4}$$

where $\theta_i = (i-1)2\pi/N$. The presented configuration allows to equally share the effort among all the robots and further evidences will be given in Chap. 6. The *contact force* $\boldsymbol{f}_i$ between the load and the robot end-effector can be modeled as a function of $\boldsymbol{p}_{Ri}$ and the corresponding contact point expressed in $\mathcal{F}_W$ $\boldsymbol{b}_i = \boldsymbol{p}_P +$

[2] $\boldsymbol{S}(\star) : \mathbb{R}^3 \to \mathbb{R}^{3\times3}$ is such that $\boldsymbol{S}(\boldsymbol{v})\boldsymbol{u} = \boldsymbol{v} \times \boldsymbol{u} \;\forall \boldsymbol{v}, \boldsymbol{u} \in \mathbb{R}^3$

$\boldsymbol{R}_P\,{}^P\boldsymbol{b}_i$. In other words, $\boldsymbol{f}_i = \boldsymbol{h}(\boldsymbol{p}_{Ri}, \boldsymbol{p}_P, \boldsymbol{R}_P)$. Assuming a friction-less contact, the interaction forces can be modeled as elastic forces

$$\begin{aligned} \boldsymbol{f}_i &= f_{Li}\boldsymbol{n}_i, \quad \text{with} \\ f_{Li} &= k_i(\|\boldsymbol{l}_i\| - l_{0i}) \end{aligned} \tag{4.5}$$

where $\boldsymbol{l}_i = \boldsymbol{p}_{Ri} - (\boldsymbol{p}_P + \boldsymbol{R}_P\,{}^P\boldsymbol{b}_i) \in \mathbb{R}^3$ is the contact displacement, $\boldsymbol{n}_i = \boldsymbol{l}_i/\|\boldsymbol{l}_i\| \in \mathbb{R}^3$ is the force direction described by a normalized vector, f_{Li} is the intensity of the contact force, $k_i \in \mathbb{R}_{>0}$ is the elastic coefficient, and $l_{0i} \in \mathbb{R}$ is a displacement offset. As previously mentioned, among the possible applications, the model can even describe the case in which each robot is connected to the load by cables. As such, k_i is the cable stiffness, l_{0i} is its nominal length and Eq. (4.5) can be slightly modified to additionally consider the case of a slack cable:

$$f_{Li} = \begin{cases} k_i(\|\boldsymbol{l}_i\| - l_{0i}) & \text{if } \|\boldsymbol{l}_i\| - l_{0i} > 0 \\ 0 & \text{otherwise} \end{cases}. \tag{4.6}$$

Finally, gathering all the contact forces between the robots and the load in the vector $\boldsymbol{f} = [\boldsymbol{f}_1^\top \dots \boldsymbol{f}_N^\top]^\top \in \mathbb{R}^{3N}$, we can write the total force and moment applied to the load which complete the load closed-loop dynamics in Eq. (4.1)

$$\begin{bmatrix} \boldsymbol{f}_P \\ {}^P\boldsymbol{\tau}_P \end{bmatrix} = \underbrace{\begin{bmatrix} \boldsymbol{I}_3 & \dots & \boldsymbol{I}_3 \\ \boldsymbol{S}({}^P\boldsymbol{b}_1)\boldsymbol{R}_P^\top & \dots & \boldsymbol{S}({}^P\boldsymbol{b}_N)\boldsymbol{R}_P^\top \end{bmatrix}}_{\boldsymbol{G}(\boldsymbol{R}_P)} \boldsymbol{f}. \tag{4.7}$$

4.2 The Kinematic Modeling of the Fly-Crane

Differently from the previous section, in the following, the purpose is to describe a less general but optimized multi-robot system which is composed of three aerial vehicles, a payload, which will be referred as *platform*, and six cables arranged as in Fig. 4.2a. The multi-robot aerial manipulator is the already mentioned Fly-Crane which has the characteristics of being the optimal setup to obtain full pose control of the platform and, at the same time, it has the characteristic of being a redundant system, three DoFs for each of the three robots to control 6 DoFs of the platform. Therefore, its peculiarities will be described in the following.

As for the previous case, the configuration of the platform is always given by the vector ${}^W\boldsymbol{p}_P \in \mathbb{R}^3$, describing the position of O_P w.r.t. $\mathcal{F}_W$, and by the Euler angles ${}^W\boldsymbol{\eta}_P = [\phi\ \theta\ \psi]^\top \in \mathbb{R}^3$ describing the orientation of $\mathcal{F}_P$ w.r.t. $\mathcal{F}_W$. The description of the platform state is completed by adding its linear velocity $\dot{\boldsymbol{p}}_P = d\boldsymbol{p}_P/dt \in \mathbb{R}^3$ w.r.t. $\mathcal{F}_W$, and the Euler angles velocities $\dot{\boldsymbol{\eta}}_P \in \mathbb{R}^3$.

The i-th cable is attached at one end to the platform at point B_i and at the other end to an aerial vehicle at point O_{Ri}. The position of B_i and O_{Ri} w.r.t. $\mathcal{F}_W$ are described by the vectors $\boldsymbol{b}_i \in \mathbb{R}^3$ and $\boldsymbol{p}_{Ri} \in \mathbb{R}^3$, respectively. Since each pair of cables $(1,2)$, $(3,4)$ and $(5,6)$ is attached to the same point of the same

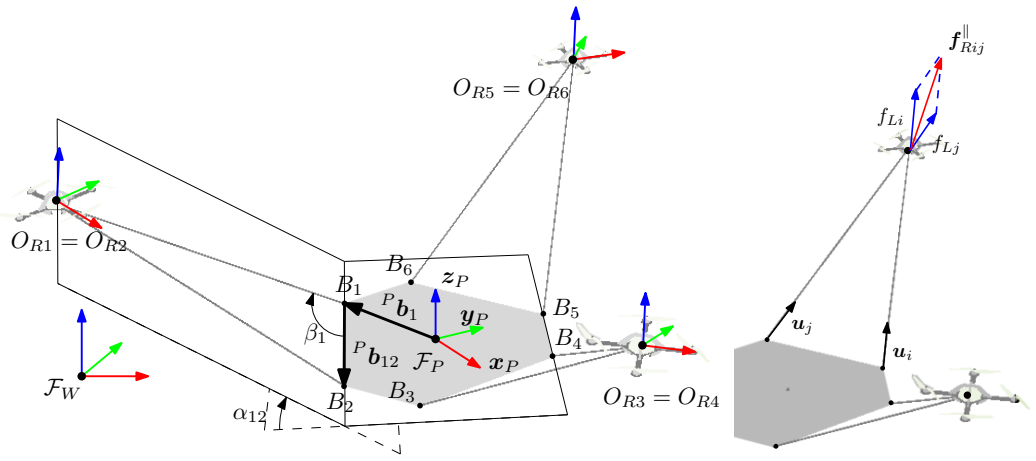

Figure 4.2: Schematic representations of the Fly-Crane system: in Fig. 4.2a the relevant variables of the system have been highlighted; in Fig. 4.2b the forces exerted by each quadrotor and projected on each pair of cables have been shown.

aerial vehicle, then $O_{R1} \equiv O_{R2}$, $O_{R3} \equiv O_{R4}$ and $O_{R5} \equiv O_{R6}$. The connections between cable-load and cable-robot are done such that no rotational constraints are conferred. Moreover, all the points B_i lie on the plane $\{\boldsymbol{x}_P, \boldsymbol{y}_P\}$. As normally done in the state-of-the-art, the model assumes that the cables have negligible mass and inertia w.r.t. the other bodies of the system, neglects phenomena like sagging and elongation and hypothesizes the cables always taut. Thus the generic i-th cable, with $i = 1, \ldots, 6$, has a constant length $l_i \in \mathbb{R}_{>0}$ in the model. These assumptions are also motivated by the fact that for the Fly-Crane system, the cable lengths never exceed certain dimensions. In fact, differently from cable-driven robots, the Fly-Crane possesses a large positional workspace regardless of the length of the cables. Furthermore, long cables are undesirable because they make the two-cable vehicle-load connection similar to a single-cable connection at the detriment of the sought static rigidity property.

The configuration of the pair of cables $(i, j) \in \{(1, 2), (3, 4), (5, 6)\}$ with respect to $\mathcal{F}_P$ is represented by the angle $\alpha_{ij} \in \mathbb{R}$ between the plane $\{\boldsymbol{x}_P, \boldsymbol{y}_P\}$ and the plane formed by the cables (i, j). The platform configuration is then entirely described by the variable $\boldsymbol{q} = [\boldsymbol{p}_P^\top \ \boldsymbol{\eta}_P^\top \ \boldsymbol{\alpha}^\top]^\top \in \mathcal{C} \subset \mathbb{R}^9$, where $\boldsymbol{\alpha} = [\alpha_{12} \ \alpha_{34} \ \alpha_{56}]^\top \in \mathbb{R}^3$.

The three positions of the robots, $\boldsymbol{p}_{Ri} \in \mathbb{R}^3$, with $i = 1, 2, 3$, depend on $\boldsymbol{q}$ through the kinematic relation:

$$\boldsymbol{p}_{Ri}(\boldsymbol{q}) = \boldsymbol{p}_P + \boldsymbol{R}_P(\boldsymbol{\eta}_P)\, {}^P\boldsymbol{p}_{Ri}(\alpha_{ij}), \tag{4.8}$$

where ${}^P\boldsymbol{p}_{Ri} = {}^P\boldsymbol{b}_i + l_i \boldsymbol{R}_{P\boldsymbol{b}_{ij}}(\alpha_{ij}) \boldsymbol{R}_{\boldsymbol{z}_P}(\beta_i) \frac{{}^P\boldsymbol{b}_{ij}}{\|{}^P\boldsymbol{b}_{ij}\|}$, ${}^P\boldsymbol{b}_{ij}$ is the position of the vector $\overrightarrow{B_iB_j}$ expressed in $\mathcal{F}_P$, and $\beta_i \in \mathbb{R}$ is the angle between $\overrightarrow{B_iB_j}$ and $\overrightarrow{B_iO_{Ri}}$. From

(4.8) we can compactly define the kinematic model of the system as

$$\boldsymbol{p}_R = \boldsymbol{f}(\boldsymbol{q}), \tag{4.9}$$

where $\boldsymbol{p}_R = [\boldsymbol{p}_{R1}^\top \;\; \boldsymbol{p}_{R2}^\top \;\; \boldsymbol{p}_{R3}^\top]^\top$. Differentiating (4.9), we obtain the differential kinematic model

$$\boldsymbol{v}_R \coloneqq \dot{\boldsymbol{p}}_R = \frac{\partial \boldsymbol{f}(\boldsymbol{q})}{\partial \boldsymbol{q}} \dot{\boldsymbol{q}} = \boldsymbol{J}(\boldsymbol{q})\dot{\boldsymbol{q}}, \tag{4.10}$$

where, $\boldsymbol{v}_R = [\boldsymbol{v}_{R1}^\top \;\; \boldsymbol{v}_{R2}^\top \;\; \boldsymbol{v}_{R3}^\top]^\top$, $\dot{\boldsymbol{q}} = [\dot{\boldsymbol{p}}_P^\top \;\; \dot{\boldsymbol{\eta}}_P^\top \;\; \dot{\boldsymbol{\alpha}}^\top]^\top \in \mathbb{R}^9$. Equation (4.10) relates velocities of the platform and cable angles rates to the velocities of the robots. The Jacobian matrix $\boldsymbol{J}(\boldsymbol{q}) \in \mathbb{R}^{9\times 9}$ is a square invertible matrix in $\mathcal{C}$, except for some singular configurations as investigated in [Six 2018]. Specifically, it can be defined as

$$\mathbf{J} = \begin{bmatrix} \boldsymbol{I}_3 & \mathbf{J}_{12} & \mathbf{R}_{12} \\ \boldsymbol{I}_3 & \mathbf{J}_{34} & \mathbf{R}_{34} \\ \boldsymbol{I}_3 & \mathbf{J}_{56} & \mathbf{R}_{56} \end{bmatrix}, \tag{4.11}$$

where $\boldsymbol{I}_n \in \mathbb{R}^{n\times n}$ is the identity matrix of dimension n,

$$\mathbf{J}_{ij} = -\left[\boldsymbol{R}_P\left({}^P\boldsymbol{b}_i + l_i \boldsymbol{R}_{P_{\boldsymbol{b}_{ij}}}(\alpha_{ij})\boldsymbol{R}_{\boldsymbol{z}_P}(\beta_i)\frac{{}^P\boldsymbol{b}_{ij}}{\|{}^P\boldsymbol{b}_{ij}\|}\right)\right]_\times,$$

$$\mathbf{R}_{ij} = -l_i \boldsymbol{R}_P \boldsymbol{R}_{P_{\boldsymbol{b}_{ij}}}(\alpha_{ij})\left[\frac{{}^P\boldsymbol{b}_{ij}}{\|{}^P\boldsymbol{b}_{ij}\|}\right]_\times \boldsymbol{R}_{\boldsymbol{z}_P}(\beta_i)\frac{{}^P\boldsymbol{b}_{ij}}{\|{}^P\boldsymbol{b}_{ij}\|}.$$

For configurations in which $\boldsymbol{J}(\boldsymbol{q})$ is non-singular, the coordinate $\boldsymbol{p}_R$ and its time-derivative $\boldsymbol{v}_R$ represent an alternative way to describe the platform configuration $\boldsymbol{q}$ and its velocity $\dot{\boldsymbol{q}}$, respectively, via the inversion of (4.9) and (4.10).

In the control and validation phases, that the reader will find in the following, quasi-static operations will be performed. Therefore, high-order dynamic effects have been considered negligible. Under this assumption, the kinematic model given by (4.9) and (4.10) results satisfactory to describe the kinematic of the system. Nevertheless, possible errors due to this assumption shall be considered.

4.3 The Dynamical Modeling of the Fly-Crane

Furthermore, thanks to the Jacobian matrix $\boldsymbol{J}(\boldsymbol{q})$, following [Six 2018, Six 2021], the dynamics of the whole system can be written. The formulation takes into account the platform and the aerial vehicles as

$$\boldsymbol{M}(\boldsymbol{q})\ddot{\boldsymbol{q}} + \boldsymbol{C}(\boldsymbol{q},\dot{\boldsymbol{q}})\dot{\boldsymbol{q}} + \boldsymbol{n}(\boldsymbol{q}) = \boldsymbol{J}^\top(\boldsymbol{q})\left(\begin{bmatrix} \boldsymbol{f}_{R12} \\ \boldsymbol{f}_{R34} \\ \boldsymbol{f}_{R56} \end{bmatrix} + \bar{\boldsymbol{w}}_e\right), \tag{4.12}$$

where $\boldsymbol{M}(\boldsymbol{q}) \in \mathbb{R}^{9\times 9}$ is the generalized inertia matrix of the system, $\boldsymbol{C}(\boldsymbol{q}, \dot{\boldsymbol{q}}) \in \mathbb{R}^9$ is the vector of Coriolis and centrifugal terms, $\bar{\boldsymbol{w}}_e = [\boldsymbol{w}_e^\top \mathbf{0}_3^\top]^\top \in \mathbb{R}^9$ and $\boldsymbol{G}(\boldsymbol{q}) \in \mathbb{R}^9$ accounts for the external distrubances and the gravitational effects.

As earlier mentioned, if the mass of the platform is uniformly distributed, the geometric center O_P will coincide with the CoM of the platform. However, when the platform is employed for manipulating objects a non-zero displacement of C from O_P (i.e. if ${}^P\boldsymbol{p}_C \neq \mathbf{0}$) induces an additional torque component $\boldsymbol{R}_P\, {}^P\boldsymbol{p}_C \times m_L \boldsymbol{g}$, where $m_L \in \mathbb{R}_{>0}$ is the mass of the loaded platform (which takes into account the platform mass m_P in addition to the extra payload). Therefore, $\boldsymbol{G}(\boldsymbol{q})$ can be defined as

$$\boldsymbol{G}({}^P\boldsymbol{p}_C, \boldsymbol{q}) = m_L \begin{bmatrix} \boldsymbol{g} \\ \boldsymbol{R}_P\, {}^P\boldsymbol{p}_C \times \boldsymbol{g} \\ \mathbf{0} \end{bmatrix} + m_R \mathbf{J}^T \begin{bmatrix} \boldsymbol{g} \\ \boldsymbol{g} \\ \boldsymbol{g} \end{bmatrix}, \tag{4.13}$$

where $m_R \in \mathbb{R}_{>0}$ is the mass of each robot (which is considered the same for ease of notation).

Differently from the generic model presented in Sec. 4.1, the *contact forces* $\boldsymbol{f}_i$ have been modeled on the basis of the thrusts $\boldsymbol{f}_{Ri} \in \mathbb{R}^3$ generated by the thrust generation units represented by the aerial vehicles as

$$\boldsymbol{f}_{Ri} = \boldsymbol{R}_{R_i} \begin{bmatrix} 0 \\ 0 \\ \sum_{k=1}^{4} c_f \omega_k^2 \end{bmatrix} - m_{Ri}\boldsymbol{g} \tag{4.14}$$

where ω_k is the spinning rate of each propeller of each quadrotor, $c_f > 0$ represents a propeller-dependent constant parameter as described in Sec. 3.3. Assuming that the cables are always taut, it is possible to define a thrust intensity vector which lies along the plane formed by each pair of cables (see Fig. 4.2b) and which can be decomposed into two components as follows

$$\boldsymbol{f}_{Ri}^{\parallel} = \left(\boldsymbol{I}_3 - \boldsymbol{n}_{ij}{\boldsymbol{n}_{ij}}^\top\right) \boldsymbol{f}_{Ri} = f_i \boldsymbol{n}_i + f_j \boldsymbol{n}_j \tag{4.15}$$

where $\boldsymbol{n}_i \in \mathbb{R}^3$ and $\boldsymbol{n}_j \in \mathbb{R}^3$ are the unit vectors associated to each pair of cables, $\boldsymbol{n}_{ij} \in \mathbb{R}^3$ is the unit normal vector of the plane generated by $\boldsymbol{n}_i$ and $\boldsymbol{n}_j$

$$\boldsymbol{n}_{ij} = \frac{\boldsymbol{n}_i \times \boldsymbol{n}_j}{\|\boldsymbol{n}_i \times \boldsymbol{n}_j\|} \tag{4.16}$$

Finally, the two obtained contributions f_i and f_j are the solutions of the following system

$$\begin{cases} f_i\,(\boldsymbol{n}_i \cdot \boldsymbol{n}_i) + f_j\,(\boldsymbol{n}_i \cdot \boldsymbol{n}_j) = & \boldsymbol{f}_{Rij}^{\parallel} \cdot \boldsymbol{n}_i \\ f_i\,(\boldsymbol{n}_j \cdot \boldsymbol{n}_i) + f_j(\boldsymbol{n}_j \cdot \boldsymbol{n}_j) = & \boldsymbol{f}_{Rij}^{\parallel} \cdot \boldsymbol{n}_j \end{cases}. \tag{4.17}$$

Concluding, the contact force along each cable pair turns out to be

$$\boldsymbol{f}_i = f_i \boldsymbol{n}_i, \;\; \boldsymbol{f}_j = f_j \boldsymbol{n}_j \;\; . \tag{4.18}$$

4.4 Comparison between the two models of multi-robot aerial systems

The purpose of this section is to delineate a final summary of the main features of the models presented in this chapter. In particular, the first model referred as generic model and the second model referred as Fly-Crane model will be related with the aid of a brief comparison.

With reference to the number of robots, the first method is quite general since N robots can be involved. Conversely, the second model has the characteristic of being the minimum setup through which it is possible to perform full pose manipulations. Therefore, it considers the minimum number of robots which - in this specific case - is three.

Concerning the tools to connect the robots with the load, the first method allows to use a broader range of tools (including ropes or cables) w.r.t. to the second one in which cables constitute the precise design choice. Moreover, while the generic case is based on the assumption that the robots manipulate the object being evenly distributed along a circle around it, the Fly-Crane model has a permanent geometrical design which consists of allocating the three robots with a displacement of 120° from each other.

If the contact forces, i.e. the forces applied by the robots on the payload, define the position of the robots in space in the first case, the position of the platform depicts the position of the robots in the second case. However, as a consequence of the redundancy of the Fly-Crane system, the robots maintain some degrees of freedom to move.

Furthermore, in the first model, the contact forces represent a function of the robot positions and the state of the payload. On the other hand, in the second model, the contact forces are acquired as measurements from the robot thrusts and then projected along each cable.

It is worth mentioning that the development of the model of a physical system is notably influenced by the design of the related controller. Therefore, the last but not least comparison heads toward the control algorithms that will be later developed. As a matter of fact, the first model is presented as a dynamical formulation of the cooperative manipulation problem and the ultimate goal is to define the accelerations of the robots to perform the task. Conversely, the second model is a kinematic formulation that relates the platform linear and angular velocities to the robots' linear velocities which are fundamental for the control loop architecture. The dynamical formulation of the Fly-Crane presented in Sec. 4.3, although crucial, has been mainly devised for estimation purposes rather than for control reasons. Therefore, it has not been considered in the comparison between the two methods.

To conclude, although they attempt to solve the same problem, the two approaches result reasonably different and with the aid of the following chapters, the reader will have the chance of going more into the details of this statement.

Chapter 5

Cooperative Manipulation: Control

In the previous chapter, the challenge of the full pose cooperative manipulation has been addressed discussing two different models capable of describing a generic configuration in the first place and a specific design in the second place. In particular, while the first model can consider different setups in terms of number of robots and tools to be employed, the latter has been designed such that the cables are the tools to manipulate the payload and the number of operating robots is the minimum possible to obtain full pose control. Preserving such dichotomy between these two approaches and the order too, the chapter's purpose is to present two control strategies, one for each mathematical representation. Specifically, for the generic model, a leader-follower paradigm based on sensing the contact forces realized through an admittance filter framework will be presented in Sec. 5.1.1. Contrarily, an inverse kinematic proportional controller augmented with a feed-forward term will be described in Sec. 5.1.2 for the Fly-Crane system. Additionally, a control optimization strategy based on the estimation of the inertial parameters, such as mass and CoM of the platform, will be the subject of Sec. 5.1.3. For each proposed control strategy, a series of analyses have been conducted to investigate the stability and the robustness of such controllers in different scenarios. Moreover, the role of inter-exchanged forces between robots, the disturbance rejection capabilities, the aptitude of dealing with model uncertainties represent some of the points which will be discussed in the following to provide a more exhaustive perspective of the faced challenges.

5.1 Control Strategies

5.1.1 Dynamical Control

This section is devoted to the description of the control strategy which has been designed to obtain the stabilization of the manipulated load in a desired configuration. It consists of a compliant control law based, first of all, on dynamical considerations and secondly, on the assumption that one or more robots can lead the working group. More into the details, the single leader or the multiple leaders have perfect knowledge of their desired position based on the desired position of the payload. Moreover, the method does not rely on explicit communication. The final goal is to regulate the position and the orientation of the load.

In addition, formal equilibria and stability analyses will be provided in the

case N robots are involved in the task. Then, the role of the number of leaders robots will be discussed. Finally, the influence of the internal forces, first, on the convergence to a desired object configuration and, secondly, on the disturbance rejection capabilities will be addressed. Besides, an extensive class of systems can make use of such a strategy due to the generality of the proposed formulation. For the implementation choices employed to validate the presented control approach, the reader is referred to Chap. 6.

5.1.1.1 Force Control

In general, in order to perform physical interaction tasks and more specifically in the scenario of accomplishing a payload manipulation, the robots have to be compliant w.r.t. external forces. Moreover, such compliance can be virtual. Using proper force-based controllers, like hybrid position–force, admittance or impedance controllers one can grant the robot the sought compliance. Therefore, under the hypothesis of perfect position tracking, the i-th agent can be modeled as mass-spring-damper system. Recalling the robot's dynamics (Eq. 4.3)

$$\ddot{\boldsymbol{p}}_{R_i} = \boldsymbol{u}_i, \tag{5.1}$$

the control force provided by each robot can be defined as

$$\boldsymbol{u}_i = \boldsymbol{M}_i^{-1}\big(- \boldsymbol{f}_i - \boldsymbol{B}_i\dot{\boldsymbol{p}}_{Ri} - \boldsymbol{K}_i(\boldsymbol{p}_{Ri} - \boldsymbol{p}_{Ri}^d) + \boldsymbol{\pi}_i\big) \tag{5.2}$$

where the three positive definite symmetric matrices $\boldsymbol{M}_i, \boldsymbol{B}_i, \boldsymbol{K}_i \in \mathbb{R}^{3\times3}$ are the virtual inertia of the robot, the virtual damping and the stiffness of a virtual spring attached to the robot; $\boldsymbol{f}_i \in \mathbb{R}^3$ is the sensed force of the interaction with the load; and $\boldsymbol{\pi}_i \in \mathbb{R}^3$ is the desired interaction force, expressed w.r.t. $\mathcal{F}_W$. In the following, we shall show that $\boldsymbol{\pi}_i$, setting nonzero internal forces on the load, plays an important role in shaping the system equilibria and its stability as well. The aim of the control strategy is, indeed, to determine the conditions for which the carried payload can stay stable in a desired configuration $\boldsymbol{q}_P^d = (\boldsymbol{p}_P^d, \boldsymbol{R}_P^d)$ considering the position without neglecting the orientation. Therefore, for the equilibria and stability analysis, and as well for the validation phase, the final goal of the multi-robot system is to maintain the load in a horizontal position which in mathematical terms can be written as $\boldsymbol{R}_P^d = \boldsymbol{R}_{\boldsymbol{z}_W}(\psi^d)$. In the following, without loss of generality, we will select $\boldsymbol{R}_P^d = \boldsymbol{I}_3$.

5.1.1.2 Equilibria and Stability Analysis

The system is said to be in *static equilibrium* when there exists a set of forces that brings the velocities and accelerations to zero. Adding this condition to (4.1) and considering that the external forces are zero, i.e. $\boldsymbol{w}_e = \boldsymbol{0}_{6\times1}$, we have that

$$[m_P g \boldsymbol{z}_W^\top \;\; \boldsymbol{0}_{1\times3}^\top]^\top = [\boldsymbol{f}_P^\top \;\; {}^P\boldsymbol{\tau}_P{}^\top]^\top \tag{5.3}$$

Replacing (5.3) into (4.7) we obtain the following equilibrium equation

$$[m_P g \boldsymbol{z}_W^\top \ \mathbf{0}_{1\times 3}^\top]^\top = \boldsymbol{G}(\boldsymbol{R}_P)\boldsymbol{f}. \tag{5.4}$$

Given the desired load configuration $(\boldsymbol{p}_P^d, \boldsymbol{R}_P^d)$ and resolving (5.4) for $\boldsymbol{f}$, we can obtain the forces that the robots should apply such that $\boldsymbol{R}_P^d$ is of equilibrium

$$\boldsymbol{f} = \boldsymbol{G}(\boldsymbol{R}_P^d)^\dagger [m_P g \boldsymbol{z}_W^\top \ \mathbf{0}_{1\times 3}]^\top + \boldsymbol{t}, \tag{5.5}$$

where † indicates a right (pseudo)inverse, and $\boldsymbol{t} = [\boldsymbol{t}_1^\top \ \boldsymbol{t}_2^\top \ \dots \ \boldsymbol{t}_N^\top]^\top \in \text{null}(\boldsymbol{G}(\boldsymbol{R}_P^d)) \subset \mathbb{R}^{3N}$ is a vector containing the robot forces belonging to the null space and that may have effects on the internal forces. We refer to such forces as internal forces acting on the object.

It is possible then to verify that a particular solution for which the efforts among the robots are balanced is

$$\boldsymbol{f}_i = \bar{\boldsymbol{f}}_i(\boldsymbol{q}_P^d, f_{int}) := \frac{m_P g}{N}\boldsymbol{z}_W + f_{int}\boldsymbol{R}_P^d \frac{{}^P\boldsymbol{b}_i}{b}, \tag{5.6}$$

where $f_{int} \in \mathbb{R}$ is the *internal force intensity* and is the same for each robot. Notice that

- If $f_{int} = 0$, the interaction forces are vertical (null in the case of ground systems). For the case of a cable-suspended load, the cables would be vertical.
- If $f_{int} > 0$, the interaction forces are radially and outward oriented w.r.t. the load CoM. In this case, the robots tend to stretch the object producing an internal tension.
- If $f_{int} < 0$, the interaction forces are radially and inward oriented w.r.t. the load CoM. In this case, the robots tend to push the object producing an internal compression.

From the kinematics of the system, using Eq. (4.5) and considering the equilibrium force $\bar{\boldsymbol{f}}_i$, we can find the position of the i-th robot such that $\boldsymbol{p}_P^d$ is of equilibrium

$$\boldsymbol{p}_{Ri}^d(\boldsymbol{q}_P^d, f_{int}) = \boldsymbol{p}_P^d + \boldsymbol{R}_P^d \, {}^P\boldsymbol{b}_i + \left(\frac{\|\bar{\boldsymbol{f}}_i\|}{k_i} + l_{0i}\right)\frac{\bar{\boldsymbol{f}}_i}{\|\bar{\boldsymbol{f}}_i\|}. \tag{5.7}$$

Finally, imposing the equilibrium condition to (5.2) (where $\ddot{\boldsymbol{p}}_{R_i} = \dot{\boldsymbol{p}}_{Ri} = \mathbf{0}$) and considering (5.6), we can find the forcing input for each robot that makes the desired load configuration $\boldsymbol{q}_P^d$ an equilibrium. In particular, it has to be that

$$\boldsymbol{\pi}_i = \boldsymbol{\pi}_{Ai}^d(\boldsymbol{q}_P^d, f_{int}) = \bar{\boldsymbol{f}}_i(\boldsymbol{q}_P^d, f_{int}) \tag{5.8}$$

.

Under the made assumptions, i.e. the followers' lack of awareness of their desired state ($\boldsymbol{p}_{Ri}^d$) and the absence of explicit communication, for every follower robot $\boldsymbol{K}_i = \boldsymbol{0}_{3\times3}$. Notice that, in order to compute the forcing input as in (5.6), the followers need to know the desired orientation of the load $\boldsymbol{R}_P^d$. By contrast, if no internal force reference is set ($f_{int} = 0$), they only require the knowledge of the load mass (and only for a floating load). In such a case, the followers will simply follow the motion of the leader, trying to match the desired interaction force with the sensed one. As a consequence, their motion and the load's one result damped.

Given a desired load equilibrium $\boldsymbol{q}_P^d$, and a value of the internal force intensity f_{int}, every robot applies the forcing input $\boldsymbol{\pi}_{Ai}^d(\boldsymbol{q}_P^d, f_{int})$. Under this condition, it is not granted that $\boldsymbol{q}_P^d$ is the unique load configuration of equilibrium. To find all the equilibria under the forcing input $\boldsymbol{\pi}_{Ai}^d(\boldsymbol{q}_P^d, f_{int})$ we need to find $\boldsymbol{p}_P$ and $\boldsymbol{R}_P$ that are solutions of (5.2) and (5.4) when $\boldsymbol{\pi}_i = \boldsymbol{\pi}_{Ai}^d$, and when the velocities and the accelerations are equal to zero (equilibrium condition). From (5.2) it has to be

$$\boldsymbol{0} = -\boldsymbol{f}_i - \boldsymbol{K}_i(\boldsymbol{p}_{Ri} - \boldsymbol{p}_{Ri}^d) + \boldsymbol{\pi}_{Ai}^d. \tag{5.9}$$

Replacing (5.9) into (5.4) and considering the first three rows, we obtain

$$m_P g \boldsymbol{z}_W = \sum_{i=1}^{N} \left(-\boldsymbol{K}_i(\boldsymbol{p}_{Ri} - \boldsymbol{p}_{Ri}^d) + \frac{m_P g}{N}\boldsymbol{z}_W + f_{int}\boldsymbol{R}_P^d \frac{{}^P\boldsymbol{b}_i}{b} \right), \tag{5.10}$$

which implies $\sum_{i=1}^{N} -\boldsymbol{K}_i(\boldsymbol{p}_{Ri} - \boldsymbol{p}_{Ri}^d) = \boldsymbol{0}$. In fact, it is possible to verify that $\sum_{i=1}^{N} {}^P\boldsymbol{b}_i = \boldsymbol{0}$. Notice that in the case of a single leader $\boldsymbol{K}_1 \neq \boldsymbol{0}$, while $\boldsymbol{K}_i = \boldsymbol{0}\ \forall\ i \neq 1$. In this case, $\boldsymbol{p}_{R1} = \boldsymbol{p}_{R1}^d$. Considering the last three rows of (5.4), and recalling that we selected $\boldsymbol{R}_P^d = \boldsymbol{I}_3$, we obtain

$$\boldsymbol{0} = \sum_{i=1}^{N} {}^P\boldsymbol{b}_i \times \boldsymbol{R}_P^\top \bar{\boldsymbol{f}}_i = \frac{f_{int}}{b}\sum_{i=1}^{N} {}^P\boldsymbol{b}_i \times \boldsymbol{R}_P^\top {}^P\boldsymbol{b}_i + \sum_{i=1}^{N} {}^P\boldsymbol{b}_i \times \boldsymbol{R}_P^\top \frac{m_P g}{N}\boldsymbol{z}_W. \tag{5.11}$$

Noticing that $b \neq 0$, and $\sum_{i=1}^{N} {}^P\boldsymbol{b}_i = \boldsymbol{0}$, (5.11) yields

$$\boldsymbol{0} = f_{int}\sum_{i=1}^{N} {}^P\boldsymbol{b}_i \times \boldsymbol{R}_P^\top {}^P\boldsymbol{b}_i. \tag{5.12}$$

If $f_{int} = 0$, then (5.12) holds for every $\boldsymbol{R}_P \in SO(3)$. Conversely, if $f_{int} \neq 0$, remembering definition (4.4), and defining $r_{ij} \in \mathbb{R}$ as the element (i,j) of $\boldsymbol{R}_P$, (5.12) can be rewritten as

$$\begin{cases} \sum_{i=1}^{N} r_{31}y_i x_i + r_{32}y_i^2 & = 0 \\ \sum_{i=1}^{N} -r_{31}x_i^2 - r_{32}x_i y_i & = 0 \\ \sum_{i=1}^{N} x_i(-y_i r_{11} + x_i r_{12}) + y_i(-y_i r_{21} + x_i r_{22}) & = 0 \end{cases}. \tag{5.13}$$

With the definition (4.4) in mind and $N > 2$, the following properties, based on

geometrical deductions, hold

$$\sum_{i=1}^{N} x_i = 0, \quad \sum_{i=1}^{N} y_i = 0, \quad \sum_{i=1}^{N} x_i y_i = 0, \quad \sum_{i=1}^{N} x_i^2 = \sum_{i=1}^{N} y_i^2 = c > 0. \tag{5.14}$$

Using the previous results into (5.13), we have that $r_{31} = r_{32} = 0$ and $r_{21} = r_{12}$. Imposing the rotation matrix conditions, i.e., $\boldsymbol{R}_P^\top \boldsymbol{R}_P = \boldsymbol{I}_3$ and $\det(\boldsymbol{R}_P) = 1$, we finally obtain $\boldsymbol{R}_P = \mathrm{diag}(1, 1, 1)$ or $\boldsymbol{R}_P = \mathrm{diag}(-1, -1, 1)$, which means $\boldsymbol{R}_P = \boldsymbol{R}_{\boldsymbol{z}}(k\pi)\boldsymbol{R}_P^d$, with $k \in \mathbb{N}$. The position of the load can be then computed by simple kinematics

$$\boldsymbol{p}_P = \boldsymbol{p}_{R1} - \boldsymbol{R}_P \, {}^P\boldsymbol{b}_1 - \left(\frac{\|\bar{\boldsymbol{f}}_1\|}{k_1} + l_{01} \right) \frac{\bar{\boldsymbol{f}}_1}{\|\bar{\boldsymbol{f}}_1\|}. \tag{5.15}$$

Summarizing, given the closed-loop system under the forcing input $\boldsymbol{\pi}_{Ai}^d(\boldsymbol{q}_P^d, f_{int})$, all the equilibrium load configurations $(\boldsymbol{p}_P, \boldsymbol{R}_P)$ are such that $\boldsymbol{p}_P$ is computed as in (5.15) and

- $\boldsymbol{R}_P \in SO(3)$ if $f_{int} = 0$;
- $\boldsymbol{R}_P = \boldsymbol{R}_{\boldsymbol{z}}(k\pi)\boldsymbol{q}_P^d$, with $k \in \mathbb{N}$, if $f_{int} \neq 0$.

Remark 1. *When $f_{int} = 0$, an infinite number of equilibrium configurations exists. For each of them, the anchoring point position of the leader remains constant, while the attitude of the load can be any. By contrast, when $f_{int} \neq 0$ there are only two equilibrium configurations. One is equal to the desired one, while the other has the load turned by π about a vertical axis passing through the leader anchoring point. We shall show that for $f_{int} > 0$, the first is asymptotically stable while the second is unstable. Therefore selecting $f_{int} > 0$ is the most suitable choice.*

Aiming to prove the stable/unstable nature of the equilibria previously identified, we define by $\boldsymbol{x} = (\boldsymbol{p}_{R1}, \ldots, \boldsymbol{p}_{RN}, \boldsymbol{p}_P, \boldsymbol{R}_P, \dot{\boldsymbol{p}}_{R1}, \ldots, \dot{\boldsymbol{p}}_{RN}, \dot{\boldsymbol{p}}_P, {}^P\boldsymbol{\omega}_P)$ the state of the system, and by $\mathbb{X}$ the relative state space.

We then define the set of zero velocity states containing all the equilibrium configurations under a specific forcing input $\boldsymbol{\pi}_{Ai}^d(\boldsymbol{q}_P^d, f_{int})$ as $\mathcal{X}(f_{int}, \boldsymbol{q}_P^d) = \{\boldsymbol{x} \in \mathbb{X} \mid \boldsymbol{p}_P, \boldsymbol{R}_P$ obey (5.15) and (5.12), $\boldsymbol{p}_{Ri}$ is given by inverse kinematics, and $\dot{\boldsymbol{p}}_{R1} = \ldots = \dot{\boldsymbol{p}}_{RN} = \dot{\boldsymbol{p}}_P = {}^P\boldsymbol{\omega}_P = \boldsymbol{0}\}$. In addition, for $f_{int} \neq 0$, we define $\boldsymbol{x}'(f_{int}, \boldsymbol{q}_P^d) \in \mathcal{X}(f_{int}, \boldsymbol{q}_P^d)$ and $\boldsymbol{x}''(f_{int}, \boldsymbol{q}_P^d) \in \mathcal{X}(f_{int}, \boldsymbol{q}_P^d)$ such that $\boldsymbol{R}_P = \boldsymbol{R}_P^d$ and $\boldsymbol{R}_P = \boldsymbol{R}_{\boldsymbol{z}}(\pi)\boldsymbol{R}_P^d$, respectively. Notice that for $f_{int} \neq 0$, $\mathcal{X}(f_{int}, \boldsymbol{q}_P^d) = \{\boldsymbol{x}'(f_{int}, \boldsymbol{q}_P^d), \boldsymbol{x}''(f_{int}, \boldsymbol{q}_P^d)\}$. At this point, the next theorem can be formulated.

Theorem 1. *Given a desired load configuration $\boldsymbol{q}_P^d$ and considering the closed-loop system* (4.1) *and* (5.2) *under the forcing input $\boldsymbol{\pi}_{Ai}^d(\boldsymbol{q}_P^d, f_{int})$:*

- *every $\boldsymbol{x} \in \mathcal{X}(f_{int}, \boldsymbol{q}_P^d)$ is stable for $f_{int} = 0$;*
- *$\boldsymbol{x}'(f_{int}, \boldsymbol{q}_P^d)$ is asymptotically stable if $f_{int} > 0$;*

- $\boldsymbol{x}''(f_{int}, \boldsymbol{q}_P^d)$ *is unstable if* $f_{int} > 0$*;*
- $\boldsymbol{x}'(f_{int}, \boldsymbol{q}_P^d)$ *is unstable if* $f_{int} < 0$*;*
- $\boldsymbol{x}''(f_{int}, \boldsymbol{q}_P^d)$ *is asymptotically stable if* $f_{int} < 0$*.*

Proof. Let us consider the following Lyapunov candidate

$$\begin{aligned} V(\boldsymbol{x}) =& \frac{1}{2}\left(\sum_{i=1}^{N} \dot{\boldsymbol{p}}_{Ri}^\top \boldsymbol{M}_i \dot{\boldsymbol{p}}_{Ri} + \boldsymbol{e}_{Ri}^\top \boldsymbol{K}_i \boldsymbol{e}_{Ri} + k_i(\|\boldsymbol{l}_i\| - l_{0i})^2 - 2\boldsymbol{l}_i^\top \bar{\boldsymbol{f}}_i\right) + \\ &+ (N f_{int} b - \sum_{i=1}^{N} \bar{\boldsymbol{f}}_i^\top \boldsymbol{R}_P \, {}^P\boldsymbol{b}_i) + m_P \dot{\boldsymbol{p}}_P^\top \dot{\boldsymbol{p}}_P + {}^P\boldsymbol{\omega}_P{}^\top \boldsymbol{J}_P \, {}^P\boldsymbol{\omega}_P + V_0, \end{aligned} \tag{5.16}$$

where $V_0 \in \mathbb{R}_{\geq 0}$ and $\boldsymbol{e}_{Ri} = \boldsymbol{p}_{Ri}^d - \boldsymbol{p}_{Ri}$. Note that for $i \neq 1$ one can arbitrarily set $\boldsymbol{e}_{Ri}$, since the terms multiply $\boldsymbol{K}_i = \boldsymbol{0}$. For an opportune choice of V_0, $V(\boldsymbol{x})$ is a positive definite, continuously differentiable function in the domain of interest for which we have that $\boldsymbol{x}_{\min}$ ($\boldsymbol{x}_{\min} = \arg\min_{\boldsymbol{x}} V(\boldsymbol{x})$) is such that $\boldsymbol{x}_{\min} \in \mathcal{X}(0, \boldsymbol{q}_P^d)$ and $\boldsymbol{x}_{\min} = \boldsymbol{x}'(f_{int}, \boldsymbol{q}_P^d)$ for $f_{int} > 0$. The proof of this result has been derived following similar reasonings applied in [Tognon 2018], and here it is omitted. Notice that $V(\boldsymbol{x}) = 0$ for all $\boldsymbol{x} \in \mathcal{X}(0, \boldsymbol{q}_P^d)$ and $\boldsymbol{x} = \boldsymbol{x}'(f_{int}, \boldsymbol{q}_P^d)$ for $f_{int} > 0$.

Let us now compute the time derivative of (5.16)

$$\begin{aligned} \dot{V}(\boldsymbol{x}) = &\left(\sum_{i=1}^{N} \dot{\boldsymbol{p}}_{Ri}^\top \boldsymbol{M}_i \ddot{\boldsymbol{p}}_{R_i} + \boldsymbol{e}_{Ri}^\top \boldsymbol{K}_i \dot{\boldsymbol{e}}_{Ri} + \dot{\boldsymbol{l}}_i^\top \boldsymbol{f}_i - \dot{\boldsymbol{l}}_i^\top \bar{\boldsymbol{f}}_i + \bar{\boldsymbol{f}}_i^\top \boldsymbol{R}_P \boldsymbol{S}({}^P\boldsymbol{\omega}_P) \, {}^P\boldsymbol{b}_i\right) \\ &+ m_P \dot{\boldsymbol{p}}_P^\top \ddot{\boldsymbol{p}}_P + {}^P\boldsymbol{\omega}_P{}^\top \boldsymbol{J}_P \, {}^P\dot{\boldsymbol{\omega}}_P, \end{aligned} \tag{5.17}$$

where we used the fact that $\frac{d}{dt}\left(\frac{1}{2}k_i(\|\boldsymbol{l}_i\| - l_{0i})^2\right) = \dot{\boldsymbol{l}}_i^\top \boldsymbol{f}_i$. Replacing (4.1) and (5.2) we obtain

$$\begin{aligned} \dot{V}(\boldsymbol{x}) = &\left(\sum_{i=1}^{N} \dot{\boldsymbol{p}}_{Ri}^\top \left(-\boldsymbol{f}_i - \boldsymbol{B}_i \dot{\boldsymbol{p}}_{Ri} - \boldsymbol{K}_i \boldsymbol{e}_{Ri} + \bar{\boldsymbol{f}}_i, \right) + \dot{\boldsymbol{p}}_{Ri}^\top \boldsymbol{K}_i \boldsymbol{e}_{Ri} + \dot{\boldsymbol{l}}_i^\top (\boldsymbol{f}_i - \bar{\boldsymbol{f}}_i) + \right. \\ &\left. + \bar{\boldsymbol{f}}_i^\top \boldsymbol{R}_P \boldsymbol{S}({}^P\boldsymbol{\omega}_P) \, {}^P\boldsymbol{b}_i\right) + \dot{\boldsymbol{p}}_P^\top \left(-m_P g \boldsymbol{z}_W - \boldsymbol{D}_P \dot{\boldsymbol{p}}_P + \sum_{i=1}^{N} \boldsymbol{f}_i\right) + \\ &+ {}^P\boldsymbol{\omega}_P{}^\top \boldsymbol{J}_P \left(-\boldsymbol{S}({}^P\boldsymbol{\omega}_P) \boldsymbol{J}_P \, {}^P\boldsymbol{\omega}_P - \boldsymbol{B}_P \, {}^P\boldsymbol{\omega}_P + \sum_{i=1}^{N} \boldsymbol{S}({}^P\boldsymbol{b}_i) \boldsymbol{R}_P \boldsymbol{f}_i\right), \end{aligned} \tag{5.18}$$

Noticing that $\dot{\boldsymbol{l}}_i = \dot{\boldsymbol{p}}_{Ri} - \dot{\boldsymbol{p}}_P - \boldsymbol{R}\boldsymbol{S}({}^P\boldsymbol{\omega}_P) \, {}^P\boldsymbol{b}_i$ and $\sum_{i=1}^{N} \bar{\boldsymbol{f}}_i = -m_P g \boldsymbol{z}_W$, after few algebraic computations we get

$$\dot{V}(\boldsymbol{x}) = \sum_{i=1}^{N} -\dot{\boldsymbol{p}}_{Ri}^\top \boldsymbol{B}_i \dot{\boldsymbol{p}}_{Ri} - \dot{\boldsymbol{p}}_P^\top \boldsymbol{D}_P \dot{\boldsymbol{p}}_P - {}^P\boldsymbol{\omega}_P{}^\top \boldsymbol{B}_P \, {}^P\boldsymbol{\omega}_P, \tag{5.19}$$

that is clearly negative semidefinite. In particular $\dot{V}(\boldsymbol{x}) = 0$ for all $\boldsymbol{x} \in \mathcal{E} = \{\boldsymbol{x} \in \mathbb{X} \mid \dot{\boldsymbol{p}}_{Ri} = \boldsymbol{0}\ \forall\ i,\ \dot{\boldsymbol{p}}_P = \boldsymbol{0},\ {}^P\boldsymbol{\omega}_P = \boldsymbol{0}\}$. Based on the *LaSalle's invariance principle* and the *Chetaev's theorem* (see [Khalil 2001]), the stability nature of the equilibria according to f_{int} can be proved.

□

Let us define the input-output pair $(\boldsymbol{u}, \boldsymbol{y})$, where $\boldsymbol{u}$ and $\boldsymbol{y}$ are, respectively, the stack vectors of $\boldsymbol{p}^d_{Ri}$ and $\dot{\boldsymbol{p}}_{Ri}$ for all i. Using the same Lyapunov function (5.16), it is possible to show that even with a time-varying desired trajectory for the leader robot, the system is output-strictly passive w.r.t. the storage function (5.16) and the input-output pair $(\boldsymbol{u}, \boldsymbol{y})$. Again, this result follows the considerations which have been already made in [Tognon 2018].

Remark 2. *Once the desired pose of the load is decided, it is advisable to choose $f_{int} > 0$. In this condition, setting the forcing inputs as $\boldsymbol{\pi}^d_{Ai}$, the robots will steer the load to the desired configuration preserving the stability without the need of sending data to each other. Moreover, by virtue of the passivity, a certain robustness w.r.t. uncertainties and external disturbances can be guaranteed by the controlled system. Finally, it has to be noticed that implicit communication has been exploited in order to execute the cooperative task. Indeed, the robots can exchange and feel the forces from the cables and the object.*

5.1.2 Kinematic Control

In the previous section, a control strategy based on dynamical considerations for a generic model has been presented. Conversely, the goal of this section is to introduce the inverse kinematic controller which has been designed for the Fly-Crane model described in 4.2. Additionally, the robustness of the controller against model parameters and dynamic uncertainties will be amply described.

5.1.2.1 Inverse Kinematic Control and Robustness Analysis

The proposed control scheme of the Fly-Crane is shown in Fig. 5.1. From left to right, the desired trajectory quantities $\boldsymbol{q}^d, \dot{\boldsymbol{q}}^d$ and the measured configuration $\boldsymbol{q}$ are used by the outer *configuration controller* to generate the reference aerial-vehicle velocities $\boldsymbol{v}^\star_R$. Using $\boldsymbol{v}^\star_R$ and the measured velocities $\boldsymbol{v}_R$, the *velocity controllers* of the aerial vehicles compute the commanded accelerations for each vehicle $\boldsymbol{u} = [\boldsymbol{u}_1^\top\ \boldsymbol{u}_3^\top\ \boldsymbol{u}_5^\top]^\top$. Such commanded accelerations are provided to the low-level actuation units of the aerial vehicles, which are in control of the orientation of the vehicles and of the rotor speeds. In the following, we detail the equations used in each controller. To face possible errors of the low-level actuation units, an uncertain model for the aerial vehicles is considered.

We denote with $\hat{\boldsymbol{J}}(\boldsymbol{q}) \in \mathbb{R}^{9\times 9}$ the nominal Jacobian of the system, such that

$$\hat{\boldsymbol{J}}(\boldsymbol{q}) = \boldsymbol{J}(\boldsymbol{q}) + \Delta\boldsymbol{J}(\boldsymbol{q}), \tag{5.20}$$

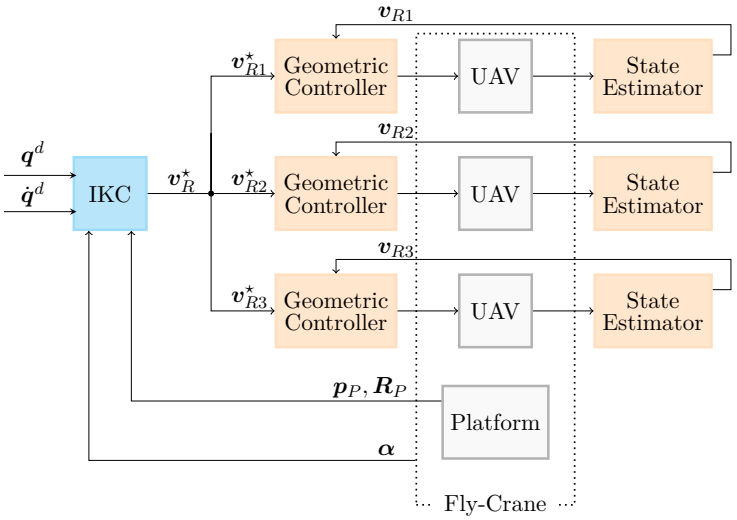

Figure 5.1: Control architecture of the inverse kinematic controller of the Fly-Crane system in which the *outer loop* has been highlighted in green, the *intermediate loop* in blue and the *inner loop* in red.

where $\Delta\boldsymbol{J}(\boldsymbol{q})$ is the error between the nominal (identified) and real (unkown) Jacobian matrices. Given the desired configuration $\boldsymbol{q}^d = [\boldsymbol{p}_P^{d\top} \;\; \boldsymbol{\eta}_P^{d\top} \;\; \boldsymbol{\alpha}^{d\top}]^\top$, the corresponding generalized velocities $\dot{\boldsymbol{q}}^d = [\boldsymbol{v}_P^{d\top} \;\; \dot{\boldsymbol{\eta}}_P^{d\top} \;\; \dot{\boldsymbol{\alpha}}^{d\top}]^\top$, and the measured configuration $\boldsymbol{q}$, the reference aerial-vehicle velocities are computed

$$\boldsymbol{v}_R^\star = \hat{\boldsymbol{J}}(\boldsymbol{q}) \left(\boldsymbol{K}_{\boldsymbol{q}} \boldsymbol{e}_{\boldsymbol{q}} + \dot{\boldsymbol{q}}^d \right), \tag{5.21}$$

where $\boldsymbol{K}_{\boldsymbol{q}} = k_{\boldsymbol{q}} \boldsymbol{I}_9 \in \mathbb{R}^{9\times 9}_{>0}$ is a positive definite matrix and $\boldsymbol{e}_{\boldsymbol{q}} = \boldsymbol{q}^d - \boldsymbol{q}$. The commanded accelerations for the vehicles are computed simply as

$$\boldsymbol{u} = \boldsymbol{K}_R \left(\boldsymbol{v}_R^\star - \boldsymbol{v}_R \right), \tag{5.22}$$

where $\boldsymbol{K}_R = k_R \boldsymbol{I}_9 \in \mathbb{R}^{9\times 9}_{>0}$ is a positive definite matrix.

Each aerial vehicle is equipped with a low-level actuation unit, as explained in Sec. 3.4, that acts on the orientation and intensity of the total force produced by its propellers in order to let $\dot{\boldsymbol{v}}_{Ri}$ match the given acceleration input $\boldsymbol{u}_i$, for $i = 1, 2, 3$. However, the non-perfect knowledge of the platform dynamics and the presence of external disturbances make such matching *inexact*. The closed-loop dynamics of the vehicle including the actuation unit is then equivalent to an *uncertain* double integrator, i.e.,

$$\boldsymbol{v}_{Ri} = \dot{\boldsymbol{p}}_{Ri}, \quad \dot{\boldsymbol{v}}_{Ri} = \boldsymbol{u}_i + \boldsymbol{d}_i, \tag{5.23}$$

where the uncontrollable signal $\boldsymbol{d}_i$ accounts for all the aforementioned dynamic uncertainties and external disturbances. In light of the generality of the disturbance modeling, such signal $\boldsymbol{d}_i$ can be large, small or even close to zero, depending on the

type of platform (e.g., under- or fully-actuated), type of controller (e.g., full dynamic model inversion, vehicle model inversion plus disturbance rejection, etc.) and the desired trajectory. Defining the vector $\boldsymbol{d} = [\boldsymbol{d}_1^\top \ \boldsymbol{d}_3^\top \ \boldsymbol{d}_5^\top]^\top$ we can write the dynamics of the three aerial vehicles as

$$\boldsymbol{v}_R = \dot{\boldsymbol{p}}_R, \quad \dot{\boldsymbol{v}}_R = \boldsymbol{u} + \boldsymbol{d}. \tag{5.24}$$

Summarizing, the closed-loop system dynamics is given by the equations (5.24), where $\boldsymbol{u}$ is computed using (5.22) and (5.21). In such a model, the terms $\Delta\boldsymbol{J}(\boldsymbol{q})$ and $\boldsymbol{d}$ account for all the non-idealities arising from modeling errors at the dynamic and kinematic level and the neglected external disturbances. To analyze the system stability under non-ideal conditions, let us write the closed-loop dynamics of the error. Replacing (5.21) and (5.22) into (5.24) and applying the differential kinematics (4.10) yield

$$\begin{aligned}\boldsymbol{J}(\boldsymbol{q})\ddot{\boldsymbol{q}} + \dot{\boldsymbol{J}}(\boldsymbol{q},\dot{\boldsymbol{q}})\dot{\boldsymbol{q}} = k_R\hat{\boldsymbol{J}}(\boldsymbol{q})k_{\boldsymbol{q}}\boldsymbol{e}_{\boldsymbol{q}} + k_R\hat{\boldsymbol{J}}(\boldsymbol{q})\dot{\boldsymbol{q}}^d \\ -k_R\boldsymbol{J}(\boldsymbol{q})\dot{\boldsymbol{q}} + \boldsymbol{d}.\end{aligned} \tag{5.25}$$

Considering the previous equation with nominal Jacobian as in (5.20), we can write the error dynamics as

$$\begin{aligned}\ddot{\boldsymbol{e}}_{\boldsymbol{q}} = &-\left(k_Rk_{\boldsymbol{q}} + k_Rk_{\boldsymbol{q}}\boldsymbol{J}^{-1}(\boldsymbol{q})\Delta\boldsymbol{J}(\boldsymbol{q})\right)\boldsymbol{e}_{\boldsymbol{q}} \\ &-\left(k_R + \boldsymbol{J}^{-1}(\boldsymbol{q})\dot{\boldsymbol{J}}(\boldsymbol{q},\dot{\boldsymbol{q}})\right)\dot{\boldsymbol{e}}_{\boldsymbol{q}} + \boldsymbol{w},\end{aligned} \tag{5.26}$$

where $\boldsymbol{w}$ contains the terms that do not depend on the error and that are considered as disturbances

$$\boldsymbol{w} = \ddot{\boldsymbol{q}}^d + \boldsymbol{J}^{-1}(\boldsymbol{q})\left(\left(\dot{\boldsymbol{J}}(\boldsymbol{q},\dot{\boldsymbol{q}}) - k_R\Delta\boldsymbol{J}(\boldsymbol{q})\right)\dot{\boldsymbol{q}}^d - \boldsymbol{d}\right). \tag{5.27}$$

Normally, the control gain $\boldsymbol{K}_R$ is tuned independently to (5.21) to achieve the best tracking of the velocity reference $\boldsymbol{v}_R^\star$. In this case, we show how to design the configuration control gain $\boldsymbol{K}_{\boldsymbol{q}} = k_{\boldsymbol{q}}\boldsymbol{I}_9$, such that to guarantee the stability of the closed-loop system with desired H_∞ performance, under some sufficient conditions on the uncertainty and disturbance magnitudes.

In the following, for an arbitrary matrix $\boldsymbol{M}$, $\lambda_{\min}[\boldsymbol{M}]$ and $\lambda_{\max}[\boldsymbol{M}]$ are its minimal and maximal eigenvalues, $\|\boldsymbol{M}\| = \sqrt{\lambda_{\max}[\boldsymbol{M}^\top\boldsymbol{M}]}$ is its induced norm, and $\boldsymbol{M} > 0$ ($\boldsymbol{M} < 0$) stands for a positive (negative) definite matrix. Finally, with the symbol $*$ we refer to the symmetric term in a matrix.

Theorem 2. *Let us consider the control laws* (5.22) *and* (5.21) *applied to the Fly-Crane under disturbance* $\boldsymbol{d}$ *and uncertain Jacobian matrix* $\hat{\boldsymbol{J}}(\boldsymbol{q})$. k_R *is given while* $k_{\boldsymbol{q}}$ *has to be designed. Assume that the following bounds hold true for given positive*

constants $\delta, \iota, \rho \in \mathbb{R}_{>0}$

$$\|\Delta \boldsymbol{J}(\boldsymbol{q})^\top \Delta \boldsymbol{J}(\boldsymbol{q})\| \leq \delta^2, \tag{5.28}$$

$$\lambda_{min}[\boldsymbol{J}(\boldsymbol{q})^\top \boldsymbol{J}(\boldsymbol{q})] \geq \iota^2, \tag{5.29}$$

$$\|\dot{\boldsymbol{J}}(\boldsymbol{q})^\top \dot{\boldsymbol{J}}(\boldsymbol{q})\| \leq \rho^2. \tag{5.30}$$

The designed control gain $k_{\boldsymbol{q}}$ *stabilizes the system with* H_∞ *performance defined by*

$$\|\boldsymbol{e_q}\| \leq \gamma \|\boldsymbol{w}\|, \tag{5.31}$$

with a given constant $\gamma > 0$*, if there exist scalars* q *and* q_k *and matrices* $\boldsymbol{P} = \boldsymbol{P}^\top$*,* $\boldsymbol{F}_1 = \boldsymbol{F}_1^\top$*,* $\boldsymbol{F}_2 = \boldsymbol{F}_2^\top$*,* $\boldsymbol{G}_1 = \boldsymbol{G}_1^\top$*, and* $\boldsymbol{G}_2 = \boldsymbol{G}_2^\top$ *of dimension* 9×9 *that satisfy the LMI conditions*

$$\begin{bmatrix} \boldsymbol{P} & q\boldsymbol{I}_9 \\ * & q\boldsymbol{I}_9 \end{bmatrix} > 0 \tag{5.32}$$

and

$$\begin{bmatrix} \boldsymbol{\Xi} & \boldsymbol{E}_2 q & \boldsymbol{E}_2 k_R q_k & \boldsymbol{E}_1 q & \boldsymbol{E}_1 k_R q_k \\ * & -2\boldsymbol{F}_1 & \boldsymbol{0}_9 & \boldsymbol{0}_9 & \boldsymbol{0}_9 \\ * & * & -2\boldsymbol{G}_1 & \boldsymbol{0}_9 & \boldsymbol{0}_9 \\ * & * & * & -2\boldsymbol{F}_2 & \boldsymbol{0}_9 \\ * & * & * & * & -2\boldsymbol{G}_2 \end{bmatrix} < 0, \tag{5.33}$$

with

$$\boldsymbol{E}_1 = [\boldsymbol{I}_9 \ \boldsymbol{0}_9 \ \boldsymbol{0}_9]^\top, \ \boldsymbol{E}_2 = [\boldsymbol{0}_9 \ \boldsymbol{I}_9 \ \boldsymbol{0}_9]^\top, \tag{5.34}$$

and $\boldsymbol{\Xi}$ *given as*

$$\begin{bmatrix} \boldsymbol{\Xi}_{1,1} & \frac{1}{2}\boldsymbol{P} - \frac{1}{2}k_R q_k \boldsymbol{I}_9 - \frac{1}{2}k_R q \boldsymbol{I}_9 & q\boldsymbol{I}_9 \\ * & \frac{\rho^2}{2\iota^2}(\boldsymbol{F}_1 + \boldsymbol{F}_2) - k_R q \boldsymbol{I}_9 + q\boldsymbol{I}_9 & q\boldsymbol{I}_9 \\ * & * & -\gamma^2 \boldsymbol{I}_9 \end{bmatrix} \tag{5.35}$$

with $\boldsymbol{\Xi}_{1,1} = \boldsymbol{I}_9 + \frac{\delta^2}{2\iota^2}(\boldsymbol{G}_1 + \boldsymbol{G}_2) - k_R q \boldsymbol{I}_9$*. In particular, the designed controller gain* $k_{\boldsymbol{q}}$ *is then given by* $k_{\boldsymbol{q}} = q_k / q$*.*

Proof. Consider the Lyapunov candidate function $V(\boldsymbol{e_q}, \dot{\boldsymbol{e}}_{\boldsymbol{q}}) = V_1 + V_2 + V_3$, with

$$V_1 = \frac{1}{2}\boldsymbol{e_q}^\top \boldsymbol{P} \boldsymbol{e_q}, \ V_2 = \frac{1}{2}\dot{\boldsymbol{e}}_{\boldsymbol{q}}^\top q \dot{\boldsymbol{e}}_{\boldsymbol{q}}, \ V_3 = \boldsymbol{e_q}^\top q \dot{\boldsymbol{e}}_{\boldsymbol{q}}. \tag{5.36}$$

To have V as a Lyapunov function we need $V > 0$, $\forall \ \boldsymbol{e_q} \neq \boldsymbol{0}, \dot{\boldsymbol{e}}_{\boldsymbol{q}} \neq \boldsymbol{0}$. Re-writing V, this is verified if

$$V = \frac{1}{2}\begin{bmatrix} \boldsymbol{e_q} \\ \dot{\boldsymbol{e}}_{\boldsymbol{q}} \end{bmatrix}^\top \begin{bmatrix} \boldsymbol{P} & q\boldsymbol{I}_9 \\ * & q\boldsymbol{I}_9 \end{bmatrix} \begin{bmatrix} \boldsymbol{e_q} \\ \dot{\boldsymbol{e}}_{\boldsymbol{q}} \end{bmatrix} > 0, \tag{5.37}$$

which is satisfied only if LMI (5.32) holds. Next, we consider the time-derivative of

V. For V_1, $\dot{V}_1 = \boldsymbol{e_q}^\top \boldsymbol{P}\dot{\boldsymbol{e}}_{\boldsymbol{q}}$. Concerning V_2, after replacing (5.26) we obtain

$$\begin{aligned}\dot{V}_Q \leq &- \dot{\boldsymbol{e}}_{\boldsymbol{q}}^\top q k_R k_{\boldsymbol{q}} \boldsymbol{J}^{-1}(\boldsymbol{q})\Delta\boldsymbol{J}(\boldsymbol{q})\boldsymbol{e_q} - \dot{\boldsymbol{e}}_{\boldsymbol{q}}^\top q k_R k_{\boldsymbol{q}} \boldsymbol{e_q} \\ &- \dot{\boldsymbol{e}}_{\boldsymbol{q}}^\top q k_R \dot{\boldsymbol{e}}_{\boldsymbol{q}} - \dot{\boldsymbol{e}}_{\boldsymbol{q}}^\top q \boldsymbol{J}^{-1}(\boldsymbol{q})\dot{\boldsymbol{J}}(\boldsymbol{q})\dot{\boldsymbol{e}}_{\boldsymbol{q}} + \dot{\boldsymbol{e}}_{\boldsymbol{q}}^\top q \boldsymbol{w}.\end{aligned} \tag{5.38}$$

Given the relation $-2\boldsymbol{a}^\top \boldsymbol{b} \leq \boldsymbol{a}^\top \boldsymbol{X}^{-1}\boldsymbol{a} + \boldsymbol{b}^\top \boldsymbol{X}\boldsymbol{b},\ \boldsymbol{X} > 0$, choosing $\boldsymbol{X}$ as $\boldsymbol{F}_1 > 0$, we can use (5.29) and (5.30) to bound

$$\begin{aligned}- \dot{\boldsymbol{e}}_{\boldsymbol{q}}^\top q \boldsymbol{J}^{-1}(\boldsymbol{q})\dot{\boldsymbol{J}}(\boldsymbol{q})\dot{\boldsymbol{e}}_{\boldsymbol{q}} &\leq \frac{1}{2}\dot{\boldsymbol{e}}_{\boldsymbol{q}}^\top q \boldsymbol{F}_1^{-1} q \dot{\boldsymbol{e}}_{\boldsymbol{q}} \\ &+ \frac{1}{2}\dot{\boldsymbol{e}}_{\boldsymbol{q}}^\top (\boldsymbol{J}^{-1}(\boldsymbol{q})\dot{\boldsymbol{J}}(\boldsymbol{q}))^\top \boldsymbol{F}_1 \boldsymbol{J}^{-1}(\boldsymbol{q})\dot{\boldsymbol{J}}(\boldsymbol{q})\dot{\boldsymbol{e}}_{\boldsymbol{q}} \\ &\leq \frac{1}{2}\dot{\boldsymbol{e}}_{\boldsymbol{q}}^\top q \boldsymbol{F}_1^{-1} q \dot{\boldsymbol{e}}_{\boldsymbol{q}} + \frac{\rho^2}{2\iota^2}\dot{\boldsymbol{e}}_{\boldsymbol{q}}^\top \boldsymbol{F}_1 \dot{\boldsymbol{e}}_{\boldsymbol{q}}.\end{aligned} \tag{5.39}$$

In the same way, choose $\boldsymbol{X}$ as $\boldsymbol{G}_1$, with (5.28), to bound

$$\begin{aligned}&-\dot{\boldsymbol{e}}_{\boldsymbol{q}}^\top q k_R k_{\boldsymbol{q}} \boldsymbol{J}^{-1}(\boldsymbol{q})\Delta\boldsymbol{J}(\boldsymbol{q})\boldsymbol{e_q} \\ &\quad\leq \frac{1}{2}\dot{\boldsymbol{e}}_{\boldsymbol{q}}^\top (q k_R k_{\boldsymbol{q}}) \boldsymbol{G}_1^{-1} (q k_R k_{\boldsymbol{q}})^\top \dot{\boldsymbol{e}}_{\boldsymbol{q}} + \frac{\delta^2}{2\iota^2}\boldsymbol{e}_{\boldsymbol{q}}^\top \boldsymbol{G}_1 \boldsymbol{e_q}.\end{aligned}$$

Finally, we have that the derivative of V_2 is bounded by

$$\begin{aligned}\dot{V}_Q \leq &\frac{1}{2}\dot{\boldsymbol{e}}_{\boldsymbol{q}}^\top (q k_R k_{\boldsymbol{q}}) \boldsymbol{G}_1^{-1} (q k_R k_{\boldsymbol{q}})^\top \dot{\boldsymbol{e}}_{\boldsymbol{q}} + \frac{\delta^2}{2\iota^2}\boldsymbol{e}_{\boldsymbol{q}}^\top \boldsymbol{G}_1 \boldsymbol{e_q} \\ &- \dot{\boldsymbol{e}}_{\boldsymbol{q}}^\top q k_R k_{\boldsymbol{q}} \boldsymbol{e_q} - \dot{\boldsymbol{e}}_{\boldsymbol{q}}^\top q k_R \dot{\boldsymbol{e}}_{\boldsymbol{q}} \\ &+ \frac{1}{2}\dot{\boldsymbol{e}}_{\boldsymbol{q}}^\top q \boldsymbol{F}_1^{-1} q \dot{\boldsymbol{e}}_{\boldsymbol{q}} + \frac{\rho^2}{2\iota^2}\dot{\boldsymbol{e}}_{\boldsymbol{q}}^\top \boldsymbol{F}_1 \dot{\boldsymbol{e}}_{\boldsymbol{q}} + \dot{\boldsymbol{e}}_{\boldsymbol{q}}^\top q \boldsymbol{w}.\end{aligned} \tag{5.40}$$

Taking the time-derivative of term V_3 and proceeding analogously, for some $\boldsymbol{F}_2 > 0$ and $\boldsymbol{G}_2 > 0$, we can obtain

$$\begin{aligned}\dot{V}_R \leq &\frac{1}{2}\boldsymbol{e}_{\boldsymbol{q}}^\top (q k_R k_{\boldsymbol{q}}) \boldsymbol{G}_2^{-1} (q k_R k_{\boldsymbol{q}})^\top \boldsymbol{e_q} + \frac{\delta^2}{2\iota^2}\boldsymbol{e}_{\boldsymbol{q}}^\top \boldsymbol{G}_2 \boldsymbol{e_q} \\ &- \boldsymbol{e}_{\boldsymbol{q}}^\top q k_R k_{\boldsymbol{q}} \boldsymbol{e_q} - \boldsymbol{e}_{\boldsymbol{q}}^\top q k_R \dot{\boldsymbol{e}}_{\boldsymbol{q}} + \dot{\boldsymbol{e}}_{\boldsymbol{q}}^\top q \dot{\boldsymbol{e}}_{\boldsymbol{q}} \\ &+ \frac{1}{2}\boldsymbol{e}_{\boldsymbol{q}}^\top q \boldsymbol{F}_2^{-1} q \boldsymbol{e_q} + \frac{\rho^2}{2\iota^2}\dot{\boldsymbol{e}}_{\boldsymbol{q}}^\top \boldsymbol{F}_2 \dot{\boldsymbol{e}}_{\boldsymbol{q}} + \boldsymbol{e}_{\boldsymbol{q}}^\top q \boldsymbol{w}.\end{aligned} \tag{5.41}$$

To show that stability with the H_∞ performance is satisfied we use the following condition

$$\boldsymbol{e}_{\boldsymbol{q}}^\top \boldsymbol{e_q} - \gamma^2 \boldsymbol{w}^\top \boldsymbol{w} + \dot{V} < 0, \tag{5.42}$$

given the Lyapunov candidate function V and a scalar $\gamma > 0$. Integrating both sides in any time-interval $[0, T]$ and assuming zero initial conditions $\boldsymbol{e_q}(0) = \boldsymbol{0}$ and

$\dot{\boldsymbol{e}}_{\boldsymbol{q}}(0) = \mathbf{0}$, we have

$$\int_0^T \left(\boldsymbol{e}_{\boldsymbol{q}}^\top \boldsymbol{e}_{\boldsymbol{q}} - \gamma^2 \boldsymbol{w}^\top \boldsymbol{w} \right) dt + V(\boldsymbol{e}_{\boldsymbol{q}}(T), \dot{\boldsymbol{e}}_{\boldsymbol{q}}(T)) < 0, \tag{5.43}$$

such that, if condition (5.42) is satisfied then (5.31) holds and the system is stable with H_∞ performance.

To verify condition (5.42), since $\dot{V} = \dot{V}_1 + \dot{V}_2 + \dot{V}_3$, we use the upper bounds in (5.40) and (5.41) into (5.42) to write

$$\boldsymbol{\xi}^\top \boldsymbol{A} \boldsymbol{\xi} < 0 \tag{5.44}$$

with $\boldsymbol{\xi}^\top = [\boldsymbol{e}_{\boldsymbol{q}}^\top \ \dot{\boldsymbol{e}}_{\boldsymbol{q}}^\top \ \boldsymbol{w}^\top]$,

$$\begin{aligned} \boldsymbol{A} = \Big[& \boldsymbol{\Xi} + \boldsymbol{E}_2 q \frac{1}{2} \boldsymbol{F}_1^{-1} (\boldsymbol{E}_2 q)^\top + \boldsymbol{E}_2 q k_R k_{\boldsymbol{q}} \frac{1}{2} \boldsymbol{G}_1^{-1} (\boldsymbol{E}_2 q k_R k_{\boldsymbol{q}})^\top \\ & + \boldsymbol{E}_1 q \frac{1}{2} \boldsymbol{F}_2^{-1} (\boldsymbol{E}_1 q)^\top + \boldsymbol{E}_1 q k_R k_{\boldsymbol{q}} \frac{1}{2} \boldsymbol{G}_2^{-1} (\boldsymbol{E}_1 q k_R k_{\boldsymbol{q}})^\top \Big], \end{aligned}$$

$\boldsymbol{\Xi}$ given in (5.35), and $\boldsymbol{E}_1$ and $\boldsymbol{E}_2$ in (5.34). Thus, for the condition (5.44) to hold, $\boldsymbol{A}$ has to be imposed negative definite. Applying the Schur's Complement on this term, and writing $q_k = q k_{\boldsymbol{q}}$ to allow for control design, yields the LMI condition in (5.33). If the LMI conditions are satisfied, $k_{\boldsymbol{q}}$ can be obtained by taking $k_{\boldsymbol{q}} = q_k / q$. This completes the proof.

□

From a design perspective, given the bounds δ, ι, ρ and the velocity controller gain k_R, we would like to find the $\boldsymbol{K}_{\boldsymbol{q}}$ that provides the best H_∞ performance. We can then rewrite Theorem 2 as a constrained minimization problem of γ

$$\begin{aligned} & \underset{\beta}{\text{minimize}} \quad \gamma \\ & \text{subject to} \quad (5.32), (5.33), \end{aligned} \tag{5.45}$$

where $\beta = (\boldsymbol{P}, \boldsymbol{F}_1, \boldsymbol{F}_2, \boldsymbol{G}_1, \boldsymbol{G}_2, q, q_k, \delta, \iota, \rho, k_R, \gamma)$. From the solution of (5.45), and in particular from q_k and q, the optimal gain $k_{\boldsymbol{q}}$ is computed as $k_{\boldsymbol{q}} = q_k / q$.

The main advantage of this method is to find a feasible controller, with the best H_∞ gain in view of Theorem 2, which formally guarantees stability within bounds of uncertainties in the Jacobian matrix (δ), the proximity to singular configurations (ι), and the rate of variation of the Jacobian (ρ).

Remark 3. *In order to solve* (5.45) *a first estimation of the bounds* δ*,* ι*, and* ρ *is needed.*

Such first estimation can be performed along the desired trajectory knowing the maximum uncertainty on the Jacobian. The latter comes from the imprecision in

the design and manufacturing of the platform. Therefore:

$$\begin{aligned} \delta^2 &> \max_{t\in\mathbb{R}^{\geq 0}} \|\Delta \boldsymbol{J}(\boldsymbol{q}^d(t))^\top \Delta \boldsymbol{J}(\boldsymbol{q}^d(t))\|, \\ \iota^2 &< \min_{t\in\mathbb{R}^{\geq 0}} \lambda_{\min}[\boldsymbol{J}(\boldsymbol{q}^d(t))^\top \boldsymbol{J}(\boldsymbol{q}^d(t))], \\ \rho^2 &> \max_{t\in\mathbb{R}^{\geq 0}} \|\dot{\boldsymbol{J}}(\boldsymbol{q}^d(t))^\top \dot{\boldsymbol{J}}(\boldsymbol{q}^d(t))\|. \end{aligned} \tag{5.46}$$

Since the bounds strongly depend on the particular trajectory, a motion planner such as the one in [Manubens 2013], could be employed in order to compute the desired trajectory that minimizes the bounds. Notice that even the magnitude of $\boldsymbol{w}$ in (5.27) depends on the particular motion, namely the system velocity and acceleration. In fact, $\|\boldsymbol{w}\|$ can be bounded as

$$\|\boldsymbol{w}\| \leq \|\ddot{\boldsymbol{q}}^d\| + \iota \left((\rho + k_R \delta) \|\dot{\boldsymbol{q}}^d\| + \|\boldsymbol{d}\| \right). \tag{5.47}$$

Therefore, the minimization of $\|\boldsymbol{w}\|$ can also be considered at the planning level. Equation (5.47) shows that the performance is related to the desired velocities and accelerations. Since we are more focused on the accuracy rather than on the agility of the maneuvers, we consider that - in the domain of interest - the motion of the system is performed in quasi-static conditions.

5.1.3 Optimization Strategies

Although a kinematic formulation of the controller results capable of dealing with model errors and dynamical uncertainties, complex and precise manipulation tasks often require that some dynamical quantities are precisely known. The real position of the CoM of the platform w.r.t. its geometric center, or the mass can be possible examples. In fact, model-based controllers can rely on the knowledge of these parameters to better compensate for the gravity effects. Besides, these parameters can make a difference in specific optimization procedures in some cases. Improvements in energy efficiency and flight-time autonomy can reasonably benefit from the knowledge of such quantities.

In light of these considerations, in the following section, the details of an observer that can estimate mass and position of the CoM of a suspended loaded platform w.r.t. its geometric center will be described. The aim is to enrich the capabilities of the already presented robust controller (see Sec. 5.1.2.1) in the tracking performances and the generation of optimal trajectories. The demonstration of the observability conditions to estimate the CoM (5.1.2.1) and its application in a specific optimization problem (5.1.2.1) will follow.

5.1.3.1 Inertial Parameter Estimation

In such a context, the main purpose is to estimate the mass m_P and to determine the location of the CoM $\boldsymbol{p}_C$. The identification is performed by generating 3D motions of the platform while measuring forces and moments that the robots apply

on the cables. Traditional methods employ both static and dynamic analyses. In our case, we make use of a static formulation of the problem. Therefore, initially, we develop the dynamical model of the platform by considering the CoM position placed in O_C (as described in Sec. 4.1). After that, the equations of the statics allow to write the produced linear system in a matrix form in which the vector of the unknowns contains the unidentified m_P and $\boldsymbol{p}_C$. Finally, the analyses on the linear system coefficients will provide information about the solutions, if any. Therefore, considering the following three main assumptions:

Assumption 1. *The geometric center of the platform differs from the platform's CoM, i.e. the dynamical model will be written with reference to $\mathcal{F}_C$ (see Sec. 4.1 for further details).*

In view of Ass. 1, the term "platform" will be replaced by the term "loaded platform" to emphasize that an additional weight, and therefore a change in the CoM position, has to be contemplated.

Assumption 2. *The drag and friction effects will be considered negligible, i.e. $\boldsymbol{D}_P = \mathbf{0}_{3\times3}$ and $\boldsymbol{B}_P = \mathbf{0}_{3\times3}$.*

Assumption 3. *No external disturbances affect the platform movements, i.e. $\boldsymbol{f}_e = \mathbf{0}_{3\times1}$ and ${}^P\boldsymbol{\tau}_e = \mathbf{0}_{3\times1}$.*

Let us consider the dynamical model described in Eq. (4.1) w.r.t. $\mathcal{F}_C$

$$\begin{cases} m_P\ddot{\boldsymbol{p}}_C &= \sum_{i=1}^{6} \boldsymbol{f}_i + m_P\boldsymbol{g} \\ \boldsymbol{J}_P\,{}^P\dot{\boldsymbol{\omega}}_P + \boldsymbol{S}({}^P\boldsymbol{\omega}_P)\boldsymbol{J}_P\,{}^P\boldsymbol{\omega}_P &= \sum_{i=1}^{6} \left[(\boldsymbol{b}_i - \boldsymbol{p}_C) \times \boldsymbol{f}_i\right] \end{cases}, \tag{5.48}$$

The equations of the statics, in $\mathcal{F}_C$, are the following

$$\begin{cases} \sum_{i=1}^{6} {}^C\boldsymbol{f}_i &= -m_P\boldsymbol{R}_C^\top\boldsymbol{g} \\ \sum_{i=1}^{6} \left({}^C\boldsymbol{b}_i \times {}^C\boldsymbol{f}_i\right) &= \mathbf{0} \end{cases}. \tag{5.49}$$

Considering that ${}^C\boldsymbol{b}_i = {}^P\boldsymbol{b}_i - {}^P\boldsymbol{p}_C$ and ${}^C\boldsymbol{f}_i = {}^P\boldsymbol{f}_i$, Eq. (5.49) can be written as

$$\begin{cases} \sum_{i=1}^{6} {}^P\boldsymbol{f}_i &= -m_P\boldsymbol{R}_P^\top\boldsymbol{g} \\ \sum_{i=1}^{6} \left[({}^P\boldsymbol{b}_i - {}^P\boldsymbol{p}_C) \times {}^P\boldsymbol{f}_i\right] &= \mathbf{0} \end{cases}. \tag{5.50}$$

Then, we can write Eq. (5.50) as a linear system

$$\boldsymbol{A}\boldsymbol{\theta} = \bar{\boldsymbol{b}} \tag{5.51}$$

where $\boldsymbol{\theta} = [m_P^{-1}\ {}^Pp_{C,x}\ {}^Pp_{C,y}\ {}^Pp_{C,z}]^\top \in \mathbb{R}^4$, $\bar{\boldsymbol{b}} = [-(\boldsymbol{R}_P^\top\boldsymbol{g})^\top\ -\sum_{i=1}^{6}({}^P\boldsymbol{b}_i \times {}^P\boldsymbol{f}_i)^\top]^\top \in \mathbb{R}^6$ and

$$\boldsymbol{A} = \begin{bmatrix} \sum_{i=1}^{6} {}^P\boldsymbol{f}_i & \mathbf{0} \\ \mathbf{0} & \left[\sum_{i=1}^{6} {}^P\boldsymbol{f}_i\right]_\times \end{bmatrix} \in \mathbb{R}^{6\times4}. \tag{5.52}$$

By observing (5.51), first, it is possible to note that the matrices $\boldsymbol{A}$ and $\bar{\boldsymbol{b}}$ depend on the specific configuration of the system (the intensity and the directions of the forces are determined by the robots' spatial distribution). The second dependency is on the orientation $\boldsymbol{R}_P$ of the loaded platform. Solely analyzing the dimensions of (5.52) and of $\boldsymbol{\theta}$, the system (5.51) could be solved with just one configuration. Nevertheless, $\boldsymbol{A}$ is rank-deficient cause

$$\operatorname{rank}(\boldsymbol{A}) = \operatorname{rank}\Big(\sum_{i=1}^{6} {}^P\boldsymbol{f}_i\Big) + \operatorname{rank}\Big(\Big[\sum_{i=1}^{6} {}^P\boldsymbol{f}_i\Big]_\times\Big) = 3.$$

Theorem 3.10 in [Buaphim 2018] has been used since $\boldsymbol{A}$ can be seen as an upper triangular block matrix. Therefore, the necessary condition for the estimation of the vector $\boldsymbol{\theta}$ requires finding two different static configurations, $\bar{\boldsymbol{q}}_1$ and $\bar{\boldsymbol{q}}_2$, that lead to the following two pairs $(\boldsymbol{A}_1, \bar{\boldsymbol{b}}_1)$ and $(\boldsymbol{A}_2, \bar{\boldsymbol{b}}_2)$. However, $\bar{\boldsymbol{q}}_1$ and $\bar{\boldsymbol{q}}_2$ have to be chosen in such a way to guarantee that $\widetilde{\boldsymbol{A}} = \begin{bmatrix}\boldsymbol{A}_1^\top & \boldsymbol{A}_2^\top\end{bmatrix}^\top \in \mathbb{R}^{12\times 4}$ is full rank. To this aim, the Gramian matrix, defined as $\mathbf{G} = \widetilde{\boldsymbol{A}}^\top\widetilde{\boldsymbol{A}}$, can be used to analyze the linear independence of the vectors in $\widetilde{\boldsymbol{A}}$. A set of vectors are linearly independent if and only if the Gramian matrix is full rank [Schwerdtfeger 1961]. Thus, the eigenvalues of $\mathbf{G}$ provide information about $\widetilde{\boldsymbol{A}}$. Specifically, if the smallest eigenvalue $\lambda_{\min}$ of $\mathbf{G}$ is non zero, then $\boldsymbol{\theta}$ can be estimated. Being $\boldsymbol{f}_P$ the resulting force acting on the loaded platform given the configuration $\bar{\boldsymbol{q}}$, the following proposition holds.

Proposition 1. *Given two configurations $\bar{\boldsymbol{q}}_1$ and $\bar{\boldsymbol{q}}_2$, the unknown vector $\boldsymbol{\theta} = [m_P^{-1} \;\; {}^Pp_{C,x} \;\; {}^Pp_{C,y} \;\; {}^Pp_{C,z}]^\top$ can be estimated if and only if $\sum_{i=1}^{6} {}^P\boldsymbol{f}_i(\bar{\boldsymbol{q}}_1) \neq \sum_{i=1}^{6} {}^P\boldsymbol{f}_i(\bar{\boldsymbol{q}}_2)$.*

Proof. Analyzing the Gramian matrix $\mathbf{G}$ defined as $\mathbf{G} = \widetilde{\boldsymbol{A}}^\top\widetilde{\boldsymbol{A}}$, it is possible to note that $\boldsymbol{A}_1$ and $\boldsymbol{A}_2$ have the same structure

$$\boldsymbol{A}_1 = \begin{bmatrix} \boldsymbol{\rho} & \mathbf{0} \\ \mathbf{0} & \big[\boldsymbol{\rho}\big]_\times \end{bmatrix}, \quad \boldsymbol{A}_2 = \begin{bmatrix} \boldsymbol{\sigma} & \mathbf{0} \\ \mathbf{0} & \big[\boldsymbol{\sigma}\big]_\times \end{bmatrix},$$

where $\boldsymbol{\rho} = \sum_{i=1}^{6} {}^P\boldsymbol{f}_i(\bar{\boldsymbol{q}}_1)$, $\boldsymbol{\sigma} = \sum_{i=1}^{6} {}^P\boldsymbol{f}_i(\bar{\boldsymbol{q}}_2)$. Thus, $\mathbf{G}$ presents the following structure

$$\mathbf{G} = \begin{bmatrix} \boldsymbol{\rho}^T\boldsymbol{\rho} + \boldsymbol{\sigma}^T\boldsymbol{\sigma} & \mathbf{0} \\ \mathbf{0} & \big[\boldsymbol{\rho}\big]_\times^T\big[\boldsymbol{\rho}\big]_\times + \big[\boldsymbol{\sigma}\big]_\times^T\big[\boldsymbol{\sigma}\big]_\times \end{bmatrix}.$$

The eigenvalues of $\mathbf{G}$, indicated with $\operatorname{eig}(\mathbf{G})$, are

$$\operatorname{eig}(\mathbf{G}) = \left\{\gamma,\, \gamma,\, \frac{\gamma}{2} \pm \frac{1}{2}\xi^{\frac{1}{2}}\right\},$$

where $\gamma = \boldsymbol{\rho}^T\boldsymbol{\rho} + \boldsymbol{\sigma}^T\boldsymbol{\sigma}$ and $\xi = \Big(\boldsymbol{\rho}^T\boldsymbol{\rho} + \boldsymbol{\sigma}^T\boldsymbol{\sigma}\Big)^2 + 4(\boldsymbol{\rho}^T\boldsymbol{\sigma})^2 - 4\boldsymbol{\rho}^T\boldsymbol{\rho}\,\boldsymbol{\sigma}^T\boldsymbol{\sigma}$. Given the

Gramian matrix defined as $\mathbf{G} = \widetilde{\mathbf{A}}^T\widetilde{\mathbf{A}}$, where $\widetilde{\mathbf{A}} = \begin{bmatrix}\mathbf{A}_1^T & \mathbf{A}_2^T\end{bmatrix}^T$ and

$$\mathbf{A}_1 = \begin{bmatrix} \boldsymbol{\rho} & \mathbf{0} \\ \mathbf{0} & \begin{bmatrix}\boldsymbol{\rho}\end{bmatrix}_\times \end{bmatrix}, \quad \mathbf{A}_2 = \begin{bmatrix} \boldsymbol{\sigma} & \mathbf{0} \\ \mathbf{0} & \begin{bmatrix}\boldsymbol{\sigma}\end{bmatrix}_\times \end{bmatrix},$$

where $\boldsymbol{\rho} = \sum_{i=1}^{6} {}^P\mathbf{f}_i(\bar{\boldsymbol{q}}_1)$, $\boldsymbol{\sigma} = \sum_{i=1}^{6} {}^P\mathbf{f}_i(\bar{\boldsymbol{q}}_2)$ and $\mathbf{f}_i(\boldsymbol{q})$ indicates the resulting force acting on the platform given the configuration $\boldsymbol{q}$. Indicated with $\rho_{1,2,3}$ and $\sigma_{1,2,3}$ the components of, respectively, $\boldsymbol{\rho}$ and $\boldsymbol{\sigma}$, let us compute the eigenvalues of $\mathbf{G}$ by solving $\mathbf{G} - \lambda\mathbf{I} = 0$ for λ leading to the following values

$$\begin{aligned}
\lambda_{1/2} = \;& \rho_1^2 + \rho_2^2 + \rho_3^2 + \sigma_1^2 + \sigma_2^2 + \sigma_3^2 = \boldsymbol{\rho}^T\boldsymbol{\rho} + \boldsymbol{\sigma}^T\boldsymbol{\sigma} \\
\lambda_3 = \;& \tfrac{\rho_1^2+\rho_2^2+\rho_3^2+\sigma_1^2+\sigma_2^2+\sigma_3^2}{2} + \\
& + \tfrac{1}{2}\Big(\rho_1^4 + 2\rho_1^2\rho_2^2 + 2\rho_1^2\rho_3^2 + 2\rho_1^2\sigma_1^2 - 2\rho_1^2\sigma_2^2 + \\
& - 2\rho_1^2\sigma_3^2 + 8\rho_1\rho_2\sigma_1\sigma_2 + 8\rho_1\rho_3\sigma_1\sigma_3 + \rho_2^4 + \\
& + 2\rho_2^2\rho_3^2 - 2\rho_2^2\sigma_1^2 + 2\rho_2^2\sigma_2^2 - 2\rho_2^2\sigma_3^2 + \rho_3^4 + \\
& + 8\rho_2\rho_3\sigma_2\sigma_3 - 2\rho_3^2\sigma_1^2 - 2\rho_3^2\sigma_2^2 + 2\rho_3^2\sigma_3^2 + \\
& + \sigma_1^4 + 2\sigma_1^2\sigma_2^2 + 2\sigma_1^2\sigma_3^2 + \sigma_2^4 + 2\sigma_2^2\sigma_3^2 + \sigma_3^4\Big)^{\frac{1}{2}} = \\
& = \tfrac{1}{2}\Big(\boldsymbol{\rho}^T\boldsymbol{\rho} + \boldsymbol{\sigma}^T\boldsymbol{\sigma}\Big) + \tfrac{1}{2}\xi^{\frac{1}{2}} \\
\lambda_4 = \;& \tfrac{\rho_1^2+\rho_2^2+\rho_3^2+\sigma_1^2+\sigma_2^2+\sigma_3^2}{2} - \\
& + \tfrac{1}{2}\Big(\rho_1^4 + 2\rho_1^2\rho_2^2 + 2\rho_1^2\rho_3^2 + 2\rho_1^2\sigma_1^2 - 2\rho_1^2\sigma_2^2 + \\
& - 2\rho_1^2\sigma_3^2 + 8\rho_1\rho_2\sigma_1\sigma_2 + 8\rho_1\rho_3\sigma_1\sigma_3 + \rho_2^4 + \\
& + 2\rho_2^2\rho_3^2 - 2\rho_2^2\sigma_1^2 + 2\rho_2^2\sigma_2^2 - 2\rho_2^2\sigma_3^2 + \rho_3^4 + \\
& + 8\rho_2\rho_3\sigma_2\sigma_3 - 2\rho_3^2\sigma_1^2 - 2\rho_3^2\sigma_2^2 + 2\rho_3^2\sigma_3^2 + \\
& + \sigma_1^4 + 2\sigma_1^2\sigma_2^2 + 2\sigma_1^2\sigma_3^2 + \sigma_2^4 + 2\sigma_2^2\sigma_3^2 + \sigma_3^4\Big)^{\frac{1}{2}} = \\
& = \tfrac{1}{2}\Big(\boldsymbol{\rho}^T\boldsymbol{\rho} + \boldsymbol{\sigma}^T\boldsymbol{\sigma}\Big) - \tfrac{1}{2}\xi^{\frac{1}{2}}
\end{aligned}.$$

Moreover, let us simplify ξ by writing the negative products as $-2\rho_i^2\sigma_j^2 = 2\rho_i^2\sigma_j^2 -$

$4\rho_i^2\sigma_j^2$ and adding the terms $-4\rho_k^2\sigma_k^2 + 4\rho_k^2\sigma_k^2$, for $k = 1, 2, 3$, leading to

$$\begin{aligned}
\xi = \quad & \Big(\rho_1^4 + \rho_2^4 + \rho_3^4 + \sigma_1^4 + \sigma_2^4 + \sigma_3^4 + 2\rho_1^2\rho_2^2 + 2\rho_1^2\rho_3^2 + \\
& + 2\rho_1^2\sigma_1^2 + 2\rho_1^2\sigma_2^2 + 2\rho_1^2\sigma_3^2 + 2\rho_2^2\rho_3^2 + 2\rho_2^2\sigma_1^2 + \\
& + 2\rho_2^2\sigma_2^2 + 2\rho_2^2\sigma_3^2 + 2\rho_3^2\sigma_1^2 + 2\rho_3^2\sigma_2^2 + 2\rho_3^2\sigma_3^2 + \\
& + 2\sigma_1^2\sigma_2^2 + 2\sigma_1^2\sigma_3^2 + 2\sigma_2^2\sigma_3^2\Big) + \\
& + \Big(4\rho_1^2\sigma_1^2 + 4\rho_2^2\sigma_2^2 + 4\rho_2^2\sigma_2^2 + \\
& + 8\rho_1\rho_2\sigma_1\sigma_2 + 8\rho_2\rho_3\sigma_2\sigma_3 + 8\rho_1\rho_3\sigma_1\sigma_3\Big) + \\
& + \Big(- 4\rho_1^2\sigma_2^2 - 4\rho_1^2\sigma_3^2 - 4\rho_2^2\sigma_1^2 - 4\rho_2^2\sigma_3^2 + \\
& - 4\rho_3^2\sigma_1^2 - 4\rho_3^2\sigma_2^2 - 4\rho_1^2\sigma_1^2 - 4\rho_2^2\sigma_2^2 - 4\rho_2^2\sigma_2^2\Big) \\
= \quad & \Big(\boldsymbol{\rho}^T\boldsymbol{\rho} + \boldsymbol{\sigma}^T\boldsymbol{\sigma}\Big)^2 + 4(\boldsymbol{\rho}^T\boldsymbol{\sigma})^2 - 4\boldsymbol{\rho}^T\boldsymbol{\rho}\,\boldsymbol{\sigma}^T\boldsymbol{\sigma}.
\end{aligned}$$

Hence, $\lambda_{\min} = 0$ iff $\xi = \gamma^2$

$$\begin{aligned}
\xi &= \gamma^2 && \Rightarrow \\
\gamma^2 + 4(\boldsymbol{\rho}^T\boldsymbol{\sigma})^2 - 4\boldsymbol{\rho}^T\boldsymbol{\rho}\,\boldsymbol{\sigma}^T\boldsymbol{\sigma} &= \gamma^2 && \Rightarrow \\
(\boldsymbol{\rho}^T\boldsymbol{\sigma})^2 &= \boldsymbol{\rho}^T\boldsymbol{\rho}\,\boldsymbol{\sigma}^T\boldsymbol{\sigma} && \Rightarrow \\
\boldsymbol{\rho}^T\Big(\boldsymbol{\sigma}\,\boldsymbol{\rho}^T\Big)\boldsymbol{\sigma} &= \boldsymbol{\rho}^T\Big(\boldsymbol{\rho}\,\boldsymbol{\sigma}^T\Big)\boldsymbol{\sigma} && \Rightarrow \\
\boldsymbol{\sigma}\,\boldsymbol{\rho}^T &= \boldsymbol{\rho}\,\boldsymbol{\sigma}^T
\end{aligned},$$

implying that $\mathbf{G}$ is singular if and only if $\boldsymbol{\rho} = \boldsymbol{\sigma}$. Then, the proposition is proved. □

To provide a physical interpretation to Proposition 1, the condition $\sum_{i=1}^{6} {}^P\boldsymbol{f}_i(\bar{\boldsymbol{q}}_1) \neq \sum_{i=1}^{6} {}^P\boldsymbol{f}_i(\bar{\boldsymbol{q}}_2)$ can be reformulated as $\boldsymbol{R}_{P1}^\top\mathbf{g} \neq \boldsymbol{R}_{P2}^\top\mathbf{g}$. $\boldsymbol{R}_{P1}$ and $\boldsymbol{R}_{P2}$ indicate the rotation matrices associated to the configuration $\bar{\boldsymbol{q}}_1$, $\bar{\boldsymbol{q}}_2$ respectively. Thus, $\bar{\boldsymbol{R}}_{P1}$ and $\bar{\boldsymbol{R}}_{P2}$ cannot represent a rotation around $\boldsymbol{z}_W$ at the same time. This clarifies that platform rotations around a vector parallel to the $\mathbf{g}$ vector do not contribute to the estimation process. Indeed, as a result of such rotations, the load balancing does not change.

Guided by this theoretical result, an estimation algorithm composed by two phases has been proposed. An initialization phase is followed by an online estimation phase reported in Algorithm 1 and Algorithm 2. The preliminary initialization phase has to be seen as a calibration step where the loaded platform is induced to perform the opportune variations of the orientation. The aim is to gather informative data for the estimation procedure and an initial estimation of ${}^P\boldsymbol{p}_C$. Afterwards, the online phase aims at improving the estimation by filtering out possible measurement noise.

Algorithm 1: Initialization

Start from a static configuration $\mathbf{q}_0$;
Stabilize the platform with orientation $\boldsymbol{R}_{\boldsymbol{x}_P}(\varsigma)$;
Collect ${}^{L}\widetilde{\mathbf{f}}(\bar{\boldsymbol{q}}_1)$ for $i = 1, \ldots, 6$ and compute $\mathbf{A}_1$;
Stabilize the platform with orientation $\boldsymbol{R}_{\boldsymbol{y}_P}(\varsigma)$;
Collect ${}^{L}\widetilde{\mathbf{f}}_i(\bar{\boldsymbol{q}}_2)$ for $i = 1, \ldots, 6$ and compute $\mathbf{A}_2$;
Solve $\widetilde{\mathbf{A}}\mathbf{x} = \widetilde{\mathbf{b}}$ for $\mathbf{x}$;
return $\widehat{\boldsymbol{p}}_C(0)$;

Algorithm 2: Online Estimation of m and ${}^{L}\mathbf{p}_C$

$\widehat{\boldsymbol{p}}_C = \widehat{\boldsymbol{p}}_C(0)$;
while *the final point is not reached* **do**
  if *there are new measurements at time t* **then**
    Collect ${}^{L}\widetilde{\mathbf{f}}_i(\bar{\boldsymbol{q}}_t)$ for $i = 1, \ldots, 6$;
    $\widehat{\boldsymbol{p}}_C = \mathit{recursiveLeastSquare}\Big(\widehat{\boldsymbol{p}}_C, {}^{L}\widetilde{\mathbf{f}}_i(\bar{\boldsymbol{q}}_t)\Big)$;
    return $\widehat{\boldsymbol{p}}_C$;

Going into the details, the initialization phase assumes to start from a generic configuration $\mathbf{q}^\star = \begin{bmatrix} \mathbf{p}_{P\star}^T & 0 & 0 & 0 & \alpha_\star & \alpha_\star & \alpha_\star \end{bmatrix}^\top$. Then, two different orientations $\boldsymbol{R}_{\boldsymbol{x}_P}(\varsigma)$ and $\boldsymbol{R}_{\boldsymbol{y}_P}(\varsigma)$ of the platform are imposed through the controller where $\boldsymbol{R}_{\boldsymbol{x}_P}(\varsigma)$ is the rotation of angle $\varsigma > 0$ around the axis $\boldsymbol{x}_P$. $\boldsymbol{R}_{\boldsymbol{y}_P}(\varsigma)$ is similarly defined. Then, the measurements acquired in these two different configurations are used to set the initial value $\widehat{\boldsymbol{p}}_C(0)$ of the estimated $\widehat{\boldsymbol{p}}_C$. Subsequently, the online phase can start from $\widehat{\boldsymbol{p}}_C(0)$ to update the estimated $\widehat{\boldsymbol{p}}_C$. A standard *Recursive Least Square* procedure [Slotine 1991] has been employed to update the estimated $\widehat{\boldsymbol{p}}_C$ whenever a new measurement is available.

5.1.3.2 Energy Effiency Optimization

As already mentioned, the inertial parameter estimation phase aims at producing useful information that can be used by the redundant manipulator afterwards. In actual fact, auxiliary null space tasks can be simultaneously performed together with the primary assignments. Thus, the redundant DoFs can be used. Performances or safety criteria, which have to be either maximized or minimized, are often applied to define the auxiliary tasks.

Profitable results in solving these optimization problems can emerge by employing the additional details coming from the estimation process. Among them, guaranteeing the precise execution of the tasks; ensuring equilibrium in terms of the produced energy effort; improving the manipulability of the end-effector. Thus, for such goals, online optimization strategies become crucial.

In this direction and for the specific case of the Fly-Crane, an online optimizer has been designed. Given the desired pose trajectory of the loaded platform, the methodology computes the remaining configuration variables (the angles of the cables $\boldsymbol{\alpha}^d$) such that the weight of the loaded platform is equally balanced among the robots, thus assuring a similar provided effort of each robot. The values of $\boldsymbol{\alpha}^d$ are computed by solving the following minimization problem

$$\begin{aligned} \boldsymbol{\alpha}_{opt} = \quad & \arg\min_{\boldsymbol{\alpha}} \mu({}^P\boldsymbol{p}_C, \boldsymbol{q}), \\ s.t.\ 0 \leq \alpha_{ij} < \tfrac{\pi}{2}, \quad & \text{for } (i,j) \in \{(1,2),\,(4,3),\,(5,6)\}\,, \end{aligned} \tag{5.53}$$

where $\mu({}^P\boldsymbol{p}_C, \boldsymbol{q}) = \Big|\|\boldsymbol{f}_{R12}\| - \|\boldsymbol{f}_{R34}\|\Big| + \Big|\|\boldsymbol{f}_{R34}\| - \|\boldsymbol{f}_{R56}\|\Big| + \Big|\|\boldsymbol{f}_{R56}\| - \|\boldsymbol{f}_{R12}\|\Big|$.

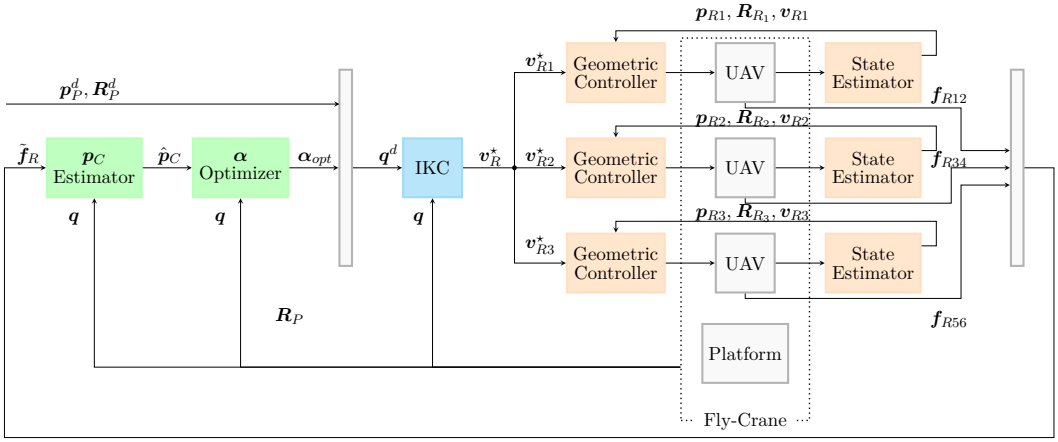

Figure 5.2: The control architecture of the Fly-Crane enhanced with the mass and CoM estimator and the $\boldsymbol{\alpha}$ optimizer block.

Analyzing the shape of the cost function depicted in (5.53), the main goal is to reach its minimum value. For this purpose, the norm of the force generated by each robot has to be the same. Thus, each aerial vehicle equally contributes to the transportation/manipulation effort. The reader is referred to Fig. 5.2 to appreciate the extended control scheme including the estimation of the inertial parameters. Although the available methods are numerous, we opted for a gradient descent iterative algorithm to solve the optimization problem. More precisely, the value of $\boldsymbol{\alpha}$ is modified of a quantity proportional to the approximate anti-gradient of $\mu({}^P\boldsymbol{p}_C, \boldsymbol{q})$.

Chapter 6

Validation of the Proposed Control Methodologies

This chapter is devoted to the validation of the control strategies in contact-free scenarios presented in the previous chapter (Chap. 5) which leverage on the two models described in Chap. 4. First, numerical simulations will be presented for the generic model (Sec. 4.1). The aim is to show the convergence of the platform configuration to certain equilibria w.r.t. the variation of the internal forces and the number of leader robots. Both nominal conditions and not ideal circumstances will be evaluated.

After that, special attention will be devoted to the specific modeled prototype (see Sec. 4.2), the Fly-Crane, which has been manufactured and then tested in real indoor scenarios. Hence, in the following, first, some details of the mechanical assembling will be presented. Afterwards, we will show the performances of the system together with the robustness of the control architecture through a campaign of experiments across several conditions of uncertainties and external disturbances. The validation of the inertial parameter estimation and the reliability of the optimization strategy will conclude the chapter.

6.1 Generic Model

In this section, we show the numerical validation of the convergence of the platform configuration to certain equilibria. In particular, first, the main focus of interest is the variation of the internal force. Then, the effects of the change in the number of leader robots will be examined. In Sec. 6.1.1, the nominal conditions have been distinguished from the not ideal circumstances which are the presence of external disturbances on one hand (Sec. 6.1.1.3) and the presence of noisy measurements on the other hand (Sec. 6.1.1.4).

Going into the details, the simulated system has the following characteristics. The platform is a rigid body with mass $m_P = 5$ [Kg] and inertia matrix $\boldsymbol{J}_P = \boldsymbol{I}_3$ [Kg m^2]. The contact stiffness is set to 900 [N m]. The leader robots gains are: $\boldsymbol{M} = 0.5\boldsymbol{I}_3$ [Kg], $\boldsymbol{B} = 100\boldsymbol{I}_3$ [Ns/m] and $\boldsymbol{K}_1 = 1000\boldsymbol{I}_3$ [N/m], and the follower robots ones are: $\boldsymbol{M} = 0.01\boldsymbol{I}_3$ [Kg], $\boldsymbol{B} = 0.15\boldsymbol{I}_3$ [Ns/m] and $\boldsymbol{K}_i = 0\boldsymbol{I}_3$ [N/m]. For the simulations with a single leader, the number of robots constituting the swarm is variable, randomly changing between 2 and 50. Conversely, for the simulations with a number of leaders different from one, swarms composed of 12 robots have been considered. The radius of the circular platform around which the robots are

attached is $b = 2.5$ [m]; the desired attitude of the object is described by the desired roll, pitch and yaw angles $\theta^d = \phi^d = \psi^d = 0$ [rad]. We will refer to this attitude as $\boldsymbol{\eta}_{P0} = [0\ 0\ 0]$ [rad]. Let us also define $\boldsymbol{\eta}_{P\pi} = [0\ 0\ \pm\pi]$ [rad]. By means of this specific choice, the desired configuration consists of maintaining the payload parallel to the ground. Although such configuration may seem the most basic one, it is particularly relevant in practical applications such as assembly or decommissioning scenarios. Note that, with a rotation of $\mathcal{F}_W$ around $\boldsymbol{z}_W$ by ψ^d, the results can be extended for any value of ψ^d.

6.1.1 Convergence Analysis

In this section, the aim is to show the convergence of the load configuration to a certain static equilibrium, w.r.t. *i)* the value of f_{int}; *ii)* the number of leader robots. If only one robot leads the swarm, the latter is usually considered the leader. The following initial conditions have been set to, first, investigate the capability of the system to bring the load to a specific configuration of equilibrium and, secondly, its stability: random values of roll ϕ, pitch θ, and yaw ψ (only roll and pitch in case of floating systems) between $-\pi/4$ [rad] and $\pi/4$ [rad].

In the performed simulations, the number of leader robots will change between 0 and 3. For each trial with a fixed number of leader robots, f_{int} will have the following values:

1) $f_{int} = 0$ [N],

2) $f_{int} = 0.8$ [N](> 0),

3) $f_{int} = -0.8$ [N](< 0).

Notice that, in cases 2) and 3), the value of f_{int} represents $\pm 0.016\%$ of the total weight-force of the load.

Moreover, 10 trajectories, starting from different initial conditions, have been performed for each one of the cases. They were obtained by combining the number of leader robots with the value of f_{int}.

6.1.1.1 Summary of the Numerical Results

In light of the large set of numerical analyses performed, we propose a preliminary summary of the more relevant results. However, although with this overview we attempt to lighten the numerous results that will be presented in the following, we refer the reader to the pursuing discussion for a wider level of detail.

The obtained results in regulating position and orientation of the manipulated payload reveal that when no leader robots rule the formation, solely stretching or compressing the carried object allows the robots to control the orientation of the load. At least one leader robot is needed to regulate the position of the payload. Moreover, the presence of two properly distributed leader robots is sufficient to steer the load to a desired position regardless of the inter exchanged forces. Conversely,

the payload attitude can be controlled by only pulling the load. Finally, three leader robots in a floating system are able to regulate position and orientation regardless of the interaction forces. Just two leaders are sufficient in a ground system. Moreover, the result of adding a second (third) leader robot for a ground (floating) system has the effect of speeding up the convergence rate.

6.1.1.2 Numerical Results

Zero leader robots Being all the robots simple followers, none of them has a desired position to follow. As a result, the convergence of the position of the load depends on the system initial condition and the presence of internal forces. However, it is not controllable at will by the robots. Regarding the attitude of the load, we can observe that:

- if $f_{int} = 0$, the final attitude of the object is not uniquely determined, but it remains equal to its initial value;
- if $f_{int} > 0$, the object attitude always converges to the desired equilibrium value $\boldsymbol{\eta}_{P0}$. Therefore, $\boldsymbol{\eta}_{P0}$ is an asymptotically stable attitude;
- for $f_{int} < 0$, the object attitude always converges to $\boldsymbol{\eta}_{P_\pi} = [0\ 0\ \pm\pi]$ [rad]. Then, for $f_{int} < 0$, the desired equilibrium attitude $\boldsymbol{\eta}_{P0}$ is unstable while $\boldsymbol{\eta}_{P_\pi}$ is asymptotically stable.

Note that for a floating system under the action of gravity, a leader-less configuration would result not applicable. Indeed, even the slightest error in estimating the platform mass would result in the falling of the entire setup. The simulation results for a floating system with $f_{int} > 0$ are shown in Fig. 6.1.

The plots highlight the internal forces relevant role in the regulation of the object attitude. In fact, any leader robot is needed for this purpose when the internal force is non-zero. Fig. 6.1 shows, as well, the results of the simulations for a floating system with $f_{int} = 0$ and $f_{int} < 0$ (second and third row respectively of Fig. 6.1).

Conversely, the results for a ground system with $f_{int} > 0$, $f_{int} < 0$ and $f_{int} = 0$ are presented in Fig. 6.2 where one can see that the attitude (exclusively the ψ angle is shown) of the object is unstable when $f_{int} < 0$, it is identically equal to its initial value when $f_{int} = 0$ and it converges to the desired value when $f_{int} > 0$. The figures of the object position are not reported here since the pose only depends on the initial conditions: a swarm with no leader robots has no control over the object position.

One leader robot The obtained results confirm the validity of the presented theoretical outcomes described in Sec. 5.1.1.2 for both floating and ground swarms, namely

- for $f_{int} = 0$, every $\boldsymbol{x} \in \mathcal{X}(f_{int}, \boldsymbol{q}_P^d)$ is stable. However, the pose of the load cannot be controlled to a desired configuration;

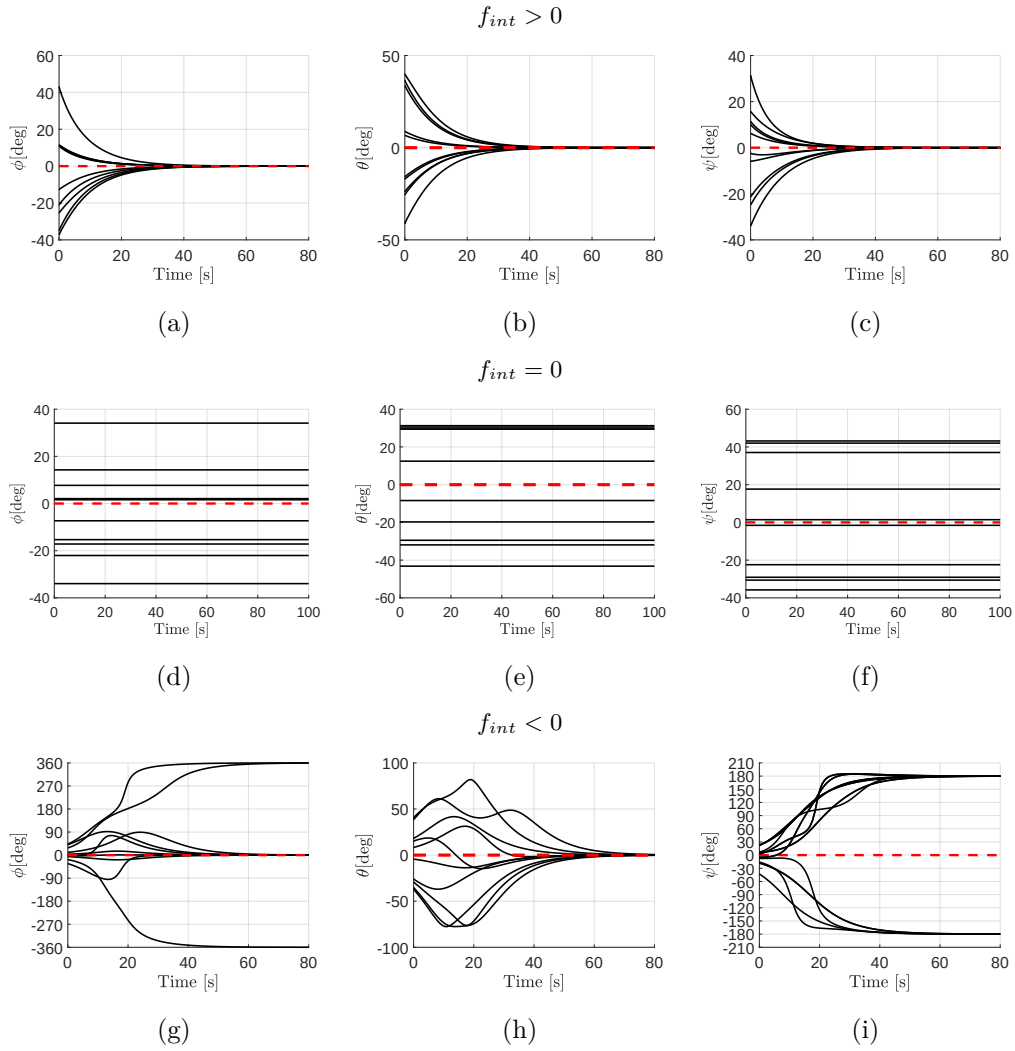

Figure 6.1: Payload *attitude* evolution with zero leader robots in a group of *floating agents*. $f_{int} > 0$ in the first row, $f_{int} = 0$ in the second row, $f_{int} < 0$ in the third row.

- for $f_{int} > 0$, $\boldsymbol{x}'(f_{int}, \boldsymbol{q}_P^d)$ is asymptotically stable;
- for $f_{int} < 0$, $\boldsymbol{x}''(f_{int}, \boldsymbol{q}_P^d)$ is asymptotically stable.

In light of the results which have been presented so far, the following observations can be made:

Observation 1. *Let us consider the presented communication-less approach employed for the manipulation of an object performed by a swarm of generic robots. From the theoretical previous analysis and observations from numerical simulations performed so far; we can conclude that:*

1. *The load orientation can be controlled to $\boldsymbol{\eta}_{P0}$ even if there are no leader robots, as long as $f_{int} > 0$, namely if the robots stretch the load producing*

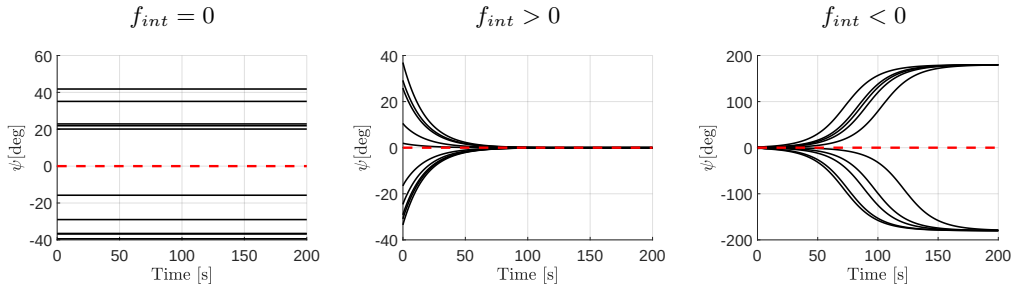

Figure 6.2: Payload *attitude* evolution (the yaw angle is the relevant quantity) with zero leader robots in a group of *ground agents*. From the left to the right, $f_{int} = 0$, $f_{int} > 0$, and $f_{int} < 0$.

an internal tension. However, the load orientation can be steered to a precise unique value even when $f_{int} < 0$. *Nevertheless, this orientation is rotated by* 180 [deg]. *Thus, just the internal forces applied by the swarm to the object are sufficient to stabilize its attitude to a precise value; any leader is required for this specific purpose.*

2. *The presence of at least one leader robot is necessary to bring the object position to a specific value.*

Two leader robots In this scenario, two leader robots are anchored to the load along the x-axis of the body frame $\boldsymbol{x}_P$, one opposite to the other. Figure 6.5a shows a schematic representation of such a configuration. When the two leaders are attached to the load either at the same point or almost close, the system behaves as if only one leader robot would be present.

A more effective behaviour can be obtained when they are equally spread around the object. Running the simulations we observed that:

- for $f_{int} = 0$, the desired position of the platform is attractive. This means that the platform position always converges to $\boldsymbol{p}_P^d$ regardless of the platform initial configuration. In attitude, pitch θ and yaw ψ always converge to zero. Hence, the desired attitude around $\boldsymbol{y}_P$ and $\boldsymbol{z}_P$ is stable and attractive. The same cannot be said for the attitude in $\boldsymbol{x}_P$, expressed by ϕ, which results stable but not attractive. Its final value is not unique and depends on the initial configuration, as shown in the second row of Fig. 6.3;

- for $f_{int} > 0$, $\boldsymbol{x}'(f_{int}, \boldsymbol{q}_P^d)$ is asymptotically stable,

- for $f_{int} < 0$, $\boldsymbol{p}_P^d$ converges to the desired value. In attitude, pitch θ and yaw ψ angles always converge to zero. Conversely, the roll angle ϕ always converges to ± 180 [deg], meaning that the system flips around $\boldsymbol{x}_P$. Thus, $\phi = 0$ [deg] is an unstable value while $\phi = \pm 180$ [deg] is stable and attractive.

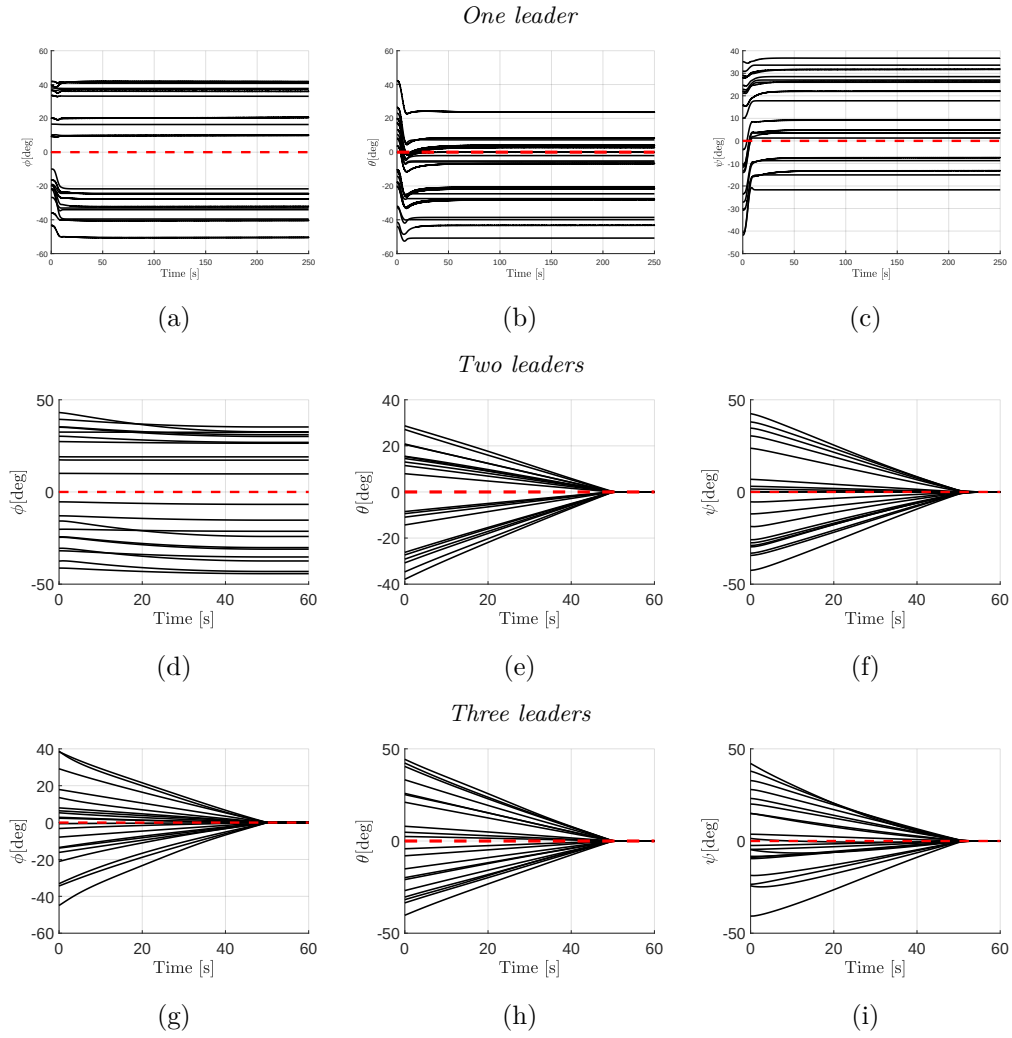

Figure 6.3: Evolution of the attitude of the object in a group of floating robots with $f_{int} = 0$. One leader in the first row,two leaders in the second row, and three leaders in the third row.

Analogous results for a ground swarm system can be found in Fig. 6.4 where the position error in $\boldsymbol{x}_W$ and $\boldsymbol{y}_W$ and the yaw ψ always converge to zero regardless of the interaction forces.

Observation 2. *Let us consider the presented communication-less approach employed for the manipulation of an object performed by a swarm of generic robots. From the theoretical previous analysis and observations from numerical simulations performed so far; we can conclude that:*

1. *Two properly distributed leader robots are enough, even without any internal force, for controlling the position of the object to a unique desired value.*

2. *The attitude in the axes perpendicular to the line* ${}^P\boldsymbol{b}_i - {}^P\boldsymbol{b}_j$*, where* i, j *are*

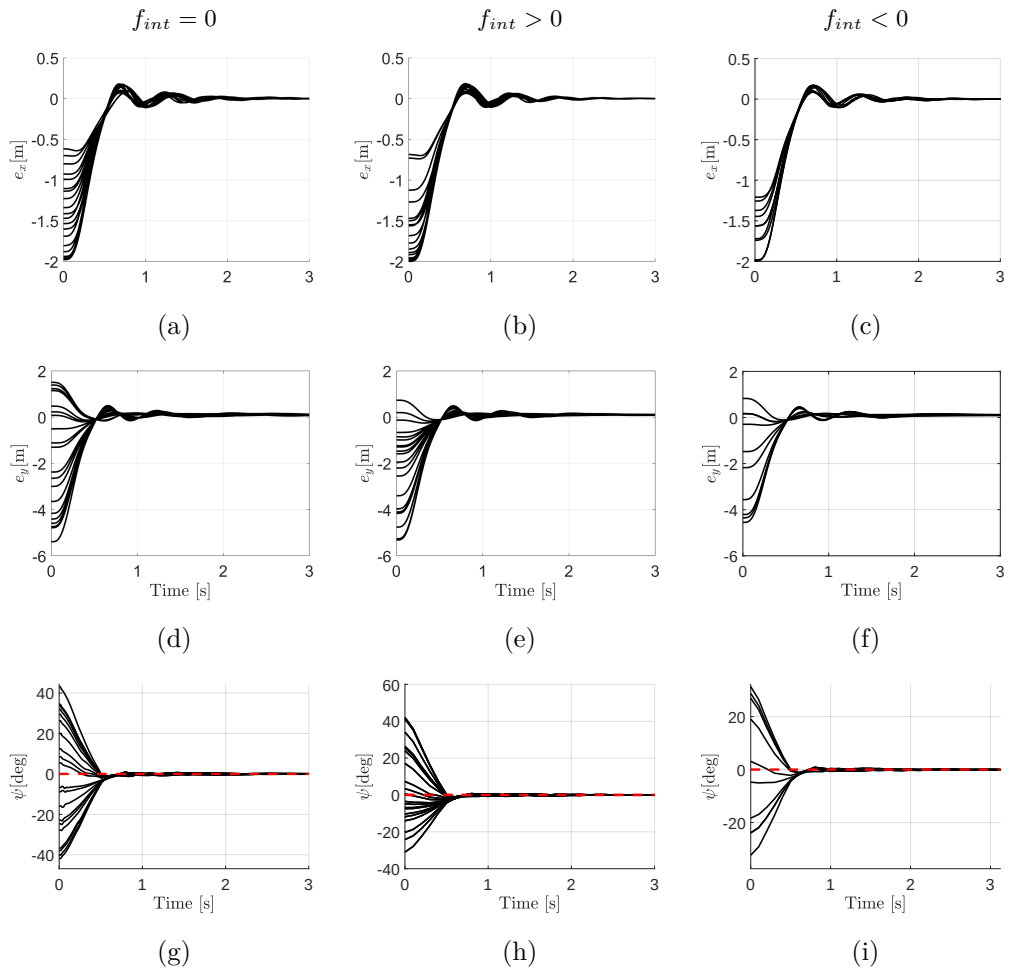

Figure 6.4: Position error (first and second rows) and attitude (third row) of the object with two leaders in a group of *ground* agents. From the left to the right, $f_{int} = 0$, $f_{int} > 0$, $f_{int} < 0$

leaders, is always stable, regardless of the f_{int} value and, it converges to the desired value. On the other hand, in the axes ${}^P\boldsymbol{b}_i - {}^P\boldsymbol{b}_j$ the convergence in attitude to the desired value is obtained only if $f_{int} > 0$.

3. *For a ground swarm system, two leader robots are sufficient for controlling the payload to a desired value both in position and in attitude (solely represented by the yaw angle), even without any internal force.*

Three leader robots As already discussed for the case when the number of leader robots is two, the most interesting scenario to examine is the one in which the leaders are evenly spread around the object. More specifically, we shall consider in these sets of simulations the distribution of leader robots schematically represented in Fig. 6.5b. Running the usual set of simulations we observed that $\boldsymbol{x}'(f_{int}, \boldsymbol{q}_P^d)$

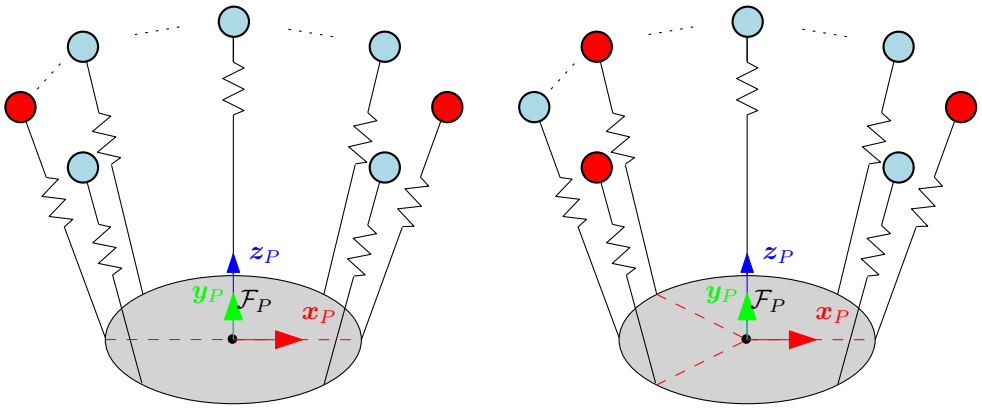

Figure 6.5: Equally spread multiple leader robots. Each leader robot is reported as a red circle, and each follower robot as a light blue one. In (a) two leader robots rule the formation while in (b) three leader robots are evenly distributed around the payload.

is asymptotically stable independently from the value of f_{int}. Note that for the ground case, same results are obtained by employing only two leader robots in the swarm.

Observation 3. *Let us consider the presented communication-less approach employed for the manipulation of an object performed by a swarm of generic robots. From the theoretical previous analysis and observations from numerical simulations performed so far; we can conclude that:*

1. *With three leader robots evenly distributed in the swarm, the attitude and position of the object suspended by a flying swarm converge to the desired values, regardless of the presence or the sign of the internal force.*

2. *For a ground swarm, having more than two evenly distributed leaders does not change the convergence behavior of the load attitude and position.*

3. *In both the floating and the ground cases the presence of non-zero internal forces speeds up the convergence rate.*

In Fig. 6.3 one can appreciate the evolution of the attitude of a floating system with one, two and three spread leader robots when $f_{int} = 0$. Figure 6.3 highlights the role of the presence of multiple leader robots for the attitude convergence.

To summarize the conclusions which have been drawn until now from the numerical results presented in this section, Table 6.1 has been created.

6.1.1.3 Robustness Analysis

This section is devoted to show the capabilities of the swarm to follow the desired platform orientation and the desired platform position when destabilizing effects

Leaders	f_{int}	Position	Orientation
0	$= 0$	The final value depends on the initial conditions.	The final value depends on the initial conditions.
	> 0		Converges to $\boldsymbol{\eta}_{P0}$.
	< 0		Converges to $\boldsymbol{\eta}_{P\pi}$.
1	$= 0$	The final value depends on the initial conditions.	The final value depends on the initial conditions.
	> 0	Converges to $\boldsymbol{p}_P^d$.	Converges to $\boldsymbol{\eta}_{P0}$.
	< 0	Converges to a different value than $\boldsymbol{p}_P^d$.	Converges to $\boldsymbol{\eta}_{P\pi}$.
2	$= 0$	Converges to $\boldsymbol{p}_P^d$.	Roll depends on the initial conditions. Yaw and pitch converge to $\boldsymbol{\eta}_{P0}$.
	> 0		Converges to $\boldsymbol{\eta}_{P0}$.
	< 0		Roll converges to $\pm 180°$.
3	$= 0$	Converges to $\boldsymbol{p}_P^d$.	Converges to $\boldsymbol{\eta}_{P0}$.
	> 0		
	< 0		

Table 6.1: Summary of the load convergence analysis.

are produced by external disturbances. More specifically, the focus is on understanding which conditions, in terms of internal forces and number of leaders, allow the system to manipulate the object without being strongly affected by the effects of the external disturbances. Constant external forces, acting on the object, can be compensated by adding integral actions in the control law w.r.t. the load position error. In such a case, the control law (5.2) has to be slightly modified. In fact, the leader robots need to measure the object position $\boldsymbol{p}_P$ besides knowing the desired one $\boldsymbol{p}_P^d$.

Moreover, in terms of orientation, a control action solely performed by one robot is insufficient to maintain the object orientation under external torques. As a matter of fact, each robot can only apply contact forces and not contact torques. Therefore, at least, a pair of contact forces are needed to react to an external torque and to track a desired attitude. A cooperative action is, then, required for this purpose and the challenge becomes regulating the object attitude subject to external torques. Thus, the subject of the following analysis will be the attitude regulation problem. The standard control law in (5.2) is applied and each component of the swarm has to know the object state.

The system is always initialized at the desired equilibrium equal to $\boldsymbol{p}_P^d = [0\ 0\ 0]$ [m], $\boldsymbol{\eta}_{P0} = [0\ 0\ 0]$ [deg]. In every simulation scenario, the system has been examined when subjected to three constant external torques expressed in body frame:

1. $\boldsymbol{\tau_{e,x}} = m_{ext}\boldsymbol{e}_1$,
2. $\boldsymbol{\tau_{e,y}} = m_{ext}\boldsymbol{e}_2$,
3. $\boldsymbol{\tau_{e,z}} = m_{ext}\boldsymbol{e}_3$.

It is worth noticing that the error cannot converge to zero in the presence of constant disturbances since there is no integral action. However, the target is to obtain a bounded and small steady-state error. In the following, the robustness has been defined in terms of the deviation of the load attitude from the desired value. The object attitude (or one of its components) will be considered *robust* if the error dynamics remains bounded in time when subject to an external disturbance. Conversely, it will be considered *not robust* if it diverges in time.

Zero leader robots The numerical simulations involving zero leader robots allow to formulate the following observations:

- for $f_{int} = 0$, the attitude of the object is *not robust*;
- for $f_{int} > 0$, the attitude of the object is *robust*;
- for $f_{int} < 0$, the attitude errors are all bounded. However, being $\boldsymbol{\eta}_{P0}$ not stable in the scenario with zero leader robots, as shown in the previous section, the system flips by 180 [deg] around the axis of the corresponding external torque.

It is not surprising that for $f_{int} = 0$, none of the components of the object attitude is robust against external torques. In fact, with no robot attracted to a precise position, the only action that may induce resistance to external disturbances is the radial stretch or compression generated by the internal forces.

In Fig. 6.6, we present the results for a floating swarm with no leader robots and different positive values of f_{int} keeping constant the values of $\tau_{e,x}, \tau_{e,y}, \tau_{e,z}$. Moreover, we evaluate the effect of the intensity of the internal force on the steady-state error. As a result, once the intensity of the reference internal force is increased, the errors' magnitude decreases. This outcome is consistent with the already obtained results (see Sec. 6.1.1.2) which suggest that the attitude errors should stay bounded in case of $f_{int} > 0$.

However, applying $\boldsymbol{\tau_{e,z}}$, the error in yaw results reduced if compared to the errors in pitch and roll, even though m_{ext} has been equally applied on each of the external torque components (see Fig. 6.6c). This can be related to the fact that all the robots apply the same torque along $\boldsymbol{z}_P$ in compensating the external torque $\boldsymbol{\tau_{ext}}$. On the other hand, along $\boldsymbol{x}_P$, the robots whose attaching points are closer to be aligned with $\boldsymbol{x}_P$ apply a smaller contribution in compensating the external torque $\boldsymbol{\tau_{e,x}}$. Then, the corrective action is overall less effective. We found analogous results for the external torque $\boldsymbol{\tau_{e,y}}$ along $\boldsymbol{y}_P$.

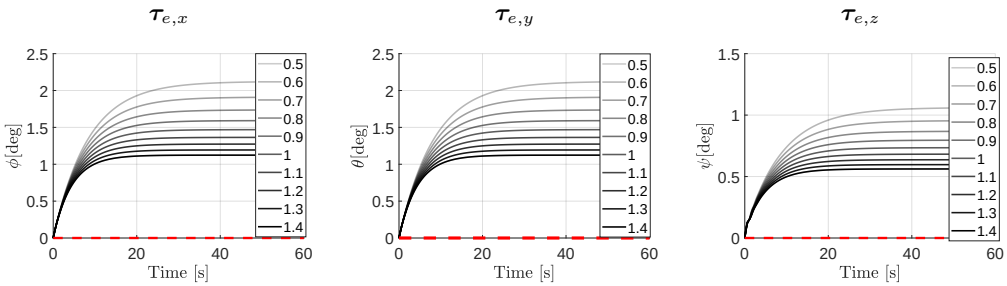

(a) (b) (c)

Figure 6.6: Evolution of the attitude of the object with no leaders in a group of floating robots for different values of $f_{int} > 0$ (whose different values are provided in the legend. The quantities are expressed in [N]). From the left to the right, $\boldsymbol{\tau_{e,x}}, \boldsymbol{\tau_{e,y}}$ and $\boldsymbol{\tau_{e,z}}$ are applied for which $m_{ext} = 1$ [Nm]. Only the rotation angle about the corresponding axis is displayed.

Observation 4. *Let us consider the presented communication-less approach employed for the manipulation of an object performed by a swarm of generic robots. From the theoretical previous analysis and observations from numerical simulations performed so far; we can conclude that:*

1. *The internal forces in the object are merely sufficient to confer robustness to the attitude of the object, even without any leader robot in the swarm.*

2. *The sensitivity of the attitude error when external disturbance torques are applied is inversely proportional to the intensity of the internal forces in the object.*

One leader robot In this paragraph, the robustness to external torques when the swarm is composed of one leader robot will be examined. In Fig. 6.7, one can appreciate the evolution of the attitude of a floating system with one leader when $f_{int} = 0$. In addition, the attitude evolution in the presence of two and three leaders are also shown.

From the simulations, we observed that:

- for $f_{int} = 0$, the attitude of the object is *not robust* (see the first column of Fig. 6.7);

- for $f_{int} > 0$, the attitude of the object is *robust*;

- for $f_{int} < 0$, the error of each rotation angle is bounded. However, the system turns around the axis of the corresponding external torque since $\boldsymbol{\eta}_{P0}$ is not stable. It is worth recalling that, in the scenario involving one leader, $\boldsymbol{\eta}_{P0}$ was already unstable when no disturbances were applied.

The presented results are similar to the ones obtained for swarms with no leaders with. The only exception is that when $\boldsymbol{\tau}_{\boldsymbol{e},\boldsymbol{z}}$ is applied, the leader robot acts as a pivot around which the system rotates. Conversely, when no leaders guide the team, the system rotates around the object's CoM. Therefore, the results obtained in this and in the previous section enforce the conclusion that the internal forces in the object play a crucial role for the swarm allowing it to cooperatively control the attitude of the object. Moreover, the presence of a leader robot, despite being essential for controlling the object position (as discussed in the previous section), emerges to be not relevant for controlling the attitude.

Two leader robots The role of multiple leaders while reacting to the usual external disturbances will be here presented. The results are related to the configuration composed of two leader robots evenly distributed around the platform as in Fig. 6.5a:

- for $f_{int} = 0$, the attitude about the axis connecting the two leader robots, $\boldsymbol{x}_P$, is *not robust*. On the other hand, pitch (θ) and yaw (ψ) are *robust*, as shown in Fig. 6.7 (see second column);
- for $f_{int} > 0$, the attitude of the object is *robust*;
- for $f_{int} < 0$, the error of each rotation angle remains bounded. However, being $\boldsymbol{\eta}_{P0}$ not even stable when $\boldsymbol{\tau}_{\boldsymbol{e},\boldsymbol{x}}$ acts on the object, the object turns by 180 [deg] around $\boldsymbol{x}_P$ (axis between the two leader robots).

For ground swarm systems identical results hold with the difference that the only allowed rotation is the one around $\boldsymbol{z}_P$.

Three leader robots The case of three evenly distributed leader robots as in Fig. 6.5b will be, in the following, considered. From the obtained results, we can conclude that by employing three leader robots, the control of the object attitude is *robust*, regardless of the presence of the internal forces or their possible signs. The results with $f_{int} = 0$ can be found in Fig. 6.7 (see third column). For ground systems, the same results can be appreciated with only two evenly distributed leader robots.

Observation 5. *Considering the presented communication-less approach for the swarm manipulation of an object, from the previous results, we can conclude that:*

1. *Two leader robots are needed for a ground swarm to robustly control the attitude of the commonly manipulated object without exerting any internal force, namely without compressing nor stretching the object itself.*
2. *Three leader robots are instead necessary for the floating swarm to achieve the same objective without applying any internal force.*

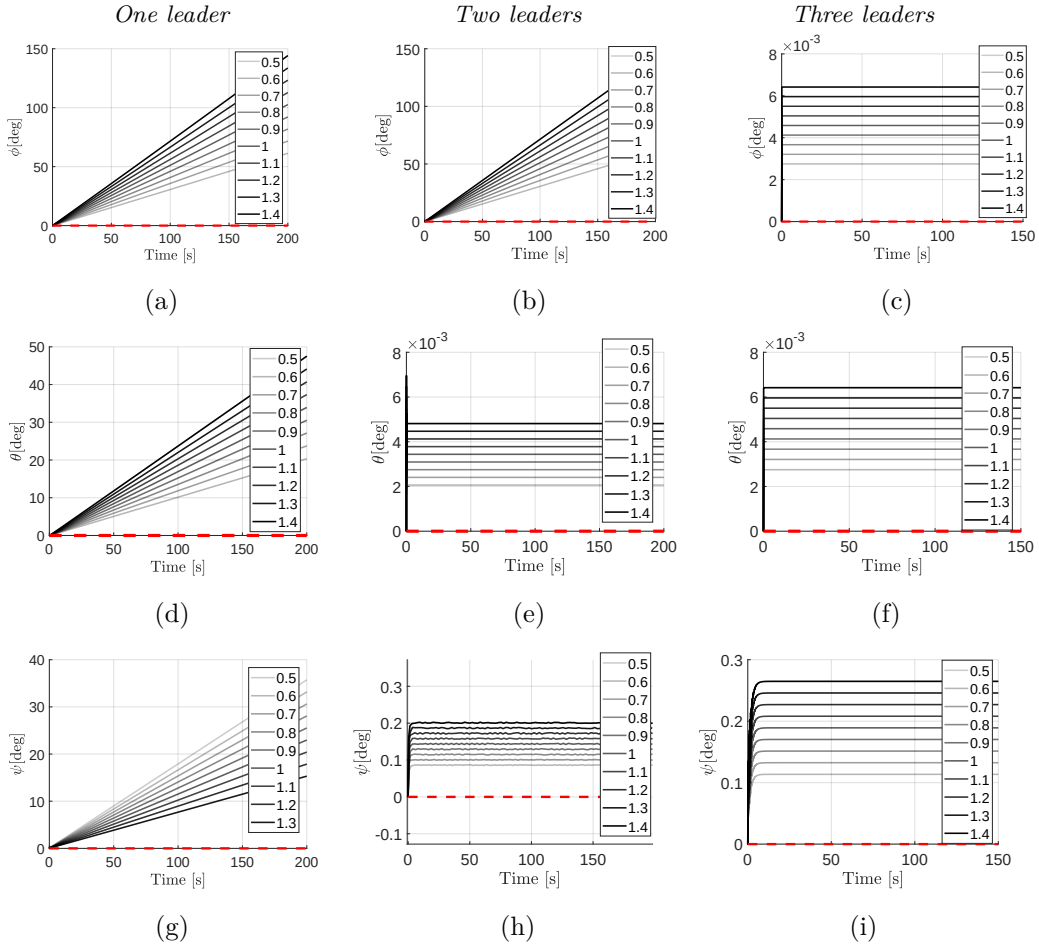

Figure 6.7: Evolution of the attitude of the object in a group of floating robots with $f_{int} = 0$. In each row, from the left to the right, one leader two leaders and three leaders are considered, respectively. $\boldsymbol{\tau_{e,x}}$ is applied in the first row, $\boldsymbol{\tau_{e,y}}$ in the second, and $\boldsymbol{\tau_{e,z}}$ in the third one. Only the rotation angle about the axis corresponding to the applied torque is displayed. The legend contains the value of m_{ext} expressed in [Nm].

Leaders	f_{int}	Orientation
0	$= 0$	not robust
	> 0	robust
	< 0	unstable. Although, all the angles stay bounded
1	$= 0$	not robust
	> 0	robust
	< 0	$\boldsymbol{\eta}_{P0}$ is unstable. Although, all the angles stay bounded
2	$= 0$	robust, except around $\boldsymbol{x}_P$.
	> 0	robust
	< 0	The desired roll angle is unstable. Nevertheless, all the angles stay bounded.
3	$= 0$	robust
	> 0	robust
	< 0	robust

Table 6.2: Summary of the load robustness analysis.

Summarizing, in Fig. 6.7, we highlight the role of the presence of multiple leader robots in the attitude robustness. In the case of two leaders, it emerges that the roll angle ϕ is *not robust* when $\boldsymbol{\tau}_{\boldsymbol{e},\boldsymbol{x}}$ acts on the system, whereas the rotations around $\boldsymbol{y}_P$ and $\boldsymbol{z}_P$, namely pitch (θ) and yaw (ψ) angles are *robust* when an external torque is applied on the corresponding axes. In the case of one leader robot, on the other hand, none of the components of the attitude is robust. This shows that the addition of one more leader robot enhances the robustness of the system when no internal forces are applied. In particular, the orientation of the load around the axes perpendicular to the axis connecting the anchoring points of the two leaders becomes robust thanks to the effect of a disturbing external torque. The conclusions drawn hitherto from the numerical results presented in this section are summarized in Table 6.2.

6.1.1.4 Robustness Analysis and noisy measurements

To conclude, in this subsection, we address the robustness of the object attitude tackling a more realistic scenario. As a matter of fact, the external torque disturbances will be considered random variables with a Gaussian distribution acting along all the axes of $\mathcal{F}_P$. In this scenario, the system is asked to perform under increasing mean value and with a standard deviation of 0.1 [Nm].

For what concerns the robots, their state and the contact force measurements will be affected by noise. In particular, the estimation related to each robot, namely own positions, velocities, and contact forces will be affected by unbiased Gaussian noise with a standard deviation of 0.01 [m], 0.01 [m/s], and 0.2 [N], respectively.

The results of the simulations substantially show the qualitative convergence

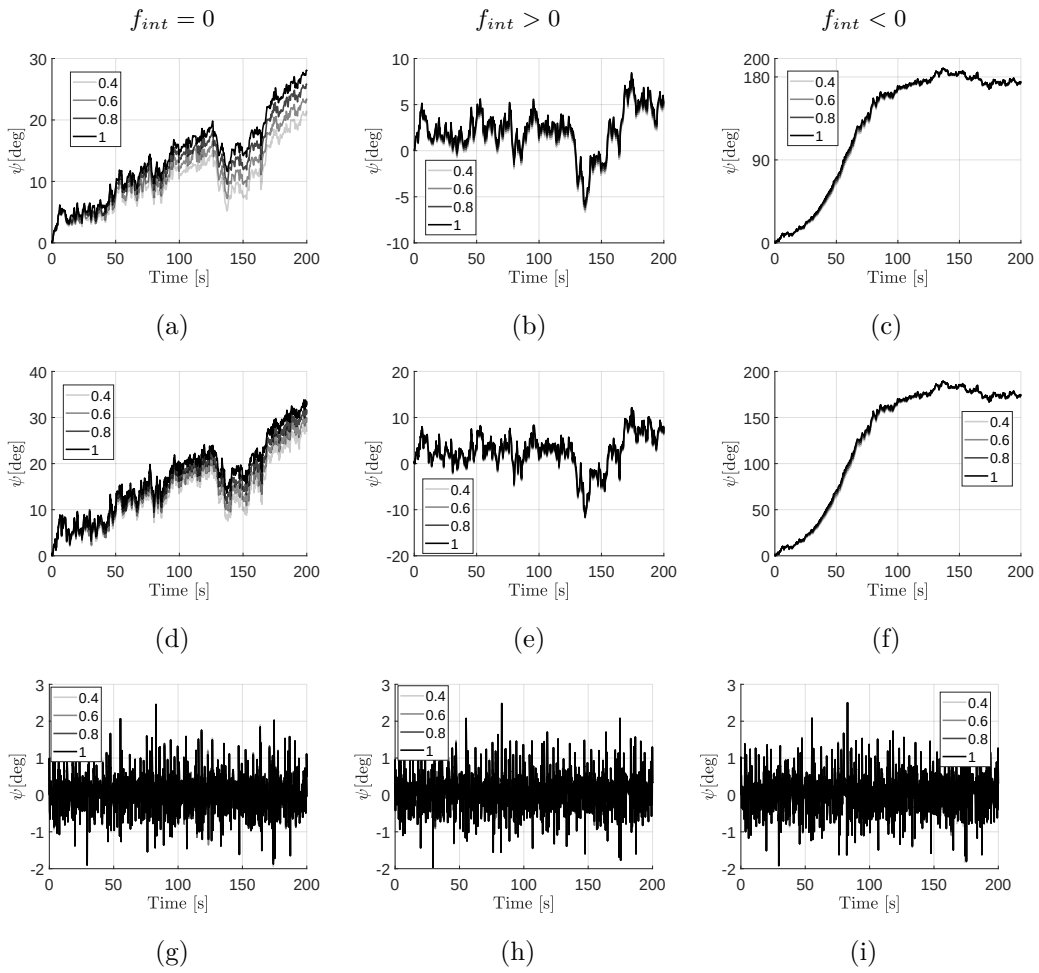

Figure 6.8: Evolution of the attitude of the object in a group of ground robots. The system is subject to an external Gaussian-distributed disturbance torque applied to the object center of mass, with increasing mean value and 0.1 [Nm] standard deviation. The mean value of the disturbance along the three orthogonal directions is reported in the legend in [Nm]. $f_{int} = 0$ in the first column, $f_{int} > 0$ in the second, and $f_{int} < 0$ in the third one. The first, second and third rows are the results for zero, one and two spread leader robots, respectively.

and robustness behavior which emerged in the previous section. In Table 6.3, the reader can find the mean value and the maximum standard deviation (std) of the attitude errors in the different simulated conditions (different number of leaders and different values of f_{int}). The case of zero leaders has not been included in the table results since it is not of practical relevance for the reasons previously explained. Then, the characteristics of the errors when $f_{int} > 0$ are reported as well, even if three leaders are enough to have bounded attitude errors with no internal forces.

Focusing on the results, first of all, it emerges that, with three leaders, the potential benefits induced by a non-zero internal force on the attitude robustness

are not significant. Moreover, they suggest that employing a group of robots with two leaders is more convenient in terms of robustness than using only one leader. In addition, the benefits of using three leaders instead of two are not so much evident if a non-zero internal force in the object is explicitly required.

To make further comparisons, an extensive set of simulations has been performed for a ground system under the previously described Gaussian external disturbance and noisy measurements. A viscous friction force on the object, inversely proportional to the velocity has been also considered with a dissipation coefficient equal to 0.01 [kg/s] for the linear component and equal to 0.01 [kg m^2/s^2] for the rotational component. Furthermore, a static friction action has been taken into account in such a way that a force of at least 0.5 [N] is required to start the object motion. Figure 6.8 contains the evolution of the attitude of the ground system with zero, one and two spread leader robots for $f_{int} = 0$, $f_{int} > 0$, $f_{int} < 0$. Moreover, in Fig. 6.8, four simulations are presented for each case corresponding to increasing mean values of the disturbance torque (for a total of 36 simulations). The mean value and the maximum standard deviation of the attitude error for a ground system are instead in Table 6.4.

Notice that, even though the behavior of the attitude is the same with zero and one leader, more advantages can be appreciated with one leader. In fact, its presence favourites better performances in regulating the object position. On the contrary, with no leader robots, there is no position reference and, the system is free to drift under the action of the external disturbance.

Leaders	f_{int}	error mean [deg]	error maximum std [deg]
1	$f_{int} > 0$	ψ: -6.2867 θ: -33.6865 ϕ: 25.4101	ψ: 2.6101 θ: 4.1459 ϕ: 3.8239
2	$f_{int} > 0$	ψ: 0.5273 θ: 0.0129 ϕ: 2.1274	ψ: 0.3659 θ: 0.5232 ϕ: 0.3746
3	$f_{int} > 0$	ψ: 0.0863 θ: -0.0380 ϕ: 0.1902	ψ: 0.2477 θ: 0.7354 ϕ: 0.7820
3	$f_{int} = 0$	ψ: 0.2050 θ: 0.0852 ϕ: 0.0875	ψ: 0.2526 θ: 0.1726 ϕ: 0.1762

Table 6.3: Summary of the statistics of the attitude errors for a floating system.

Leaders	f_{int}	error mean [deg]	error maximum std [deg]
0	$f_{int} > 0$	1.9475	2.4201
1	$f_{int} > 0$	2.4513	3.7961
2	$f_{int} > 0$	0.0862	0.3580
2	$f_{int} = 0$	0.0674	0.3911

Table 6.4: Summary of the statistics of the attitude errors for a ground system.

6.2 The Fly-Crane

Proceeding with the dichotomy of the two proposed approaches, this section is devoted to the specific model prototype of the Fly-Crane (see Sec. 4.2), which has been manufactured and then tested in real indoor scenarios. Starting from the mechanical details, the Fly-Crane consists of three Quadrotor UAVs connected by six cables to a platform made of carbon fiber bars. The Fly-Crane system while flying in an indoor scenario is shown in Fig. 6.9. Each vehicle weights 1.03 [Kg], the platform weights 0.338 [Kg], and the length of each cable is 1.2 [m]. The aerial vehicles are equipped with a standard flight-controller (Mikrokopter FlightCtrl V2.1), four brushless motor controllers regulating the propeller speed in closed-loop (ESC's BL-CTRL2.0c which use custom firmware) and an on-board PC (Odroid XU4) that runs the state estimator and the velocity controller[1]. The available payload of each robot is 0.4 [Kg] and, using a battery LiPo 4S 2200 [mAh], they possess 10 [min] of time flight without load. Moreover, the proposed kinematic controller, implemented in Matlab-Simulink, runs on a desktop PC sending the commanded velocities to the quadrotors through a WiFi connection at 100 [Hz]. The control loop is then closed based on the estimated state of the vehicles and of the platform. These estimations are computed onboard at 1 [kHz] by an Unscented Kalman Filter (UKF) that fuses the MoCap System measurements (at 120 [Hz]) with the IMU measurements (at 1 [kHz]). In the first phase of each experiment, the platform is lifted from the ground, and the system is brought to a non-singular initial configuration. The aerial vehicles are independently controlled by a standard position controller. The proposed control strategy, presented in Sec. 5.1.2, is activated right after.

The trajectory is designed to take the system from its initial configuration, $\boldsymbol{q}^d(0)$, to the final desired configuration $\boldsymbol{q}^d(T)$ where $\boldsymbol{p}_P^d = [0.28 \;\; -0.06 \;\; 0.7]^\top$[m], $\boldsymbol{\eta}_P^d = [8 \;\; 13 \;\; 53]^\top$[deg], $\boldsymbol{\alpha}^d = [32 \;\; 20 \;\; 62]^\top$[deg], and $T = 20$ [s]. The gain of the velocity controller is set to $k_R = 15$ (this value provides the smallest velocity error considering our low-level controller).

Given the desired trajectory and a maximum model uncertainty of 10% for each parameter, (5.46) allows computing the bounds needed for the design of $k_{\boldsymbol{q}}$. In particular, remembering that a first estimation of the bounds on the particular

[1]The full software framework is based on *TeleKyb* which is open-source and available at `https://git.openrobots.org/projects/telekyb3`

Figure 6.9: Experimental screenshot of the Fly-Crane flying while controlling the platform in full pose (position and orientation).

trajectory has to be performed, knowing the maximum uncertainty on the Jacobian, the following bounds have been considered, $\delta^2 = 0.055$, $\iota^2 = 0.078$, and $\rho^2 = 0.01$.

The gain $k_{\boldsymbol{q}}$ has been then designed using Theorem 2, described in Sec. 5.1.2.1, and the solution to the minimization problem (5.45) provides $k_{\boldsymbol{q}} = 0.38$ and the H_∞ gain $\gamma = 1$.

Considering this setup, we performed four experiments under different conditions that are summarized in the following. Moreover, we refer to the provided multimedia material to appreciate the system in action [**video-1**].

1. *Optimal conditions:* the model parameters are the measured ones with no additional errors. However, measurement errors and noise are still present. External disturbances were applied neither. Fig. 6.10 shows the obtained results.

2. *Model error:* an additional model error in the length of the cables equal to 10% of their nominal value is added. The corresponding results are shown in Fig. 6.11a, Fig. 6.11b and Fig. 6.13a.

3. *External disturbance:* an artificial force equal to $[1.7\ 1.7\ 1.7]^\top$ [N] is added to the low-level controller of the aerial vehicles. The effect simulates the action of an external disturbance on the vehicles' motion. The corresponding results are shown in Fig. 6.12.

4. *Fast-Trajectory*: the system has to accelerate the platform up to $3.2\,[\mathrm{m/s^2}]$ reaching a velocity up to $1.6\,[\mathrm{m/s}]$. In this case, the assumption of quasi-static trajectory is largely violated, i.e. the tracking of far from quasi-static

trajectories is requested to the system. For this last case, the reader is referred to Fig. 6.14.

In Experiment 1), the model parameters are the measured ones with no additional errors. Any external disturbance is applied. However, measurement errors and noise are still present. Fig. 6.10a shows the reference trajectories (in dashed lines) and the actual ones (in solid lines). The system exhibits good capabilities of tracking the desired configuration, as the plots of the tracking error demonstrate (see Fig. 6.10b). As a matter of fact, at steady state, they are less than 0.02 [m] in position, 2 [deg] in attitude and 2 [deg] in $\boldsymbol{\alpha}$.

For Experiment 2), Fig. 6.11a shows the bounds for which the controller gain $k_{\boldsymbol{q}}$ has been computed. In particular, the actual values (blue lines) are derived and compared w.r.t. the pre-computed ones (red dashed lined). It is possible to notice that the conditions (5.28), (5.29) and (5.30) are always verified. This means that the system, under the chosen limits, stays away from the effects of the variations on the model errors (δ), possible singularities (ι) and sudden changes in terms of reached configurations (ρ) throughout the entire duration of the experiment. Moreover, it is worth noting that the same considerations can be expressed for Experiments 3) (see Fig. 6.12a). In Fig. 6.11b, the norm and the components of the tracking error are shown. In particular, the first graph shows the indicator of the robustness of the system. In the plot, we compare the tracking error dynamics $||\boldsymbol{e_q}||$ with the disturbance dynamics $||\boldsymbol{w}||$. In this scenario, $||\boldsymbol{e_q}||$ keeps bounded under $||\boldsymbol{w}||$, suggesting that the robustness of the system has been guaranteed throughout the execution of the experiment. Moreover, while the transient phase results more critical w.r.t. optimal case, the same cannot be said at a steady-state, where similar achievements can be appreciated. In actual fact, as can be seen in the last three rows of Fig. 6.11b, similar results are obtained: the position error results to be 0.02 [m], the orientation error 2 [deg] and the error in tracking the angles $\boldsymbol{e_\alpha} = \boldsymbol{\alpha}^d - \boldsymbol{\alpha}$, 3 [deg].

The same analysis is proposed for Experiment 3). The reference and the actual trajectories are presented in Fig. 6.13b while the norm and the tracking errors are shown in Fig. 6.12b. In this case, the tracking error does not accurately converge to zero. This characteristic is more evident in the position error, due to the effects of the applied external disturbances. As expected, these non-idealities affects the exactness of the nominal model and the tracking of the aerial vehicles. However, considering the first row of Fig. 6.12b where $\|\boldsymbol{e_q}\|$ and $\|\boldsymbol{w}\|$ are compared, it is clear that condition (5.31) is verified and the maximum H_∞ performance is guaranteed. Therefore, it is possible to conclude that, under the fulfillment of conditions (5.28), (5.29), and (5.30) in Theorem 2, the proposed controller and tuning method guarantee the maximum H_∞ performance.

Lastly, in Experiment 4), the aim was to bring the system to reach its limits asking to obtain far from quasi-static motions. The system had to accelerate the platform up to $3.2\,[\mathrm{m/s^2}]$ obtaining a velocity up to $1.6\,[\mathrm{m/s}]$ covering up to 2 [m] in 2 [s] and changing the platform orientation of 15 [deg] in 2 [s]. The results show that, as expected, the tracking error increases while the bounds and the H_∞ gain of

Theorem 2 are still verified. As can be seen in Fig. 6.14a, the developed controller is able to quickly follow, once again, the given reference trajectory trying to minimize the tracking error. Even though $||\boldsymbol{e_q}||$ increases as expected during the quick variation of the desired trajectory, it still remains bounded by $||\boldsymbol{w}||$ and subsequently decreases to zero when the trajectory becomes smoother (see Fig. 6.14b).

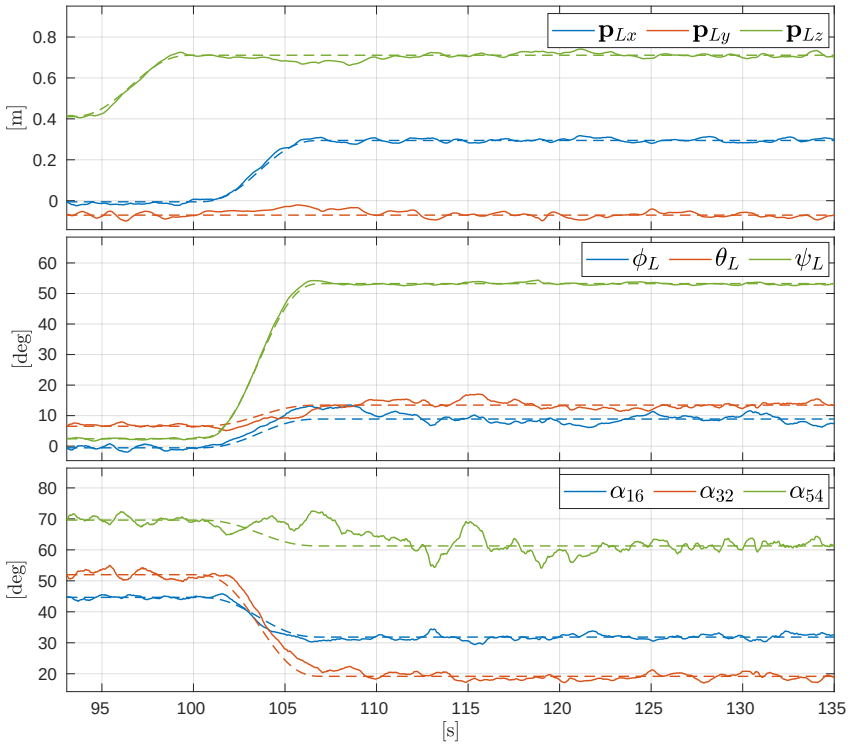

(a)

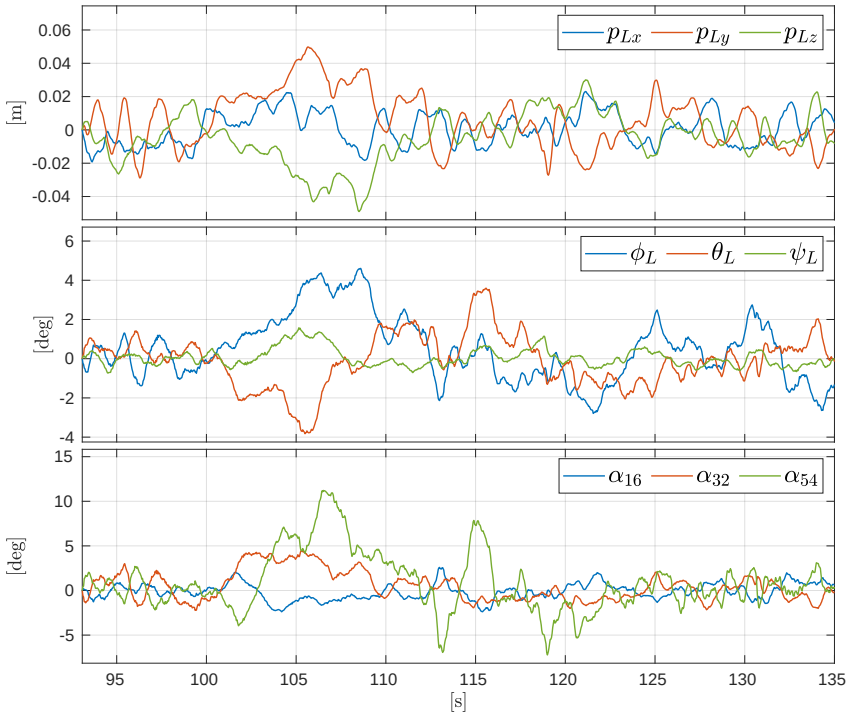

(b)

Figure 6.10: Plots for experiment 1): (a)Tracking of the desired trajectory. (b) Tracking errors.

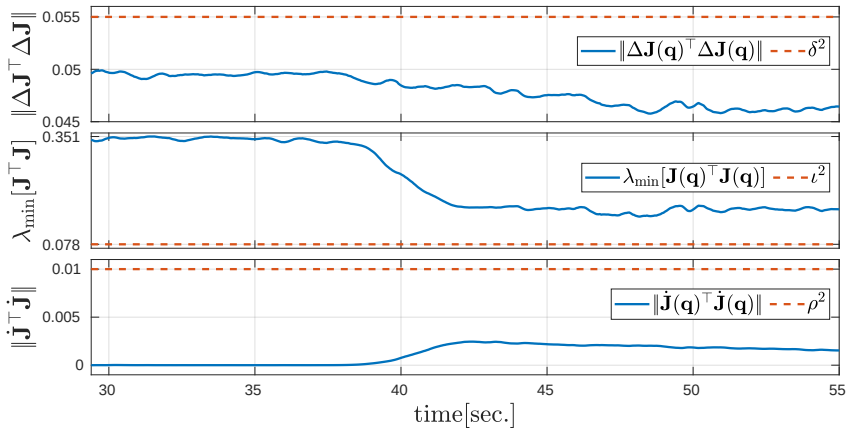

(a)

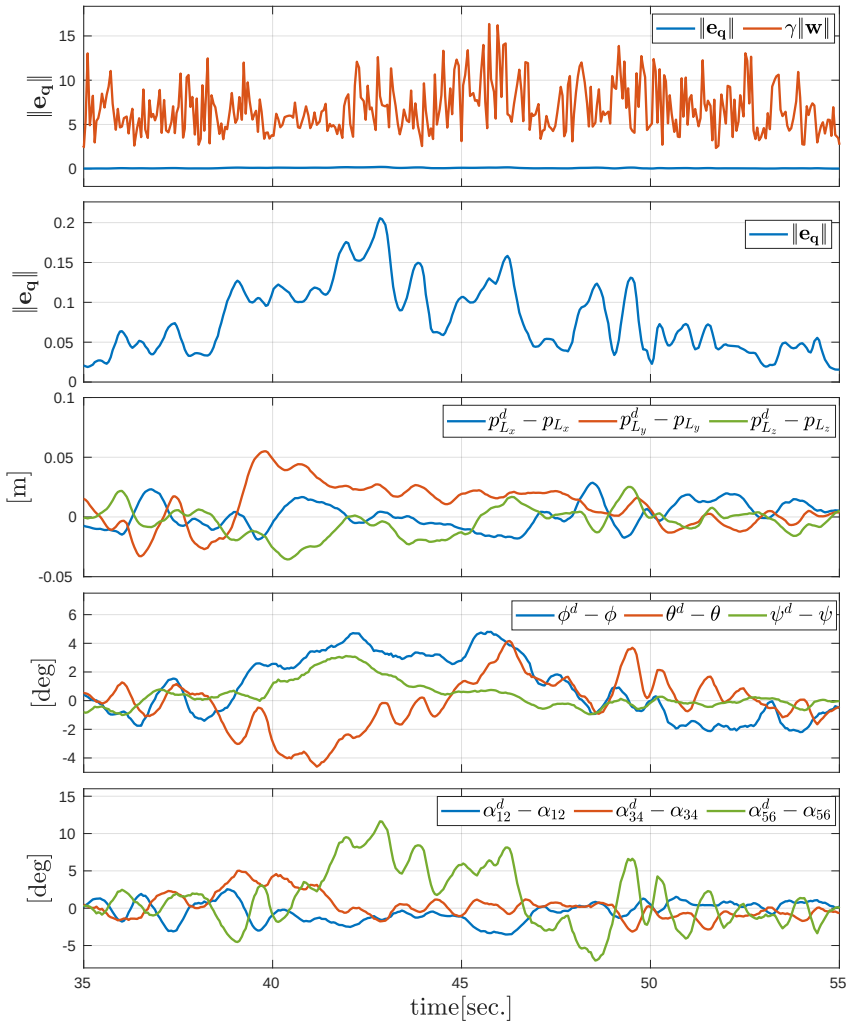

(b)

Figure 6.11: (a) Verification of conditions (5.28)-(5.30) for experiment 2).(b) Tracking error for experiment 2)

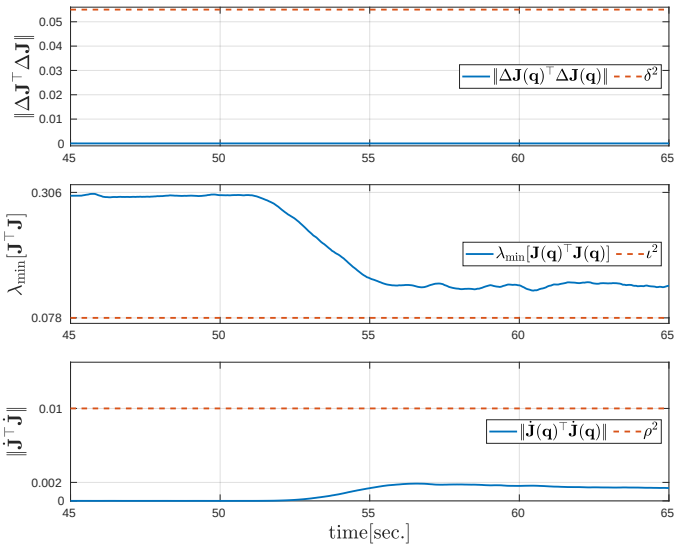

(a)

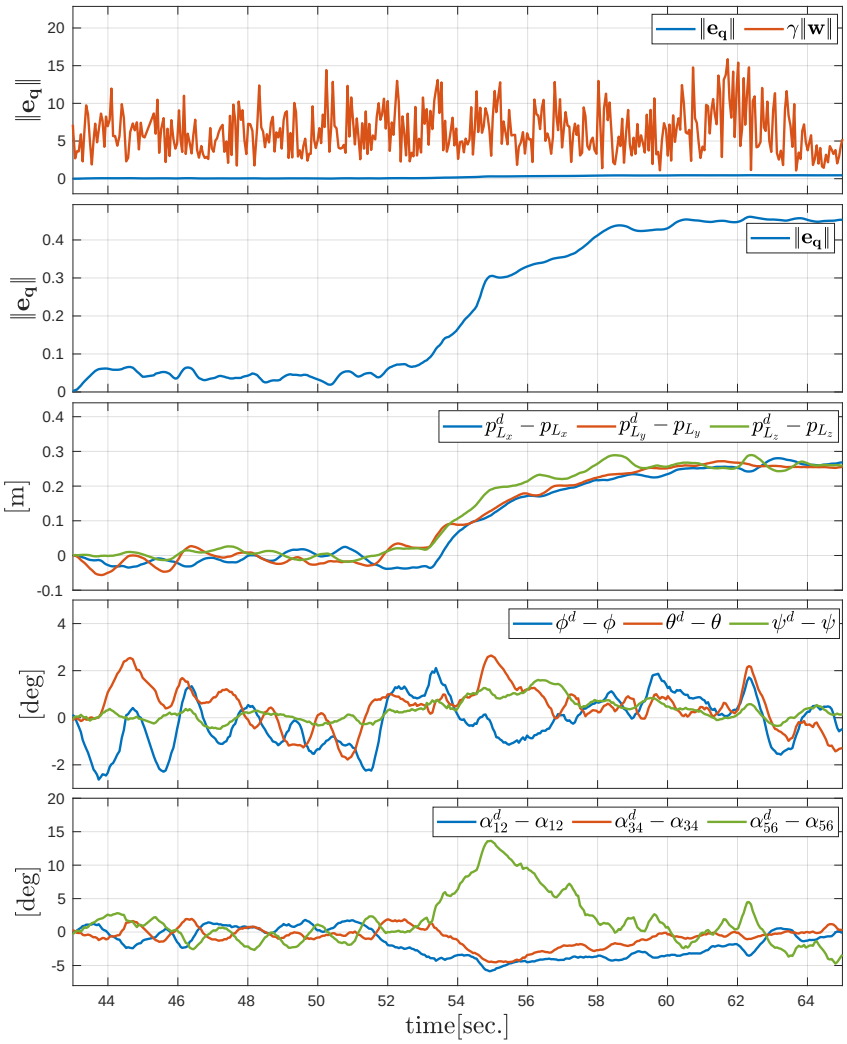

(b)

Figure 6.12: (a) Verification of conditions (5.28)-(5.30) for experiment 3); (b) Tracking error for experiment 3). At time 52 [s] the virtual disturbance has been introduced. This causes the increasing of the tracking error in position.

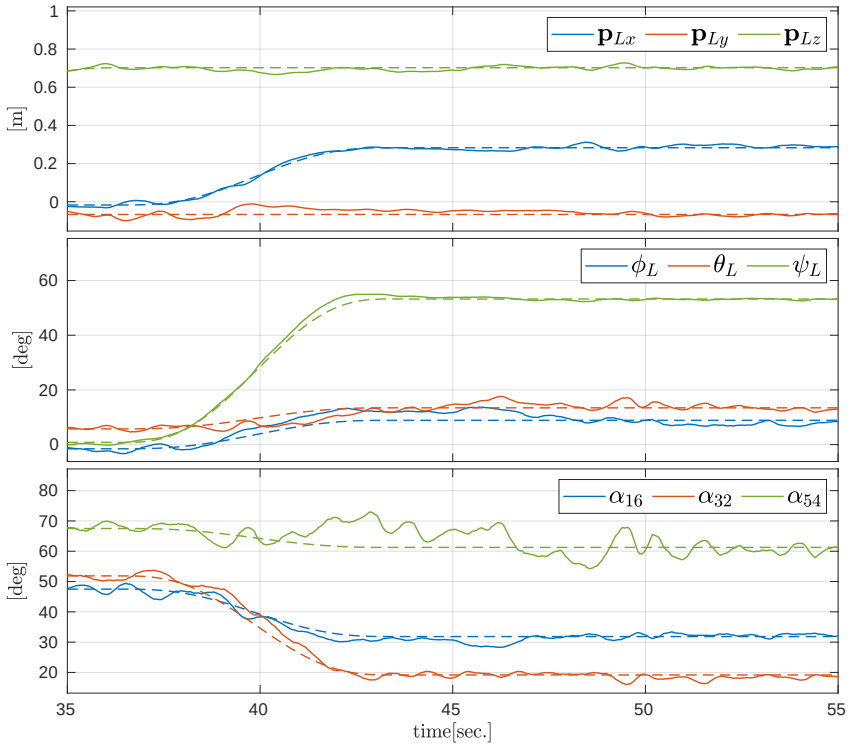

(a)

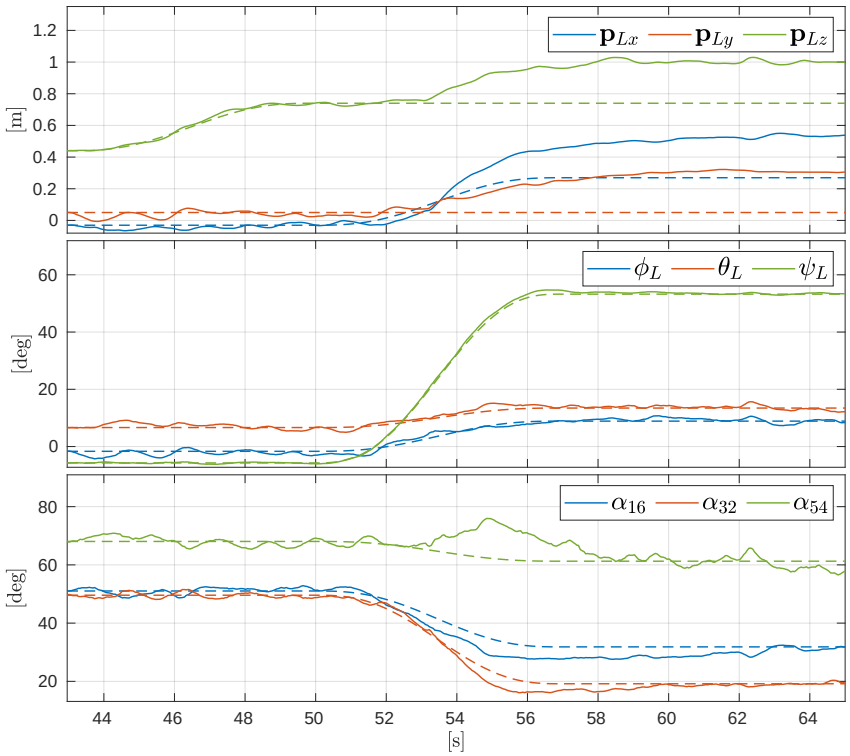

(b)

Figure 6.13: (a) Tracking of the desired trajectory during the system's evolution for experiment 2). (b) Tracking of the desired trajectory during the system's evolution for experiment 3)

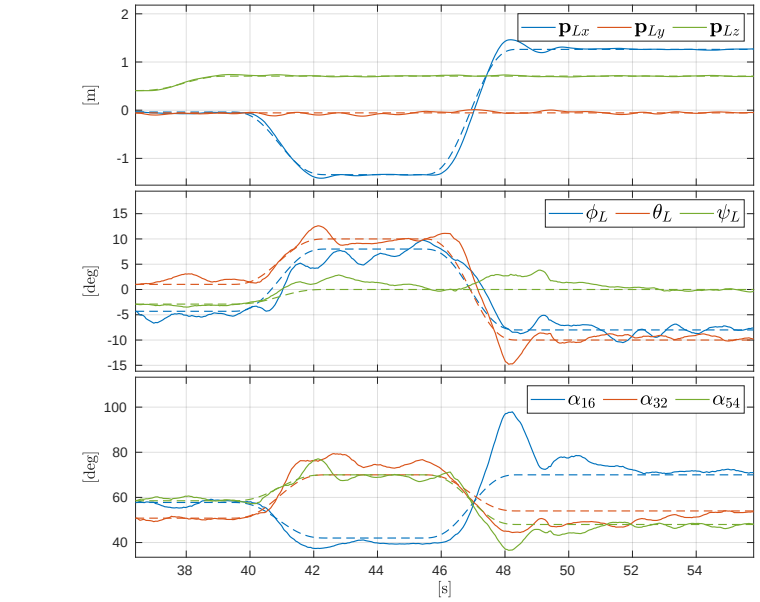

(a)

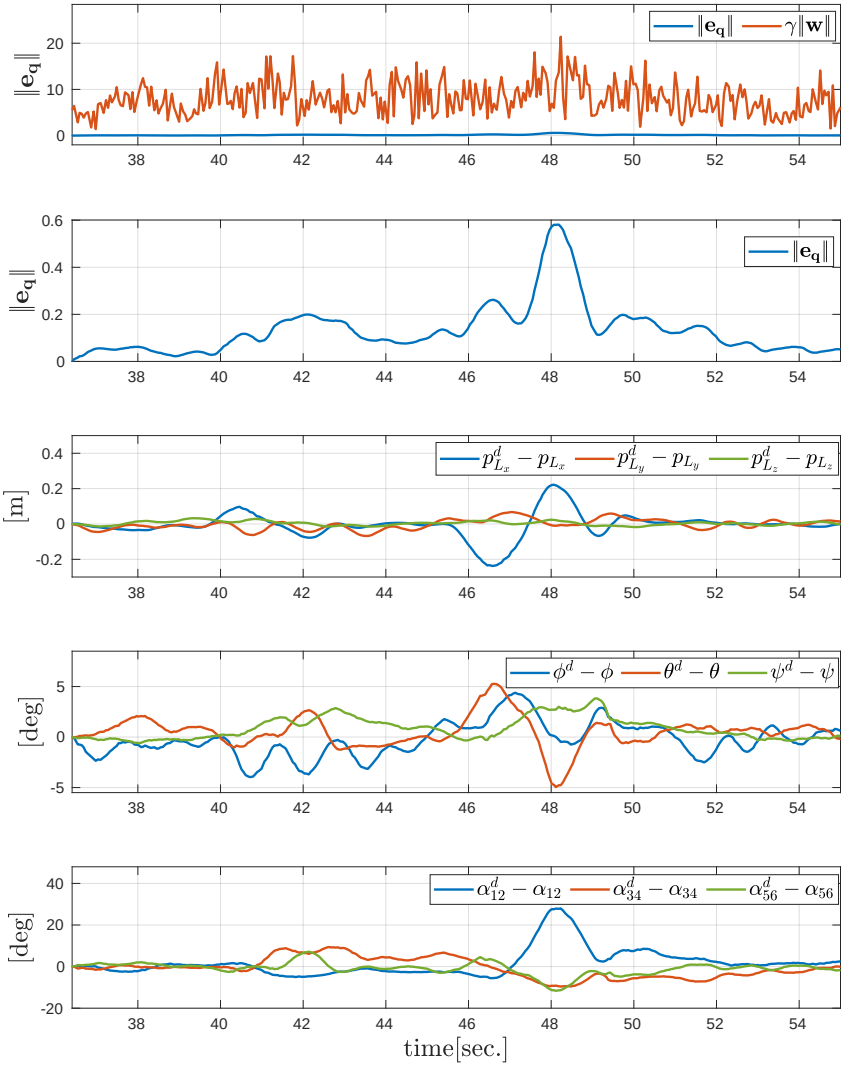

(b)

Figure 6.14: Plots for experiment 4): a) Tracking of the desired trajectory, b) Tracking errors

6.3 Optimization Strategy Validation

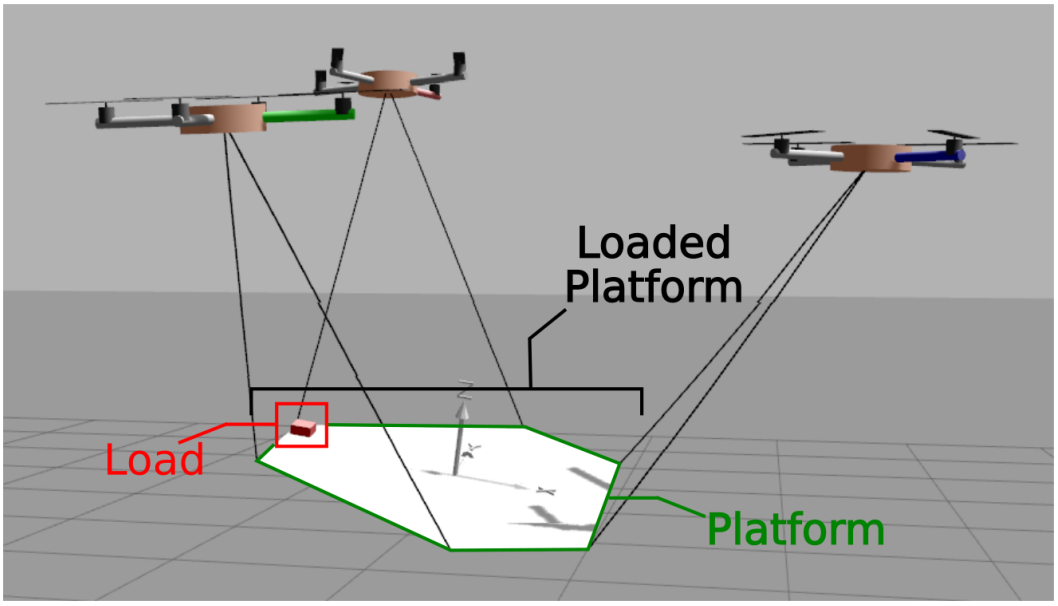

Figure 6.15: Picture of the Fly-Crane in the Gazebo simulation scenario and of the loaded platform which highlights its composition.

With the aim of performing more accurate manipulation tasks, in Sec. 5.1.3, we have presented a methodology to estimate the inertial parameters of the platform of the Fly-Crane and an approach to resolve the redundancy of the CS-AMRM. The two strategies have been included in the entire control architecture and, therefore, in the following, we provide their validation.

To this aim, first, we simulate the estimation of the loaded platform[2] mass and its CoM. Then, the optimization algorithm makes use of the performed estimation to solve the redundancy of the system, locally optimizing the force distribution among the robots.

The considered simulation scenario is implemented using Gazebo, modeling the cables as a set of serially-connected links, such that non-ideal effects such as cable deformations, cable vibrations and sagging, and noisy measurements are taken into account. An image of the simulation scenario is shown in Fig. 6.15 and, the additional multimedia material displays the system in the described phases [**video-2**].

For the simulations, the system has been simulated using the following parameters: the length of each cable is 1 [m], the weight of each vehicle is set to 1.03 [Kg], the mass of the platform is 0.2 [Kg]. Moreover, each cable is attached to the platform anchor points located in ${}^{P}\boldsymbol{b}_1 = [-0.433\ 0.15\ 0]\,[\text{m}]$, ${}^{P}\boldsymbol{b}_2 = [-0.433\ -0.15\ 0]\,[\text{m}]$, ${}^{P}\boldsymbol{b}_3 = [0.0866\ -0.45\ 0]\,[\text{m}]$, ${}^{P}\boldsymbol{b}_4 = [0.3464\ -0.3\ 0]\,[\text{m}]$, ${}^{P}\boldsymbol{b}_5 = [0.3464\ 0.3\ 0]\,[\text{m}]$,

[2]As already mentioned in Sec. 5.1.3.1 the term "loaded platform" is used to underline that the platform carries an additional weight that produces a change in its CoM. See Fig. 6.15 for major comprehension

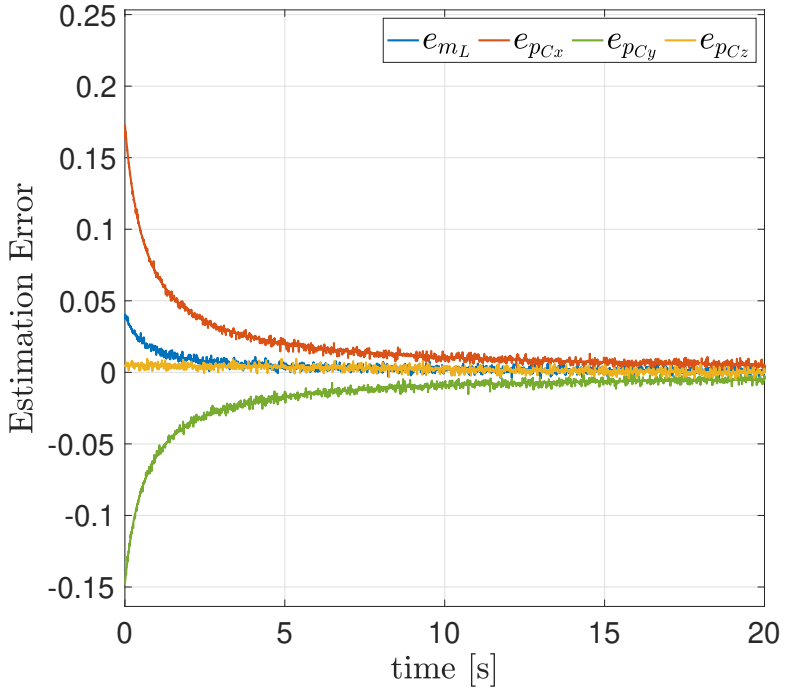

Figure 6.16: The estimation errors (in kilograms for the mass and meters for the position coordinates) computed during the online estimation procedure. At time $t = 0$ the errors correspond to the one obtained after the Initialization procedure.

${}^P\boldsymbol{b}_6 = [0.0866\ 0.45\ 0]\,[\text{m}]$. Then, we assume a load with mass $0.2\,[\text{Kg}]$ located in ${}^L\mathbf{p}_O = [-0.4\ 0.1\ 0]\,[\text{m}]$, resulting in an increase of 100% in the loaded platform total mass. The presence of the load moves the center of mass to $\mathbf{p}_C = [-0.2\ 0.05\ 0]\,[\text{m}]$.

Before starting with the trajectory tracking task, we run the estimation procedure in order to identify the value of the mass and the position of the CoM of the loaded platform. First, we run the initialization phase of the estimation procedure, described in Algorithm 1, with $\varsigma = 15$ [deg]. The outcome of this preliminary phase is an initial estimate $\widehat{\boldsymbol{p}}_C(0) = [-0.143\ \ -0.081\ 0.015]\,[\text{m}]$ and $\widehat{m} = 0.405\,[\text{Kg}]$. To average out the noise, we run also the online estimation phase that leads the estimation errors to converge to zero, on average. The results of the online estimator are reported in Fig. 6.16. As can be seen, the estimation errors tend to go to zero thanks to the least-squares method whose robustness to the noise is given by its ability to fit all the data till the current time. The online phase of the estimation procedure runs at a frequency of $500\,[\text{Hz}]$.

Once the estimation phase is completed, the system is demanded to track a trajectory which takes the system from its initial configuration, $\boldsymbol{q}^d(0)$ where $\boldsymbol{\alpha} = [60\ \ 60\ \ 60]\,[\text{deg}]$, to a configuration $\boldsymbol{q}^d(T_1)$ where $\boldsymbol{p}_P^d = [0\ \ 0\ \ 1.5]\,[\text{m}]$ and $\boldsymbol{\eta}_P^d = [0\ \ 0\ \ 0]\,[\text{deg}]$ with $T_1 = 60\,[\text{s}]$, to the final desired configuration $\boldsymbol{q}^d(T_2)$ where $\boldsymbol{p}_P^d = [0.2\ \ 0\ \ 1.5]\,[\text{m}]$, $\boldsymbol{\eta}_P^d = [10\ \ 8\ \ 45]\,[\text{deg}]$ with $T_2 = 120\,[\text{s}]$. While the system tracks the

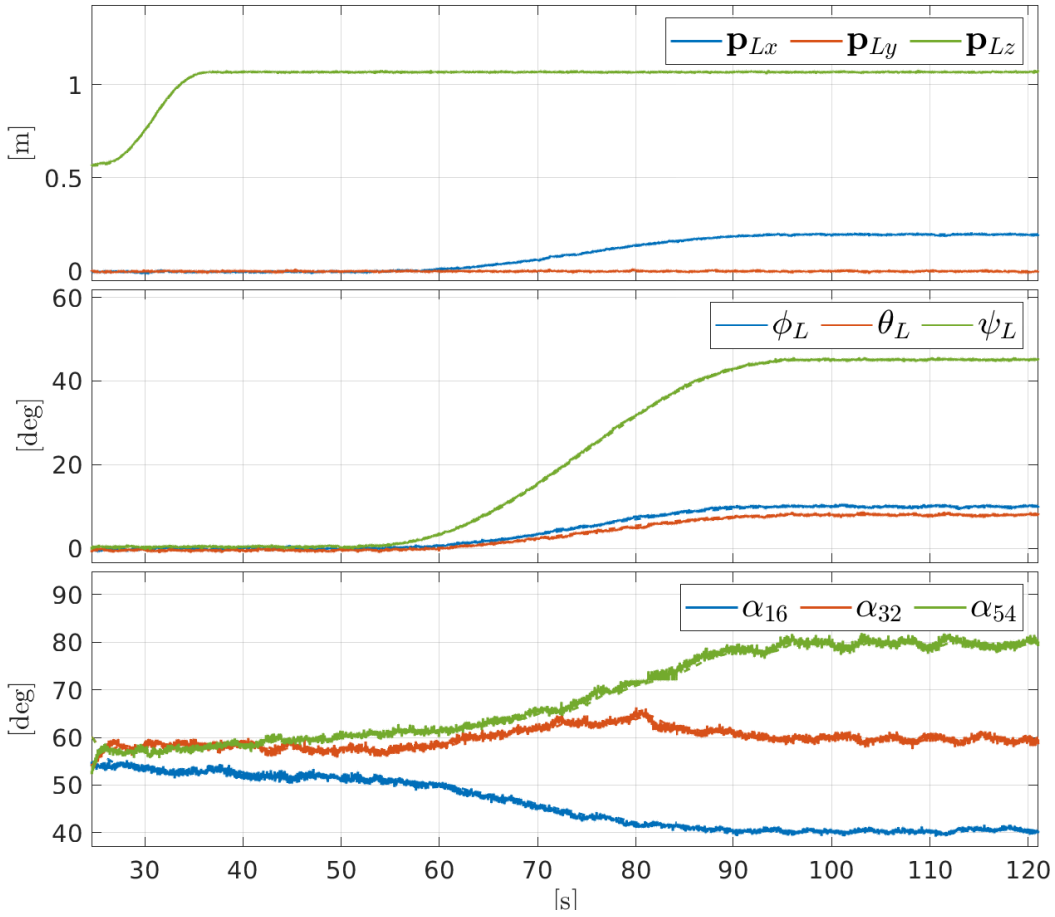

Figure 6.17: The evolution of the configuration $\boldsymbol{q} = \left[\boldsymbol{p}_P^\top \ \boldsymbol{\eta}_P^\top \ \boldsymbol{\alpha}^\top\right]^\top$ of the Fly-Crane while tracking a desired trajectory and optimizing $\boldsymbol{\alpha}$.

trajectory, the quantities $\boldsymbol{\alpha}$ are optimized to distribute the entire payload among the robots in the best possible way. To better illustrate the performance of the algorithm, the optimization results will be compared with a not optimized case, where the desired angles of the configuration of the system are equal to $\boldsymbol{\alpha}_c = [38\ 56\ 46]$ [deg]. Notice that this particular choice leads to a feasible trajectory.

In Fig. 6.17, we present the results of the tracking of the desired trajectory while the optimization is running. The controller is considerably robust in maintaining the desired platform position and orientation while following the output of the optimization algorithm, i.e. $\boldsymbol{\alpha}_{opt}$, that varies significantly during the tracking task. On the other hand, Fig. 6.18 shows the optimized configuration compared to $\boldsymbol{\alpha}_c$. As can be seen, the optimization procedure, aware of the loaded platform CoM position and mass, forces the system to reach different angles $\boldsymbol{\alpha}$, if compared with the not optimized case. This guarantees to reach an optimal configuration with respect to the minimization of the total exerted actuation effort. Furthermore, Fig. 6.19 shows how the cost function μ reaches a lower value as a result of the

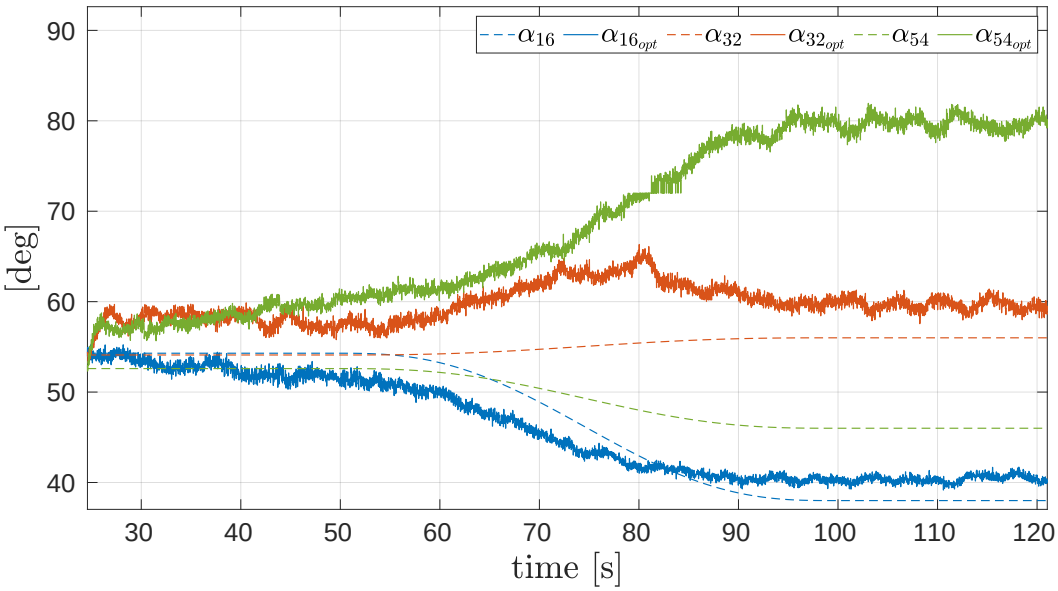

Figure 6.18: The evolution of the angles $\boldsymbol{\alpha}$ in the case in which the optimization procedure is running (solid lines) and is not running (dashed lines).

optimization process when compared to the one obtained in the not optimized case. The optimization runs since the beginning of the task, in $\boldsymbol{q}^d(0)$, leading μ_{opt} to decrease and $\boldsymbol{\alpha}$ to move from their initial values. Then, at T_1, when the new robot arrangement $\boldsymbol{q}^d(T_1)$ is required, the evolution of the cost function μ_{opt} is distinctly below the not optimized μ, as a consequence of the $\boldsymbol{\alpha}$ gradual variation. Then, the cost function keeps such a beneficial gap until the end of the simulation. It is worth observing that the cost function's rise is caused by the transition between two different system setups for which the required thrusts must be different enough among the three UAVs. For the sake of completeness, Fig. 6.20 shows the trend of the robot thrusts in the optimized case compared to the not optimized one. As can be seen, the optimization algorithm reduces the dispersion of the three total thrusts by increasing $\boldsymbol{f}_{R56_{opt}}$ and decreasing $\boldsymbol{f}_{R12_{opt}}$ and $\boldsymbol{f}_{R34_{opt}}$. This brings to the minimization of the maximum total thrust exerted by the system and, as a consequence, the extension of the overall flight time.

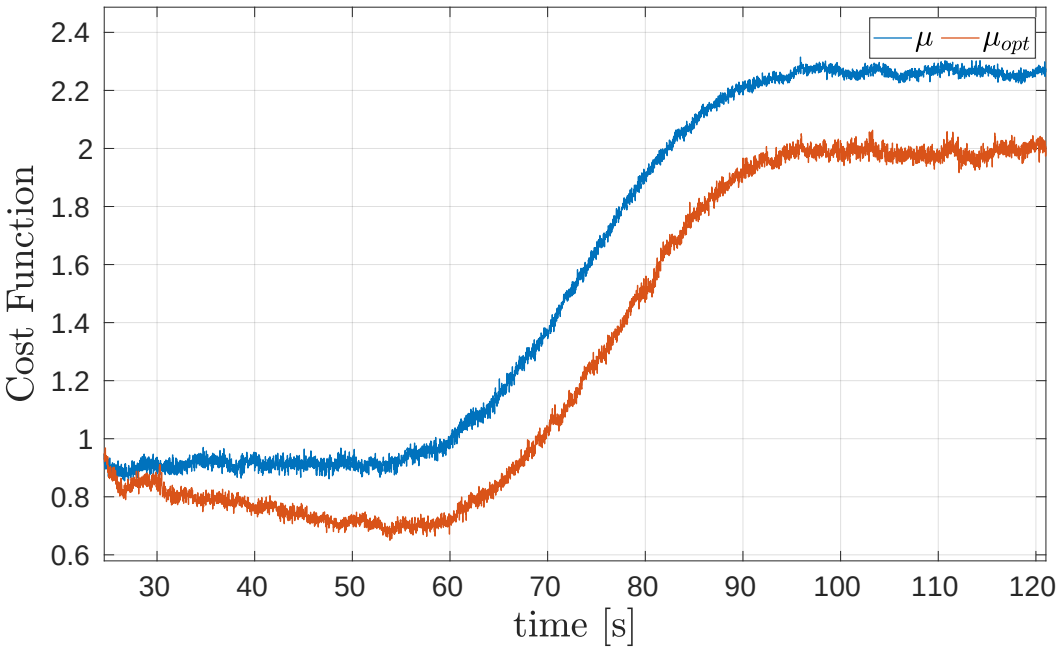

Figure 6.19: The evolution of the cost function during the trajectory tracking: in red, the case with the optimization of $\boldsymbol{\alpha}$, i.e. $\boldsymbol{\alpha} = \boldsymbol{\alpha}_{opt}$, and, in blue, the case with constant $\boldsymbol{\alpha} = \boldsymbol{\alpha}_c$.

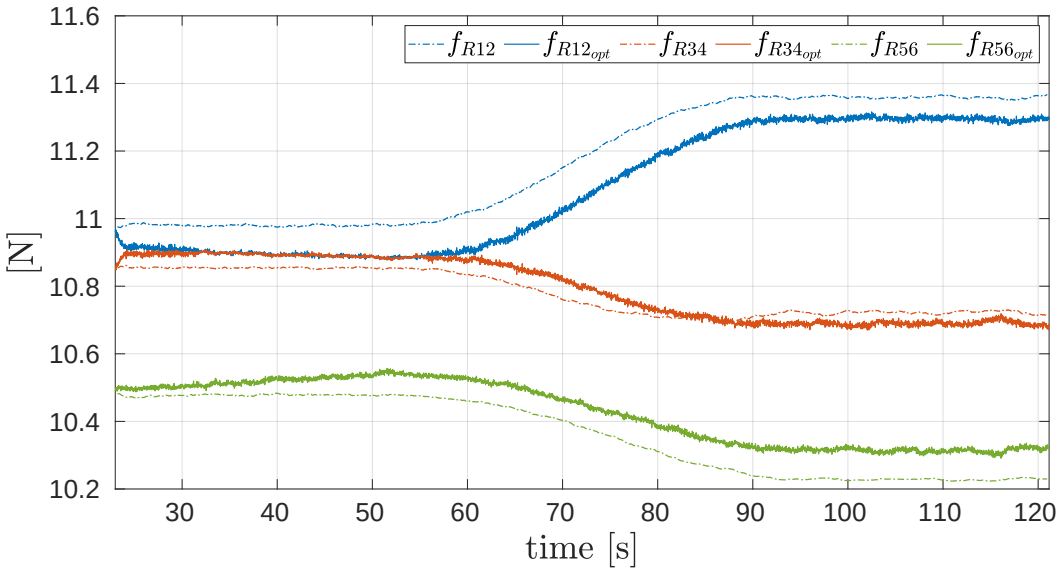

Figure 6.20: The evolution of the UAV total thrusts in the optimized case (solid line) and not optimized case (dashed line).

Part III

Aerial Cooperative Manipulations in interaction with the environment

Chapter 7

Shared Control Strategy of the Fly-Crane System performing pick-and-place operations

Throughout the chapters of Part II, possible solutions for the problem of the cooperative manipulation have been presented and then validated. In particular, we focused on the problem of the full-pose manipulation. A reasonable range of useful applications can be performed as introduced in Chapt. 1. However, all the presented work suppose that cooperative manipulations happen in *contact-free* conditions. Therefore, in this chapter, the proposed methodologies have been complemented to regulate the operations of teams of multiple aerial robots involved in activities *in contact* with the external environment. Motion control strategies, alone, illustrate their inadequacies w.r.t. uncertainties and errors which may arise during interactions. Therefore, they show unpredictable and possibly unstable behaviours. Such shortcomings are more accentuated when those systems have to deal with rigid and non-deformable environments. Although new and improved solutions can be found, the growing complexity of the problem may, as well, require human intervention for safety and regulatory reasons. Thence human operators may take part in the specific control loop while the cooperative manipulation advances in autonomous or semi-autonomous ways.

In this line, the following chapters will develop the conceived approaches adopted to deal with the interactions with the environment which on the one hand is represented by humans and on the other hand is represented by the objects surrounding the system. In particular, in this chapter, we illustrate the experimental results of a multi-robot system able to perform manipulation operations as pick-and-place in construction and decommissioning scenarios. Human involvement in the presented supervised/shared control approach represents the main peculiarity (see Sec. 7.1) besides being the first time in which an aerial multi-robot system is able to perform such assignments. Moreover, the experimental results presented in Sec. 7.2 constitute a preliminary but fundamental step towards real-world outdoor applications where advancements in terms of onboard sensors, grasping tools and payload capabilities have been made. We performed the mentioned experimental campaign with the G-Fly-Crane system. It represents an extended version of the Fly-Crane already presented in Chapt. 5. The main difference between the G-Fly-Crane and the Fly-Crane is the ability of the G-Fly-Crane to hold objects through a magnetic gripping system. Additionally, a novel software architecture has been combined with

the physical system in order to match the needs of the shared control framework.

7.1 Shared Control Strategy

The G-Fly-Crane principal purpose is to perform complex tasks for the construction/decommission of structures. Because of the complexity of the related problems such as object localization and classification, obstacle avoidance, etc., real application scenarios and the corresponding regulations require the presence of a human operator that can supervise or drive, if necessary, the robotic system. However, when the system possesses the control of a high number of DoFs, which is the case of the G-Fly-Crane (9 DoF), their simultaneous control becomes arduous for a single operator. Therefore, a human shared control strategy has been developed to facilitate assistance in such scenarios. Such a control strategy aims at focusing exclusively on the end-effector and the proper execution of the task. The remaining DoFs and the guidance of each robotic agent are left to the conceived controller. We refer to such a strategy as *Crane Mode* (see Sec. 7.1.1). In addition, two other ways of controlling the system have been developed in case of take-off/landing or emergency operations. They consist of rigid translations for the whole system on the one hand and/or the guidance of just one robot at a time on the other hand. This modality will be referred as *Manual Mode* (see Sec. 7.1.2). The picture of the entire software architecture is presented in Fig. 7.1. The shared control layer which allows the smooth transition between the different modalities, is presented in Fig. 7.2. A standard joystick has been used to handle the interactions between the human operator and the G-Fly-Crane system. A mapping between the available commands for the user and the commands required from the system has been developed. Finally, as in many examples in the state-of-the-art, the feedback used to help the telemanipulation is visual, i.e. the operators command the system relying on their view.

7.1.1 Crane Mode

This modality represents the situation where the shared strategy plays its decisive role. The human operator commands the end-effector desired pose, i.e. position $\boldsymbol{p}_P^d$ and orientation $\boldsymbol{\eta}_P^d$ of the platform. The combination of the inverse kinematic controller already presented in Sec. 5.1.2 and the optimization strategy shown in Sec. 5.1.3 to resolve the system redundancy allows to control all the DoFs of the G-Fly-Crane, i.e position $\boldsymbol{p}_P$, orientation $\boldsymbol{\eta}_P$ and the angles $\boldsymbol{\alpha}$. In order to do so, the joystick commands available to the operator are mapped into the desired translational and rotational velocities of the platform, i.e., $\boldsymbol{v}_P^d$ and $\dot{\boldsymbol{\eta}}_P^d$. Such quantities are then integrated (starting from the initial configuration) to obtain the desired position and rotation of the platform, i.e., $\boldsymbol{p}_P^d$ and $\boldsymbol{\eta}_P^d$. At this stage, the given desired trajectory $\boldsymbol{q}^d(t) = [\boldsymbol{p}_P^{d\top}\ \boldsymbol{\eta}_P^{d\top}\ \boldsymbol{\alpha}^{d\top}]^\top$ is available and the reference velocities of the aerial vehicles are computed as

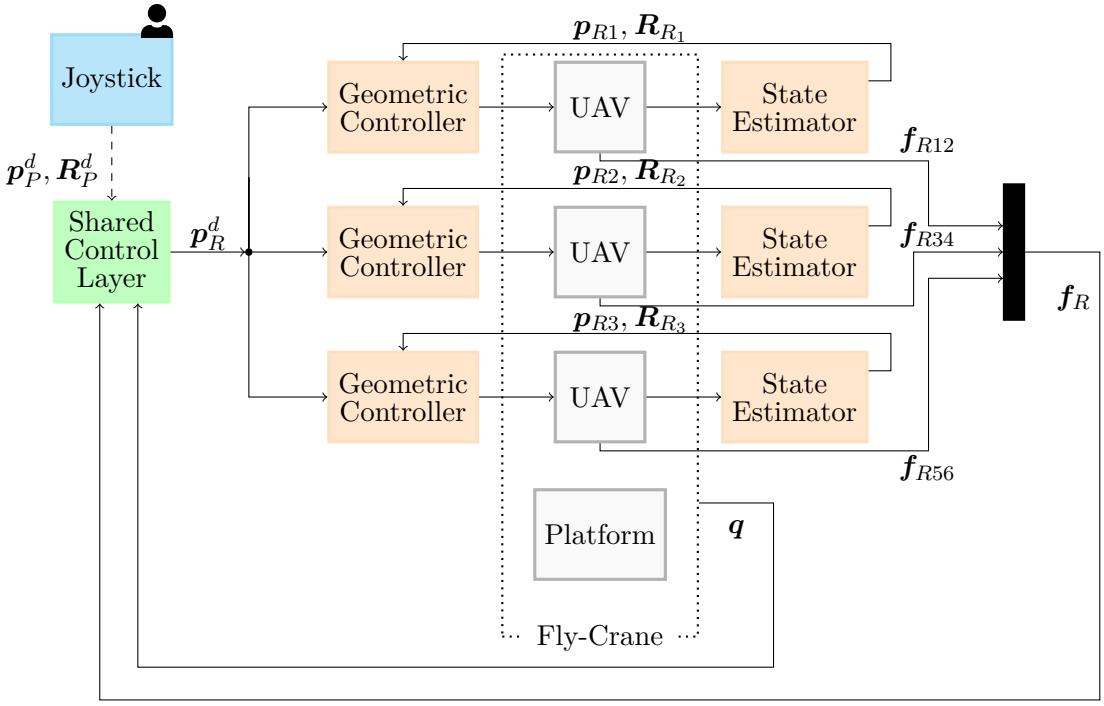

Figure 7.1: Control architecture of the G-Fly-Crane system.

$$\boldsymbol{v}_R^\star = \boldsymbol{J}(\boldsymbol{q}) \left(\boldsymbol{K}_{\boldsymbol{q}} \boldsymbol{e}_{\boldsymbol{q}} + \dot{\boldsymbol{q}}^d \right). \tag{7.1}$$

The integration of such velocities allows to obtain the reference position which each onboard geometric PID controller, based on [Lee 2010], will then follow. Significant benefit can be assessed to the integral action in case of possible external disturbances during contacts and changes in the platform mass during pick-and-place operations. Moreover, the remaining degrees of freedom to accomplish the desired configuration trajectory, namely $\boldsymbol{\alpha}^d$, are computed by means of the online planner already presented in Sec. 5.1.3 as a result of the following optimization problem

$$\boldsymbol{\alpha}^d = \underset{\boldsymbol{\alpha} \text{ s.t. } 0<\alpha_i<\frac{\pi}{2}}{\arg\min} \lambda_1 J_1(\boldsymbol{q}) - \lambda_2 J_2(\boldsymbol{q}), \tag{7.2}$$

where $J_1(\boldsymbol{q}), J_2(\boldsymbol{q})$ are two configuration-dependent cost functions and $\lambda_1, \lambda_2 \in \mathbb{R}_{>0}$ are the corresponding weights. In particular,

$$J_1(\boldsymbol{q}) = |f_{R1} - f_{R2}| + |f_{R1} - f_{R3}| + |f_{R3} - f_{R2}| \tag{7.3}$$

$$J_2(\boldsymbol{q}) = \sqrt{\det(\boldsymbol{J}(\boldsymbol{q})\boldsymbol{J}(\boldsymbol{q})^\top)} \tag{7.4}$$

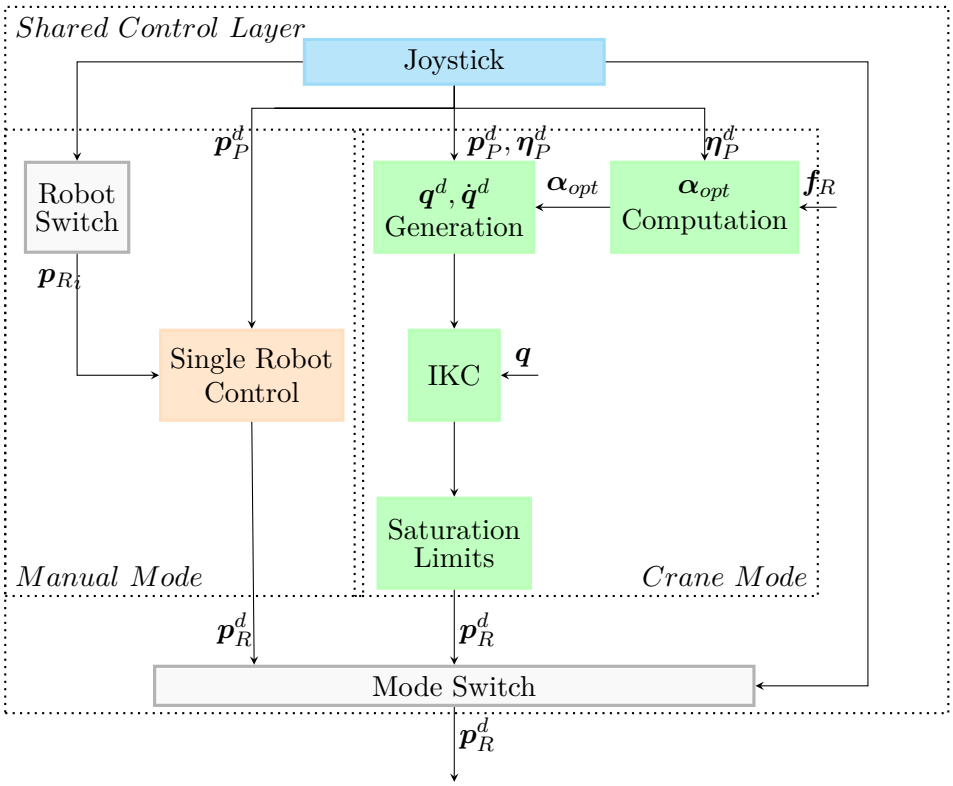

Figure 7.2: Shared Control Strategy for the G-Fly-Crane system.

Solving (7.2), the local planner sorts out the redundancy such that the effort among all the robots $J_1(\boldsymbol{q})$ results to be balanced while the manipulability index $J_2(\boldsymbol{q})$ results maximized. The effort distribution among the robots depends on the position of the CoM of the platform which, in this first proof of concept, has been assumed constant during the pick-and-place operations.

7.1.2 Manual Mode

If the operators choose the manual modality, they can command the position of the aerial vehicles in two different ways. The desired velocities are always sent through the joystick and, they are then integrated to obtain the desired positions. The first sub-mode consists of controlling all the robots as a rigid body such that $\boldsymbol{v}_{R1} = \boldsymbol{v}_{R2} = \boldsymbol{v}_{R3} = \boldsymbol{v}_R$. This approach has been largely used for take off and landing operations. By contrary, the second sub-mode allows to have control of one robot at a time independently from the others. This solution can be particularly suited in case of emergencies.

7.2 Experiments

Two experiments have been performed in an indoor scenario, to demonstrate and validate the pick-and-place and manipulation capabilities of the G-Fly-Crane. Here, the construction of a wall (Exp-1), with bricks in-house made, and its decommissioning (Exp-2) are proposed to emulate a possible outdoor assembly task. Initially, the wall is incomplete. The two missing bricks are located in a random position on the ground. In Exp-1, the aim is to finalize the wall. The first missing brick has to be positioned on a lying flat surface, whereas the other has to be placed on a tilted surface. The second assignment requires 6D (position and orientation) manipulation capabilities and, it satisfactorily mimics possible unevenness of the ground. In these experiments, the G-Fly-Crane is operated by a single person via a Logitech F310 gamepad, supported by the presented shared-control strategy. A video of the salient moments is provided as supplementary material (see [**video-3**]) and Figure 7.5 shows the different phases of the experiment which can be summarized in the following stages:

1) *Take-off*: the user commands the vertical position of the robots in manual mode to lift the platform;

2-4) *Pick-and-place brick-1*: the user commands the position of the platform in *crane mode* placing the platform on top of the brick and triggering the magnetic gripper. Subsequently, the user commands the G-Fly-Crane to lift the brick, bring it to the target position, and place it on the wall.

5-8) *Pick-and-place brick-2*: operations 2-4 are repeated to pick-and-place the second brick. However, the second brick needs a preliminary manipulation to be placed on a tilted wall. Therefore, before placing the brick, when the platform is above the target position, the operator regulates the platform orientation such that the brick is parallel to the wall slope.

9-10) *Landing*: finally, the G-Fly-Crane is driven to its initial position for landing in manual mode.

Considering the more challenging pick-and-place operation of brick-2, Fig. 7.3 shows the position tracking of the G-Fly-Crane during the phases 5, 6, 7, and 8 starting at time $t_5 = 175\,[\text{s}]$, $t_6 = 195\,[\text{s}]$, $t_7 = 205\,[\text{s}]$, $t_8 = 250\,[\text{s}]$. Brick-2 is successfully placed on the wall at time $t = 285\,[\text{s}]$. Notice that during the pick operation (phase-5), the position error along $\boldsymbol{z}_W$ increases. The cause is related to the fact that the user has to command the desired platform position such that it slightly enters the brick. The natural compliance of the cables results crucial in this operation. Thus, the brick can be gently grasped. In addition, during the lifting phase of the brick (phase-6) the position error along $\boldsymbol{z}_W$ increases. The effect is given by the additional mass of the brick that each robot's position controller compensates through the integral action. In fact, after a few seconds (around $t = 225\,[\text{s}]$), the error returns to zero. The tracking of the desired trajectory for the

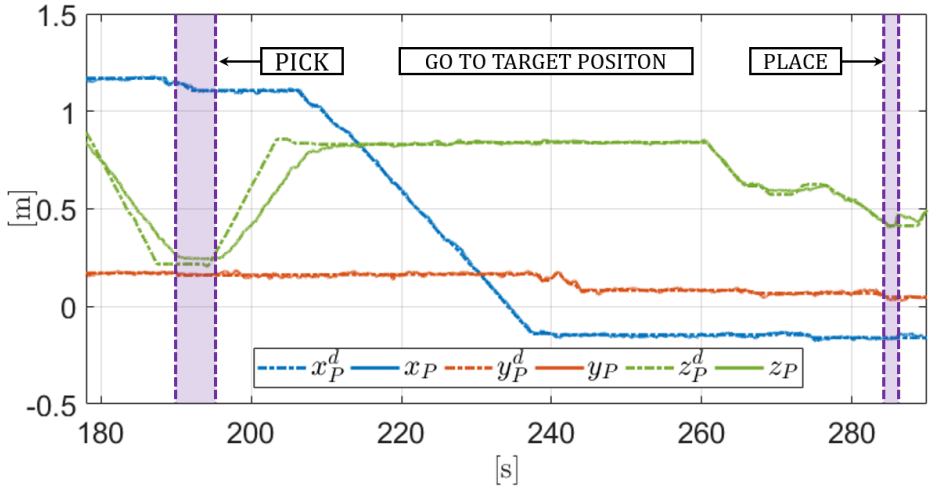

Figure 7.3: Position Tracking for the operation of pick-and-place for the second brick.

	$\boldsymbol{e}_{\boldsymbol{p}_P}$ [m]	$\boldsymbol{e}_{\boldsymbol{\eta}_P}$ [Deg]	$\boldsymbol{e}_{\boldsymbol{\alpha}}$ [Deg]
Mean	0.026	0.2	0.7
Variance	0.078	1.2	2.8

Table 7.1: Mean and variance of the norm of the position, attitude and cable angles errors

attitude and $\boldsymbol{\alpha}$ angles are shown in Fig. 7.4. Defining the position, attitude and cable angles errors as $\boldsymbol{e}_{\boldsymbol{p}_P} = \boldsymbol{p}_P^d - \boldsymbol{p}_P$, $\boldsymbol{e}_{\boldsymbol{\eta}_P} = \boldsymbol{\eta}_P^d - \boldsymbol{\eta}_P$ and $\boldsymbol{e}_{\boldsymbol{\alpha}} = \boldsymbol{\alpha}^d - \boldsymbol{\alpha}$, the mean and variance of the norm of $\boldsymbol{e}_{\boldsymbol{p}_P}$, $\boldsymbol{e}_{\boldsymbol{\eta}_P}$ and $\boldsymbol{e}_{\boldsymbol{\alpha}}$ have been reported in Tab. 7.1 .

Moreover, Figure 7.4 shows the extra thrust for each robot, $\tilde{\boldsymbol{f}}_{Rij}$, defined as the difference between the total thrust and the amount of thrust needed by each robot to hover the platform without the load. Thanks to the local optimization of the angles $\boldsymbol{\alpha}$, each robot thrust value remains close to the other ones, indicating a good effort balance among the quadrotors. Therefore, the robots show a similar energy consumption.

At $t = 270$ [s], during phase-8, the brick is located over the wall surface. Interestingly, as shown in the third row of Fig. 7.4, the extra thrust for each quadrotor has a sudden decrease because the weight of the brick is temporarily compensated by the contact with the wall. It is worth mentioning that the overall system stability is maintained by the ability of the operator to perform the task through its visual feedback.

Additionally, we performed a second experiment further showing the manipulation capabilities of the G-Fly-Crane. This test emulates a structure decommissioning where bricks have to be removed from the inclined wall. As in the first experiment, the operator takes off and drives the G-Fly-Crane on top of the target brick. Before descending to perform the pick, the pilot steers the platform to reach

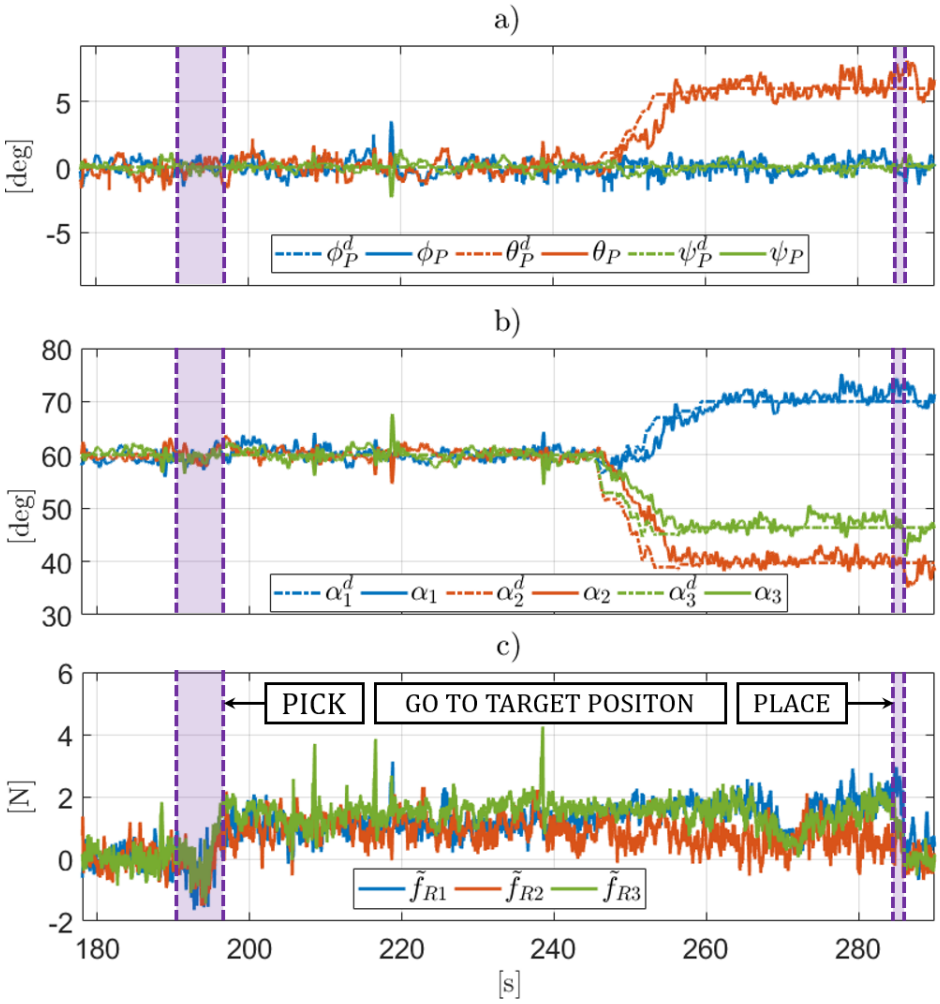

Figure 7.4: Tracking of the desired trajectory for the attitude and α angles and comparing with the extra thrust.

an orientation in accordance with the inclination of the brick. The brick can be then removed from the wall in a safe and accurate way, thanks to the dexterity provided by the G-Fly-Crane.

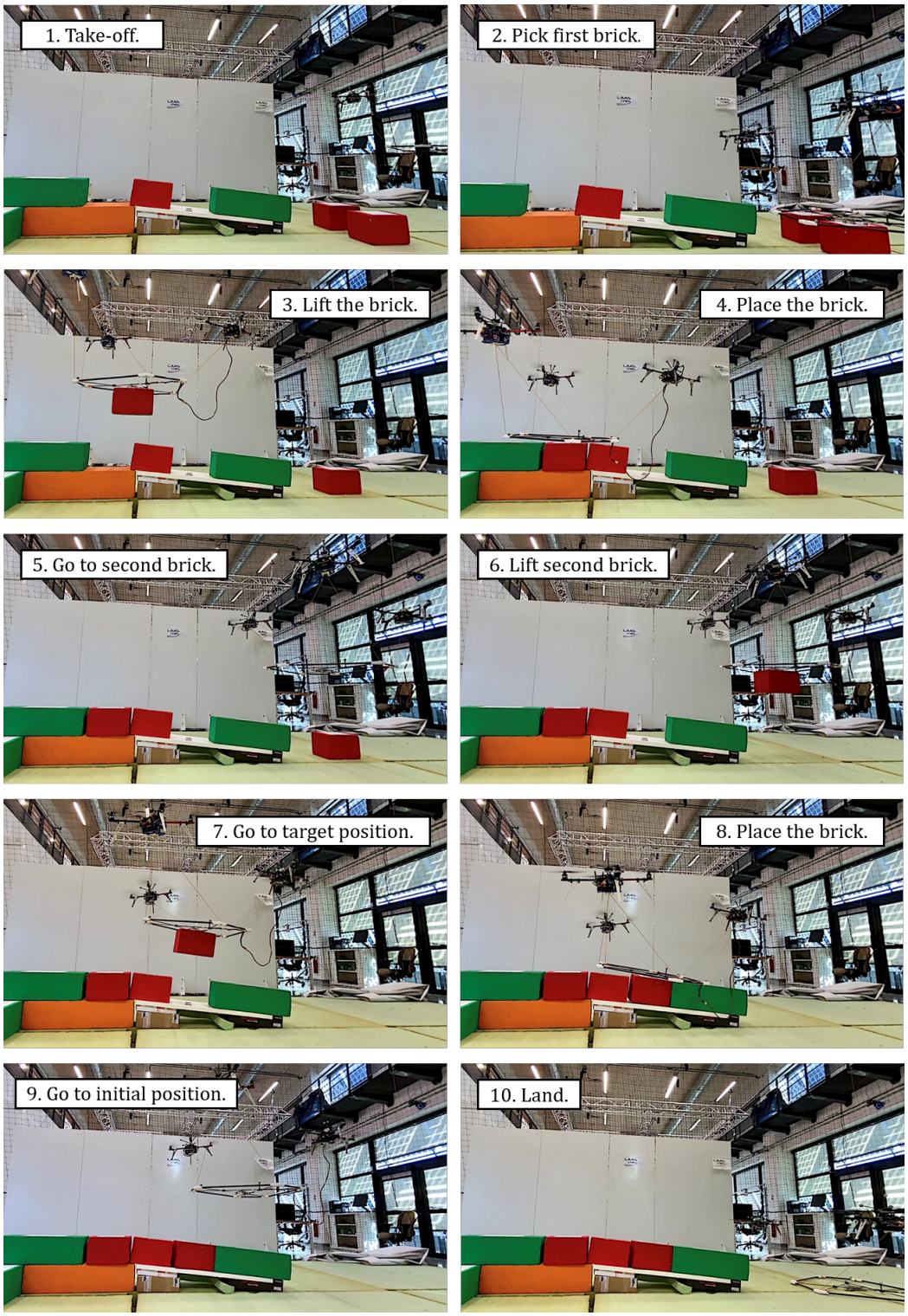

Figure 7.5: Snapshots of the wall construction task with the G-Fly-Crane, illustrating the different phases.

Chapter 8

From motion control to interaction control of the Fly-Crane System

In the previous chapter, we have presented and validated a shared control strategy to accomplish *in-contact* assignments with the presence of a human operator as a supervisor of the task. In line with the aim of Part. II of this manuscript, the proposed technique supposes that the cooperative manipulations take place while the system is physically touching the surrounding environment. For example, this could mean that the multi-robot aerial manipulator collaborates with another robot or human, or more in general, interacts with another physical body. However, in that case, the fulfillment of the operations strictly depended on the human who controlled the multi-robot system.

Conversely, if self-regulatory behaviors are desired when the multi-robot systems perform *in-contact* assignments, they have to be made capable of managing the interactions, especially in the presence of rigid, non-deformable environments.

In light of these considerations, this chapter will be devoted to address such scenarios, presenting the theoretical control framework through which we have shaped the behavior of the CS-AMRM under exam, the Fly-Crane. Then, the validation of such methodologies will be presented, outlining a use-case scenario.

Before diving into the details of the employed technique, differently from *contact-free* circumstances, it has to be recalled that, this time, the contribution of the external wrench cannot be neglected and therefore, it has to be taken into account to accurately describe the platform model. The result of neglecting this contribution would bring the system to instability. Therefore, recalling Eq. (4.1), $\boldsymbol{f}_e$ and ${}^P\boldsymbol{\tau}_e$ will be considered different than zero. Moreover, in most cases, the physical interaction between the multi-robot system and the external source takes place in specific points. In our case, without loss of generality, we persist in considering the whole platform of the Fly-Crane our physical interaction tool and our contact point with the environment.

Once the external wrench has been considered in the model, two additional steps are needed to complete the definition of the control framework. First, such a wrench has to be suitably measured or estimated. Secondly, the Fly-Crane motion controller requires an improvement to ensure a compliant behavior of the system. For the first step, a monitoring method based on the generalized momentum has been selected (see Sec. 8.1). For the second step, we made use of an admittance

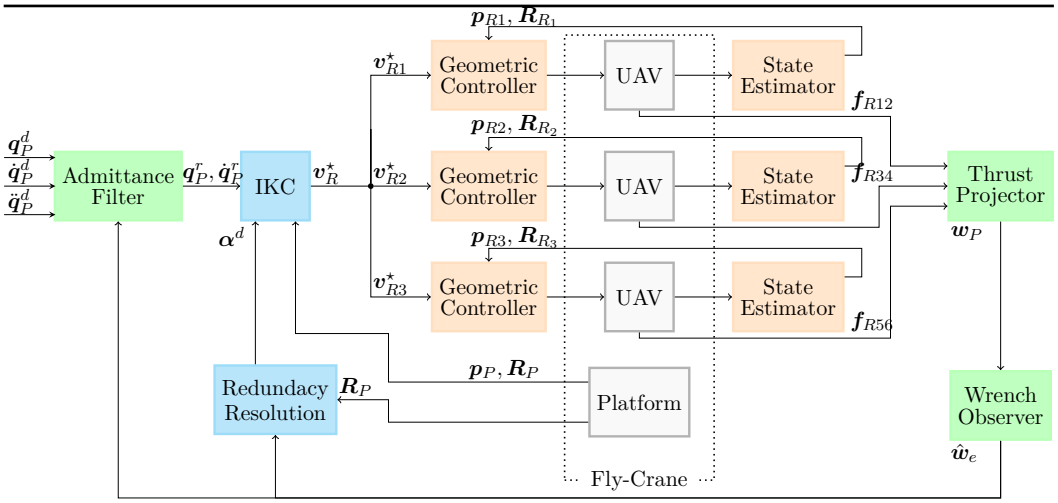

Figure 8.1: Control architecture of the admittance framework of the Fly-Crane system. The *outer loop* has been highlighted in green, the *intermediate loop* in blue, and the *inner loop* in red.

control paradigm (see Sec. 8.2). Under this condition, the platform of the Fly-Crane can be described as a mass-spring-damper system whose parameters can be suitably tuned according to the requested behavior. In particular, the method allows to impose a deviation from the desired motion as a reaction to interaction forces and moments. Therefore, the CS-AMRM will follow the trajectory which comes from the admittance filter rather than tracking the reference coming from a motion planner. In such a way, all the external actions acting on the multi-robot system can be considered with sufficient accuracy. A scheme of the proposed control architecture is depicted in Fig. 8.1. In detail, building on top of the already presented motion IKC controller, an outer loop has been added. A summary of the three nested loops is depicted in the following:

1. The *outer control loop* takes care of the interaction task by generating compliant system trajectories based on the external wrenches acting on the platform;

2. The *intermediate control loop* is a centralized controller that produces the velocity reference for each aerial vehicle given the desired platform pose. At this level, the redundancy of the Fly-Crane w.r.t. the 6D positioning task, is exploited to balance the robot efforts;

3. The *inner control loop* running on each aerial vehicle is a position controller computing the motors commands given the desired robot trajectory.

8.1 Generalized Momentum Based Estimation

Interactions knowledge is fundamental when a robot moves in cluttered environments. The direction and the intensity of the interaction forces are particularly

relevant. Force-torque sensors could be integrated into the architectures to measure such quantities. However, their main limitation of providing only local information makes them deficient with wide-ranging end-effectors. As a consequence, a monitoring method, based on the generalized momentum [Haddadin 2017], has been considered. In this way, collision detection and collision identification can be always guaranteed at any platform point providing sufficiently accurate estimations. Additionally, the generalized momentum method represents a less expensive solution that avoids the need of equipping the aerial manipulator with additional weight. Following the approach introduced in [De Luca 2005] for robotic manipulators, let us define the generalized momentum of the platform $\boldsymbol{p} \in \mathbb{R}^6$

$$\boldsymbol{p} = \boldsymbol{M}_P(\boldsymbol{q}_P)\dot{\boldsymbol{q}}_P, \tag{8.1}$$

where $\boldsymbol{q}_P = [\boldsymbol{p}_P^\top \ \boldsymbol{\eta}_P^\top]^\top$ and $\dot{\boldsymbol{q}}_P = [\dot{\boldsymbol{p}}_P^\top \ \dot{\boldsymbol{\eta}}_P^\top]^\top$ are the configuration of the platform and its derivative. From ((4.1)), the time evolution of $\boldsymbol{p}$ can be written as

$$\dot{\boldsymbol{p}} = \boldsymbol{\tau}_m + \dot{\boldsymbol{M}}_P(\boldsymbol{q}_P)\dot{\boldsymbol{q}}_P - \boldsymbol{C}_P(\boldsymbol{q}_P, \dot{\boldsymbol{q}}_P)\dot{\boldsymbol{q}}_P - \boldsymbol{g}_P(\boldsymbol{q}_P), \tag{8.2}$$

where $\boldsymbol{\tau}_m = \boldsymbol{w}_P + \boldsymbol{w}_e \in \mathbb{R}^6$ represents the total wrench applied on the platform and it is the sum of the active force and torques, $\boldsymbol{w}_P \in \mathbb{R}^6$, and the external wrenches, $\boldsymbol{w}_e = [\boldsymbol{f}_e{}^\top \ {}^P\boldsymbol{\tau}_e{}^\top]^\top \in \mathbb{R}^6$. Subsequently, the momentum observer dynamics derived from 8.2 is

$$\begin{array}{rl} \dot{\hat{\boldsymbol{p}}} = & \boldsymbol{w}_P - \boldsymbol{C}_P^\top(\boldsymbol{q}_P, \dot{\boldsymbol{q}}_P)\dot{\boldsymbol{q}}_P - \boldsymbol{g}(\boldsymbol{q}_P) + \hat{\boldsymbol{w}}_e \\ \dot{\hat{\boldsymbol{w}}}_e = & \boldsymbol{K}_O(\dot{\boldsymbol{p}} - \dot{\hat{\boldsymbol{p}}}) \end{array}, \tag{8.3}$$

where the property $\dot{\boldsymbol{M}}_P(\boldsymbol{q}_P) = \boldsymbol{C}_P(\boldsymbol{q}_P, \dot{\boldsymbol{q}}_P) + \boldsymbol{C}_P^\top(\boldsymbol{q}_P, \dot{\boldsymbol{q}}_P)$ has been used and $\boldsymbol{K}_O = diag\{k_O\} > 0 \in \mathbb{R}^{6\times 6}$ is the diagonal observer gain matrix. For the sake of compactness, let us write $\boldsymbol{\beta}_P = \boldsymbol{C}_P(\boldsymbol{q}_P, \dot{\boldsymbol{q}}_P)\dot{\boldsymbol{q}}_P + \boldsymbol{g}(\boldsymbol{q}_P)$. The signal $\hat{\boldsymbol{w}}_e(t)$, which represents the estimated external disturbance, is obtained integrating (8.3) as follow

$$\hat{\boldsymbol{w}}_e = \boldsymbol{K}_O\Big(\boldsymbol{p}(t) - \int_{t_0}^{t} \dot{\hat{\boldsymbol{p}}}(s)ds - \boldsymbol{p}(0)\Big) \tag{8.4}$$

$$= \boldsymbol{K}_O\Big(\boldsymbol{p}(t) - \int_{t_0}^{t} (\boldsymbol{w}_P - \boldsymbol{\beta}_P + \hat{\boldsymbol{w}}_e)ds - \boldsymbol{p}(0)\Big), \tag{8.5}$$

where t and t_0 are the current and initial time instant. In ideal conditions, the residual vector $\hat{\boldsymbol{w}}_e$ can be seen as a virtual sensor for external wrenches acting on a rigid body. As a matter of fact, the relation between $\boldsymbol{w}_e$ and $\hat{\boldsymbol{w}}_e$ is

$$\dot{\hat{\boldsymbol{w}}}_e = \boldsymbol{K}_O(\boldsymbol{w}_e - \hat{\boldsymbol{w}}_e), \tag{8.6}$$

and represents a first-order low-pass filter with the property that $\hat{\boldsymbol{w}}_e \to \boldsymbol{w}_e$ when $t \to \infty$ and $\hat{\boldsymbol{w}}_e \simeq \boldsymbol{w}_e$ when $\boldsymbol{K}_O \simeq \infty$.

8.2 Admittance filter

To handle the physical interactions and make the platform of the Fly-Crane compliant to interaction wrenches with the environment, we choose the admittance control framework over the impedance one. This choice is grounded on the fact that the admittance controller shows better performances for trajectory tracking in free space and disturbance rejection [Villani 2016]. Specifically, the framework possesses the characteristic of generating system motion variables from force measurements. In our particular case, given a platform desired trajectory $\boldsymbol{q}_P^d = [\boldsymbol{p}_P^{d\top} \ \boldsymbol{\eta}_P^{d\top}]^\top$, a platform desired velocity $\dot{\boldsymbol{q}}_P^d = [\dot{\boldsymbol{p}}_P^{d\top} \ \dot{\boldsymbol{\eta}}_P^\top]^\top$ and a platform desired acceleration $\ddot{\boldsymbol{q}}_P^d = [\ddot{\boldsymbol{p}}_P^{d\top} \ \ddot{\boldsymbol{\eta}}_P^{d\top}]^\top$, the set of references $(\boldsymbol{q}_P^r, \dot{\boldsymbol{q}}_P^r, \ddot{\boldsymbol{q}}_P^r)$ are generated and provided to the Fly-Crane inverse kinematic motion controller by taking into account the effect of the external disturbances $\hat{\boldsymbol{w}}_e$. The reference set can be conceived such that the controlled platform behaves similarly to an admittance model characterized by the following equation

$$\boldsymbol{M}_A(\ddot{\boldsymbol{q}}_P^d - \ddot{\boldsymbol{q}}_P^r) + \boldsymbol{D}_A(\dot{\boldsymbol{q}}_P^d - \dot{\boldsymbol{q}}_P^r) + \boldsymbol{K}_A(\boldsymbol{q}_P^d - \boldsymbol{q}_P^r) = \hat{\boldsymbol{w}}_e \tag{8.7}$$

where $\boldsymbol{M}_A = diag\{M_A\} \in \mathbb{R}^{6\times6}_{>0}$, $\boldsymbol{D}_A = diag\{d_A\} \in \mathbb{R}^{6\times6}_{>0}$ and $\boldsymbol{K}_A = diag\{K_A\} \in \mathbb{R}^{6\times6}_{>0}$ are matrices representing the desired (apparent) inertia, damping and stiffness, and

$$\boldsymbol{q}_P^d - \boldsymbol{q}_P^r = \begin{bmatrix} \boldsymbol{p}_P^d - \boldsymbol{p}_P^r \\ \frac{1}{2}(\boldsymbol{R}_P^d \boldsymbol{R}_P^{r\top} - \boldsymbol{R}_P^r \boldsymbol{R}_P^{d\top})^\vee \end{bmatrix} \tag{8.8}$$

where the operator $[\cdot]^\vee$ represents the mapping from $SO(3)$ to $\mathbb{R}^3$. Regarding the stability of the overall system, the bandwidth of the admittance controller has to be lower than the equivalent bandwidth of the inverse kinematic motion control loop. The parameter matrices $\boldsymbol{K}_A$, $\boldsymbol{D}_A$, $\boldsymbol{M}_A$ in (Eq. 8.7) can be modified to shape the admittance filter physical properties. As a result, the behavior of the mass-spring-damper system can be tuned at will and consequently, the desired behavior can be changed according to the particular task to be accomplished. In the following, we shall show the different responses that we obtained modulating such parameters in the validation of our system.

8.3 Validation of the interaction framework

In this section, we present the experimental results that show the effectiveness of the presented control framework. First, we highlight the variety of behaviors that the system is capable of performing changing the physical properties of the admittance filter in Sec. 8.3.1. Then, we test the multi-robot aerial manipulator system in a *unexpected-collision* scenario, confirming its suitability in executing tasks while being in contact with the environment (see Sec. 8.3.2). The interested reader can watch the attached video to see the system in action [**video-4**].

8.3.1 Admittance Shaping

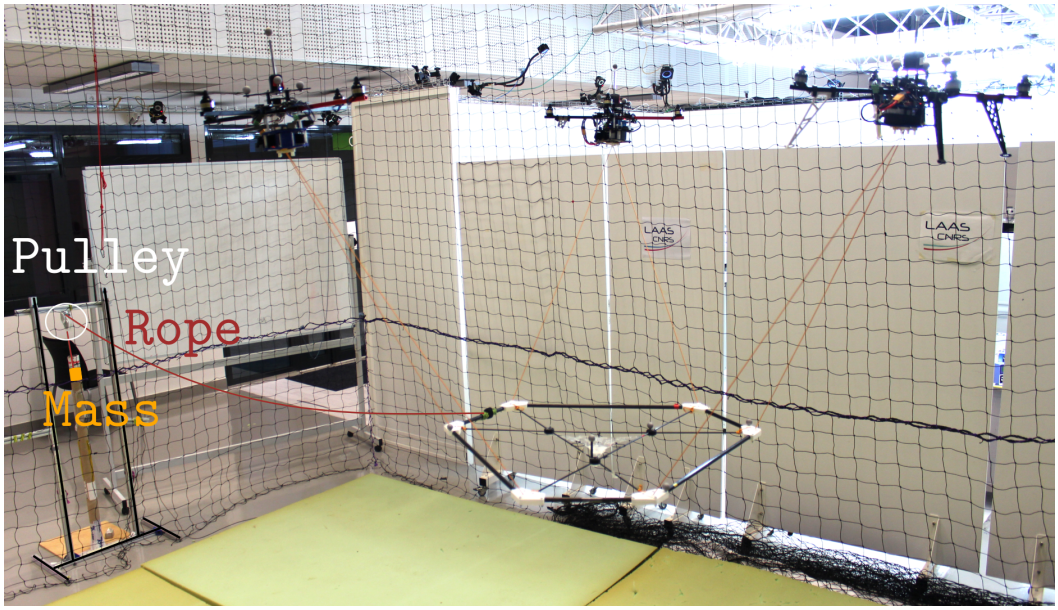

Figure 8.2

Figure 8.3: The pulley-cable system which has been employed for the admittance property shaping;

This section illustrates the different behaviors obtained in the step response of the system when changing the admittance parameters.

In all the experiments, the equilibrium pose for the platform, in absence of external disturbances, is $\boldsymbol{p}_P^d = [0\ 0\ 1.28]^\top$ [m] and $\boldsymbol{R}_P^d = \boldsymbol{I}_3$. Two sets of experiments are presented: *Set-1* (Fig. 8.4d–8.4f) and *Set-2* (Fig. 8.4g–8.4i).

- *Set-1*: at the equilibrium pose and in absence of external force, a constant virtual external force of $f_{n,x} = -1.7$ [N] is suddenly applied along $\boldsymbol{x}_W$, as shown in dashed lines in Fig. 8.4a-8.4c.
- *Set-2*: at the equilibrium pose and in absence of external force, a real external force is suddenly applied along $\boldsymbol{x}_W$ using a weight suspended by a pulley-cable system. The reached final force depends only on the weight of the mass and it is about -1.7 [N] (see Fig. 8.2) for the case in exam. However, the system is unaware of the mass amount, and the force is estimated using the wrench observer described in (8.6). The behavior through the different experiments is shown in Fig. 8.4a-8.4c in solid lines. In the practical realization, a constant bias in $\hat{\boldsymbol{w}}_e$ has been noticed. We believe that this is caused by modeling errors in the aerial vehicles and platform manufacturing, as well as model uncertainties like rotors and cables models. To mitigate the effect of the bias, a simple calibration is done in order to compensate for the steady-state error at rest.

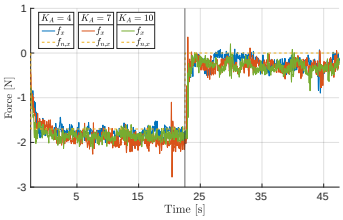

(a) Stiffness tests: virtual and estimated force.

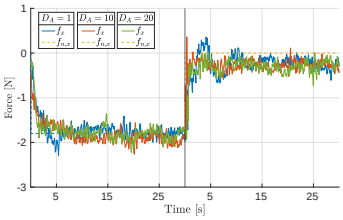

(b) Damping tests: virtual and estimated force.

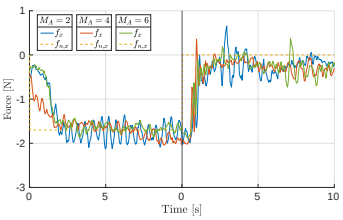

(c) Inertia tests: virtual and estimated force.

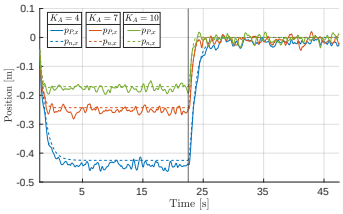

(d) Stiffness tests with perfectly known force: nominal and real position.

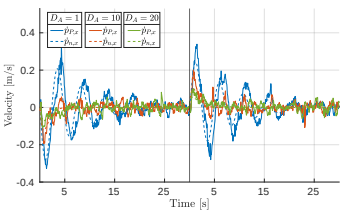

(e) Damping tests with perfectly known force: nominal and real velocity.

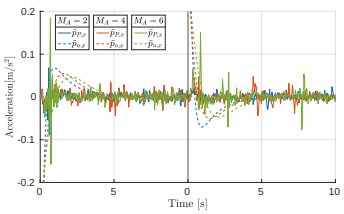

(f) Inertia tests with perfectly known force: nominal and real acceleration.

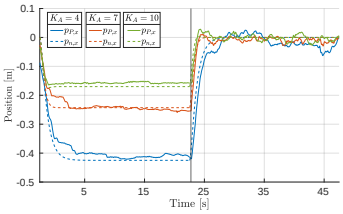

(g) Stiffness tests with estimated force: nominal and real position.

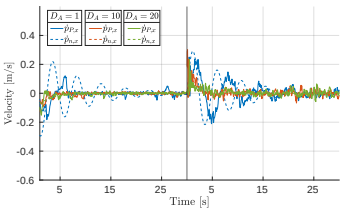

(h) Damping tests with estimated force: nominal and real velocity.

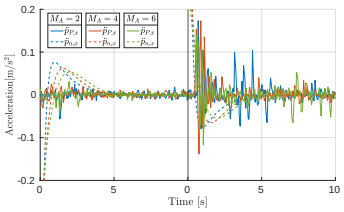

(i) Inertia tests with estimated force: nominal and real acceleration.

Figure 8.4: Admittance Shaping step responses: The graphs show two phases: on the left of the black line we apply the constant force (charging phase), right after the black line the constant force is removed (discharging phase). Since the force has only been applied along $\boldsymbol{x}_W$, we show the first component of the position/velocity/acceleration vector (solid lines). We make the comparison with the ideal mass-spring-damper system (dashed lines) to underline the admittance shaping capability. In Fig. 8.4d the stiffness $\boldsymbol{K}_A$ has been changed, obtaining three different steady-state positions. On the contrary, in Fig. 8.4e the $\boldsymbol{D}_A$ has been the subject of the variation. Fig. 8.4f shows the effects of changing the virtual mass $\boldsymbol{M}_A$.

Testing the system both with a virtual disturbance (perfectly known) and a real force estimated through the wrench observer, let us assess the impact of the wrench observer and other non-modeled effects, such as, the friction of the pulley, on the entire closed loop architecture. The three parameters $\boldsymbol{M}_A$, $\boldsymbol{D}_A$, $\boldsymbol{K}_A$, which define the virtual admittance, have been individually manipulated in the different experiments. Additionally, to make further comparisons, we also show the nominal output

of an ideal mass-spring- damper system with the same characteristic and subjected to the same external input. As reference values, we have chosen $\boldsymbol{M}_A = 4\boldsymbol{I}_3$ [Kg], $\boldsymbol{D}_A = 10\boldsymbol{I}_3$ [Ns/m], $\boldsymbol{K}_A = 7\boldsymbol{I}_3$ [N/m] and all the other values have been generated by increasing or decreasing such values by suitable deltas. In the first set of comparisons, see Fig. 8.4d and Fig. 8.4g, the focus is on the stiffness constant $\boldsymbol{K}_A$. We purposefully select $\boldsymbol{K}_A = 4\boldsymbol{I}_3$ [N/m] and $\boldsymbol{K}_A = 10\boldsymbol{I}_3$ [N/m]. The behavior of the system when the external force is both applied (charging phase) and removed (discharging phase), are shown in the graphs in their left and right halves, respectively. The admittance scheme performs suitably at steady-state, where the position of the platform remains close to the nominal one according to the corresponding stiffness value. The maximum error ($e_{P_x} = p_{n,x} - p_{P,x}$) between the nominal position and the actual one does not exceed 0.01 [m]. As expected, three different steady-state positions, -0.1 [m], -0.2 [m], -0.4 [m], have been obtained during the experimental campaign as a consequence of three different stiffness values. On the other side, in the transient of the charging phase of *Set-2*, the filtering action of the wrench observer has a non-negligible role in slowing down the reactivity of the system, as it can be clearly seen comparing Fig. 8.4g with Fig. 8.4d.

The second set of comparisons, Fig. 8.4e and Fig. 8.4h, shows the effects of the damping constant variation. The chosen values for the comparison are $\boldsymbol{D}_A = 1\boldsymbol{I}_3$ [Ns/m] and $\boldsymbol{D}_A = 20\boldsymbol{I}_3$ [Ns/m]. Moreover, the nominal velocity reference $\dot{\boldsymbol{p}}_n$ of the ideal mass-spring-damper system and the actual platform velocity $\dot{\boldsymbol{p}}_P$ have been examined side by side. Two major behaviors can be extrapolated from the observation of the graphs. At first, in *Set-2* (Fig. 8.4h), the ideal mass-spring-damper system is better emulated during the discharging phase rather than the charging one. Unavoidable sticky-slips effects and friction in the pulley-cable significantly affect the natural evolution of the system. As a matter of fact, they do not arise during the discharging phase. Secondly, there is a small tracking delay of $\dot{\boldsymbol{p}}_P$ with respect to $\dot{\boldsymbol{p}}_n$ which is much more accentuated in *Set-2* when $\boldsymbol{D}_A = 1\boldsymbol{I}_3$ [Ns/m]. This latter result is a direct consequence of using the wrench estimator. No differences can be appreciated in the reached steady-state value of the position ($\simeq$-0.2 [m], not shown in the plots), which remains unchanged in all three cases.

The last experimental tests, Fig. 8.4f and Fig. 8.4i, let us understand the effects of the variations of the virtual inertia from the reference value $\boldsymbol{M}_A = 4\boldsymbol{I}_3$ [Kg]. In both of the examined cases, results show the impossibility for the system to satisfactorily shape the inertia, i.e., to track the ideal acceleration output corresponding to different virtual inertias. Several plausible reasons can be given. A good tracking of the virtual mass requires a very precise and theoretically instantaneous control of the thrust, which is impossible in our setup since the thrust is indirectly controlled through the rotor speeds, which are also subject to their own first order dynamics. On the other hand, the developed IKC controller is designed for tracking velocities rather than accelerations, and in general the controller is purely based on feedback and it lacks of the proper feedforward term that is required to compensate for the inertial dynamics. A precise knowledge of such term is indeed very difficult to be

obtained in practice.

8.3.2 Unexpected-collision interaction

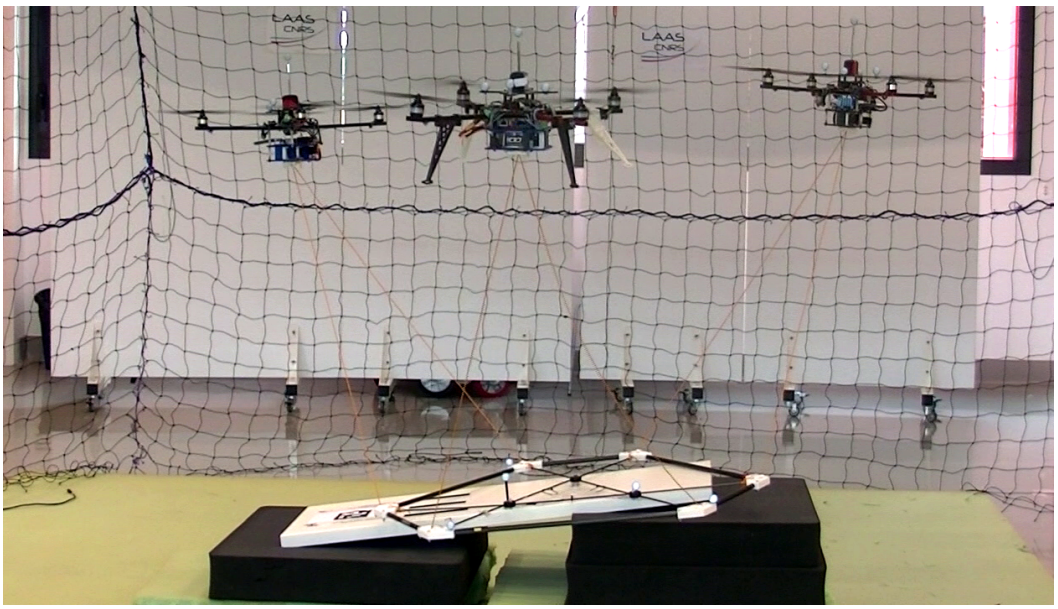

Figure 8.5: The figure shows the real-case scenario where the Fly-Crane has to approach a tilted surface being compliant with it.

This experiment is designed to test the capability of the proposed aerial manipulation system to react stably to unexpected collisions and to adapt its behavior to such interactions. Additionally, the experiments also test the capabilities of the three aerial vehicles to maintain the cables' tightness despite the contacts. To this end, a surface is placed in the middle of the arena, obstructing the way to the platform. The center of the surface is positioned at $[-1.55\ 0\ 0.50]$[m] and its inclination about $\boldsymbol{x}_W$ is 8 [deg] (see Fig. 8.5). The admittance parameters have been set as follows: $\boldsymbol{K}_{A\boldsymbol{p}} = 15\boldsymbol{I}_3$ [N/m] $\boldsymbol{D}_{A\boldsymbol{p}} = 50\boldsymbol{I}_3$ [Ns/m], $\boldsymbol{K}_{A\boldsymbol{\eta}} = 2\boldsymbol{I}_3$ [N/rad], $\boldsymbol{D}_{A\boldsymbol{\eta}} = 14\boldsymbol{I}_3$ [Ns/rad], $\boldsymbol{M}_{A\boldsymbol{p}} = 2\boldsymbol{I}_3$ [Kg] and $\boldsymbol{M}_{A\boldsymbol{\eta}} = 20\boldsymbol{I}_3$ [Kgm^2]. The experiment starts with the platform positioned at $\boldsymbol{p}_P = [-1.55\ 0\ -0.55]$[m], followed by a descending phase toward $\boldsymbol{p}_P^d = [-1.55\ 0\ -0.43]$[m]. On its way, the platform collides with the surface. Figures 8.6 and 8.7 present the crucial phases of the experiments, where the area in which contacts occur has been highlighted in green. Figure 8.6a shows the z components of the platform position, the desired trajectory, and the reference generated by the admittance filter. It can be appreciated how the admittance filter lets the reference deviate from the desired trajectory during the contact phase, thus indirectly keeping the pushing force limited in the direction of motion. In Fig. 8.6b, we illustrate the position error $\boldsymbol{e}_{\boldsymbol{p}_P} = \boldsymbol{p}_P^r - \boldsymbol{p}_P$ between the reference trajectory and the actual position of the robot. The norm $||\boldsymbol{e}_{\boldsymbol{p}_P}||$ stays bounded around ± 4 [cm] in position during the experiment assuring, in such a way,

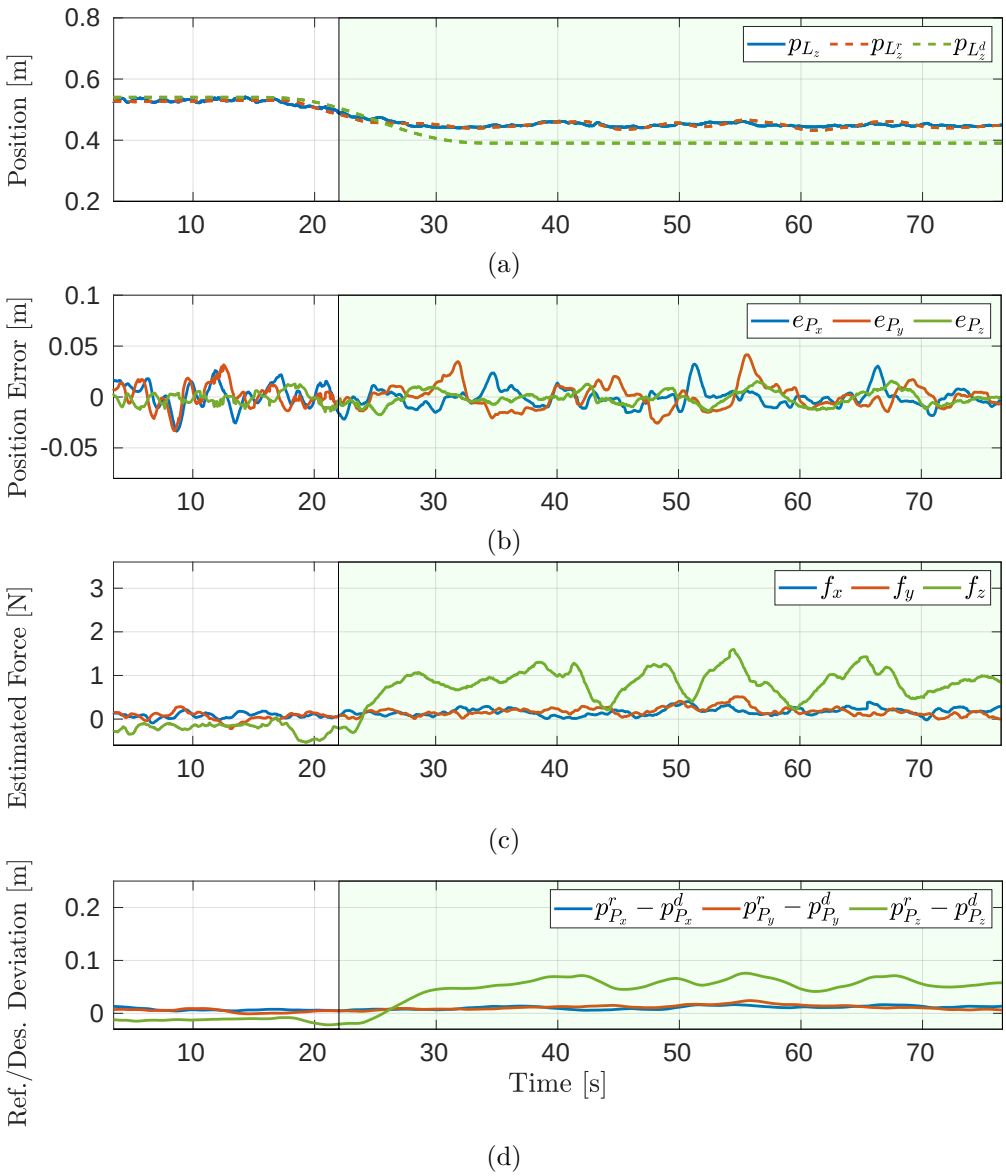

Figure 8.6: Unexpected-collision interaction: positional and force signals.

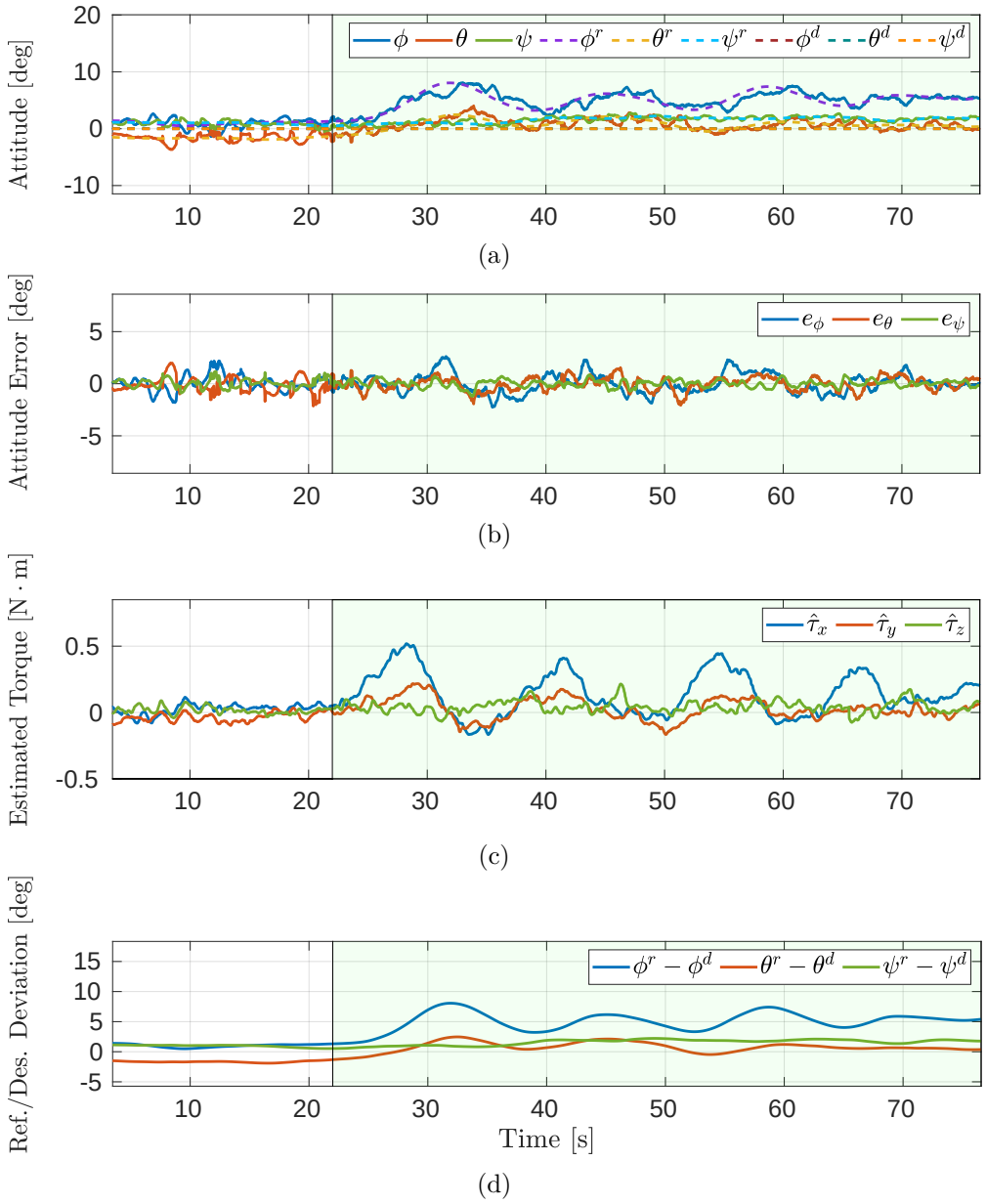

Figure 8.7: Unexpected-collision interaction: angular and moment signals.

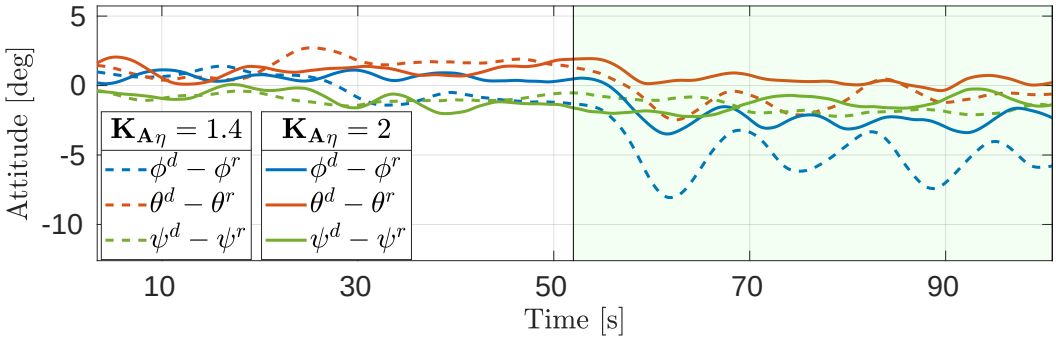

Figure 8.8: The effect of changing the rotational stiffness about $\boldsymbol{x}_W$ between two experiments.

good position tracking. With Fig. 8.6c, we show the first three components of $\hat{\boldsymbol{w}}_e$, namely the forces resulting from the external wrench estimation. In this graph, the contact, happening at 140[s], is fully recognizable in f_z, as expected.

Figures 8.7a and 8.7b present similar plots for the orientational coordinates. The desired orientation changes from $\boldsymbol{\eta}_P = [0\ 0\ 0]$[deg] to $\boldsymbol{\eta}_P \approx [-8\ 0\ 0]$[deg] as a consequence of a non-zero estimated torque. In this variation, the norm of the orientation error $||\boldsymbol{e}_{\boldsymbol{R}_P}||$ holds at 2 [deg] which therefore allows to affirm that a reliable orientation tracking has been achieved despite the already discussed delay introduced by the wrench observer. The estimated torque experienced by the platform is shown in Fig. 8.7c and the orientation error between the pre-planned trajectory and the trajectory produced by the admittance filter is presented in Fig. 8.7d. Similarly to the translation case, during the contact phase, the multi-robot system is capable of adapting the platform orientation with considerable accuracy.

The experiment has been conducted again choosing $\boldsymbol{K}_{A\boldsymbol{\eta}} = \text{diag}(1.4, 2, 2)$ [N/rad], thus changing the rotational compliance of the platform about $\boldsymbol{x}_W$. Figure 8.8, shows the difference of the attitude behavior between the previous experiment with larger stiffness (dotted lines) and the last one (dashed lines) in which the platform results more compliant. The added compliance allows the platform to lean completely against the tilted surface.

To conclude, the goal of all the previous experiments was to assess the well-thought selection of methods that allowed us to solve the aforementioned problems for the control of the Fly-Crane while physically interacting with the environment. Aware that the employed algorithms are well known in the robotics community, especially in the context of ground manipulators, the challenge has been to endow the particular CS-AMRM under exam with such techniques facing all the possible obstacles that we could encounter. In particular, we showed the reliability of the selected monitoring method for estimating the external disturbances, the capabilities of the admittance filter to preserve the stability despite the contacts with the environment, and finally, we evaluated the ability of the aerial vehicles to maintain the cables' tightness in scenarios where such property can be lost.

Part IV

Conclusions

Chapter 9

Conclusions

The methodology of using UAVs to perform physical interaction tasks has considerable potential in a broad range of scenarios. Scaling this methodology up for teams of aerial robots enables achieving an increased set of tasks. Among them, there are objects transportation and manipulation. Nevertheless, multi-robot systems introduce the additional challenge of the coordination between team members. In this thesis, with particular attention on cable-suspended transportation and manipulation, we have focused on proposing control algorithms to make possible such cooperation with the final purpose of obtaining full pose manipulations in air and in interaction with the environment.

The contribution of the thesis is a succession of control algorithms designed for different setups of multi-robot systems. The final purpose was obtaining full pose control of payloads. We both considered a decentralized and a centralized approach, with a major emphasis on the latter. The results describe the useful properties of the algorithms and their applicability for real-world applications.

In this conclusive chapter, we provide a summary of this thesis in Sec. 9.1 and a summary of the main contributions in Sec. 9.2. In Sec. 9.3, we discuss potential future extensions of this work.

9.1 Summary

9.1.1 Modeling approaches (Chapter 4)

First we introduced a generic dynamical formulation of the problem of cooperative manipulation of a payload, in Sec. 4.1, defining the three main players of the scenario. The robots modeled through a double integrator model, the payload modeled as a rigid body applying the Newton-Euler formalism and the connection between the robots and the payload modeled as virtual spring-mass-damping systems. Moreover, a model has been provided when the employed tools for such connections are cables. The relevant nature of this formulation is confirmed by its applicability to a general family of systems and tools. Therefore, a wider class of possible applications can be contemplated. Moreover, it is scalable to the number of robots.

Focusing on aerial robots, we then passed to the design of the minimum setup to achieve cooperative manipulations having the six-dimensional control of the payload employing cables. It turned out to be a system composed of three robots connected to the payload by means of six cables, two for each robot. In particular, we developed a kinematic formulation which relates the velocities of the robots to the linear

and angular velocities of the payload. The advantage of reasoning at the kinematic level was that we needed to identify a smaller set of parameters. Furthermore, such parameters are related only to geometric quantities, which are easier to measure with high accuracy.

In the case the payload is used as a tool for manipulating objects - which is the case of the CS-AMRM Fly-Crane - the condition for which the CoM and the geometric CoM coincide does not always hold. Moreover, in cooperative manipulations in contact with the environment, external forces undoubtedly affect the behavior of the system. Therefore, in such cases, the knowledge of the dynamical parameters resulted beneficial for the control actions that we subsequently took. In light of this, in Sec. 4.3, we first introduced the possible displacement of the CoM in an already existent dynamical formulation of a generic manipulator. Then, we conceived a methodology to assess the intensity of the force along each cable of the Fly-Crane system. A small comparison between the two approaches, in Sec. 4.4, brings to an end the chapter.

9.1.2 Control Strategies (Chapter 5)

Subsequently to the definition of the models, we passed to the second step through the implementation in real-world case scenarios, i.e. the design of the control strategies.

Proceeding with the dichotomy between the two models, we conceived two different control approaches to accomplish the same objective of controlling the full pose of the payload.

The first one, detailed in Sec. 5.1.1, consists of a leader-follower paradigm based on the assumption that one or more robots can lead the working group. The single leader or the multiple leaders have perfect knowledge of their desired position based on the desired position of the payload. The follower robots, while damping the oscillations of the system, try to bring the sensed contact forces to the desired value. Therefore, the regulation is achieved through local communication. The payload represents the mean through which the interactions take place. The main theoretical findings show that given a null internal force, an infinite number of equilibrium configurations exists. Conversely, two equilibrium configurations can be assessed in the case of a non-null internal force. Only in the particular case that the force is the result of a pulling action, the equilibrium point is stable.

The second one, detailed in Sec. 5.1.2, addresses the problem of the cooperative manipulation in a centralized manner through a proportional inverse kinematic controller augmented with a feed-forward term. Furthermore, we demonstrate how the control gain of such controller can be designed *i)* to cope with the parametric uncertainty of the system model and ensure stability despite the non-perfect knowledge of its kinematic parameters and *ii)* to minimize the effect of external disturbances by optimizing the H_∞ performance index.

Besides, to improve the tracking performances and the energy efficiency of the system when it has to work as an aerial manipulator, we designed an observer

capable of estimating the mass and the position of the CoM of the loaded platform (see Sec. 5.1.3). In detail, we found that the necessary condition to estimate those quantities is to perform two different platform rotations. Afterwards, the online recursive least square algorithm provides assistance by filtering out possible measurement noise improving the overall estimation. The knowledge of these two dynamical quantities was then used in the control loop in order to resolve the redundancy of the system guaranteeing a similar effort provided by each robot, improving the flight autonomy and the overall tracking capabilities.

9.1.3 Validations (Chapter 6)

Numerical simulations and empirical results were presented for the full pose manipulation in contact-free scenarios of the two different control strategies presented in the previous chapters. For what concerns the first approach, given the theoretical results, the numerical analysis corroborated such findings w.r.t. the variation of the internal forces and the number of leader robots. More specifically, we showed that the payload orientation is controllable, even if the team has no leaders, while the position is not, as long as an interexchange of forces exists. Moreover, we assessed that two evenly distributed leader robots are sufficient, for a ground swarm, to control the pose of the payload to a uniquely determined value, not generating any compression or tension in the object. To accomplish the same control objective in a floating swarm, the presence of at least three leader robots is required. The analysis on the robustness of the system confirmed the important role of the internal forces in maintaining bounded attitude errors when external forces are applied to the system. The presence of no leaders or one leader does not change the capability to bound the errors (robustness). To have the robustness in some components of the object attitude with a zero internal force reference, at least two leader robots spread in the group are required for a ground swarm, while three leader robots for a floating swarm. In the case of only two leaders in a floating swarm, the error resulted not bounded when a rotation about the axis connecting the two leader robots is performed and if no internal forces are applied to the object. Ultimately, the presence of one leader robot and positive reference internal forces are enough to robustly control the position and the attitude of a ground or floating object.

In the case of the kinematic controller, we provided the empirical results designing and building the CS-AMRM under exam, i.e the Fly-Crane. The proposed framework has been tested through indoor experiments under different conditions, such as uncertainty on the cable lengths, external disturbances and high dynamic trajectories. The system guaranteed the bounds defined through the planned trajectories. In such a way, the robustness of the system has been assessed in real scenarios. Conversely, the numerical simulations performed to validate the algorithm to estimate mass and position of the CoM of the loaded platform show the accuracy of the online estimation when different platform orientations are performed during the trajectory. By using the estimation outcomes in the control loop, the gazebo simulations allowed to show that the difference between the thrusts exerted

by each robot decreased. In such a way, we could assess the realization of the energy-efficiency optimization.

9.1.4 Shared Control for the Fly-Crane System in pick-and-place operations (Chapter 7)

After having addressed the problem of cooperative manipulations in contact-free scenarios, the next step was to introduce the particular CS-AMRM under exam into the environment to execute physical interaction tasks *in-contact* conditions. In light of the complexity of the problem, we considered the human intervention opportune for safety and regulatory reasons in real-world scenarios.

Thus, we proposed a shared control strategy through which the human operators can focus on the main task rather than taking into account all the aspects of the multi-robot system. In our particular case, the core task was to control the full pose of the platform of the Fly-Crane. The objective was to demonstrate, through an experimental validation, that such a strategy represents an effective approach in construction/decommissioning scenarios.

The provided results showed two pick-and-place operations, one on a lying flat surface and the other on a tilted surface. The latter required 6D pose control of the Fly-Crane platform which has been obtained leveraging on the cooperation between the operator and the CS-AMRM.

9.1.5 Interaction control of the Fly-Crane System (Chapter 8)

The final control architecture presented in this last chapter represents an expansion of the motion controller presented for contact-free scenario. As a matter of fact, if self-regulatory behaviors are desired when the multi-robot systems perform in-contact assignments, they have to be made capable of managing the interactions, especially in the presence of rigid, non-deformable environments.

Thus, we provided a solution that deals with the interaction task by generating compliant system trajectories through an admittance filter. The external wrenches, acting on the platform, are estimated through a generalized momentum-based approach.

The proposed results first show the variety of behaviors that the system is capable of performing by changing the physical properties of the admittance filter. In particular, we illustrated that the admittance scheme suitably performs at steady-state in response to step or step-like disturbances when the stiffness constant is varied. Moreover, it presents some tracking delays when the damping is modified. These results are much more accentuated when the system experiences additional delay introduced by the wrench estimator. Ultimately, it exhibits the impossibility of tracking high ideal accelerations.

By taking into account all the previous considerations, we tested the suitability of the designed approach in an unexpected-collision scenario. In the act of colliding with a tilted surface, the admittance filter was able to produce a modified reference

from the desired trajectory during the contact phase, thus indirectly keeping the pushing force limited in the direction of motion and allowing the manipulator to reach the desired compliant behavior. Ultimately, the last presented experiment compared the rotation stiffness variation when the system was involved in the collision. The result illustrated that the added compliance allowed the platform to lean completely against the tilted surface.

9.2 Summary of contributions

The work in this thesis addresses the problem of the cooperative full pose manipulation of payloads performed by multi-robot systems with a particular focus on cable-suspended solutions in air and interaction with the environment. The research community has considerably attempted to address the issue and, there are still ongoing investigations. However, most of the presented works tackled the problem proposing solutions that are partially able to control the pose of the manipulated objects or accept undesired payloads' oscillations.

Within this thesis, with the aid of an extensive set of simulations and empirical results we demonstrated that the problem can be entirely solved. First, using a general single/multi leader-follower paradigm based on the force exchanged between the components of the team, and secondly, by means of a centralized kinematic approach implemented for a CS-AMRM with the property of being the minimal set-up that can have the control of the six DoF of a payload.

In the first case, we contributed with a generic model and a formal analysis on the equilibrium configurations and their stability, when N robots compose the formation. Furthermore, we provided some considerations regarding the role of the inter exchanged forces and the presence of more than one leaders w.r.t. the convergence of the object position and orientation to the desired values. The approach could therefore be interesting for various applications and scenarios in virtue of its generality, scalability and the property of being distributed.

In the second case, we contributed with the conception of a kinematic model to describe the *in-house* designed CS-AMRM, the Fly-Crane. Additionally, we furnished such a system with a control strategy robust to possible model uncertainties and external disturbances such that the system could perform manipulations in real-case scenarios. Subsequently, we improved the control architecture proposing an estimation algorithm of the inertial parameters of the suspended-payload (mass and CoM's position). The method relies on a methodology to project the thrusts generated by the robots on each cable of the system. The approach - which represents another contribution presented in this manuscript - results particularly useful in cases where the CS-AMRM is used to grasp objects in possible interactions with the environment.

In such a context of physical interactions *in-contact* scenarios, we contributed with a shared control strategy that allowed the cooperation between a human operator and the CS-AMRM. At the best of our knowledge, this represented the

first time pick-and-place operations in construction/decommissioning scenarios are accomplished with a multi-robot aerial manipulator which makes use of cables. Last but not least, in the same context, to provision the Fly-Crane with more autonomous capabilities, we contributed by expanding the motion control framework with an admittance filter and a wrench observer. Although the employed algorithms were well known in the robotics community, they were mainly conceived for ground manipulators, and have never been implemented and evaluated on aerial multi-robot manipulators. Therefore, we investigated for the first time the reliability of an external wrench estimation method for the control of a CS-AMRM, we integrate, for the first time, a 6D impedance shaping algorithm within the control architecture of the complex CS-AMRM under exam.

9.3 Future works

Throughout the pages of this thesis, we analyzed the problem of the cooperative full pose manipulation with teams of robots going from the design to the estimation and control of such complex systems. The problem has been addressed from a theoretical perspective and a practical one. Nevertheless, in light of the complexity of the domain, additional challenges could still be faced.

As a matter of fact, although the wide set of simulations provided and the promising results obtained, the first proposed approach, the leader-follower paradigm, lacks a fundamental experimental validation in a real-world scenario that could implicate to consider further details. Among them, the accurate measure or the precise estimation of the interaction force experienced by each robot is a primary aspect for the proper functioning of the proposed control strategy. Additionally, the dynamics of the robots' position controllers should be fast enough to guarantee reliable tracking performances. Hence, the challenge would be to refine the position controller in order to fulfill such requirements. Lastly, the closeness of the robots could cause collisions between the involved vehicles which a collision avoidance strategy would enable to avoid. In any case, we believe that this could be achieved with a reasonable additional effort.

Secondly, in relation to the kinematic approach devised to describe and then to control the Fly-Crane system, advancements could be done in the direction of the reformulation of the approach to avoid the use of coordinates derived from a global frame. As a matter of fact, the proposed centralized approach relies on a MoCap system which provides precise and high-rate exteroceptive pose measurements. To overcome such limitation, the control strategy could be rearranged into a distributed approach. This would open new challenges in terms of pose estimation and inter-agent communication. Moreover, solving these issues would fill the gap which we experience in finally bringing the system into outdoor scenarios.

Another direction could be represented by the design of a dynamic controller to realize high-speed dynamic payload manipulations with our system. For example, such ability could be advantageous when the system needs to rapidly escape obsta-

cles. This would require, first, the derivation of a detailed dynamic model of the Fly-Crane and, afterwards, the conception of its dynamic controller. An extensive validation of the approach in simulation and real-world scenarios would follow. Hence, in our belief, the results would come with considerable effort. Moreover, some dynamical feasibility conditions already investigated in [Manubens 2013, Erskine 2018] have to be considered in the development phase. In actual fact, the system has to, first, statically counteract the forces applied on the platform with positive and acceptable cable tensions to guarantee the tightness of the cables all the time. Secondly, the thrusts exerted by the robots cannot exceed the maximum value they can de facto produce. Therefore, it is reasonable to contemplate possible constrained optimal control algorithms to deal with such restrictions. Subsequently, in light of the presence of such constraints, the results could be compared with a Model Predictive Control framework (MPC) that could be implemented to perform tasks at high dynamics while dealing with the aforementioned challenges.

Another attractive extension could be done towards the accomplishment of physical interaction tasks. The knowledge of the dynamical model of the Fly-Crane could promote the implementation of an impedance controller. Besides testing the extended control architecture in real-world scenarios, it would be interesting to make further comparisons with the already proposed admittance framework. In fact, the impedance control strategy provides robustness against uncertainties in the model parameters and stable contacts in interaction with stiff environments. Conversely, the admittance approach is much better suited for exchanges with soft environments [Ott 2015]. Therefore, the analysis of the complementary characteristics which distinguish these two approaches would pave the way for new challenges in the context of CS-AMRMs. However, the two approaches are not free of shortcomings. While the impedance approach is well-known to bring to an amplification of the noise when stiff behaviors are requested, the admittance strategy causes instability when contacts with stiff environments occur. Therefore, a hybrid framework which deals with such limitations and, at the same time, benefits from the skills of the admittance and the impedance framework could be conceived.

Furthermore, a fruitful enhancement in the shared control functionalities could be realized. Human operators could perform the tasks relying on haptic force feedback in addition to their visual one. The realization of such improvement would provide the operator with a new capability that, in turn, would improve the final outcome in the execution of the assignment. Additionally, to better perform the manipulation tasks or to provide the ability of autonomous navigation in cluttered environments, as construction/decommissioning scenarios are, the platform of the Fly-Crane could be equipped with a vision system that could be exploited as well for the state estimation or localization of the entire system.

Bibliography

[Albers 2010] Albert Albers, Simon Trautmann, Thomas Howard, Trong Anh Nguyen, Markus Frietsch and Christian Sauter. *Semi-autonomous flying robot for physical interaction with environment.* In 2010 IEEE Conference on Robotics, Automation and Mechatronics, pages 441–446, 2010. (Cited in pages 1 and 16.)

[Bernard 2010] M Bernard, K Kondak and G Hommel. *Load transportation system based on autonomous small size helicopters.* The aeronautical journal, vol. 114, no. 1153, pages 191–198, 2010. (Cited in pages 16 and 21.)

[Bernard 2011] Markus Bernard, Konstantin Kondak, Ivan Maza and Anibal Ollero. *Autonomous transportation and deployment with aerial robots for search and rescue missions.* Journal of Field Robotics, vol. 28, no. 6, pages 914–931, 2011. (Cited in pages 16 and 21.)

[Brescianini 2018] Dario Brescianini and Raffaello D'Andrea. *Computationally efficient trajectory generation for fully actuated multirotor vehicles.* IEEE Transactions on Robotics, vol. 34, no. 3, pages 555–571, 2018. (Cited in page 17.)

[Briot 2015] Sébastien Briot, Wisama Khalil*et al. Dynamics of parallel robots.* From rigid bodies to flexible elements. Springer, 2015. (Cited in pages 38 and 42.)

[Buaphim 2018] N. Buaphim, K. Onsaard, P. Songoen and T. Rungratgasame. *Some reviews on ranks of upper triangular block matrices over a skew field.* International Mathematical Forum, vol. 13, no. 7, pages 559–566, 2018. (Cited in page 77.)

[Cai 2014] Guowei Cai, Jorge Dias and Lakmal Seneviratne. *A survey of small-scale unmanned aerial vehicles: Recent advances and future development trends.* Unmanned Systems, vol. 2, no. 02, pages 175–199, 2014. (Cited in page 15.)

[Cataldi 2016] E. Cataldi, G. Muscio, M. A. Trujillo, Y. Rodriguez, F. Pierri, G. Antonelli, F. Caccavale, A. Viguria, S. Chiaverini and A. Ollero. *Impedance Control of an aerial-manipulator: Preliminary results.* In 2016 IEEE/RSJ International Conference on Intelligent Robots and Systems (IROS), pages 3848–3853, 2016. (Cited in page 24.)

[Connelly 2015] R. Connelly and S. D. Guest. *Frameworks, tensegrities and symmetry: understanding stable structures.* Cornell University, College of Arts and Sciences, 2015. (Cited in page 22.)

[Danko 2015] Todd W. Danko, Kenneth P. Chaney and Paul Y. Oh. *A parallel manipulator for mobile manipulating UAVs.* In 2015 IEEE International Conference on Technologies for Practical Robot Applications (TePRA), pages 1–6, 2015. (Cited in page 17.)

[De Luca 2005] A. De Luca and R. Mattone. *Sensorless robot collision detection and hybrid force/motion control.* In 2005 IEEE Int. Conf. on Robotics and Automation, pages 999–1004, Barcelona, Spain, Apr. 2005. (Cited in page 125.)

[De Marina 2019] Hector Garcia De Marina and Ewoud Smeur. *Flexible collaborative transportation by a team of rotorcraft.* In 2019 International Conference on Robotics and Automation (ICRA), pages 1074–1080. IEEE, 2019. (Cited in pages 21 and 23.)

[Dhiman 2018] K. K. Dhiman, A. Abhishek and M. Kothari. *Cooperative Load Control and Transportation.* In 2018 AIAA Information Systems-AIAA Infotech@ Aerospace, page 0895. 2018. (Cited in page 23.)

[Erskine 2018] Julian Erskine, Abdelhamid Chriette and Stéphane Caro. *Wrench capability analysis of aerial cable towed systems.* In International Design Engineering Technical Conferences and Computers and Information in Engineering Conference, volume 51807, page V05AT07A032. American Society of Mechanical Engineers, 2018. (Cited in page 143.)

[Erskine 2019] Julian Erskine, Abdelhamid Chriette and Stéphane Caro. *Control and configuration planning of an aerial cable towed system.* In 2019 International Conference on Robotics and Automation (ICRA), pages 6440–6446. IEEE, 2019. (Cited in pages 1, 20, and 21.)

[Farivarnejad 2018] Hamed Farivarnejad and Spring Berman. *Stability and convergence analysis of a decentralized proportional-integral control strategy for collective transport.* In 2018 annual American control conference (ACC), pages 2794–2801. IEEE, 2018. (Cited in page 23.)

[Fink 2011] J. Fink, N. Michael, S. Kim and V. Kumar. *Planning and control for cooperative manipulation and transportation with aerial robots.* The International Journal of Robotics Research, vol. 30, no. 3, pages 324–334, 2011. (Cited in pages 21 and 22.)

[Franchi 2012] A. Franchi, C. Masone, V. Grabe, M. Ryll, H. H. Bülthoff and P. Robuffo Giordano. *Modeling and Control of UAV Bearing-Formations with Bilateral High-Level Steering.* The International Journal of Robotics Research, Special Issue on 3D Exploration, Mapping, and Surveillance, vol. 31, no. 12, pages 1504–1525, 2012. (Cited in page 25.)

[Franchi 2017] A. Franchi and A. Mallet. *Adaptive Closed-loop Speed Control of BLDC Motors with Applications to Multi-rotor Aerial Vehicles.* In 2017

IEEE Int. Conf. on Robotics and Automation, pages 5203–5208, Singapore, May 2017. (Cited in page 50.)

[Gabellieri 2018] C. Gabellieri, M. Tognon, L. Palottino and A. Franchi. *A Study on Force-based Collaboration in Flying Swarms.* In 11th Int. Conf. on Swarm Intelligence, pages 3–15, Rome, Italy, Oct. 2018. (Cited in page 23.)

[Gabellieri 2020] C. Gabellieri, M. Tognon, D. Sanalitro, L. Palottino and A. Franchi. *A Study on Force-based Collaboration in Swarms.* Swarm Intelligence, vol. 14, pages 57–82, 2020. (Cited in page 27.)

[Gassner 2017] M. Gassner, T. Cieslewski and D. Scaramuzza. *Dynamic collaboration without communication: Vision-based cable-suspended load transport with two quadrotors.* In 2017 IEEE Int. Conf. on Robotics and Automation, pages 5196–5202, Singapore, May 2017. (Cited in pages 1, 20, and 21.)

[Geng 2019] J. Geng and J. W. Langelaan. *Implementation And Demonstration Of Coordinated Transport Of A Slung Load By A Team Of Rotorcraft.* In AIAA Scitech 2019 Forum, page 0913, 2019. (Cited in page 23.)

[Goodarzi 2016] Farhad A Goodarzi and Taeyoung Lee. *Stabilization of a rigid body payload with multiple cooperative quadrotors.* Journal of Dynamic Systems, Measurement, and Control, vol. 138, no. 12, 2016. (Cited in page 47.)

[Haddadin 2017] Sami Haddadin, Alessandro De Luca and Alin Albu-Schäffer. *Robot Collisions: A Survey on Detection, Isolation, and Identification.* IEEE Transactions on Robotics, vol. 33, no. 6, pages 1292–1312, 2017. (Cited in pages 23 and 125.)

[Hamandi 2021] M. Hamandi, F. Usai, Q. Sable, N. Staub, M Tognon and A. Franchi. *Design of Multirotor Aerial Vehicles: a Taxonomy Based on Input Allocation.* accepted, The International Journal of Robotics Research, vol. 40, no. 8-9, pages 1015–1044, 2021. (Cited in page 50.)

[Hamel 2002] Tarek Hamel, Robert Mahony, Rogelio Lozano and James Ostrowski. *Dynamic modelling and configuration stabilization for an X4-flyer.* IFAC Proceedings Volumes, vol. 35, no. 1, pages 217–222, 2002. (Cited in page 49.)

[Hofer 2016] Matthias Hofer, Michael Muehlebach and Raffaello D'Andrea. *Application of an approximate model predictive control scheme on an unmanned aerial vehicle.* In 2016 IEEE International Conference on Robotics and Automation (ICRA), pages 2952–2957, 2016. (Cited in page 15.)

[Jiang 2013] Qimi Jiang and Vijay Kumar. *The Inverse Kinematics of Cooperative Transport With Multiple Aerial Robots.* IEEE Transactions on Robotics, vol. 29, no. 1, pages 136–145, 2013. (Cited in page 21.)

[Jiang 2015] Jingjing Jiang and Alessandro Astolfi. *Shared-control for a UAV operating in the 3D space.* In 2015 European Control Conference (ECC), pages 1633–1638, 2015. (Cited in page 24.)

[Jimenez-Cano 2013] A.E. Jimenez-Cano, J. Martin, G. Heredia, A. Ollero and R. Cano. *Control of an aerial robot with multi-link arm for assembly tasks.* In 2013 IEEE International Conference on Robotics and Automation, pages 4916–4921, 2013. (Cited in page 17.)

[Jimenez Cano 2021] Antonio Enrique Jimenez Cano, Dario Sanalitro, Marco Tognon, Antonio Franchi and Cortés Juan. *Precise Cable-suspended Pick-and-Place with an Aerial Multi-robot System: A proof of concept for novel robotics-based construction techniques.* submitted to International Journal of Intelligent and Robotics Systems, 2021. (Cited in page 27.)

[Kamel 2016] Mina Kamel, Kostas Alexis and Roland Siegwart. *Design and modeling of dexterous aerial manipulator.* In 2016 IEEE/RSJ International Conference on Intelligent Robots and Systems (IROS), pages 4870–4876, 2016. (Cited in page 17.)

[Kanellakis 2017] Christoforos Kanellakis, Matteo Terreran, Dariusz Kominiak and George Nikolakopoulos. *On vision enabled aerial manipulation for multirotors.* In 2017 22nd IEEE International Conference on Emerging Technologies and Factory Automation (ETFA), pages 1–7. IEEE, 2017. (Cited in page 17.)

[Khalil 2001] H. K. Khalil. Nonlinear systems. Prentice Hall, 3rd edition, 2001. (Cited in page 69.)

[Kim 2018a] Hyoin Kim, Hoseong Seo, Clark Youngdong Son, Hyeonbeom Lee, Suseong Kim and H. Jin Kim. *Cooperation in the Air: A Learning-Based Approach for the Efficient Motion Planning of Aerial Manipulators.* IEEE Robotics Automation Magazine, vol. 25, no. 4, pages 76–85, 2018. (Cited in page 20.)

[Kim 2018b] Suseong Kim, Hoseong Seo, Jongho Shin and H. Jin Kim. *Cooperative Aerial Manipulation Using Multirotors With Multi-DOF Robotic Arms.* IEEE/ASME Transactions on Mechatronics, vol. 23, no. 2, pages 702–713, 2018. (Cited in pages 1 and 20.)

[Kim 2018c] Suseong Kim, Hoseong Seo, Jongho Shin and H. Jin Kim. *Cooperative Aerial Manipulation Using Multirotors With Multi-DOF Robotic Arms.* IEEE/ASME Transactions on Mechatronics, vol. 23, no. 2, pages 702–713, 2018. (Cited in page 24.)

[Kondak 2014] K. Kondak, F. Hubert, M. Schwarzbach, M. Laiacker, D. Sommer, M. Bejar and A. Ollero. *Aerial manipulation robot composed of an autonomous helicopter and a 7 degrees of freedom industrial manipulator.* In

2014 IEEE Int. Conf. on Robotics and Automation, pages 2108–2112, Hong Kong, China, May 2014. (Cited in page 16.)

[Lee 2010] T. Lee, M. Leoky and N. H. McClamroch. *Geometric tracking control of a quadrotor UAV on SE(3).* In 49th IEEE Conf. on Decision and Control, pages 5420–5425, Atlanta, GA, Dec. 2010. (Cited in page 117.)

[Lee 2013] D. J. Lee, A. Franchi, H. I. Son, H. H. Bülthoff and P. Robuffo Giordano. *Semi-Autonomous Haptic Teleoperation Control Architecture of Multiple Unmanned Aerial Vehicles.* IEEE/ASME Trans. on Mechatronics, Focused Section on Aerospace Mechatronics, vol. 18, no. 4, pages 1334–1345, 2013. (Cited in page 24.)

[Lee 2015] Hyeonbeom Lee, Hyoin Kim and H. Jin Kim. *Path planning and control of multiple aerial manipulators for a cooperative transportation.* In 2015 IEEE/RSJ International Conference on Intelligent Robots and Systems (IROS), pages 2386–2391, 2015. (Cited in page 20.)

[Lee 2017] Taeyoung Lee. *Geometric control of quadrotor UAVs transporting a cable-suspended rigid body.* IEEE Transactions on Control Systems Technology, vol. 26, no. 1, pages 255–264, 2017. (Cited in page 22.)

[Li 2020] Zhen Li, Julian Erskine, Stéphane Caro and Abdelhamid Chriette. *Design and Control of a Variable Aerial Cable Towed System.* IEEE Robotics and Automation Letters, vol. 5, no. 2, pages 636–643, 2020. (Cited in page 21.)

[Lindsey 2012] Q. Lindsey, D. Mellinger and V. Kumar. *Construction with quadrotor teams.* Autonomous Robots, vol. 33, no. 3, pages 323–336, 2012. (Cited in page 16.)

[Lippiello 2015] Vincenzo Lippiello, Jonathan Cacace, Angel Santamaria-Navarro, Juan Andrade-Cetto, Miguel Angel Trujillo, Yamnia Rodríguez Rodríguez Esteves and Antidio Viguria. *Hybrid visual servoing with hierarchical task composition for aerial manipulation.* IEEE Robotics and Automation Letters, vol. 1, no. 1, pages 259–266, 2015. (Cited in page 17.)

[Loianno 2018] Giuseppe Loianno and Vijay Kumar. *Cooperative Transportation Using Small Quadrotors Using Monocular Vision and Inertial Sensing.* IEEE Robotics and Automation Letters, vol. 3, no. 2, pages 680–687, 2018. (Cited in page 20.)

[Lupashin 2013] S. Lupashin and R. D'Andrea. *Stabilization of a Flying Vehicle on a Taut Tether using Inertial Sensing.* In 2013 IEEE/RSJ Int. Conf. on Intelligent Robots and Systems, pages 2432–2438, Tokyo, Japan, Nov 2013. (Cited in page 46.)

[Lynch 2017] Kevin M Lynch and Frank C Park. Modern robotics. Cambridge University Press, 2017. (Cited in page 34.)

[Mahony 2012] Robert Mahony, Vijay Kumar and Peter Corke. *Multirotor aerial vehicles: Modeling, estimation, and control of quadrotor.* IEEE Robotics and Automation magazine, vol. 19, no. 3, pages 20–32, 2012. (Cited in pages 42, 49, and 52.)

[Manubens 2013] M. Manubens, D. Devaurs, L. Ros and J. Cortés. *Motion Planning for 6-D Manipulation with Aerial Towed-cable Systems.* In 2013 Robotics: Science and Systems, Berlin, Germany, May 2013. (Cited in pages 22, 75, and 143.)

[Masone 2016] C. Masone, H. H. Bülthoff and P. Stegagno. *Cooperative transportation of a payload using quadrotors: A reconfigurable cable-driven parallel robot.* In 2016 IEEE/RSJ Int. Conf. on Intelligent Robots and Systems, pages 1623–1630, Oct 2016. (Cited in pages 1 and 22.)

[Masone 2018] C. Masone, M. Mohammadi, P. Robuffo Giordano and A. Franchi. *Shared Planning and Control for Mobile Robots with Integral Haptic Feedback.* The International Journal of Robotics Research, vol. 37, no. 11, pages 1395–1420, 2018. (Cited in page 24.)

[Masone 2021] Carlo Masone and Paolo Stegagno. *Shared Control of an Aerial Cooperative Transportation System with a Cable-suspended Payload.* Journal of Intelligent & Robotic Systems, vol. 103, no. 3, pages 1–29, 2021. (Cited in page 25.)

[Mellinger 2011] D. Mellinger, Q. Lindsey, M. Shomin and V. Kumar. *Design, modeling, estimation and control for aerial grasping and manipulation.* In 2011 IEEE/RSJ Int. Conf. on Intelligent Robots and Systems, pages 2668–2673, San Francisco, CA, Sep. 2011. (Cited in page 16.)

[Mellinger 2013] Daniel Mellinger, Michael Shomin, Nathan Michael and Vijay Kumar. Cooperative grasping and transport using multiple quadrotors, pages 545–558. Springer Berlin Heidelberg, Berlin, Heidelberg, 2013. (Cited in page 20.)

[Meng 2018] Xiangdong Meng, Yuqing He, Qi Li, Feng Gu, Liying Yang, Tengfei Yan and Jianda Han. *Contact Force Control of an Aerial Manipulator in Pressing an Emergency Switch Process.* In 2018 IEEE/RSJ International Conference on Intelligent Robots and Systems (IROS), pages 2107–2113, 2018. (Cited in page 24.)

[Merlet 2005] Jean-Pierre Merlet. Parallel robots, volume 128. Springer Science & Business Media, 2005. (Cited in pages 38 and 39.)

[Michael 2009] N. Michael, J. Fink and V. Kumar. *Cooperative Manipulation and Transportation with Aerial Robots.* In 2009 Robotics: Science and Systems, Seattle, WA, Jun. 2009. (Cited in pages 21 and 22.)

[Michael 2011] Nathan Michael, Jonathan Fink and Vijay Kumar. *Cooperative manipulation and transportation with aerial robots.* Autonomous Robots, vol. 30, no. 1, pages 73–86, 2011. (Cited in pages 21 and 22.)

[Mohammadi 2016] Mostafa Mohammadi, Antonio Franchi, Davide Barcelli and Domenico Prattichizzo. *Cooperative aerial tele-manipulation with haptic feedback.* In 2016 IEEE/RSJ International Conference on Intelligent Robots and Systems (IROS), pages 5092–5098, 2016. (Cited in page 20.)

[Morin 2015] P. Morin. *Modeling and control of convertible Micro Air Vehicles.* In 2015 10th International Workshop on Robot Motion and Control (RoMoCo), pages 188–198, 2015. (Cited in page 15.)

[Morton 2016] Kye Morton and Luis Felipe Gonzalez Toro. *Development of a robust framework for an outdoor mobile manipulation UAV.* In 2016 IEEE Aerospace Conference, pages 1–8, 2016. (Cited in pages 1 and 17.)

[Muscio 2018] G. Muscio, F. Pierri, M. A. Trujillo, E. Cataldi, G. Antonelli, F. Caccavale, A. Viguria, S. Chiaverini and A. Ollero. *Coordinated Control of Aerial Robotic Manipulators: Theory and Experiments.* IEEE Transactions on Control Systems Technology, vol. 26, no. 4, pages 1406–1413, 2018. (Cited in pages 1 and 17.)

[Nava 2020] G. Nava, Q. Sablé, M. Tognon, D. Pucci and A. Franchi. *Direct Force Feedback Control and Online Multi-task Optimization for Aerial Manipulators.* IEEE Robotics and Automation Letters, vol. 5, no. 2, pages 331–338, 2020. (Cited in page 24.)

[Nguyen 2015] H.-N. Nguyen, S. Park and D. J. Lee. *Aerial Tool Operation System using Quadrotors as Rotating Thrust Generators.* In 2015 IEEE/RSJ Int. Conf. on Intelligent Robots and Systems, pages 1285–1291, Hamburg, Germany, Oct. 2015. (Cited in pages 1 and 20.)

[Nguyen 2018] H. N. Nguyen, S. Park, J. Park and D. Lee. *A Novel Robotic Platform for Aerial Manipulation Using Quadrotors as Rotating Thrust Generators.* IEEE Trans. on Robotics, vol. 34, no. 2, pages 353–369, 2018. (Cited in pages 20 and 24.)

[Nicotra 2017] Marco M Nicotra, Roberto Naldi and Emanuele Garone. *Nonlinear control of a tethered UAV: The taut cable case.* Automatica, vol. 78, pages 174–184, 2017. (Cited in page 46.)

[Ollero 2018] Anibal Ollero, Guillermo Heredia, Antonio Franchi, Gianluca Antonelli, Konstantin Kondak, Alberto Sanfeliu, Antidio Viguria, J. Ramiro Martinez-de Dios, Francesco Pierri, Juan Cortes, Angel Santamaria-Navarro, Miguel Angel Trujillo Soto, Ribin Balachandran, Juan Andrade-Cetto and Angel Rodriguez. *The AEROARMS Project: Aerial Robots with Advanced*

Manipulation Capabilities for Inspection and Maintenance. IEEE Robotics Automation Magazine, vol. 25, no. 4, pages 12–23, 2018. (Cited in pages 1, 17, and 18.)

[Ollero 2021] A. Ollero, M. Tognon, A. Suarez, D. J. Lee and A. Franchi. *Past, Present, and Future of Aerial Robotic Manipulators.* IEEE Trans. on Robotics, 2021. (Cited in page 16.)

[Orsag 2016] M. Orsag, T. Haus, D. Tolić, A. Ivanovic, M. Car, I. Palunko and S. Bogdan. *Human-in-the-loop control of multi-agent aerial systems.* In 2016 European Control Conference (ECC), pages 2139–2145, 2016. (Cited in page 25.)

[Ott 2015] Christian Ott, Ranjan Mukherjee and Yoshihiko Nakamura. *A hybrid system framework for unified impedance and admittance control.* Journal of Intelligent & Robotic Systems, vol. 78, no. 3, pages 359–375, 2015. (Cited in page 143.)

[Pajares 2015] Gonzalo Pajares. *Overview and current status of remote sensing applications based on unmanned aerial vehicles (UAVs).* Photogrammetric Engineering & Remote Sensing, vol. 81, no. 4, pages 281–330, 2015. (Cited in page 14.)

[Palunko 2012] Ivana Palunko, Patricio Cruz and Rafael Fierro. *Agile Load Transportation : Safe and Efficient Load Manipulation with Aerial Robots.* IEEE Robotics Automation Magazine, vol. 19, no. 3, pages 69–79, 2012. (Cited in page 16.)

[Palunko 2013] Ivana Palunko, Aleksandra Faust, Patricio Cruz, Lydia Tapia and Rafael Fierro. *A reinforcement learning approach towards autonomous suspended load manipulation using aerial robots.* In 2013 IEEE International Conference on Robotics and Automation, pages 4896–4901, 2013. (Cited in page 16.)

[Paul 1983] RP Paul. *Mathematics, Programming and Control. The Computer Control of Robot Manipulators*, 1983. (Cited in page 13.)

[Peric 2021] Lazar Peric, Maximilian Brunner, Karen Bodie, Marco Tognon and Roland Siegwart. *Direct Force and Pose NMPC with Multiple Interaction Modes for Aerial Push-and-Slide Operations.* In International Conference on Robotics and Automation (ICRA 2021), 2021. (Cited in page 24.)

[Petitti 2020] A. Petitti, D. Sanalitro, M. Tognon, A. Milella, J. Cortés and A. Franchi. *Inertial Estimation and Energy-Efficient Control of a Cable-suspended Load with a Team of UAVs.* In 2020 Int. Conf. on Unmanned Aircraft Systems, Athens, Greece, Sep. 2020. (Cited in page 27.)

[Pounds 2010a] Paul Pounds, Robert Mahony and Peter Corke. *Modelling and control of a large quadrotor robot.* Control Engineering Practice, vol. 18, no. 7, pages 691–699, 2010. (Cited in page 49.)

[Pounds 2010b] Paul EI Pounds and Aaron Dollar. *Hovering stability of helicopters with elastic constraints.* In Dynamic Systems and Control Conference, volume 44182, pages 781–788, 2010. (Cited in page 16.)

[Pounds 2012] Paul EI Pounds, Daniel R Bersak and Aaron M Dollar. *Stability of small-scale UAV helicopters and quadrotors with added payload mass under PID control.* Autonomous Robots, vol. 33, no. 1, pages 129–142, 2012. (Cited in pages 1 and 16.)

[Prajapati 2020] Pratik Prajapati, Sagar Parekh and Vineet Vashista. *On the Human Control of a Multiple Quadcopters with a Cable-suspended Payload System.* In 2020 IEEE International Conference on Robotics and Automation (ICRA), pages 2253–2258, 2020. (Cited in page 25.)

[Prattichizzo 2008] D. Prattichizzo and J. C. Trinkle. *Grasping.* In B. Siciliano and O. Khatib, editors, Springer Handbook of Robotics, pages 671–700. Springer, 2008. (Cited in pages 21 and 22.)

[Pucci 2013] Daniele Pucci, Tarek Hamel, Pascal Morin and Claude Samson. *Nonlinear control of aerial vehicles subjected to aerodynamic forces.* In 52nd IEEE Conference on Decision and Control, pages 4839–4846. IEEE, 2013. (Cited in page 49.)

[Pumarola 2019] Albert Pumarola, Alexander Vakhitov, Antonio Agudo, Francesc Moreno-Noguer and Alberto Sanfeliu. *Relative localization for aerial manipulation with PL-SLAM.* In Aerial Robotic Manipulation, pages 239–248. Springer, 2019. (Cited in page 17.)

[Ren 2012] Beibei Ren, Shuzhi Sam Ge, Chang Chen, Cheng-Heng Fua and Tong Heng Lee. Modeling, control and coordination of helicopter systems. Springer Science & Business Media, 2012. (Cited in page 15.)

[Rossomando 2020] Francisco Rossomando, Claudio Rosales, Javier Gimenez, Lucio Salinas, Carlos Soria, Mario Sarcinelli-Filho and Ricardo Carelli. *Aerial load transportation with multiple quadrotors based on a kinematic controller and a neural SMC dynamic compensation.* Journal of Intelligent & Robotic Systems, vol. 100, no. 2, pages 519–530, 2020. (Cited in page 21.)

[Ryll 2019] M. Ryll, G. Muscio, F. Pierri, E. Cataldi, G. Antonelli, F. Caccavale, D. Bicego and A. Franchi. *6D Interaction Control with Aerial Robots: The Flying End-Effector Paradigm.* The International Journal of Robotics Research, vol. 38, no. 9, pages 1045–1062, 2019. (Cited in pages 1, 17, 18, and 24.)

[Sanalitro 2020] D. Sanalitro, H. J. Savino, M. Tognon, J. Cortés and A. Franchi. *Full-pose Manipulation Control of a Cable-suspended load with Multiple UAVs under Uncertainties*. IEEE Robotics and Automation Letters, vol. 5, no. 2, pages 2185–2191, 2020. (Cited in page 27.)

[Sanalitro 2022] Dario Sanalitro, Marco Tognon, Antonio Enrique Jimenez Cano, Antonio Franchi and Cortés Juan. *Indirect Force Control of a Cable-suspended Aerial Multi-Robot Manipulator*. submitted to Robotics Automation Letters, 2022. (Cited in page 27.)

[Sandino 2015] Luis A Sandino, Manuel Bejar, Konstantin Kondak and Anibal Ollero. *A Square-Root Unscented Kalman Filter for attitude and relative position estimation of a tethered unmanned helicopter*. In 2015 International Conference on Unmanned Aircraft Systems (ICUAS), pages 567–576. IEEE, 2015. (Cited in page 47.)

[Sarkisov 2019] Y. Sarkisov, M. J. Kim, D. Bicego, D. Tsetserukou, C. Ott, A. Franchi and K. Kondak. *Development of SAM: cable-Suspended Aerial Manipulator*. In 2019 IEEE Int. Conf. on Robotics and Automation, Montreal, Canada, May 2019. (Cited in page 17.)

[Schwerdtfeger 1961] H. Schwerdtfeger. Introduction to linear algebra and the theory of matrices. Noordhoff, Groningen, 1961. (Cited in page 77.)

[Siciliano 2009] Bruno Siciliano, Lorenzo Sciavicco, Luigi Villani and Giuseppe Oriolo. *Modelling, planning and control*. Advanced Textbooks in Control and Signal Processing. Springer„ 2009. (Cited in pages 13 and 34.)

[Six 2018] D. Six, S. Briot, A. Chriette and P. Martinet. *The Kinematics, Dynamics and Control of a Flying Parallel Robot With Three Quadrotors*. IEEE Robotics and Automation Letters, vol. 3, no. 1, pages 559–566, Jan 2018. (Cited in page 60.)

[Six 2021] Damien Six, Sébastien Briot, Abdelhamid Chriette and Philippe Martinet. *Dynamic modelling and control of flying parallel robots*. Control Engineering Practice, vol. 117, page 104953, 2021. (Cited in pages 20 and 60.)

[Slotine 1991] J. J. E. Slotine and W. Li. Applied nonlinear control. Prentice Hall, 1991. (Cited in page 80.)

[Spong 2006] Mark W Spong, Seth Hutchinson, Mathukumalli Vidyasagar*et al.* Robot modeling and control, volume 3. wiley New York, 2006. (Cited in page 34.)

[Sreenath 2013] K. Sreenath and V. Kumar. *Dynamics, Control and Planning for Cooperative Manipulation of Payloads Suspended by Cables from Multiple Quadrotor Robots*. In Robotics: Science and Systems, Berlin, Germany, June 2013. (Cited in pages 1 and 22.)

[Suarez 2020] Alejandro Suarez, Fran Real, Víctor M. Vega, Guillermo Heredia, Angel Rodriguez-Castaño and Anibal Ollero. *Compliant Bimanual Aerial Manipulation: Standard and Long Reach Configurations.* IEEE Access, vol. 8, pages 88844–88865, 2020. (Cited in page 17.)

[Sugasawa 2021] Shoko Sugasawa, Barbara Webb and Susan D Healy. *Object manipulation without hands.* Proceedings of the Royal Society B, vol. 288, no. 1947, page 20203184, 2021. (Cited in page 19.)

[Tagliabue 2019] Andrea Tagliabue, Mina Kamel, Roland Siegwart and Juan Nieto. *Robust collaborative object transportation using multiple mavs.* The International Journal of Robotics Research, vol. 38, no. 9, pages 1020–1044, 2019. (Cited in page 20.)

[Tan 2018] Y. H. Tan, S. Lai, K. Wang and B.M. Chen. *Cooperative control of multiple unmanned aerial systems for heavy duty carrying.* Annual Reviews in Control, vol. 46, pages 44–57, 2018. (Cited in page 23.)

[Tognon 2018] M. Tognon, C. Gabellieri, L. Pallottino and A. Franchi. *Aerial Co-Manipulation with Cables: The Role of Internal Force for Equilibria, Stability, and Passivity.* IEEE Robotics and Automation Letters, Special Issue on Aerial Manipulation, vol. 3, no. 3, pages 2577 – 2583, 2018. (Cited in pages 21, 24, 57, 68, and 69.)

[Umili 2020] E. Umili, M. Tognon, D. Sanalitro, G. Oriolo and A. Franchi. *Communication-based and Communication-less approaches for Robust Cooperative Planning in Construction with a Team of UAVs.* In 2020 Int. Conf. on Unmanned Aircraft Systems, Athens, Greece, Sep. 2020. (Cited in page 31.)

[Villa 2021] Daniel Khede Dourado Villa, Alexandre Santos Brandão, Ricardo Carelli and Mário Sarcinelli-Filho. *Cooperative Load Transportation With Two Quadrotors Using Adaptive Control.* IEEE Access, vol. 9, pages 129148–129160, 2021. (Cited in page 21.)

[Villani 2016] Luigi Villani and Joris De Schutter. *Force control.* In Springer handbook of robotics, pages 195–220. Springer, 2016. (Cited in page 126.)

[Yang 2015] Hyunsoo Yang and Dongjun Lee. *Hierarchical cooperative control framework of multiple quadrotor-manipulator systems.* In 2015 IEEE International Conference on Robotics and Automation (ICRA), pages 4656–4662, 2015. (Cited in page 20.)

[Yiğit 2021] Arda Yiğit, Miguel Arpa Perozo, Mandela Ouafo, Loïc Cuvillon, Sylvain Durand and Jacques Gangloff. *Aerial Manipulator Suspended from a Cable-Driven Parallel Robot: Preliminary Experimental Results.* In 2021 IEEE/RSJ International Conference on Intelligent Robots and Systems (IROS), pages 9662–9668, 2021. (Cited in page 17.)

[Zienkiewicz 2005] Olek C Zienkiewicz and Robert L Taylor. The finite element method for solid and structural mechanics. Elsevier, 2005. (Cited in page 47.)